

Towards next-generation enzymatic generators of hydrogen peroxide in quantitative redox biology

by

Joseph Benigno Lim

M.S. Chemical Engineering Practice
Massachusetts Institute of Technology, 2013

B.S. Chemical Engineering, B.S. Biochemistry
University of Maryland, College Park, 2010

Submitted to the Department of Chemical Engineering
in partial fulfillment of the requirements for the degree of
Doctor of Science in Chemical Engineering

Submitted to the Faculty
in partial fulfillment of the requirements for the degree of
Doctor of Science in Chemical Engineering

at the

Massachusetts Institute of Technology

May 2015 [June 2015]

©Massachusetts Institute of Technology 2015
All rights reserved.



Signature redacted

Signature of author.....

Joseph Benigno Lim
Department of Chemical Engineering
May 15, 2015

Signature redacted

Certified by.....

Hadley D. Sikes
Assistant Professor of Chemical Engineering
Thesis supervisor

Signature redacted

Accepted by.....

Richard D. Braatz
Edwin R. Gilliland Professor
Chairman, Committee for Graduate Students

Towards next-generation enzymatic generators of hydrogen peroxide in quantitative redox biology

by

Joseph Benigno Lim

Abstract

Hydrogen peroxide (H_2O_2) is a natural byproduct of cellular metabolism that has also been implicated in numerous biological processes, including the respiratory burst, proliferation, apoptosis, and cellular signaling. H_2O_2 has been well studied using methodologies to both measure and perturb H_2O_2 levels inside and outside cells. To perturb H_2O_2 levels, researchers have historically used bolus addition to cell culture or stimulation and inhibition of nicotinamide adenine dinucleotide phosphate (NADPH) oxidase. However, these methodologies add conflating variables of extracellular H_2O_2 , a gradient between extracellular and intracellular species, and production of superoxide (O_2^-) as an intermediate, complicating interpretation of resulting biological effects. Furthermore, bolus addition in particular adds H_2O_2 in nonphysiological amounts, which may result in effects not seen when H_2O_2 is produced endogenously during events in which H_2O_2 has been implicated.

To more accurately mimic physiological production of H_2O_2 , researchers have recently turned to soluble, localizable enzymes, including glucose oxidase (GOX), xanthine oxidase (XO), and D-amino acid oxidase (DAAO). GOX, modulated by the H_2O_2 scavenger catalase, has been primarily used for extracellular generation, as has been XO; neither can be used effectively inside the cell because of GOX's requirement of a valuable metabolite, glucose, and XO's promiscuous activity on a variety of substrates and production of O_2^- in addition to H_2O_2 . DAAO has been genetically encoded and used for intracellular H_2O_2 production in numerous studies; however, its requirement of exogenous substrate, typically D-alanine, and production of byproducts ammonia and α -keto acid may still introduce conflating effects.

The objective of this thesis was to develop criteria for an ideal H_2O_2 generator and methodologies to engineer enzymes that meet those criteria. An ideal enzymatic H_2O_2 generator would enable meaningful perturbations to H_2O_2 levels and enable its kinetic production and steady state concentration to be quantitatively linked with signaling events and phenotypes. We first describe the criteria of an ideal H_2O_2 generator and use current kinetic parameters and concentrations of enzymes involved in H_2O_2 scavenging in HeLa cells to determine the production rate of H_2O_2 required to overcome the cell's antioxidant capacity, which constitutes one of the criteria of an ideal generator.

To develop a methodology to engineer H_2O_2 -generating enzymes, we sought to use an H_2O_2 sensor and *Escherichia coli* as a platform. Thus, in the first aim, we describe use of HyPer, a proteinaceous H_2O_2 sensor, in *E. coli* when H_2O_2 is added in bolus. We demonstrated that experimental parameters typically not reported, including amount of H_2O_2 per cell, cell density, *E. coli* strain, and timing of measurement, can significantly impact the signal. We also showed that the sensor's signal lags behind the actual amount of H_2O_2 remaining in culture during diffusion into and scavenging by *E. coli*, making HyPer a reversible, rather than real-time, sensor. We also generated dose-response curves and fitted these to the Hill equation, acquiring parameters that enable meaningful comparisons of the signal across studies, including dynamic range, signal-to-noise ratio, and half saturation constant. This new framework for

characterizing HyPer's signal in *E. coli* is relevant not only to the respiratory burst, in which H₂O₂ and other related reactive species are generated to destroy invasive pathogens, but also to our work in devising a new methodology for engineering enzymes with higher H₂O₂ production.

After developing a protocol to use HyPer in *E. coli*, we co-expressed the sensor with cytochrome P450 BM3 in *E. coli* to demonstrate the efficacy of a novel whole-cell screen for H₂O₂ production. We chose P450 BM3 as the target enzyme because of its satisfaction of all criteria of an ideal H₂O₂ generator except total activity in mammalian cells. We chose a co-expression scheme that minimizes variability in expression of the sensor, to avoid obfuscating interpretation of the signal. We then demonstrated that a higher signal is attained when HyPer is co-expressed with I401P, a P450 BM3 variant known to produce H₂O₂ at a higher rate versus the wild-type enzyme. Finally, we applied a directed evolution approach to generate a library of random P450 BM3 variants and used the screen to find novel variants with enhanced H₂O₂ production, confirming the screen's efficacy. The screen significantly improves upon previous methodologies for enhancing H₂O₂ production by avoiding the need to lyse the cells and add extra reagents, reducing the amount of time required for each round of evolution. We expect the screen to find use in finding and optimizing both candidate enzymes that meet the criteria of an ideal H₂O₂ generator, as well as enzymes that produce a valuable byproduct alongside H₂O₂.

Finally, we note the importance of localization of H₂O₂ generation in transducing its effects. While the current kinetic model allows calculation of the H₂O₂ production rate required to overcome the cell's antioxidant capacity, it does not account for localization and resulting spatial variations in the concentration of intracellular H₂O₂. In the last section, we describe development of a transport model that predicts H₂O₂ concentration profiles inside the cell. We found that the kinetic model can be approximated by accounting for only peroxiredoxin as the sole H₂O₂ scavenger that does not become depleted by H₂O₂ oxidation. We thus reduced the model to a single equation, allowing us to use the finite Fourier Transform (FFT) method to develop an analytical transport model. This should enable feedback between theory and experiment, allowing us to refine the model parameters used to determine the H₂O₂ production rate necessary for an ideal generator.

Together, these findings advance the field of redox biology by laying the methodologies and framework for engineering an ideal enzymatic H₂O₂ generator, the development of which should enable physiologically meaningful perturbations of H₂O₂ levels inside the cell.

Thesis supervisor: Hadley D. Sikes

Title: Assistant Professor of Chemical Engineering

Acknowledgements

When I first arrived in Cambridge, I did not realize how profoundly life-changing my experience at MIT would be, and it would not have been possible without so many people.

I first want to thank Hadley Sikes. I appreciate her reaching out to me while I was still at the University of Maryland, and feel privileged that she allowed me to join her emerging research group. I'm grateful for her tolerance of my numerous faults and mistakes which I've strived to correct over the past few years, and can't say enough how much she has helped me to become a true scientist and engineer, even in spite of difficult peer review and other mishaps in the lab. I could not have asked for a better mentor.

I'd also like to thank my thesis committee, Gerald Wogan and Kris Prather. Not only do I appreciate their insightful comments regarding my thesis work, I'm grateful for their guidance with regards to why they pursued their chosen professions.

I must also thank Bill Deen. Not only did he teach me transport well, he gave me faith that everything in that horrid first semester would be okay, and ended up becoming instrumental in my last thesis aim. I'm grateful not just for the principles of transport that he taught me twice as a first year and fifth year, but also for his calm patience and reassurances, which made my Ph.D. all the more better.

I'm proud to say that I feel I work alongside some of the best people at the Institute. Many thanks to Brandon Heimer, Beijing Kara Huang, Shefali Lathwal, Sohail Ali, Kaja Kaastrup, Jung Kyu Lee, and Ji Sam Wong. Without Brandon, I'm not sure I would have been able to trudge through my many cloning projects, learn so much about space exploration, or talk all things sports and general life while in the lab. Thank you, Kara, for being one of the most rigorous scientists I know and holding me to a standard appropriate for a Ph.D. Shefali, I'm glad we were able to work right next to each other with the best view in the lab of Ames Street and Main Street, and thank you for helping spur my interest in global health. Thanks to everyone else, and thanks also to newest members of the lab, namely Troy Langford, Eric Miller, Brooke Tam, Kassi Stein, and Alan Aguirre. I feel utterly confident that the lab will be in great shape after some of us have departed.

I feel privileged to have mentored numerous undergraduate students as well. I'd like to acknowledge Veronica Molina, Shara Srinivasan, Kim Barker, Gabby Kwon, Linda Jiang, Abbey Diener, Jess Saiffee, Tricia Lu, and Avira Som. Thank you for making meaningful contributions to this work and helping me become a better mentor and teacher.

I would be remiss to not acknowledge the National Science Foundation for funding this work and the MIT School of Chemical Engineering Practice for giving me a view of work in a corporate setting. I met really great colleagues through the Practice School Program, namely Anto Ponselvan, Andrew Tsavaris, Will Gunther, Fitri Juniwati, Chunyan Zhang, Stephanie Schulze, and Aly Eltayeb. I really do feel our experiences at Merck in Belgium and Corning in upstate New York enriched me and helped me return to MIT as a better student and researcher.

I must say thanks to my classmates as well. Justin Kleingartner, thank you for becoming my friend during the first week of our first dreadful semester and continuing to stay in touch once we set off on our own research paths. Aditya Kunjapur, thanks so much for all the shared lunches at Chipotle and Clover and giving insightful guidance into research and issues of personal importance. Chris Lam, thank you for commiserating with me during particularly difficult times in our research projects and being available as

a friend. Thanks to the rest of my class for making me proud to be your classmate; it is humbling and rewarding to watch as you all accomplish amazing things in your research and other endeavors.

Thanks so much to my friends outside MIT, who have helped make sure I enjoy life outside the lab. George Luo, you have become the brother I never had. Thank you for providing me a place to live with a well-stocked kitchen and precisely sharpened knives; for coming with me on countless adventures and misadventures throughout Boston, Cambridge, and the rest of New England; and for being there when I needed someone most. Many thanks to Ana Chen, for giving me a way to stay in touch with my Baltimore roots, baking me the most incredible desserts, and being a great friend through and through. Thanks also to Fan Liu, for inviting me to the music concerts, setting an unparalleled example for what a work ethic is, and getting together with me and George for continual support to work out the issues in our lives. I'd like to also thank Victoria Lo; while we might have had only a year to get to know each other while in Boston, I'm glad we did, starting with when you reached out to invite me to a group outing to the movies and extending into our shared interest in global health as well as our personal values. Thanks also to Dinesh Mahadeo, for being one of my best friends in college and continuing to be one of my best friends afterward, in spite of being separated by an 8-hour plane ride. Thank you so much to Yike Jiang, another one of my best friends in college who has continued to support me and take me on adventures through New England while nearby at Dartmouth. Thanks also to Dan Jang, Ty Lin, Amanda Mok, Elan Hourticolon, John Silberholz, Sarah Peitzmeier, Eric Li, Tuquynh Le, and anyone else I might have forgotten – you're all friends for whom I'm grateful to have had in my life!

Finally, I thank my parents, Blesilda and Joseph Edward Lim, and my sister, Meilin Lim, as well as the rest of my family. Thank you for your unconditional love and support.

With gratitude,
Joseph Benigno Lim

Table of contents

Abstract	3
Acknowledgements	6
List of figures	13
List of tables.....	15
1 Introduction	17
Abstract.....	19
1.1 Overview of biology of hydrogen peroxide (H ₂ O ₂)	21
1.2 Localization of sources and targets of H ₂ O ₂	23
1.3 Past methodologies for perturbing extracellular and intracellular levels of H ₂ O ₂	23
1.4 Criteria for an ideal H ₂ O ₂ generator.....	24
1.5 Evaluation of past enzymes and small molecules used for H ₂ O ₂ generation	25
1.6 Thesis objectives	27
2 Characterization of signal of a genetically encoded H ₂ O ₂ sensor in bacteria.....	30
Abstract.....	32
2.1 Introduction	34
2.2 Materials and methods.....	35
2.2.1 Expression of HyPer in <i>Escherichia coli</i>	35
2.2.2 Measurement of HyPer's signal in <i>E. coli</i> over time.....	35
2.2.3 Measurement of kinetics of H ₂ O ₂ scavenging by <i>E. coli</i>	37
2.2.4 Measurement of HyPer's spectrum in <i>E. coli</i> at selected time points	38
2.2.5 Statistical analysis.....	39
2.3 Results.....	39
2.3.1 Temporal behavior of HyPer's signal.....	39
2.3.2 Effects of cell density on dose-response curves	42
2.3.3 Effects of expression host strain on dose-response curves and formalized quantitative characterization of the signal	44
2.4 Discussion	46
2.5 Conclusions.....	46
3 Exploration of cytochrome P450 BM3 as an H ₂ O ₂ generator	49
Abstract.....	51
3.1 Introduction	53

3.2	Materials and methods	55
3.2.1	Kinetic simulations	56
3.2.2	Site-directed mutagenesis	56
3.2.3	Protein expression and purification	57
3.2.4	Spectrophotometric analysis of oxidized enzyme and carbon monoxide binding	58
3.2.5	Steady state kinetics	58
3.2.6	Thermostability	58
3.2.7	Analysis of reaction products	58
3.2.8	Transfer of P450 gene to mammalian vector	59
3.3	Results	60
3.3.1	Modeling effects of leakage on coupling with respect to hydroxylation	60
3.3.2	Expression and purification	61
3.3.3	Steady state kinetics, spin state, and analysis of reaction products	62
3.3.4	Thermostability	65
3.3.5	Mammalian expression and activity	66
3.4	Discussion and conclusions	68
4	Use of a genetically encoded H ₂ O ₂ sensor for whole cell screening for enzyme activity	71
	Abstract	73
4.1	Introduction	75
4.2	Materials and methods	76
4.2.1	Construction of control plasmids and a random mutation library	76
4.2.1.1	Construction and transformation of plasmids to test schemes for co-expression	76
4.2.1.2	Construction and transformation of library of P450 BM3 variants	77
4.2.2	Testing effects of scheme on co-expression	78
4.2.3	Testing effects of timing, measurement frequency, pH, and buffer composition on signal	78
4.2.4	Screening for variants with elevated H ₂ O ₂ production	79
4.2.5	Confirmation of elevated H ₂ O ₂ production by HRP/ABTS assay	80
4.2.6	Exploring the efficacy of the screen in fluorescence-activated cell sorting	80
4.3	Results	81
4.3.1	Design of scheme for co-expression	81
4.3.2	Validation of baseline and positive controls and effects of timing, measurement frequency, pH, and buffer composition on signal	82
4.3.3	Application of the screen to find variants with enhanced H ₂ O ₂ production	84

4.3.4	Efficacy of the screen in fluorescence-activated cell sorting	86
4.3.5	Exploration of additional variants for H ₂ O ₂ generation	89
4.4	Discussion	92
4.5	Conclusions	93
5	Development of a transport model for H ₂ O ₂ in mammalian cells	95
	Abstract	97
5.1	Introduction	99
5.2	Computational methods and modeling	100
5.2.1	Overview of kinetic model	100
5.2.2	Sensitivity analysis	101
5.2.3	Transport model formulation	102
5.2.3.1	Calculation of permeability constant	102
5.2.3.2	Justification of assumptions	102
5.2.3.3	Governing equations	103
5.2.3.4	Parameter values and additional dimensionless groups	103
5.2.4	COMSOL simulations	105
5.3	Results	105
5.3.1	Order-of-magnitude estimations for length and time scales for H ₂ O ₂ diffusion generated in the cytosol	105
5.3.2	Comparison of reaction rates and sensitivity analysis	106
5.3.3	Reduction of kinetic model	108
5.3.4	Time scale for consumption of bolus addition of H ₂ O ₂ and expected gradient	110
5.3.5	Time and length scales for intracellular H ₂ O ₂ diffusion after step change in external concentration and justification of intracellular pseudo-steady state	111
5.3.6	Pseudo-steady state concentration profiles over time	113
5.3.7	Comparison of computational and analytical solutions	113
5.4	Discussion	114
5.5	Conclusions	115
6	Conclusions and future directions	118
	Abstract	120
6.1	Conclusions	122
6.1.1	Use of an H ₂ O ₂ sensor <i>in vivo</i>	122
6.1.2	Screening for enzymatic H ₂ O ₂ production	122
6.1.3	Development of a transport model for H ₂ O ₂	123

6.2 Future directions.....	123
6.2.1 Exploration of P450 BM3 as an H ₂ O ₂ generator.....	123
6.2.2 Verification and extension of a transport model for H ₂ O ₂	124
6.2.3 Next-generation generators and sensors of H ₂ O ₂	124
References.....	126
Appendix A	142
Appendix B.....	145
Appendix C	157

List of figures

1.1 Model of H ₂ O ₂ elimination in the cytosol of mammalian cells	22
1.2 Design criterion specifying the total amount of H ₂ O ₂ production required for an ideal generator	25
2.1 Time-course plots of F500 at cell densities of 60, 240, and 480 x 10 ⁶ per 200 µl.....	36
2.2 Time-course plots of F420 at cell densities of 60, 240, and 480 x 10 ⁶ per 200 µl.....	37
2.3 Standard curves of nmol H ₂ O ₂ versus A405 for H ₂ O ₂ uptake kinetics assay	38
2.4 Time-course plots of F500/F420 at cell densities of 60, 240, and 480 x 10 ⁶ per 200 µl	40
2.5 Time-course plots of H ₂ O ₂ scavenging and F500/F420 measured at cell density of 60 x 10 ⁶ cells per 200 µl.....	41
2.6 Dose-response curves of F500/F420 or fold change versus [H ₂ O ₂] or H ₂ O ₂ amount normalized to number of cells in assay solution of particular volume.....	43
2.7 Dose-response curves of F500/F420 versus H ₂ O ₂ amount normalized to number of cells in assay solution and fitted to Hill equation	45
3.1 Schematic of P450 hydroxylation and leakage.....	54
3.2 Schematic for lineage of variants with enhanced leakage derived from WT P450 BM3	55
3.3 Scheme modeling the competing reactions of hydroxylation and leakage	56
3.4 Time-course plots of NADPH and hydroxylated product R-OH with different $k_{cat, leakage}$ values and coupling plotted against different $k_{cat, leakage}$ values.....	61
3.5 Absorption spectra of oxidized variants of P450 BM3	63
3.6 Plot showing $k_{cat, leakage}$ and T ₅₀ of P450 BM3 variants and plot of high-spin state content versus $k_{cat, leakage}$	64
3.7 Linear correlation between k_{cat} and T ₅₀	66
3.8 Western blot of P450 BM3 variants encoded in a pTRE3G-IRES vector and expressed in HyPer-HeLa cells.....	67
3.9 Design criterion specifying the total amount of H ₂ O ₂ production required for a generator with WT P450 BM3 placed.....	67
3.10 Signal of HyPer when co-expressed with P450 BM3 variants in HyPer-HeLa cells.....	68
4.1 Schematic of HyPer-based screen for enhanced enzymatic production of H ₂ O ₂	76
4.2 Fluorescence spectra of HyPer co-expressed with WT or the I401P variant	82
4.3 Temporal behavior of HyPer's signal (F500/F420) measured from intact <i>E. coli</i> cells co-expressing the sensor and either WT P450 BM3 or the I401P variant.....	83
4.4 HyPer's signal when co-expressed with WT or the I401P variant after resuspension in different buffers	84
4.5 HyPer's signal when co-expressed with hits from a library of P450 BM3 variants	85
4.6 <i>In vitro</i> evaluation of putative H ₂ O ₂ generators identified using the HyPer-based screen.....	86

4.7 Fluorescence histograms depicting HyPer's signal co-expressed with WT, I401P, or variants derived from WT via error-prone PCR for different sorting rounds.....	87
4.8 Fluorescence histograms depicting HyPer's signal co-expressed with WT, I401P, or variants derived from WT via error-prone PCR at different time points after sorting	88
4.9 Expression levels of P450 BM3 variants measured in lysate and expressed in a 96-well microplate .	89
4.10 Specific and total leak rates of P450 BM3 variants measured in lysate and expressed in a 96-well microplate	90
4.11 Design criterion specifying the total amount of H ₂ O ₂ production required for a generator with WT and other variants placed	91
5.1 Rates of reactions directly involved in H ₂ O ₂ scavenging and concentrations of antioxidant enzymes directly involved in H ₂ O ₂ scavenging over time	107
5.2 Sensitivity of [H ₂ O ₂] to reaction rate constants	108
5.3 Simulated kinetic curves for clearance of a pulse addition of H ₂ O ₂ to baseline levels in a single compartment.....	109
5.4 Extracellular and intracellular H ₂ O ₂ over time upon bolus addition of 100 μM to HeLa cells	111
5.5 Development of intracellular concentration profile of H ₂ O ₂ after bolus addition of 25 μM to HeLa cells.....	112
5.6 Development of pseudo-steady state intracellular concentration profile of H ₂ O ₂ after bolus addition of 100 μM to HeLa cells.....	113
5.7 Development of intracellular concentration profile of H ₂ O ₂ after bolus addition of 25 μM to HeLa cells with analytical and computational solutions	114

List of tables

1.1 Key characteristics of previously used enzymatic H ₂ O ₂ generators	27
2.1 Selected time points of measurement of HyPer's spectrum for each combination of cell strain and cell density	39
2.2 H ₂ O ₂ scavenging rate constants (min ⁻¹) for each strain in each trial.....	42
2.3 Quantitative parameters of the fluorescent signal of HyPer in <i>E. coli</i> measured at 60 x 10 ⁶ cells per 200 µl.....	45
3.1 Maximum velocity rates of CYPs on native substrates	53
3.2 Primers used for sequencing and site-directed mutagenesis of cytochrome P450 BM3 in its native sequence	57
3.3 Primers used for sequencing, PCR, and site-directed mutagenesis of cytochrome P450 BM3 codon optimized for mammalian expression.....	60
3.4 Yields of protein per liter of culture	62
3.5 Measured K _{m, leakage} and proportion of product comprised by H ₂ O ₂	64
5.1 Model parameters for the kinetic redox model	100
5.2 Species initial concentrations for the kinetic redox model specific to HeLa cells.....	101
5.3 Model parameters for the transport model.....	104

Chapter 1

Introduction

Abstract

Hydrogen peroxide (H_2O_2) is a principal reactive oxygen species (ROS) involved in numerous physiological processes, including the respiratory burst, inflammation, proliferation, apoptosis, and signaling. As such, H_2O_2 and other ROS have been an active research area in recent years. However, it is still not well understood at what steady state levels and kinetic rates of production of H_2O_2 these biological events and phenotype transitions occur. This chapter discusses the physiology of H_2O_2 as well as these remaining open questions in the field. Methodologies for perturbing H_2O_2 levels are then discussed, including bolus addition for transient bursts as well as use of small molecules and enzymes for more continuous generation, the latter of which more closely resembles physiological production of H_2O_2 . The criteria for an ideal enzymatic H_2O_2 generator are presented, followed by a critical evaluation of whether enzymes currently in use meet those criteria. The chapter ends with an outline of the aims of this thesis, which are designed to enable the development of next-generation enzymatic H_2O_2 generators that fulfill the criteria of an ideal generator.

Portions of this chapter are included in:

Lim, J. B. and Sikes, H. D. Beyond bolus: molecular tools for continuous generation of hydrogen peroxide. In preparation.

1.1 Overview of biology of hydrogen peroxide (H₂O₂)

Hydrogen peroxide (H₂O₂) and other related reactive oxygen species (ROS) such as superoxide (O₂⁻) were once believed to be an unfortunate consequence of aerobic metabolism, which results in their production and potentially damage of biomolecules, including lipids, proteins, and DNA. However, it is now understood that organisms have evolved to integrate H₂O₂ into their essential physiology, including the respiratory burst [1,2], inflammation [3], proliferation [4], apoptosis [5], and signaling [6,7]. Given its high stability relative to other related ROS and prominent physiological role, H₂O₂ has stirred a surge of interest and research in redox biology, and as such has been extensively studied.

While H₂O₂ has been shown to be useful for survival, its levels are tightly controlled by efficient and abundant enzymatic scavengers, including peroxiredoxin (Prx), thioredoxin (Trx), and glutathione peroxidase (GPx), as well as other protein reductants that regenerate these scavengers in the reduced form (Figure 1.1). All scavengers rely on a mechanism in which a thiol group reacts with H₂O₂, followed by disulfide formation with another thiol group. Knowledge of the pathways by which H₂O₂ is produced and scavenged presents a systems model that, in conjunction with quantitative, mechanistic data, can be used to understand how H₂O₂ transduces its effects. A kinetic model integrating this knowledge has recently been developed to determine which reactions are most important in H₂O₂ scavenging upon bolus addition to cell culture, with a focus on Jurkat cells [8].

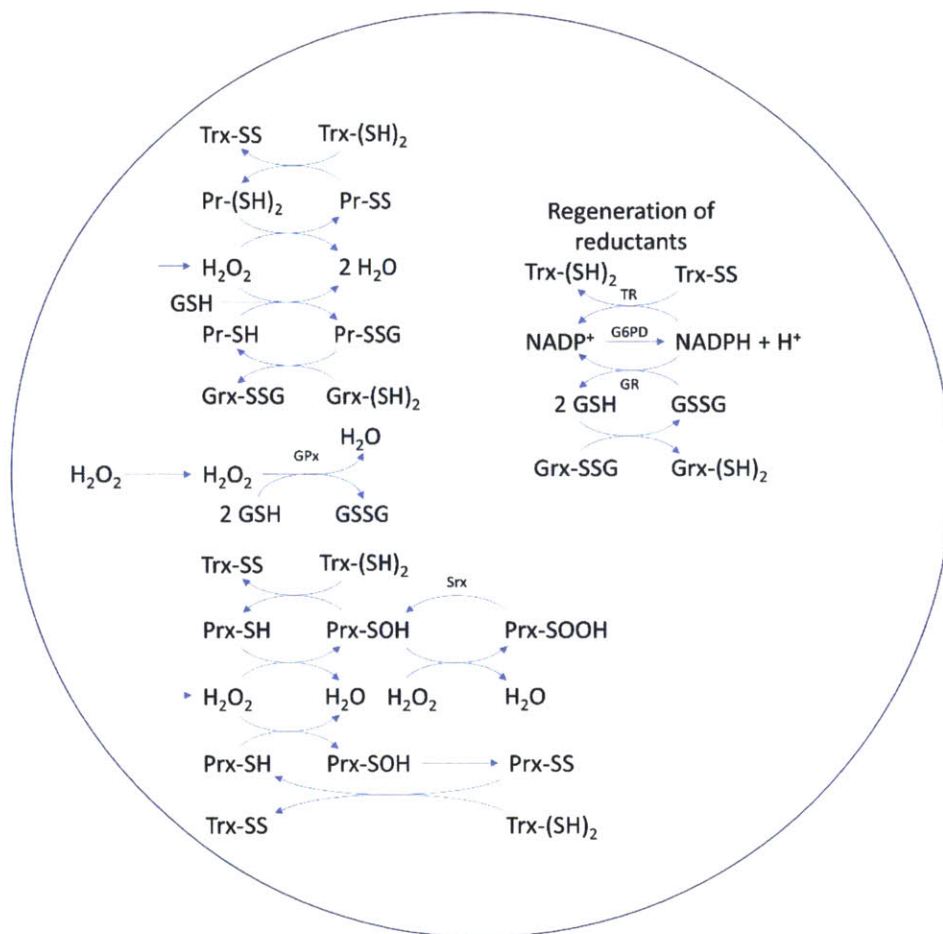


Figure 1.1. Model of H_2O_2 elimination in the cytosol of mammalian cells based upon a model for Jurkat T cells [8]. Only cytosolic components were considered in this schematic; thus, catalase, which is known to be contained exclusively in peroxisomes [9,10], was excluded, as well as any processes involving the transfer of a species to another compartment. H_2O_2 undergoes three main pathways of scavenging: general protein thiols ($\text{Pr}-(\text{SH})_2$ and $\text{Pr}-\text{SH}$), glutathione (GSH)/glutathione peroxidase (GPx), and peroxiredoxin (Prx). In scavenging H_2O_2 , vicinal dithiols can form disulfide groups that are reduced by thioredoxin (Trx), while other general thiol groups can be glutathionylated and reduced by glutathione reductase (Grx). GPx can also catalyze H_2O_2 scavenging by GSH alone, leading to GSH disulfide (GSSG). In the last pathway, Prx can scavenge H_2O_2 and be oxidized into $\text{Prx}-\text{SOH}$, which can scavenge H_2O_2 again, leading to overoxidation ($\text{Prx}-\text{SOOH}$), which can be reduced with sulfiredoxin (Srx). $\text{Prx}-\text{SOH}$ can also form an intramolecular disulfide bond, resulting in $\text{Prx}-\text{SS}$. For clarity, reactions leading to regeneration of reductants are shown apart from the pathways of H_2O_2 scavenging: Trx is reduced by NADPH and Trx reductase (TR), GSSG is reduced by GSH reductase (GR), and GSH is used to generate Grx . NADPH , a key base reductant in the network, is regenerated from NADP^+ by glucose-6-phosphate dehydrogenase (G6PD).

It has been observed that whether H_2O_2 effects physiological processes such as signaling cascades or cytotoxic damage is dependent upon its concentration within the cell [7]. Furthermore, cancerous cells

have been observed to hold higher levels of H₂O₂ than non-cancerous cells [11]. However, the relationship between changes in H₂O₂ concentration and the resulting biology is only qualitative in nature due to lack of tools to control and measure H₂O₂ levels with spatiotemporal precision. It thus remains unknown at what levels and by what mechanisms these effects occur. While tools have been developed to begin to probe this open question, their limitations prevent a definitive answer with confidence from being posed.

1.2 Localization of sources and targets of H₂O₂

The aforementioned kinetic model assumes completely mixed compartments of H₂O₂ in the extracellular media, cytosol, and peroxisomes, with no spatial component, thus ignoring potential localization. Several models have emerged to highlight the importance of H₂O₂ localization. In the floodgate model [12], 2-cys Prxs act as floodgates, keeping H₂O₂ at low resting levels until a transient burst of H₂O₂ production results in overoxidation of the Prxs and consequent reaction with protein thiols to initiate signaling cascades. Another model suggests that Prxs are inhibited by phosphorylation, decreasing their overall H₂O₂ scavenging capacity and allowing local concentrations to increase [10,13]. The most recent model suggests that Prx acts as a mediator, relaying electrons from H₂O₂ to a signaling target [14,15]; this model is more amenable to Prx's abundance and efficiency, which allow it and other scavengers to highly impede H₂O₂ from reacting directly with other proteins.

In any case, it has been widely observed that H₂O₂ production, as well as that of other ROS, is often localized [16–20]. More specifically, H₂O₂ and other ROS are produced in phagosomes (in cells of the immune system specialized for destroying invasive pathogens), peroxisomes, mitochondria, the endoplasmic reticulum, and by nicotinamide adenine dinucleotide phosphate (NADPH) oxidases within the cell membrane [21]; sources and targets of ROS are thought to be generally colocalized in the cell for a further element of redox control [21,22] and signaling specificity [7], suggesting that the ROS produced at subcellular locations only act upon nearby targets. Indeed, evidence has also emerged that ROS generated in different locations, including H₂O₂, result in different phenotypic effects [23,24].

With the importance of ROS localization becoming increasingly revealed, important questions arise, which are posed here in relation to H₂O₂ specifically: To what extent is H₂O₂ localized? How far does H₂O₂ produced in a particular subcellular location diffuse before reacting with a signaling target? How much H₂O₂ is required to reach and react with a key protein thiol to initiate a signaling cascade? Although the previously mentioned kinetic model has been matched to experimental data for Jurkat cells, it does not take into consideration potential spatial variations in the concentration of H₂O₂, leaving the above questions unanswered.

1.3 Past methodologies for perturbing extracellular and intracellular levels of H₂O₂

Researchers have historically used bolus addition [25,26] or stimulation/inhibition of NADPH oxidase [27] to perturb intracellular levels of H₂O₂ and study its effects. However, bolus treatment can only add H₂O₂ to the extracellular medium, requiring H₂O₂ to diffuse through the cell membrane, which results in a gradient. In the case of NADPH oxidase, O₂⁻ is generated, but due to limited membrane permeability to ions, this species often converts to H₂O₂, which then diffuses through the membrane, as is the case with bolus addition of H₂O₂. While generation of ROS external to the cell is relevant to certain cellular processes, such as inflammation [28] and the respiratory burst [1,2], this is not the case with respect to many other processes, such as proliferation and apoptosis [29]. In such processes, generation of H₂O₂

outside the cell complicates interpretation of data because the resulting gradient conflates the effects of intracellular and extracellular species.

Furthermore, bolus addition of H_2O_2 , particularly in nonphysiological amounts, may result in effects not seen when H_2O_2 is produced using endogenous cellular sources [25,26]. While bolus addition is expected to produce a sudden increase in intracellular H_2O_2 concentration followed by exponential decay due to antioxidant scavengers, endogenous H_2O_2 production at steady state results in constant H_2O_2 over a more prolonged period of time. Indeed, continuous generation of H_2O_2 in localized settings within the cell may better reflect physiological processes with respect to spatiotemporal changes in H_2O_2 levels during the actions of certain drugs and pathologies, as performed or noted in several studies [21,30,31], making this a preferred method of perturbation in quantitative redox biology. Both enzymes and small molecules have been used in this capacity, and will be described in more detail later in this chapter.

1.4 Criteria for an ideal H_2O_2 generator

Before reviewing past tools used for continuous H_2O_2 generation, it is important to denote the criteria of an ideal generator, to provide standards against which such tools can be evaluated. We define these criteria here:

1. Soluble
2. Localizable
3. Genetically encoded or diffuse easily through the membrane and remain inside the cell (for intracellular generation)
4. Use of native endogenous substrates that are abundant in the cell (for intracellular generation)
5. Produces H_2O_2 in a specific manner with minimal, if any, byproducts
6. Exhibit total activity capable of overcoming the cell's antioxidant capacity
7. Exhibit activity that is tunable

Criterion (6) can be quantified by utilizing the previously mentioned kinetic model [8]. We updated this model with parameters specific to HeLa cells [32] and used the model to determine the total H_2O_2 production rate required to overcome the antioxidant network and increase H_2O_2 levels in the cytosol (Figure 1.2). A similar approach could be taken for other related species and cell lines.

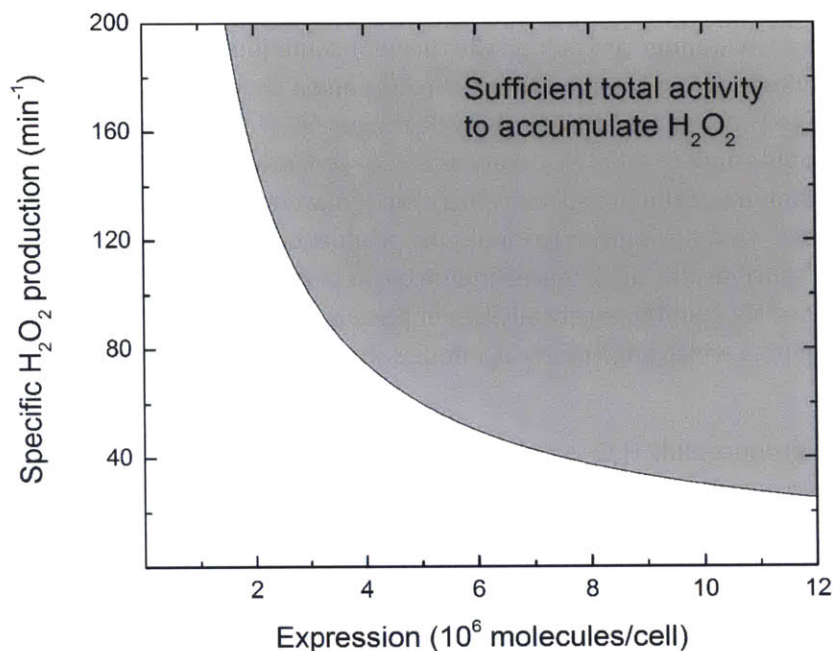


Figure 1.2. Design criterion specifying the total amount of H₂O₂ production required for a generator, as a product of specific production rate and total amount of generator, to overcome cellular antioxidant capacity and sustain generation. The criterion is shown as a contour; any generator in the shaded, grey region surpasses the required threshold. The criterion calculated here is specific to HeLa cells.

However, we also note that this assumes well-mixed compartments of H₂O₂ in the cytosol, peroxisomes, and extracellular media. This does not accommodate the emerging importance of H₂O₂ localization [16–20,23,24], which we acknowledge in criterion (2). Indeed, in a recent study, the diffusion of H₂O₂ through the cytosol in the face of antioxidant scavengers was claimed to be no more than a few microns, a fraction of the cell’s radius [33]. Thus, while the quantitative threshold shown in Figure 1.2 is appropriate for determining the production rate required to perturb *global* levels of H₂O₂, a transport model incorporating a spatial dimension will be needed to elucidate the effects of a localized production rate, which may lead to a different quantitative criterion.

A tool that fulfills the above criteria, in conjunction with appropriate sensors, would allow H₂O₂ steady state levels and kinetics of production to be controlled and thus quantitatively and systematically correlated with cellular phenotypes and signaling cascades. This would enable tests of long-standing hypotheses regarding the mechanism of how [10,12–15] and at what levels [6,7,11] H₂O₂ and related species transduce biological effects and phenotypes as well as signaling cascades.

1.5 Evaluation of past enzymes and small molecules used for H₂O₂ generation

The three main enzymes that have been used in past studies to perturb H₂O₂ levels are oxidases: xanthine oxidase (XO), glucose oxidase (GOX), and D-amino acid oxidase (DAAO).

XO and GOX have been extensively used for extracellular generation of O₂⁻ [34–39] and H₂O₂ [25,40–44], respectively, in a wide variety of contexts. Yet XO has also been purportedly used to generate both O₂⁻

and H_2O_2 [45–47]; indeed, XO is known to produce either species [48], and was recently found to predominantly produce H_2O_2 under physiologically relevant conditions [49]. Furthermore, while extracellular O_2^- can diffuse across the membrane through anion channels to enact intracellular effects, it may also dismutate to H_2O_2 , either outside or inside the cell [50], as is the case with use of NADPH oxidase. It is thus inappropriate to label XO solely as an O_2^- -generating agent, and it is important to determine the stoichiometry of the products from a reaction catalyzed by XO in a given set of experimental conditions. That XO is given to catalyzing production of a mixture of H_2O_2 and O_2^- , along with other byproducts such as uric acid, makes it difficult to pinpoint any resulting biological effects to a particular species. While XO could theoretically be genetically encoded for intracellular perturbation, its promiscuous activity with a wide range of endogenous substrates would add another undesirable complication [51].

GOX is well known to produce only H_2O_2 and has often been used in conjunction with catalase, an H_2O_2 scavenger, to modulate steady state levels of H_2O_2 [52]. It thus offers product specificity that is difficult to control in reactions catalyzed by XO. However, GOX has only ever been used for extracellular generation, likely because it requires use of a valuable metabolite that would greatly perturb cellular metabolism and obfuscate any resulting effects that could be attributed to either H_2O_2 or glucose consumption. Furthermore, any H_2O_2 produced outside the cell must migrate through aquaporins in the membrane to exert intracellular effects [50], resulting in a conflating gradient between extracellular and intracellular species. While this may be relevant for studying inflammatory processes [52], this may not be the case for processes involving only intracellular species. It is also important to note that both XO and GOX require exogenous substrate, which is adequate for controlling and tuning extracellular activity, but would not be ideal for intracellular generation.

DAAO has been used extensively for this purpose. Stegman et al. noted that endogenous DAAO is generally localized in peroxisomes with catalase, thereby neutralizing H_2O_2 production by native DAAO [53]. Thus, they genetically encoded DAAO from *Rhodotorula gracilis* without a peroxisomal targeting sequence to express the enzyme in the cytosol; this particular isoform of DAAO is specific to D-amino acids, which are rare in mammalian organisms [54], allowing control of activity by administration of a D-amino acid, notably D-alanine. DAAO has since been used in this manner in numerous other studies [30,55–58], giving insights into the effects of endogenously produced H_2O_2 . Matlashov et al. also fused DAAO with the H_2O_2 sensor HyPer [59], showing that localizing the sensor with the source of generation results in a higher signal [60]. Although expression of DAAO has never been formally quantified, it is likely that it expresses well enough with sufficient activity to perturb H_2O_2 levels given its previous effective use in cell cultures to initiate changes in cell phenotype and cytotoxicity.

While DAAO provides functionality, i.e. intracellular generation, for which XO and GOX have not been used, it also falls short of meeting the criteria of an ideal H_2O_2 generator because of its requirement of exogenous substrate. Although activity can be tuned by the amount of exogenous substrate administered, this introduces a conflating variable, as D-alanine must diffuse through the membrane to bind to DAAO, introducing a gradient between extracellular and intracellular species. Furthermore, in addition to H_2O_2 , the reaction catalyzed by DAAO also results in α -keto acid and ammonia, which may introduce perturbations in addition to the effects caused by H_2O_2 .

In short, XO, GOX, and DAAO have all proven useful in perturbing H₂O₂ levels, but none yet meets the criteria of an ideal intracellular generator, as noted above. Their properties as generators are summarized in Table 1.1.

Table 1.1. Key characteristics of previously used enzymatic H₂O₂ generators.

Enzyme	Source	ROS generation rate (min ⁻¹)	Intracellular versus extracellular	Substrates	Products
Xanthine oxidase	Bovine milk	~550 [61]-630 [62]	Extracellular	Xanthine/hypoxanthine + O ₂	Uric acid/xanthine + H ₂ O ₂ /O ₂ ⁻
Glucose oxidase	<i>Aspergillus niger</i>	~56000 [63]	Extracellular	β-D-glucose + O ₂	Gluconic acid + H ₂ O ₂
D-amino acid oxidase	<i>Rhodotorula gracilis</i>	~20000 [64]	Intracellular	D-amino acid + H ₂ O + O ₂	α-keto acid + NH ₄ ⁺ + H ₂ O ₂

While we focus on enzymes in this thesis, it is important to note that small molecules have also been used for this purpose. In particular, Miller et al. developed a photocaged H₂O₂ generator termed Caged Peroxide Generator 1 (CPG1) that produces H₂O₂ upon activation by light and used this functionality to trigger cofilin-actin rod formation in enhanced green fluorescent protein (GFP)-cofilin HeLa cells [31]. CPG1 was able to produce H₂O₂ on the order of tens of μM, with the total amount and kinetic rate modulated by the amount of CPG1 loaded into the cell. In a similar system, Cheong et al. used a photosensitizer, hematoporphyrin, and light to activate intracellular ROS generation in dendritic cells, demonstrating activation of the cells that led to stimulation of T-cell responses and antitumor effects [65]. It is of note that these biological processes were not observable in this study when bolus additions of H₂O₂ were used in place of activation of hematoporphyrin for intracellular production.

Small molecules such as CPG1 and hematoporphyrin thus have functionality similar to that provided by XO, GOX, and DAAO. However, they lack two key characteristics of an ideal generator: localizability and generation of specific species. Both probes were loaded into the cytosol of cells, as they currently do not have any tag to direct them to a particular subcellular compartment. For generation of specific species, CPG1 generates O₂⁻ as an intermediate, which spontaneously dismutates into H₂O₂. The amount of H₂O₂ generated was shown to be less than the amount of CPG1 loaded, leaving open the possibility that not all of the CPG1 molecules were activated or that the intermediate O₂⁻ did not spontaneously dismutate but rather reacted with an intracellular target. Cheong et al. also noted that hematoporphyrin produces singlet oxygen (¹O₂), hydroxyl radical (OH[•]), and O₂⁻, in addition to H₂O₂. The lack of localizability and specific species generation make it difficult to use these tools to pinpoint with more precise spatial resolution the effects of a particular species such as H₂O₂.

1.6 Thesis objectives

Given our evaluation of the tools currently used to perturb H₂O₂ levels, it is clear that there remains a need for an ideal generator. To that end, the overarching objective of this dissertation is two-fold: (1) to develop a screening platform to detect, engineer, and optimize candidate enzymes for potential applications as ideal H₂O₂ generators in mammalian cells, and (2) to develop and use a transport model

of H₂O₂ in mammalian cells to generate testable predictions of H₂O₂ concentration profiles. The former is intended to produce a novel experimental system that facilitates development of next-generation enzymatic H₂O₂ generators; the latter is intended to refine the design criteria for an ideal H₂O₂ generator by providing predictions that can be validated *in vivo*, thus directly testing the model. These aims, which we discuss at length in later chapters, are outlined as follows, along with underlying objectives for each:

1. Develop a quantitative framework for using a state-of-the-art H₂O₂ sensor in *Escherichia coli* to generate reproducible dose-response curves in a physiological context.
 - a. Quantify the effects of relevant experimental parameters on HyPer's fluorescent response.
 - b. Characterize the fluorescent response of HyPer expressed in *E. coli* to bolus additions of H₂O₂.
 - c. Develop a systematic framework to enable side-by-side quantitative comparisons of HyPer's signal across studies.
2. Develop a novel platform using a state-of-the-art H₂O₂ sensor in *E. coli* for engineering H₂O₂-generating enzymes.
 - a. Determine a scheme for co-expression of HyPer and a candidate enzyme for H₂O₂ generation in *E. coli*.
 - b. Establish the efficacy of the platform for finding enzyme variants with enhanced H₂O₂ production using known controls and optimize fold difference in signal by tuning assay parameters.
 - c. Use the platform to scan through a library of random variants of a candidate enzyme and find novel variants with enhanced H₂O₂ production.
3. Develop a transport model for H₂O₂ in mammalian cells to refine the design criteria by which H₂O₂-generating enzymes would be evaluated to determine their use in quantitative redox biology studies.
 - a. Use known kinetic model parameters to calculate the time and length scales for H₂O₂ diffusion within a mammalian cell line of interest.
 - b. Use kinetic model to determine the most significant reactions for H₂O₂ scavenging and reduce the model to an analytical form.
 - c. Introduce a spatial component into the existing kinetic model to develop a complete transport model and generate testable H₂O₂ concentration profiles.

Achievement of these aims should advance development of next-generation H₂O₂ generators and also yield a model that can be used to quantitatively verify experimental observations, providing valuable novel tools in quantitative redox biology.

Chapter 2

Characterization of signal of a genetically encoded H₂O₂ sensor in bacteria

Abstract

Genetically encoded, fluorescent biosensors have been developed to probe the activities of various signaling molecules inside cells ranging from changes in intracellular ion concentrations to dynamics of lipid second messengers. HyPer is a member of this class of biosensors and is the first to dynamically respond to hydrogen peroxide (H_2O_2), a reactive oxygen species that functions as a signaling molecule. However, detailed characterization of HyPer's signal is not currently available within the context of bacteria exposed to external oxidative stress, which occurs in the immunological response of higher organisms against invasive pathogenic bacteria. Here, we performed this characterization, specifically in *Escherichia coli* exposed to external H_2O_2 . We found that the temporal behavior of the signal does not correspond exactly to concentration of H_2O_2 in the system as a function of time and expression of the sensor decreases the H_2O_2 scavenging ability of the cell. We also determined the effects of cell density, both before and after normalization of externally added H_2O_2 to the number of cells. Finally, we report quantitative characteristics of HyPer's signal in this context, including the dynamic range of the signal, the signal-to-noise ratio, and the half saturation constant. These parameters show statistically meaningful differences in signal between two commonly used strains of *E. coli*, demonstrating how signal can vary with strain. Taken together, our results establish a systematic, quantitative framework for researchers seeking to better understand the role of H_2O_2 in the immunological response against bacteria, and for understanding potential differences in the details of HyPer's quantitative performance across studies. Furthermore, they enable use of HyPer in a protein engineering screen for enhanced enzymatic H_2O_2 production with *E. coli* as a platform, which should prove useful in developing methodologies for finding and optimizing H_2O_2 generators in redox biology and biotechnology, as described later in Chapter 4.

Portions of this chapter have been published in:

Lim, J. B., Barker, K. A., Huang, B. K., and Sikes, H. D. In-depth characterization of the fluorescent signal of HyPer, a probe for hydrogen peroxide, in bacteria exposed to external oxidative stress. *Journal of Microbiological Methods*, 106, 33-39, 2014. doi: 10.1016/j.mimet.2014.07.038

2.1 Introduction

In seeking to develop a screening platform to engineer novel H₂O₂ generators, we first examined current state-of-the-art redox sensors to determine which would be most suitable for implementation in a protein engineering screen. ROS have historically been detected and measured using small-molecule fluorescent dyes, most notably dihydrodichlorofluorescein (DCFH₂) [66]. Although DCFH₂ has been used extensively to presumably detect H₂O₂, its use in assays poses a number of limitations, including artifactual H₂O₂ generation, potential oxidation by light, requirement of peroxidase or other transition metal catalysts, lack of specificity and localization, etc. [66].

Newer generation probes for H₂O₂ detection use a blocking group that is released upon reaction with H₂O₂, unmasking a fluorescent product [67–70]; probes in this class have also been localized in particular organelles [71,72]. While these probes circumvent many of the problems associated with DCFH₂ and other similar oxidant dyes, they still have their own limitations. Many of them are based on boronate derivatives and thus react quite slowly with H₂O₂ ($k \sim 1 \text{ M}^{-1} \text{ s}^{-1}$) [68], presenting a daunting challenge in competing with antioxidant scavengers. Furthermore, tests of specificity did not include peroxyxynitrite, with which this class of probes has a much higher reaction rate constant ($k \sim 10^6 \text{ M}^{-1} \text{ s}^{-1}$) [73–75], and also were performed in 4-(2-hydroxyethyl)-1-piperazineethanesulfonic acid buffer, which is known to scavenge hypochlorous acid, another potential reactant with the probes with a higher reaction rate constant ($k \sim 10^4 \text{ M}^{-1} \text{ s}^{-1}$) [75]. Thus, while the probes have shown use in demonstrating a change in overall redox state in physiological contexts such as cell stimulation by epidermal growth factor [68], the specificity of the probes to H₂O₂ needs further testing.

A promising methodology for H₂O₂ detection and measurement previously mentioned is use of genetically encoded fluorescent sensors that change in conformation and consequently fluorescence spectrum upon reaction with the species of interest [76]. These sensors capture many of the characteristics of an “ideal” probe [77], exhibiting a signal that is species-specific, ratiometric, and reversible, and enables measurements in specific compartments of the cell [78]. The ratiometric nature of the signal makes it independent of the concentration of the sensor *in vivo*, unlike most small-molecule probes. Furthermore, the reversibility of the signal allows real-time, dynamic measurements; non-reversible small-molecule probes can only offer a cumulative measure.

Two sensors have so far been developed specifically for H₂O₂ measurement: HyPer [59] and roGFP2-Orp1 [79]. HyPer was developed as a fusion of circularly permuted yellow fluorescent protein (cpYFP) and OxyR, a bacterial transcription regulator specific to H₂O₂. H₂O₂ oxidizes one of OxyR’s two key Cys residues, after which the two Cys residues form a disulfide bond. This results in a conformational change in the sensor, whereupon cpYFP exhibits an increase and decrease in the excitation spectral features at 500 (F500) and 420 nm (F420), respectively, when emission is monitored at 530 nm; the signal correlates with H₂O₂ concentration in solution. HyPer’s signal has been characterized to an extent and used in multiple contexts [80–86].

The other sensor, roGFP2-Orp1, was generated as a fusion of a variant of reduction-oxidation sensitive GFP and Orp1/Gpx3, a yeast glutathione peroxidase [79]. Like OxyR, one of Orp1’s Cys residues is also oxidized by H₂O₂ and mediates oxidation of two surface-exposed Cys residues on roGFP2, which form a disulfide bond concurrently with changes in the conformation and fluorescence spectrum. More specifically, the excitation spectral features at 390 and 480 nm increase and decrease, respectively, when emission is monitored at 510-530 nm. Similar to HyPer’s signal, the ratio of the excitation spectral

features correlates with H₂O₂ concentration. roGFP2-Orp1 has also been applied in a variety of studies [25,87–90].

Although genetically encoded H₂O₂ sensors have certainly advanced the state-of-the-art in measuring H₂O₂ *in vivo*, many of the studies that have employed their use did not characterize their signals in a quantitative, reproducible manner. Furthermore, while HyPer has been used in bacteria [59,86], the signals of both sensors have never been fully quantitatively characterized in this context, which particularly holds relevance as a potential platform for engineering novel H₂O₂ generators, as described later in Chapter 4.

Because of HyPer's extensive use by other research groups in the field and its numerous useful properties as noted above, we characterized the fluorescent response of HyPer expressed in *E. coli* when exposed to bolus additions of H₂O₂ [91]. In doing so, we sought to mimic the immunological response against pathogenic bacteria, as well as expand upon the original proof-of-concept [59] and determine statistically meaningful quantitative properties of the response, to enable comparisons of the signal across studies.

2.2 Materials and methods

2.2.1 Expression of HyPer in *E. coli*

A recombinant pQE30 plasmid containing the HyPer construct was obtained from Evrogen. *E. coli* BL21 (DE3) and DH5 α cells were transformed with the recombinant HyPer plasmid via electroporation. To express the protein in a bacterial culture, a single colony was used to inoculate 5 ml of Luria-Bertani (LB) medium (Becton Dickinson) in a 14 ml culture tube (17 x 100 mm, VWR) and incubated at 37 °C with orbital shaking of 250 rpm overnight. This overnight culture was then used to inoculate 50 ml of Terrific Broth (TB) medium (Becton Dickinson) in a non-baffled 250 ml Erlenmeyer flask (VWR) and incubated at 37 °C with orbital shaking of 250 rpm. When cultures reached an OD₆₀₀ of 0.6, cytoplasmic recombinant protein expression was induced by the addition of isopropyl β -D-1-thiogalactopyranoside (0.05 mM; Omega Bio-Tek), after which cultures were incubated for 17 hours at 20 °C with orbital shaking of 250 rpm.

2.2.2 Measurement of HyPer's signal in *E. coli* over time

After expression of HyPer, cells were centrifuged at 4 °C and 14000 g for 5 min. The supernatant was discarded and cells were resuspended in Tris buffer (25 mM Tris-HCl obtained from MP Biomedicals, LLC, 150 mM NaCl obtained from Mallinckrodt Pharmaceuticals, pH 8). Cells were washed twice to remove traces of interfering fluorescent components of the growth medium and aliquoted in cell concentrations of 60, 240, and 480 x 10⁶ cells per 195 μ l based on optical density at 600 nm. A stock solution of H₂O₂ (VWR) was quantified based on absorbance at 240 nm ($\epsilon = 43.6 \text{ M}^{-1} \text{ cm}^{-1}$) and used to prepare serial dilutions of H₂O₂. Cells were added (195 μ l) to H₂O₂ (5 μ l) in a 96-well microtiter plate (Greiner) to final cell concentrations of 60, 240, and 480 x 10⁶ cells per 200 μ l and final H₂O₂ concentrations of 0, 1, 1.5, 2, 2.5, 3, 5, 10, and 20 μ M; given the final volume of 200 μ l, these concentrations equate to 0, 0.2, 0.3, 0.4, 0.5, 0.6, 1, 2, and 4 nmol. Fluorescence emission intensity was measured upon excitation at 500 nm (9 nm bandwidth) and 420 nm (9 nm bandwidth) with emission monitored at 545 nm (20 nm bandwidth) at 30 second intervals for 20 min using a Tecan Infinite M200 plate reader. Measurements were performed at room temperature (~22 °C) and pH 8. To examine whether the kinetics of HyPer's

response changed with the availability of an energy source, the above measurement was repeated with the same buffer containing glucose for HyPer expressed in DH5 α at a cell density of 60×10^6 cells per $200 \mu\text{l}$ in response to $20 \mu\text{M}$ H_2O_2 ; all conditions were identical except for addition of D-glucose (25 mM, Macron Fine Chemicals) to the assay buffer.

With or without glucose, measurements of the signal showed that both F500 and F420 increased over time, even when no H_2O_2 was exogenously added to the cell suspension (Figures 2.1 and 2.2). Both spectral features should in principle remain unchanged when no H_2O_2 is introduced; additionally, the cell suspensions used to measure different amounts of H_2O_2 (0-4 nmol/ 60×10^6 cells) were all taken from the same aliquot of cells. Thus, the increases in F500 and F420 with no exogenous H_2O_2 were subtracted from the time-course plots for F500 and F420 measured with non-zero amounts of exogenously added H_2O_2 ; all F500/F420 time-course plots were then derived after this treatment of the data.

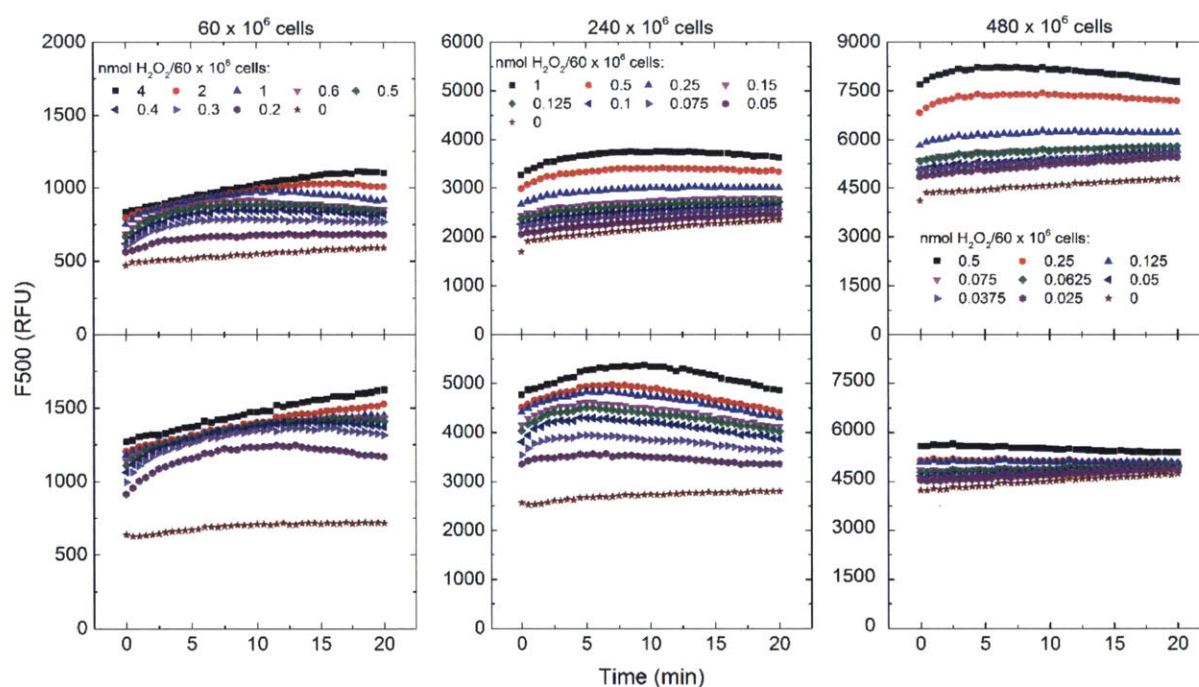


Figure 2.1. Time-course plots of F500 at cell densities of 60, 240, and 480×10^6 per $200 \mu\text{l}$ for BL21 (DE3) (top) and DH5 α (bottom).

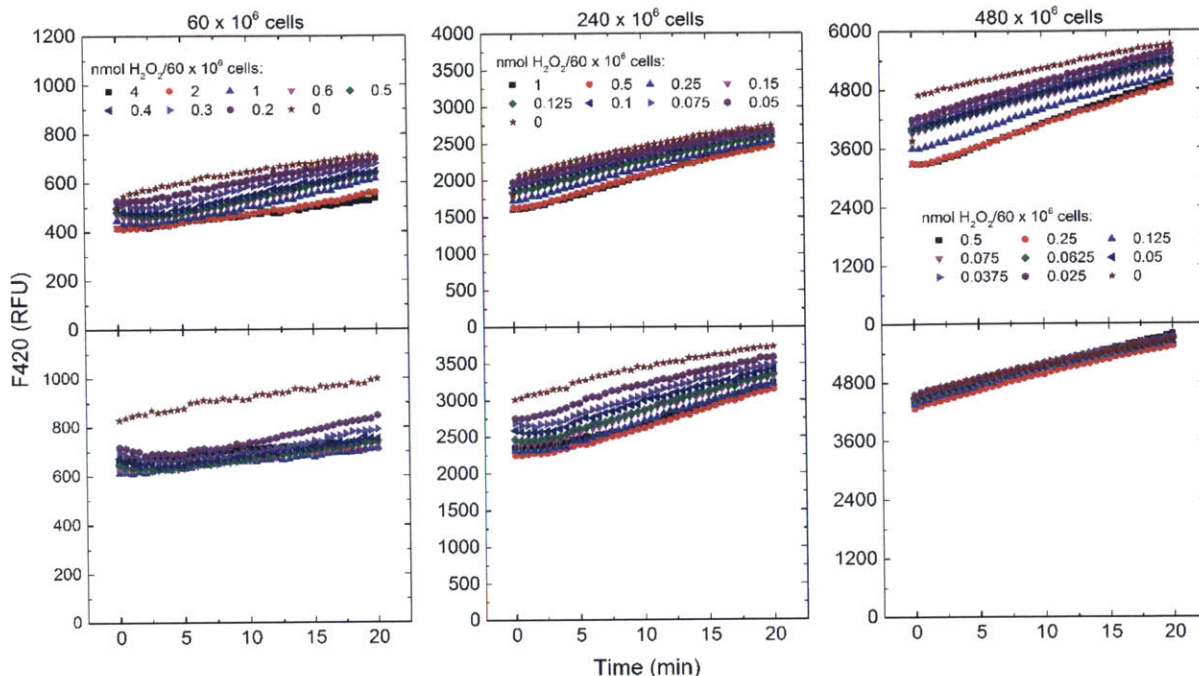


Figure 2.2. Time-course plots of F420 at cell densities of 60, 240, and 480 x 10⁶ cells per 200 μl for BL21 (DE3) (top) and DH5α (bottom).

2.2.3 Measurement of kinetics of H₂O₂ scavenging by *E. coli*

Rates of removal of H₂O₂ from solution by DH5α, DH5α expressing HyPer, and BL21 (DE3) expressing HyPer were measured using a horseradish peroxidase (HRP) assay. Cells were washed twice in Tris-glucose buffer (25 mM Tris-HCl obtained from MP Biomedicals, LLC, 150 mM NaCl obtained from Mallinckrodt Pharmaceuticals, 25 mM D-glucose obtained from Macron Fine Chemicals, pH 8) in the manner described in Section 2.2.2. Glucose was added to this resuspension buffer to ensure regeneration of bacterial antioxidants such as catalase and alkyl hydroperoxide reductase (Ahp) [92].

For experimental reactions, cells were added (195 μl) to H₂O₂ (5 μl) to a final cell concentration of 60 x 10⁶ cells per 200 μl and a final H₂O₂ concentration of 20 μM (4 nmol). In another set of solutions to determine a standard curve, final H₂O₂ concentrations of 20, 16, 12, 8, 4, and 0 μM were prepared in a volume of 200 μl; these concentrations equate to 4, 3.2, 2.4, 1.6, 0.8, and 0 nmol, respectively.

To quench the experimental reactions at certain time points, 10 μl of hydrochloric acid (HCl, 5 N; Mallinckrodt Pharmaceuticals) was added to a sample containing cells at 2, 4, 6, 8, and 10 min. 10 μl of HCl was also added to each standard curve reaction. All samples, both experimental reactions and standard curve reactions, were centrifuged at 4 °C and 14000 g for 10 min. 160 μl of the supernatant of each sample was added to a 96-well microtiter plate (Greiner). 50 μl of potassium phosphate buffer (KPi, 1 M, pH 8; VWR) was added to each sample in the plate, followed by 50 μl of 2,2'-azino-bis(3-ethylbenzothiazoline-6-sulphonic acid) (ABTS, 2.5 mM; Tokyo Chemical Industry, Co., Ltd.) in KPi (0.1 M, pH 8, composed of monopotassium phosphate and dipotassium phosphate obtained from VWR). 10 μl of horseradish peroxidase (HRP, 3 mg/ml; Thermo Scientific) in KPi (0.1 M, pH 8) was then added. All

samples were mixed and the absorbance at 405 nm was measured using a Tecan Infinite M200 plate reader. All samples were repeated twice for a total of three technical replicates for each time point in the experimental runs and each concentration in the standard curve solutions.

The absorbances of the standard curve reactions, i.e. samples without cells were plotted against the final concentrations of H₂O₂ in those samples (Figure 2.3). Linear least squares regression was performed using Origin software (Origin Labs); this calibration was used to determine H₂O₂ amounts in the experimental reactions, i.e. samples containing cells at each time point. Origin software was used to fit a model of exponential decay to the data for each strain to calculate the rate constant for H₂O₂ scavenging (Section 2.2.5).

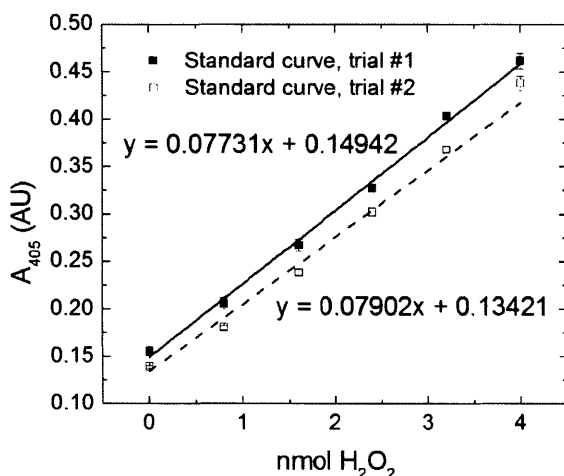


Figure 2.3. Standard curves of nmol H₂O₂ versus A405 for H₂O₂ uptake kinetics assay. The equations of linear regression are shown; x is nmol H₂O₂ and y is A405. Slope is given in units of absorbance units (AU)/nmol H₂O₂ and y-intercept is given in units of AU.

Two separate biological replicates (independent cultures) were analyzed by repeating the above described measurements, both standard curve reactions and experimental reactions at all time points, for a total of n = 6 for each strain.

2.2.4 Measurement of HyPer's spectrum in *E. coli* at selected time points

To reduce the parameter space, HyPer's signal was determined at single, selected time points (Table 2.1) by measuring spectra at 5 nm intervals from 400 to 510 nm, with emission at 545 nm. The measurement was repeated for three total trials at the same experimental conditions used to measure the signal over time (Section 2.2.2) except only at the aforementioned time points. The resulting dose-response curves were characterized by using Origin software to fit the Hill equation to the curves (Section 2.2.5). The dynamic range was calculated by dividing the maximum ratiometric signal F500/F420 by the signal with no exogenous H₂O₂ added, i.e. the signal at basal levels of H₂O₂ (F500/F420_{basal}). The signal-to-noise ratio was calculated by dividing the maximum ratiometric signal by the standard deviation of F500/F420_{basal}.

Table 2.1. Selected time points of measurement of HyPer’s spectrum for each combination of cell strain and cell density.

Cell number (x 10 ⁶ per 200 µl)	BL21 (DE3)	DH5α
60	17.5 min	20 min
240	2.5 min	7.5 min
480	1.5 min	0.5 min

2.2.5 Statistical analysis

Each data point in the dose-response curves and time-course plots of H₂O₂ scavenging represents mean ± standard deviation of replicate trials.

Origin software was used to fit the following exponential decay function to time-course plots of H₂O₂ scavenging:

$$[nmol H_2O_2 \text{ per } 60 \times 10^6 \text{ cells}] = [initial \text{ nmol } H_2O_2 \text{ per } 60 \times 10^6]e^{-at}$$

where t is the time in minutes and a is the time constant of H₂O₂ decay in min⁻¹. Origin software was also used to fit the following Hill equation to dose-response curves:

$$\frac{F500}{F420} = \frac{F500}{F420_{basal}} + \left(\frac{F500}{F420_{max}} - \frac{F500}{F420_{basal}} \right) \frac{[nmol H_2O_2 \text{ per } 60 \times 10^6 \text{ cells}]^n}{K_{1/2} + [nmol H_2O_2 \text{ per } 60 \times 10^6 \text{ cells}]^n}$$

where $F500/F420_{max}$ is the maximum signal upon saturation of the sensor, n is the Hill coefficient, and $K_{1/2}$ is the half saturation constant, i.e. the amount of H₂O₂ per 60 x 10⁶ cells when signal reaches half of its maximum.

All parameters determined by Origin in the fitting of the Hill equation and exponential decay are reported as the calculated parameter ± standard error. To determine the statistical significance of any discrepancies, two-tailed Student’s t-tests were used to compare H₂O₂ scavenging time constants between the strains.

2.3 Results

HyPer’s signal in the cytoplasm of *E. coli* in response to exogenously added H₂O₂ was measured for BL21 (DE3) and DH5α. For each strain, cell densities of 60, 240, and 480 x 10⁶ per 200 µl were tested to determine the impact of cell density on the signal. Each combination of strain and cell density was incubated with different amounts of H₂O₂, and the ratiometric signal (F500/F420) was measured over time (Section 2.2.2) and at selected time points to reduce the parameter space (Section 2.2.3 and Table 2.1).

We report HyPer’s signal in two ways common among users of the probe: the raw ratio F500/F420 and the fold change. Fold change is calculated by dividing the ratio F500/F420 measured in response to a non-zero amount of H₂O₂ by the raw ratio F500/F420_{basal}, i.e. the ratio for which no exogenous H₂O₂ was added.

2.3.1 Temporal behavior of HyPer’s signal

HyPer's signal was measured over time after an exogenous addition of H_2O_2 (Figure 2.4). On the basis of existing literature, we expected the ratio F500/F420 to reach a peak value and then decay toward the initial ratio. Figure 2.4 shows that the rise and decay time scales are not identical for every condition examined. For most combinations of cell density and H_2O_2 amount (Figure 2.4a, b, c, e) the rise and decay were captured. However, in Figure 2.4d, the curves for the two highest H_2O_2 concentrations did not decay on the time scale of the experiment, and in Figure 2.4f, only the tail end of the decay was captured. The rise and peak for this set of conditions likely occurred on a faster time scale than was accessible for these spectroscopic readings. Figure 2.4 demonstrates that the kinetics of HyPer's response are complex and non-linear in some regimes when the number of cells and the amount of H_2O_2 are varied. As the amount of H_2O_2 increased, the time required to reach a peak response increased. As a consequence of the observation that the signal can peak at different times in response to the addition of different H_2O_2 amounts, the dose-response curve can evolve over time; hence, the quantification of H_2O_2 depends heavily in some cases upon the timing of the measurement.

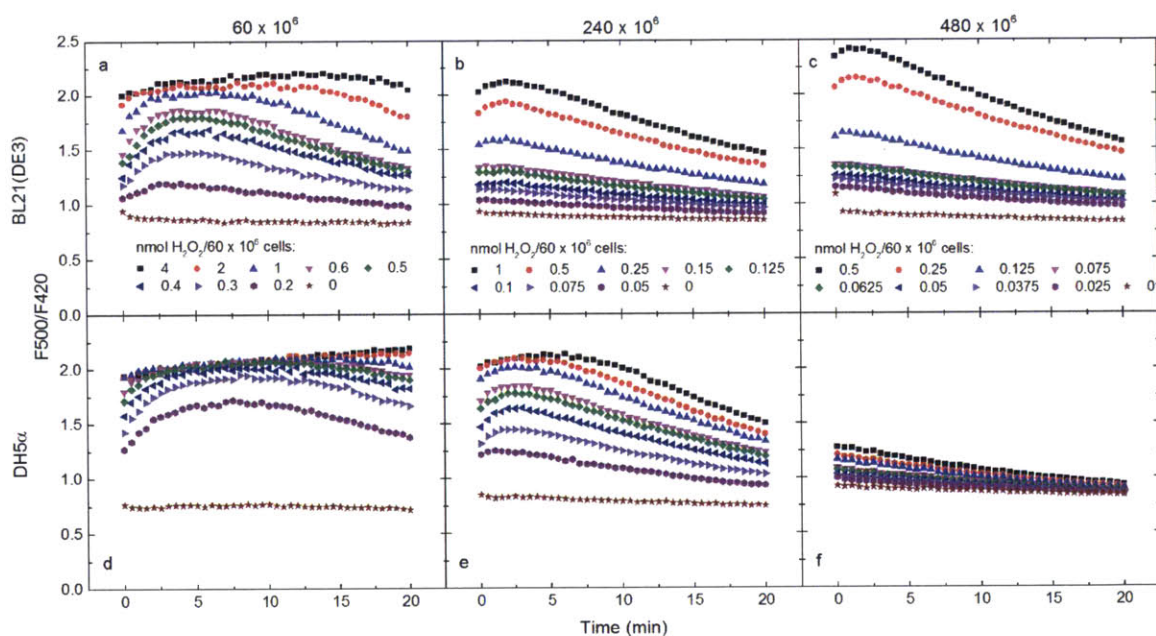


Figure 2.4. Time-course plots of F500/F420 at cell densities of 60 (a, d), 240 (b, e), and 480×10^6 (c, f) per 200μ l for BL21 (DE3) (a, b, c) and DH5 α (d, e, f).

To examine the extents to which HyPer acts as a real-time sensor of H_2O_2 concentration and perturbs the H_2O_2 scavenging capacity of the cell, an additional measurement technique was used to measure the concentration of H_2O_2 as a function of time in the cell suspension. BL21 (DE3) and DH5 α expressing HyPer and DH5 α without HyPer were incubated with H_2O_2 . The scavenging of H_2O_2 by cells was then stopped via acidification of the entire solution using HCl at different time points, and the amount of remaining H_2O_2 was measured using an HRP/ABTS assay (Figure 2.5). 60×10^6 cells were used for this measurement because the scavenging rate for this number of cells was slow enough for several time points to be assayed. Higher scavenging rates are expected for cell numbers of 240 and 480×10^6 . The kinetic measurements of HyPer's signal in BL21 (DE3) and DH5 α at 60×10^6 cells were repeated as

described above in buffer supplemented with glucose to compare the temporal behavior of HyPer's signal with the rate at which external H_2O_2 is scavenged by cells.

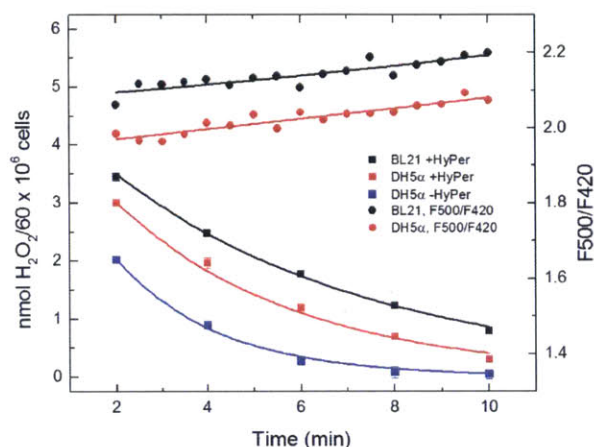


Figure 2.5. Time-course plots of H_2O_2 scavenging (squares) and F500/F420 (circles) measured at cell density of 60×10^6 cells per $200 \mu\text{l}$. An absorbance-based HRP assay was used to measure H_2O_2 concentration in solution as a function of time for an initial $20 \mu\text{M}$ addition of H_2O_2 (4 nmol). Absorbance values were converted to amounts of H_2O_2 using a standard curve (Figure 2.3). F500/F420 signal is shown in response to this same exogenous addition on the y-axis on the right. Data shown from 2 to 10 min.

The data show that the behavior of HyPer's signal as a function of time differs significantly from the exponential decay of H_2O_2 concentration after bolus, exogenous addition indicated by the ABTS signal. This temporal behavior is due to HyPer's reliance on oxidation and reduction of two key Cys residues to exhibit its signal. The oxidation reaction competes with scavenging by antioxidants such as catalase and Ahp [92]. After oxidation, slow reduction of HyPer due to disulfide reductase activity within the cell occurs, which leads to eventual decreases in the signal (Figure 2.4). The observation that oxidation occurs more rapidly than reduction is consistent with previous characterization of HyPer's signal in mammalian cells [93,94]. Because of its mechanism of action, HyPer can function as an intracellular, reversible sensor, but researchers should note that its signal reverses well after H_2O_2 has been removed from the system by cellular antioxidants. We also note that HyPer's signal was elevated when measured with glucose present in the assay buffer, with the basal signal and the signal at $4 \text{ nmol } \text{H}_2\text{O}_2/60 \times 10^6$ cells each increased by 2-3 fold; buffer composition is thus another assay variable that must be carefully controlled in measurements of HyPer's signal.

The calculated H_2O_2 scavenging rate constants are shown in Table 2.2. Two separate biological replicates were performed to determine culture-to-culture variability of H_2O_2 scavenging by *E. coli*. While BL21 (DE3) and DH5 α without HyPer exhibited H_2O_2 scavenging rate constants that were consistent between the two separate trials, DH5 α with HyPer had two statistically different rate constants. In both trials, the scavenging rate constant of each strain was statistically different from the other two, with BL21 (DE3) being the slowest, followed by DH5 α , and then DH5 α without HyPer (Table A.1). Although HyPer could

be considered a scavenger because of its reaction with H₂O₂, its expression in *E. coli* results in decreased overall H₂O₂ scavenging activity, as DH5α without HyPer exhibited higher H₂O₂ scavenging rate constants than DH5α with HyPer in both trials. Given the effects of HyPer expression on H₂O₂ scavenging, the difference in rate constant between the two different trials for DH5α with HyPer but lack of any significant difference for BL21 (DE3) suggests that HyPer expression has more variability in DH5α than in BL21 (DE3).

Table 2.2. H₂O₂ scavenging rate constants (min⁻¹) for each strain in each trial.

Strain	BL21 (DE3) + HyPer	DH5α + HyPer	DH5α – HyPer
Trial #1	0.17 ± 0.003	0.25 ± 0.01	0.44 ± 0.02
Trial #2	0.17 ± 0.01	0.34 ± 0.02	0.42 ± 0.02

Overall, timing of the measurement clearly has an impact on the dose-response curve developed due to the kinetics of HyPer’s signal. Furthermore, HyPer appears to significantly perturb the cell’s scavenging capacity; this effect should also be taken into account when integrating HyPer’s signal into a quantitative model of redox biology. Dose-response curves were measured at selected time points (Table 2.1) to further investigate the effects of two other assay variables (cell density and cell strain) and also capture statistically meaningful parameters that quantitatively characterize HyPer’s signal, as discussed in Sections 2.3.2 and 2.3.3.

2.3.2 Effects of cell density on dose-response curves

Dose-response curves often correlate the signal from cells expressing HyPer with the molar concentration of H₂O₂ added to the cell suspension, as shown in the left-hand panels of Figure 2.6. The right-hand panels of Figure 2.6 show the same data in the left-hand panels but correlate the signal with the amount of H₂O₂ per number of cells, rather than the concentration of H₂O₂ of the entire system. The left-hand panels would suggest that the signal, when calculated by either the raw ratio (Figures 2.6a and 2.6e) or the fold change (Figures 2.6c and 2.6g), has different dynamic ranges at different cell numbers. However, when accounting for the number of cells in the right-hand panels, the signal across different cell numbers collapses such that the dose-response curves for different cell numbers tend to more closely match for both strains at higher amounts of H₂O₂ as evidenced by two-tailed Welch’s t-tests (Tables A.2-A.5).

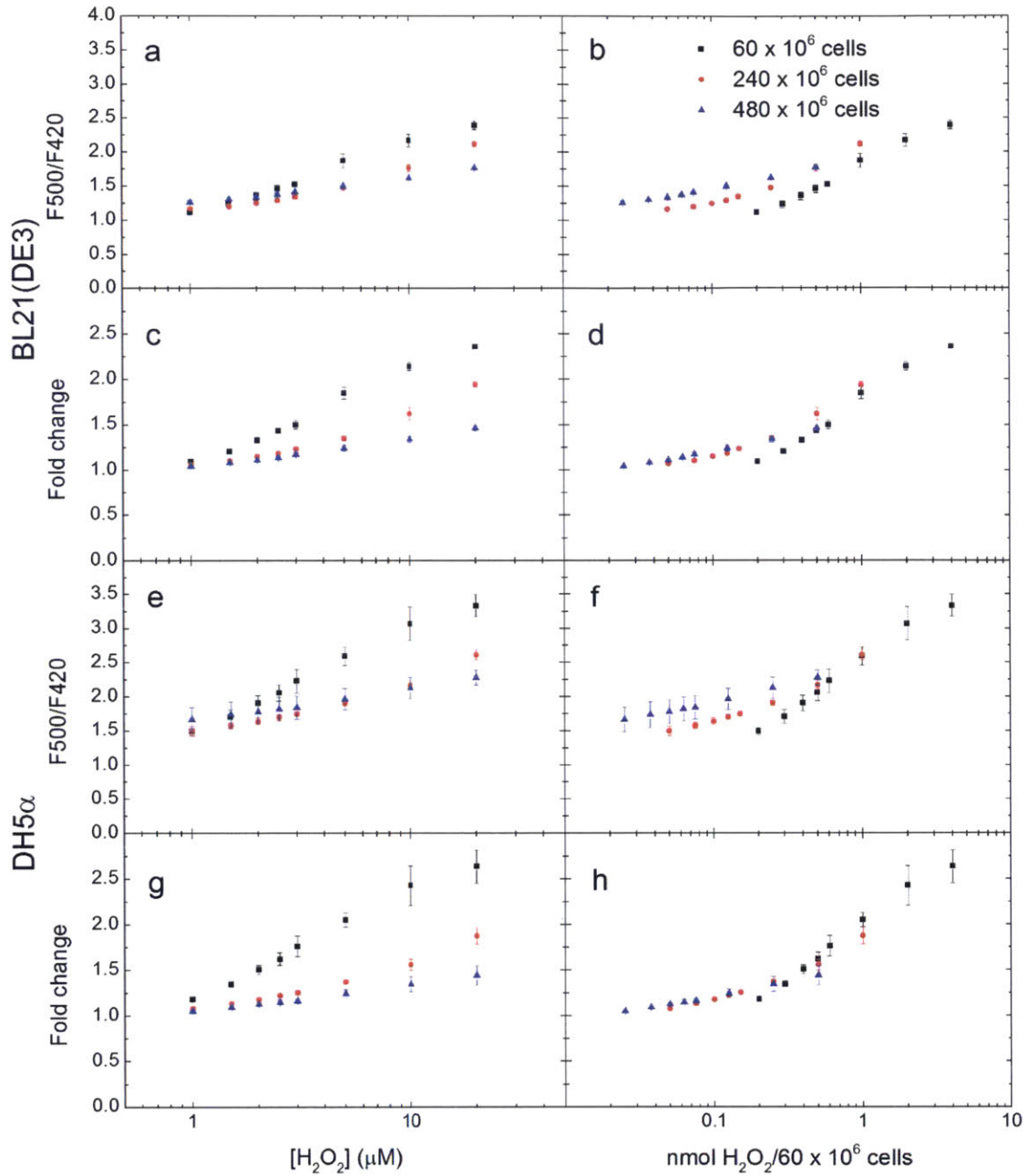


Figure 2.6. Dose-response curves of F500/F420 or fold change versus $[H_2O_2]$ or H_2O_2 amount normalized to number of cells in assay solution of particular volume. $[H_2O_2]$ is concentration of the entire assay solution. Curves for both strains (BL21 (DE3) and DH5 α) at three different cell numbers (60 , 240 , and 480×10^6) are shown. F500/F420 is shown for BL21 (DE3) (a, b) and DH5 α (e, f). Fold change is also shown for BL21 (DE3) (c, d) and DH5 α (g, h).

It should be noted that even though the amount of exogenously added H_2O_2 is normalized to the number of cells in the right-hand panels of Figure 2.6, some slight differences in the signal still persist across different cell numbers. However, these differences do not show different dynamic ranges as in the left-hand panels; rather, the differences lie in the fact that the raw ratio increases with the number of *E. coli* at lower amounts of H_2O_2 , even when no H_2O_2 is added ($F_{500}/F_{420_{\text{basal}}}$). Given that measurements at all cell numbers were performed on cells taken from the same solution, the increase in signal for higher cell numbers may be due to light scattering by *E. coli*; Kiefer et al., for instance, showed that the absorbance at 500 nm increases more than at 420 nm when the number of cells in solution is increased from 70×10^6 to 700×10^6 [95]. Thus, it is quite feasible that increases in cell number from 60×10^6 to 240×10^6 and then to 480×10^6 may lead to greater increases in scattering at 500 nm than at 420 nm, which would explain why $F_{500}/F_{420_{\text{basal}}}$ and other raw ratios at low H_2O_2 levels generally increase with cell number. The use of fold change to measure the signal takes this variation in raw ratio across different cell numbers into account and effectively eliminates statistically significant differences in the signal (Tables A.2-A.5). Thus, while the raw ratio may vary with cell number at particularly low levels of H_2O_2 likely due to light scattering, the fold change can be used to somewhat account for this variation.

The differences in dose-response curve behavior between the left-hand and right-hand panels of Figure 2.6 demonstrate the importance of controlling the number of cells when measuring HyPer's signal in response to oxidative stress. Given a fixed number of cells and fixed amount of externally added H_2O_2 , each cell is exposed to a fraction of the H_2O_2 ; thus, HyPer exhibits a signal within the cell in response to this fraction of the H_2O_2 . Therefore, the amount of H_2O_2 added when measuring HyPer's signal should, in principle, be normalized to the number of cells. Furthermore, even when the number of cells is accounted for in measurement of the signal, light scattering as a function of the number of cells can also impact the raw ratio, particularly at relatively low levels of H_2O_2 . The amount of H_2O_2 per some fixed number of cells as well as the total number of cells being measured in a given volume are both variables to which dose-response curves can be quite sensitive.

2.3.3 Effects of expression host strain on dose-response curves and formalized quantitative characterization of the signal

The proof-of-concept work by Belousov et al. [59] did not address the question of whether and how the strain of *E. coli* used affects the signal. The difference in the kinetics of H_2O_2 scavenging between the two strains in this study (Figure 2.5), as well as the apparent differences in the dose-response curves in the right-hand panels of Figure 2.6, suggest that the use of HyPer in two different *E. coli* strains does have an effect on the resulting dose-response curve. To further quantify the differences in the signal between the two strains, we focused on the dose-response curves measured using 60×10^6 cells and fitted the Hill equation (Section 2.2.5) to the raw ratiometric signal (Figure 2.7). The parameters quantifying the dose-response curve according to a fit with an unconstrained Hill coefficient are shown in Table 2.3.

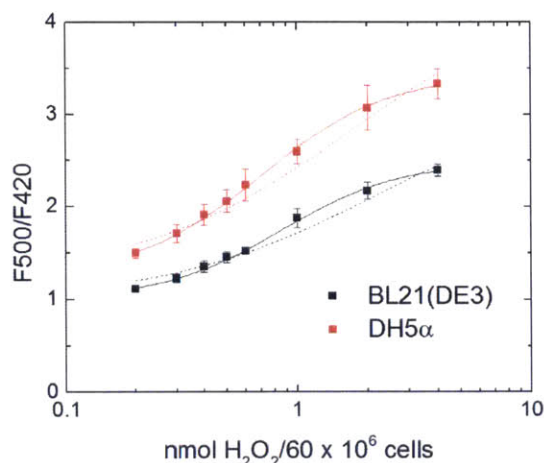


Figure 2.7. Dose-response curves of F500/F420 versus H_2O_2 amount normalized to number of cells in assay solution. Curves for both strains BL21(DE3) and DH5 α at cell number of 60×10^6 are shown. The Hill equation was fit to the data, with n fixed at 1 (dashed) and not fixed but allowed to be fitted to the data (solid).

Table 2.3. Quantitative parameters of the fluorescent signal of HyPer in *E. coli* measured at 60×10^6 cells per $200 \mu\text{l}$.

E. coli strain	BL21 (DE3)	DH5 α
Dynamic range ($[\text{F500}/\text{F420}_{\text{max}}]/[\text{F500}/\text{F420}_{\text{basal}}]$)	2.45 ± 0.06	2.71 ± 0.11
$K_{1/2}$ (nmol $\text{H}_2\text{O}_2/60 \times 10^6$ cells)	0.86 ± 0.04	0.71 ± 0.03
Hill coefficient n	1.72 ± 0.09	1.62 ± 0.06
Signal-to-noise ratio	120.4	57.2

The dose-response curves in each strain differ in dynamic range, $K_{1/2}$, and signal-to-noise ratio, while the difference in the Hill coefficient n is not statistically significant (Table A.6). Also notable is that the Hill coefficient n is greater than 1 for both strains. This suggests positive cooperativity in the reaction between HyPer and H_2O_2 , which in turn suggests that oxidized HyPer may interact in some way with another HyPer molecule that is reduced, facilitating its oxidation by H_2O_2 ; this would be consistent with the behavior of the OxyR transcription factor [96]. While purified HyPer has been characterized as a monomer, it is also known that it can exist as a mixture of dimers and monomers at higher concentrations [93,94].

The results of assuming the reaction of HyPer with H_2O_2 to be an independent event, fixing n at 1, and fitting the Hill equation accordingly are also shown in Figure 2.7. To fit the equation to the data, the parameter reduced χ^2 was minimized, and was 2.5 and 1.1 for BL21 (DE3) and DH5 α , respectively, when n was fixed at 1; when n was not fixed, the reduced χ^2 was 0.17 and 0.059 for BL21 (DE3) and DH5 α , respectively, showing that the equation converged to a better fit.

Overall, Figure 2.7, Table 2.3, and Table A.6 confirm the differences in signal between the two strains suggested by other data in this work. The apparent differences between two different strains of *E. coli*

also suggest that other microbes, with possible differences in scavenging capacity, disulfide reductase activity, and HyPer expression level, may also exhibit different dose-response curves. Thus, dose-response curves should be developed specific to the expression host, without preemptively assuming that a single HyPer molecule reacts with H₂O₂ in an independent fashion.

2.4 Discussion

One possible reason for the difference in HyPer's signal measured in DH5 α and BL21 (DE3) is the presence of the *recA* null mutation in the former, which results in approximately 50% cell viability at the time of measurement [97]. While expressed HyPer may still be able to detect H₂O₂ in dead cells, the disulfide reductase machinery is no longer active; thus, HyPer in the oxidized state in dead cells can no longer be reduced to reverse its signal and may become overoxidized. Because of the *recA* null mutation, this would be more frequent in the DH5 α strain than in BL21 (DE3).

Figure 2.5 clearly showed that the strains also have different scavenging rates, suggesting that they have different expression levels of H₂O₂ scavengers. The primary scavengers in *E. coli* are the catalases, KatG and KatE, and Ahp [98]. Ahp is the primary scavenger of endogenously produced H₂O₂ in routine growth conditions [92], while KatE and KatG are better suited for scavenging much higher levels of exogenously introduced H₂O₂ [92]; the scavenging activity of cells containing only Ahp with *katE* and *katG* null mutations, for instance, became saturated at an extracellular H₂O₂ concentration of 20 μ M with 45 x 10⁶ cells (assuming that an OD₆₀₀ of 1 approximately equates to 10⁹ cells/ml) present in a 0.45 ml volume (6.75 nmol H₂O₂/60 x 10⁶ cells), while the scavenging activity of cells expressing only catalase did not become saturated even in the presence of millimolar concentrations of H₂O₂ [92]. Given the concentrations of H₂O₂ used in this study, it is likely that KatG and KatE were the primary scavengers in the initial parts of our measurements, and possible that the expression levels of these scavengers differ not only between different strains but also between different isolates of the same strain. KatE, for instance, is induced by the RpoS system [99]; because the level of RpoS factor can vary between strains and isolates of the same strain, this may result in different expression levels of KatE. The expression levels and *in vivo* activities of the primary scavengers in *E. coli* may vary between strains, which would affect the signal due to potential kinetic competition between scavengers and HyPer for H₂O₂.

We also note that the induction of certain genes in *E. coli* depend on growth conditions. Expression of Ahp and KatG are primarily regulated by the OxyR transcription factor [100], while KatE is strongly expressed only in the stationary phase and induced by the RpoS system [99]. In our experiments, the cultures were grown to stationary phase and introduced to exogenous H₂O₂, meaning that all three scavengers were induced. Thus, a different set of conditions in which HyPer might have been expressed could have changed the expression levels of the primary scavengers and consequently their competition with HyPer and the resulting fluorescent signal. If the cultures had not been grown to stationary phase, for instance, then the KatE catalase could have been removed as a potential contributor to scavenging activity. Because growth conditions affect the expression levels of the primary scavengers, growth conditions are also an important variable to consider when measuring HyPer's signal in cells in response to exogenous H₂O₂.

2.5 Conclusions

Overall, the work described in this chapter shows the importance of controlling several variables when assaying HyPer's intracellular signal in response to external oxidative stress. The timing of the

measurement is important in the generation of a dose-response curve and the resolution it provides, since this curve evolves over time after exposure to oxidative insult. Furthermore, expression of HyPer may reduce the cell's H₂O₂ scavenging capacity; this effect should be taken into account by measuring the scavenging rate both with and without HyPer. The number of cells should also be controlled to allow normalization of the amount of exogenously added H₂O₂ and also to account for variations in the signal due to possible light scattering by the cells themselves, particularly at low levels of H₂O₂ per cell. The expression host used also affects the signal, likely due to differences in scavenging capacity, disulfide reductase activity, HyPer expression, and cell viability. Growth conditions also influence scavenging capacity by affecting which scavengers are expressed and to what levels, making growth conditions for HyPer expression another important variable to control.

We establish a framework for systematically measuring dose-response curves in this physiological context and generating statistically meaningful properties of the response. When the variables mentioned above – timing of measurement, effects of HyPer expression on the cell's scavenging capacity, number of cells, and expression host – are well controlled and accounted for, the parameters obtained from a dose-response curve should facilitate meaningful comparisons of the signal across different studies. This framework should enable reproducible use of HyPer in more quantitative studies of biological processes in which cells are exposed to external oxidative stress. Furthermore, our work establishes a protocol for expressing HyPer in *E. coli* for *in vivo* measurements of H₂O₂ and interpreting the resulting signal, which should prove useful in protein engineering applications, as we describe later in Chapter 4.

Chapter 3

Exploration of cytochrome P450 BM3 as an H₂O₂ generator

Abstract

In searching for a candidate enzyme that meets the criteria of an ideal hydrogen peroxide (H_2O_2) generator, we turned to cytochrome P450 BM3, a soluble enzyme with an established history of being engineered for biotechnological applications and the capability of producing H_2O_2 or superoxide using only nicotinamide adenine dinucleotide phosphate (NADPH) and molecular oxygen through a reaction termed leakage. While the wild-type (WT) enzyme exhibits a relatively low leak rate orders of magnitude less than the H_2O_2 production rates of previously used oxidases, the A82W, T268N/F393H, and I401P variants in past studies have demonstrated enhanced leakage. Leakage also holds interest since it has often been correlated with decreased coupling efficiency between P450 BM3's two domains for its native function of hydroxylation, lessening its value in biotechnological applications. Furthermore, the physical basis for leakage is not yet well understood in this particular member of the cytochrome P450 family.

We used simulations to show that in kinetic competition with hydroxylation, the correlation between leakage and decreased coupling can be explained by leakage's consumption of electrons that would have otherwise been used to hydroxylate substrate, even with substrate in solution. We further explored leakage and P450 BM3's potential as an H_2O_2 generator by introducing the above leakage-enhancing mutations and combining these mutations. The variants in this chapter show that combining leakage-enhancing mutations can increase leakage further. They also provide evidence that while a transition to high spin may be vital for coupled hydroxylation, this is not the case for leakage, showing that substrate binding and the consequent shift in spin state are not strictly necessary as a redox switch for catalytic action. While each variant exhibited leak and H_2O_2 production rates significantly higher than those of WT, they also experienced severe decreases in bacterial expression and thermostability, suggesting a tradeoff between leakage and stability and thus evolvability. Indeed, mutations in this chapter were far more deleterious than other mutations that have been used in other studies to change substrate specificity. When expressed in mammalian cells, none of the variants except for WT were detectable by a carbon monoxide assay that measures for active enzyme. Although none of the variants were suitable for H_2O_2 generation in that particular context, they do suggest a linkage between bacterial expression, thermostability, and mammalian expression, which could be tested by exploring the remainder of P450 BM3's sequence space, as was performed in Chapter 4.

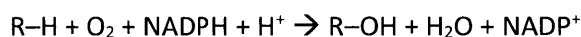
Portions of this chapter are included in:

Lim, J. B., Barker, K. A., Jiang, L., Molina, V., Saifee, J. F., and Sikes, H. D. Insights into electron leakage in the reaction cycle of cytochrome P450 BM3 revealed by kinetic modeling and mutagenesis. Submitted.

3.1 Introduction

In seeking to create a novel screen to engineer enzymes with enhanced H₂O₂ production, we sought a candidate enzyme to both explore as a potential H₂O₂ generator in mammalian cells and test in the pending screen. Since the previously used oxidases XO, GOX, and DAAO have demonstrated activity levels high enough to induce biological effects associated with H₂O₂ (Table 1.1), we aimed to explore use of another enzyme that fulfills the criteria of an ideal generator unmet by previous oxidases.

We turned our attention to cytochrome P450s (CYPs), a family of heme-containing enzymes that generally perform hydroxylation and are found in almost all organisms. The hydroxylation reaction proceeds as follows:



where R-H is substrate, O₂ is molecular oxygen, NADPH/NADP⁺ is nicotinamide adenine dinucleotide phosphate, and R-OH is hydroxylated product. The reaction requires coupling of activities between a reductase, to which NADPH transfers its electrons, and an oxidase, which binds O₂ and R-H and receives electrons from the reductase to perform catalysis (Figure 3.1). While the electron transfer is usually well-coupled with the reaction, uncoupling sometimes occurs, albeit at low frequencies, resulting in production of either H₂O₂ or O₂⁻.

One member of the CYP family, P450 BM3, is of particular interest because it captures many of the qualities that define an ideal H₂O₂ generator. Unlike membrane-bound mammalian CYPs, P450 BM3 is water-soluble and is found in the cytosol of *Bacillus megaterium*. While many other CYPs rely on a protein partner for electron transfer, P450 BM3 fuses the reductase and oxidase domains into one polypeptide. As a result of this and perhaps other factors, P450 BM3 has the highest reported activity in the CYP family; indeed, its activity is several orders of magnitude higher than those reported for mammalian CYPs, as shown in Table 3.1.

Table 3.1. Maximum velocity rates of CYPs on native substrates.

CYP	Source	Activity (min ⁻¹)
CYP102A1 (BM3)	<i>Bacillus megaterium</i>	17000 [101]
CYP101 (cam)	<i>Pseudomonas putida</i>	4200 [102]
CYP4F2	Human liver	7.4 [103]
CYP4A11	Human liver	49.1 [103]
CYP1A1	Human liver	7.25 [104]
CYP1A2	Human liver	3.34 [104]

When in contact with non-native substrate or when certain mutations are introduced, P450 BM3 performs the leakage reaction whereby electrons are transferred from NADPH to reduce O₂, producing either water or the ROS H₂O₂ and O₂⁻ in a reproducible fashion (Figure 3.1). P450 BM3 is thus of interest because it captures nearly all the qualities of an ideal H₂O₂ generator; while its activity cannot be tuned by substrate amounts because of its reliance on ample, endogenous substrate, a set of variants with activity levels spanning a relevant range could be used instead for tuning.

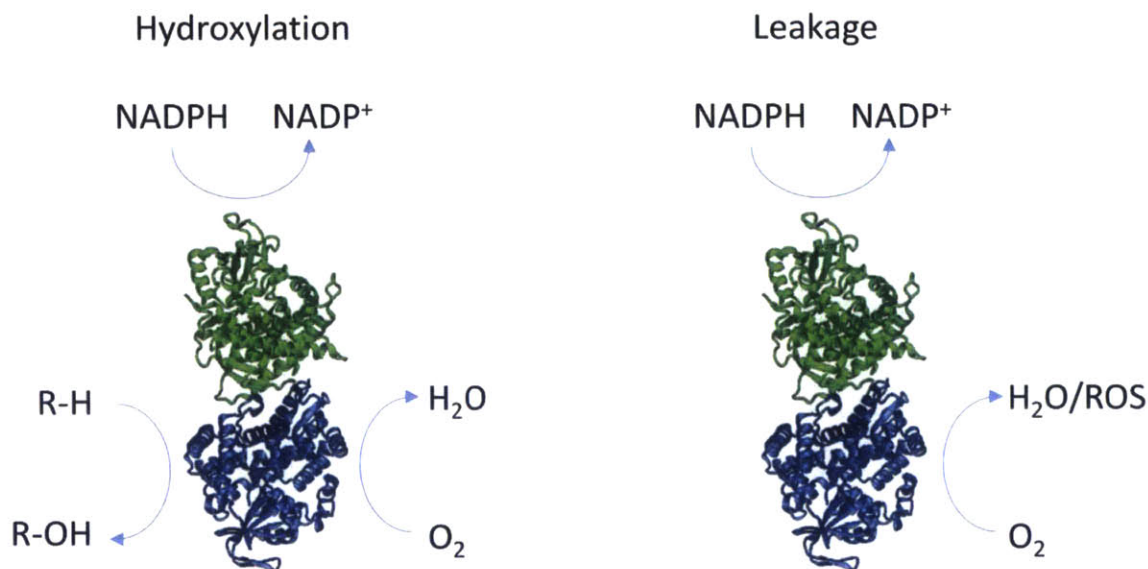


Figure 3.1. Schematic of P450 hydroxylation and leakage. NADPH binds to the reductase domain and donates electrons to the FAD and then FMN cofactors, which then transfer the electrons to the heme in the oxidase domain. In coupled hydroxylation, O₂ and R-H bind at distinct sites, and O₂ is reduced and activated to hydroxylate R-H, transforming it into R-OH. In leakage, the electrons are still transferred to the heme and used to reduce O₂, but this may result in water, H₂O₂, or O₂⁻. R-H is not involved in the leakage reaction.

The single characteristic that the wild-type (WT) P450 BM3 may be lacking, however, is high enough activity to sustain accumulation of intracellular H₂O₂. While its native activity (Table 3.1) is on par with the activity levels of past enzymes used for H₂O₂ generation (Table 1.1), its reported leak rate ranges from 12 ± 6 [105] to $28 \pm 0.7 \text{ min}^{-1}$ [106], depending on experimental conditions, making it several orders of magnitude less than the activities of previously used oxidases.

Yet previous studies demonstrated certain variants, i.e. A82W [107], T268N/F393H [105], and I401P [106], that exhibit leakage significantly higher than that of WT. Furthermore, P450 BM3 has an extensive history of being engineered for many different biotechnological purposes [108–112], providing a key precedent that opens the possibility of engineering P450 BM3 for higher H₂O₂ production and thus transforming it into an ideal generator.

In addition to its potential relevance to practical engineering applications, leakage also holds interest as it relates to a fundamental understanding of P450 biocatalysis. A substrate for P450 BM3 to hydroxylate has historically been considered necessary for any significant activity because the binding of target substrate to the enzyme is thought to induce required changes in conformation, reduction potential, and spin state that make the electron transfers favorable [113]. Leakage is essentially catalysis without bound R-H substrate, raising the question of whether certain mutations induce similar protein property changes thought to be required for favorable electron transfer.

While leakage in P450 cam, another member of the P450 family, has been extensively studied, leakage in P450 BM3 is relatively unexplored [114]. The reaction conditions in the studies that have noted variants with enhanced leakage [105–107] were not consistent, complicating comparison of these variants. These mutations were also associated with different property changes without bound substrate, including structural conformation, reduction potential, and spin state content of the heme domain. Systematic and quantitative investigation of these mutations should increase knowledge of which mechanistic properties are important with respect to leakage in P450 BM3's catalytic cycle.

In this chapter, we asked the following: do combinations of individual leakage-enhancing mutations increase leakage even further? Are the properties known to be important in hydroxylation also relevant in leakage? To what extent is leakage of electrons coupled with ROS generation? Are any other protein properties associated with increases in leakage? Can P450 BM3 be engineered into an ideal H₂O₂ generator? To address these questions, we explored leakage in P450 BM3 and its potential use as an H₂O₂ generator by generating and combining past mutations mentioned above and previously shown to induce higher leakage [105–107], resulting in four new variants: A82W/I401P, A82W/T268N/F393H, T268N/F393H/I401P, and A82W/T268N/F393H/I401P (Figure 3.2). We did not investigate T268N or F393H without the other since it has already been reported that only combining these two mutations together results in enhanced leakage; each of these mutations alone does not enhance leakage [105]. Using this set of variants, we investigated the relationship between increased leakage and other key properties of the enzyme, such as the stability of the protein fold and electronic properties of the heme. We also probed the potential of P450 BM3 and related variants as H₂O₂ generators.

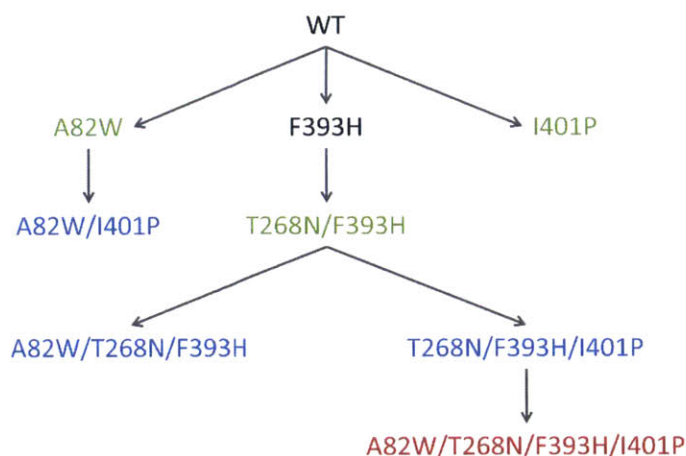


Figure 3.2. Schematic for lineage of variants with enhanced leakage derived from WT P450 BM3. Variants found to exhibit enhanced leakage in previous studies colored in green. Variants directly derived from variants measured in previous studies colored in blue. Variant containing all mutations in this chapter colored in red. The T268N variant was not generated since it was already known that only combining this mutation with the F393H mutation, rather than either of these mutations alone, increases leakage [105].

3.2 Materials and methods

3.2.1 Kinetic simulations

Differential equations modeling leakage, association and dissociation of substrate R-H to the enzyme, and hydroxylation of bound substrate were implemented using the ode15s function in Matlab (MathWorks). The reactions used and their respective rate constants are shown in Figure 3.3, and the differential equations and code are shown in Appendix B.

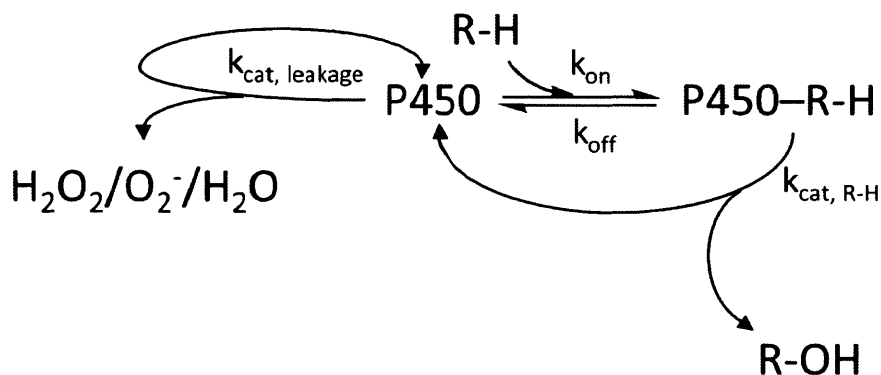


Figure 3.3. Scheme modeling the competing reactions of hydroxylation and leakage. In both cases, NADPH was used. It was assumed that P450 is saturated with O_2 . When P450 binds R-H, it was assumed that hydroxylation occurs with 100% coupling, which is the case for native substrate. Unbound P450 was subject to leakage and produced H_2O , H_2O_2 , or O_2^- . H_2O_2 and O_2^- were assumed to not react with and deactivate P450.

3.2.2 Site-directed mutagenesis

Wild-type and variants were expressed using the plasmid pCWori [115], encoding full-length P450 BM3, which was a kind gift of Professor Frances Arnold, Caltech, Pasadena, CA. All variants described in this chapter were obtained by site-directed mutagenesis (see Table 3.2 for primer sequences). Codons that occur most frequently in *E. coli* were chosen for the mutagenic primers. Oligonucleotides were purchased from Integrated DNA technologies. All variants were fully sequenced to confirm the absence of any undesired mutations.

Table 3.2. Primers used for sequencing and site-directed mutagenesis of cytochrome P450 BM3 in its native sequence.

Primer name	Sequence
Heme_for	5'-CAG GAA ACA GGA TCA GCT TAC TCC CC-3'
Heme_rev	5'-CGC GCC GTT CCT TCA GCT GTT CCC-3'
FMN_for	5'-GCT GGT ACT TGG TAT GAT GCT-3'
FMN_rev	5'-CCA GAC GGA TTT GCT GTG AT-3'
FAD_for	5'-CGT GTA ACA GCA AGG TTC GG-3'
FAD_rev	5'-CTG CTC ATG TTT GAC AGC TTA TC-3'
A82W_for	5'-CGT GAT TTT TGG GGA GAC GGG-3'
A82W_rev	5'-CCC GTC TCC CCA AAA ATC ACG-3'
T268N_for	5'-GCG GGA CAC GAA AAC ACA AGT GGT CTT-3'
T268N_rev	5'-AAG ACC ACT TGT GGT TTC GTG TCC CGC-3'
F393H_for	5'-GCG TTT AAA CCG CAT GGA AAC GGT CAG CGT GCG-3'
F393H_rev	5'-CGC ACG CTG ACC GTT TCC ATG CGG TTT AAA CGC-3'
I401P_for	5'-CGG TCA GCG TGC GTG TCC GGG TCA GCA GTT CGC-3'
I401P_rev	5'-GCG AAC TGC TGA CCC GGA CAC GCA CGC TGA CCG-3'

3.2.3 Protein expression and purification

Reagents for making growth media were obtained from Becton Dickinson. A single colony of *E. coli* DH5 α cells harboring the expression plasmid was used to inoculate 5 ml of LB medium (Becton Dickinson) containing ampicillin (100 μ g/ml; USB Corporation) in a 14 ml culture tube (17 x 100 mm, VWR) and incubated at 37 °C with orbital shaking of 250 rpm overnight. This overnight culture was then used to inoculate 250 ml of TB medium (Becton Dickinson) containing ampicillin at the same concentration in a non-baffled 1 liter Erlenmeyer flask (VWR). The culture was incubated at 37 °C with orbital shaking of 250 rpm until the end of log phase (OD₆₀₀ ~0.9). Expression was induced by the addition of IPTG (1 mM; Omega Bio-Tek) and occurred at 30 °C with orbital shaking of 200 rpm for 24 hours. Cells were harvested by centrifugation at 4000 g and 4 °C for 10 min and stored at -20 °C.

For purification, the cell pellet was resuspended in Tris buffer (20 ml, 25 mM Tris-HCl, pH 7.9; MP Biomedicals, LLC) and lysed by sonication (7 x 1 min; output control = 5, duty cycle 50%; Sonicator, S-250A analog, Branson). The lysate was centrifuged at 18000 g and 4 °C for 10 min and the supernatant was filtered using a 0.8/0.2 μ m Acrodisc syringe filter with Supor membrane (Pall Corporation). The filtrate was loaded onto a 1 ml HiTrap Q Sepharose FF anion exchange column via a superloop; the column and superloop were integrated into an ÄKTApurifier with a UNICORN control system v5.20 and a Frac-950 collector (GE Life Sciences). Non-P450 BM3 proteins (as evidenced by absorbance at 280 nm and lack of absorbance at 417 nm) were eluted in a first step from 0 to 0.2 M NaCl (Mallinckrodt Pharmaceuticals). P450 BM3 and related variants were eluted in a second step to 0.4 M NaCl. Any remaining protein on the column was eluted in a third step to 1 M NaCl. The purification was performed at 1 ml/min and 4 °C. Purified P450 BM3 fractions were centrifuged through an Amicon Ultra-15 Centrifugal Filter Unit with Ultracel-100 membrane with nominal molecular weight limit of 100 kDa (Millipore). After centrifugation at 4000 g and 4 °C for 10 min, 3 ml of KPi (100 mM, composed of monopotassium phosphate and dipotassium phosphate purchased from VWR, pH 8) was added to the remaining sample and centrifuged again through the filter unit at the same conditions. 3 ml of KPi (100

mM, pH 8) was added to the supernatant and centrifuged through the filter unit at the same conditions, generally resulting in 200-400 μ l supernatant of protein solution. The remaining supernatant was diluted by adding 200-400 μ l of KPi (100 mM, pH 8) and then dispensed into 20 μ l aliquots and stored at -80 °C.

3.2.4 Spectrophotometric analysis of oxidized enzyme and carbon monoxide binding

Purified protein (20-200 μ l) stored at -80 °C was thawed on ice and introduced into KPi (100 mM, pH 8) to make a 1 ml solution. Absorption spectra were recorded from 350 to 750 nm at room temperature (22 °C) using a Varian Cary 50 spectrophotometer and a polystyrene cuvette (VWR) with path length of 1 cm. The enzyme was reduced with a spatula tip of sodium dithionite before introducing 30 bubbles of carbon monoxide (CO; Airgas, Inc.) at 1 bubble/s into the assay solution, and absorption spectra were recorded before reduction, after reduction, and after reduction and treatment with CO. Reduced CO-bound difference spectra and the extinction coefficient $\epsilon_{450-490} = 91 \text{ mM}^{-1} \text{ cm}^{-1}$ were used to calculate the concentration of correctly folded full-length protein. Experiments were carried out in duplicate save for A82W/T268N/F393H/I401P due to prohibitively low expression of correctly folded protein. P450 concentrations were recorded as a mean \pm standard deviation save for A82W/T268N/F393H/I401P.

3.2.5 Steady state kinetics

Absorbance data was collected using a Varian Cary 50 spectrophotometer. Reactions (1 ml) were carried out at room temperature in KPi (100 mM, pH 8) using enzyme (10-100 nM) and NADPH (1-100 μ M; Roche). Absorbance was followed at 340 nm and leak rates were calculated using the initial 12-30 seconds of a reaction and $\epsilon_{340} = 6.22 \text{ mM}^{-1} \text{ cm}^{-1}$. Experiments were carried out in triplicate and each leak rate was reported as a mean \pm standard deviation. For each variant, Origin software (Origin Labs) was used to fit the leak rates at different concentrations of NADPH to the Michaelis-Menten equation to obtain $k_{\text{cat, leakage}}$ and $K_{\text{m, leakage}}$.

3.2.6 Thermostability

Activity-based thermostability values (T_{50}) were determined as follows. Samples of purified enzyme (2.5-5 μ M) were incubated for 10 min at different temperatures (from 30 to 65 °C) in an Eppendorf Mastercycler gradient thermocycler. Samples were then centrifuged at 4700 g and 4 °C for 12 min. After centrifugation, protein solutions (160 μ l) were mixed with sodium dithionite (40 μ l, 0.1 M; JT Baker) in a transparent 96-well microtiter plate (Greiner). Spectra from 400 to 500 nm were measured using a Tecan Infinite M200 plate reader and samples were incubated for 15 min with saturating CO in a sealed chamber, after which spectra were measured again. Reduced CO-bound difference spectra were used to calculate the concentrations of correctly folded protein of each sample, and T_{50} values were calculated by fitting heat-inactivation curves to the resulting data using Origin software. Experiments were carried out in duplicate save for T268N/F393H/I401P, for which only one trial was performed, and A82W/T268N/F393H/I401P, for which not enough protein could be obtained to perform the assay. Each T_{50} was reported as mean \pm standard deviation.

3.2.7 Analysis of reaction products

The proportion of H_2O_2 production formation was determined by an HRP/ABTS assay. To develop a standard curve, a stock solution of H_2O_2 was quantified based on absorbance at 240 nm ($\epsilon_{240} = 43.6 \text{ M}^{-1} \text{ cm}^{-1}$) and used to prepare serial dilutions of H_2O_2 . Purified enzyme (100 nM) was incubated with aliquots of the H_2O_2 dilutions; enzyme was included to account for the possible effects of antioxidants such as

catalase and Ahp, which may have been present in the enzyme purifications in at least trace amounts. For trial reactions to measure H₂O₂ formation by P450 BM3, purified enzyme (100 nM) was incubated with NADPH (100 μM).

All reactions, both those to develop a standard curve and those to measure H₂O₂ formation by P450 BM3, were performed at a fixed volume (150 μl) and room temperature (22 °C). Reactions were performed in KPi (100 mM, pH 8) with sodium azide (NaN₃, 10 mM; Sigma-Aldrich Corporation), an inhibitor of catalase activity. Reactions were stopped after an initial incubation period of 2-6 min using hydrochloric acid (10 μl, 5 N; Mallinckrodt Pharmaceuticals); for each P450 BM3 variant, the incubation period was held constant between trials. The reaction was centrifuged at 14000 g and 4 °C for 10 min. A portion of the supernatant (140 μl) was added to KPi (20 μl, 100 mM, pH 8), more concentrated KPi (50 μl, 1 M, pH 8), ABTS (50 μl, 2.5 mM; Tokyo Chemical Industry, Co., Ltd.), and HRP (10 μl, 3 mg/ml, Thermo Scientific) in a transparent 96-well microtiter plate (Greiner) and mixed. The absorbance at 405 nm was read using a Tecan Infinite M200 plate reader.

Experiments were carried out in triplicate. Absorbances of the standard curve reactions were averaged and standard deviations were calculated. These were then correlated with the initial H₂O₂ concentrations to develop a standard curve via linear regression, which was used to convert the absorbances of the trial reactions to the amount of H₂O₂ produced by each variant of P450 BM3 (Figures B.9-B.13). To calculate the proportion of product comprised by H₂O₂, the amount of H₂O₂ was normalized by the amount of NADPH consumed by P450 BM3 during the incubation period as measured by steady state kinetics assays.

3.2.8 Transfer of P450 gene to mammalian vector

The gene for the WT heme domain codon optimized for mammalian expression using Gene Designer software (DNA 2.0, Menlo Park, CA) and encoded in a pCMV-Sport vector was provided as a kind gift from Professor Mikhail Shapiro, Caltech, Pasadena, CA. The gene was transferred to the pTRE3G-IRES vector (Clontech) by PCR. A Kozak sequence was added immediately upstream of the gene to enhance expression, and a 6X His-tag was added immediately downstream to enable detection by a Western blot. The reductase domain was then codon optimized by GenScript (Piscataway, NJ) and fused with the heme domain by PCR. Mutations were implemented using site-directed mutagenesis, as was done in Section 3.2.2. Codons that occur most frequently in mammalian cells were chosen for the mutagenic primers. Primers are listed in Table 3.3.

Table 3.3. Primers used for sequencing, PCR, and site-directed mutagenesis of cytochrome P450 BM3 codon optimized for mammalian expression.

Primer name	Sequence
pIRES_MCS1_for	5'-CCG TCA GAT CGC CTG GAG C-3'
pIRES_MCS1_rev	5'-CGG CTT CGG CCA GTA ACG-3'
FMN_for	5'-GCT GGT ACT TGG TAT GAT GCT-3'
FMN_rev	5'-CCA GAC GGA TTT GCT GTG AT-3'
FAD_for	5'-CGT GTA ACA GCA AGG TTC GG-3'
FAD_rev	5'-CTG CTC ATG TTT GAC AGC TTA TC-3'
A82W_for_codon_opt	5'-GTC AGA GAT TTT TGG GGA GAT GGC TTG-3'
A82W_rev_codon_opt	5'-CAA GCC ATC TCC CCA AAA ATC TCT GAC-3'
T268N_for_codon_opt	5'-GCC GGA CAC GAG AAC ACT TCA GGC CTG-3'
T268N_rev_codon_opt	5'-CAG GCC TGA AGT GTT CTC GTG TCC GGC-3'
F393H_for_codon_opt	5'-GCG TTT AAA CCC CAC GGC AAC GGA CAG CGC GCC-3'
F393H_rev_codon_opt	5'-GGC GCG CTG TCC GTT GCC GTG GGG TTT AAA CGC-3'
I401P_for_codon_opt	5'-CGG ACA GCG CGC CTG TCC CGG CCA ACA GTT CGC-3'
I401P_rev_codon_opt	5'-GCG AAC TGT TGG CCG GGA CAG GCG CGC TGT CCG-3'

3.3 Results

We first modeled leakage and hydroxylation as competing kinetic reactions to quantify leakage's potential impact on coupling. We then engineered previous leakage-enhancing mutations [105–107] into P450 BM3 and combined them, determining the effects of these mutations on leak rate, spin-state content, thermostability/evolvability, and H₂O₂ production, and thus exploring the relationship between leakage and other key protein properties. Finally, we transferred each variant's gene to a vector for inducible mammalian expression, used these vectors to transfect HeLa cells, and measured their expression and H₂O₂ production.

3.3.1 Modeling effects of leakage on coupling with respect to hydroxylation

To quantify the potential effects of increasing leakage, we modeled leakage and hydroxylation of palmitate [116,117] as two competing kinetic reactions, implementing them as differential equations in Matlab (Mathworks, Inc.). Since k_{on} and k_{off} values have never been measured for P450 BM3 and a particular substrate, we used a k_{on} range of 10^5 to 10^8 M⁻¹ s⁻¹ for association of enzyme with R–H (typical for association of enzyme with substrate [118]) and calculated the effects of increasing $k_{cat, leakage}$ (i.e. k_{cat} measured for NADPH consumption in the absence of an R–H substrate), which resulted in higher rates of overall NADPH consumption as well as lower coupling percentages (Figure 3.4 and Figures B.1-B.3). While these simulations do not include the microscopic rate constants of the individual steps in the catalytic cycle, using k_{cat} and K_m values to capture the entire cycle instead for both leakage and hydroxylation, they still provide order-of-magnitude estimates of the effects of leakage on coupling.

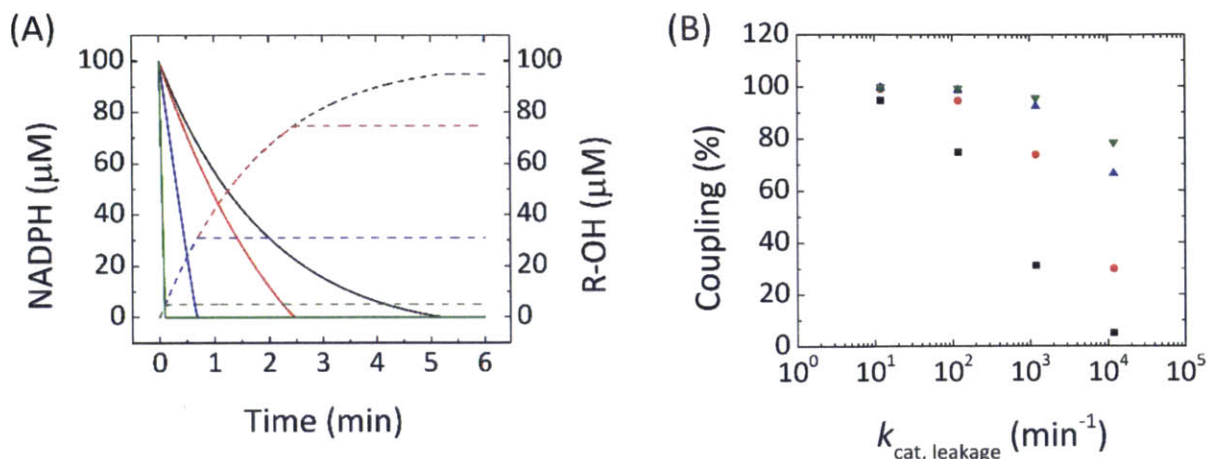


Figure 3.4. (A) Time-course plots of NADPH and hydroxylated product R–OH with different $k_{cat,leakage}$ values, assuming k_{on} for R–H and P450 BM3 to be $10^5 \text{ M}^{-1} \text{ s}^{-1}$ and using K_d , K_m , and $k_{cat,R-H}$ values for palmitate [117]. Black, red, blue, and green represent $k_{cat,leakage}$ of WT (as measured and later reported in this study) multiplied by 10^0 , 10^1 , 10^2 , and 10^3 , respectively. Solid lines represent concentration of NADPH. Dashed lines represent concentration of R–OH. $k_{cat,R-H}$ and $K_m,R-H$ with respect to NADPH in hydroxylation of palmitate were used for the hydroxylation reaction in competition with leakage [116]. (B) Coupling plotted against the different $k_{cat,leakage}$ values used in (A). Coupling is defined as the percentage of NADPH used for hydroxylation. Black, red, blue, and green symbols represent k_{on} values for enzyme binding to R–H of 10^5 , 10^6 , 10^7 , and $10^8 \text{ M}^{-1} \text{ s}^{-1}$, respectively.

The extent to which mutations decrease coupling in P450 BM3 can vary widely. In hydroxylation of lauric acid, for example, the I401P variant exhibited a significantly higher leak rate but did not have a diminished coupling ratio compared to WT [106], suggesting that the leakage reaction in this variant does not effectively compete against native function. Variants in the alkane hydroxylation lineage, on the other hand, showed both higher leakage and significantly lower coupling than WT with respect to P450 BM3’s native substrates [115]. The results in Figure 3.4 show that this discrepancy in leakage’s effects on coupling may be due to differences between these variants in terms of the magnitude of k_{on} relative to that of $k_{cat,leakage}$. For example, if k_{on} is set at $10^8 \text{ M}^{-1} \text{ s}^{-1}$, then leakage is generally outcompeted, as even $k_{cat,leakage}$ greater than 10^4 min^{-1} , an amount on par with P450 BM3’s highest reported activity [119], only diminishes the coupling ratio to 78%; a $k_{cat,leakage}$ value on par with that typical for WT [106] would decrease the coupling ratio by less than 0.1%. On the other hand, if k_{on} is set as low as $10^5 \text{ M}^{-1} \text{ s}^{-1}$, then leakage could have a more drastic effect and potentially decrease coupling by up to 95%. This divergence in leakage’s effect on coupling shows the importance of considering not only the absolute magnitudes of k_{on} and $k_{cat,leakage}$ but also these values relative to each other.

3.3.2 Expression and purification

All proteins were overexpressed and purified. The final preparations of the WT protein and A82W, I401P, T268N/F393H, and A82W/I401P variants had purities in excess of 95% as evidenced by strong single bands in SDS-PAGE analysis (Figures B.4-B.8). The A82W/T268N/F393H, T268N/F393H/I401P, and

A82W/T268N/F393H/I401P preparations showed a weaker P450 band and a significant band between 50 and 75 kDa (Figures B.7 and B.8). The A82W/T268N/F393H preparation was mostly comprised of P450, but the T268N/F393H/I401P and A82W/T268N/F393H/I401P preparations had purities less than 50%. The decrease in purity may be due to the fact that expression of the protein decreased when leakage-enhancing mutations were introduced, and decreased even further when mutations were combined (Table 3.4).

Table 3.4. Yields of protein per liter of culture.

Variant	Yield (mg/l)	Fold less than yield of WT
WT	14.10	1.00
A82W	9.64	1.46
T268N/F393H	10.19	1.38
I401P	9.99	1.41
A82W/I401P	5.69	2.48
A82W/T268N/F393H	2.22	6.35
T268N/F393H/I401P	0.49	28.84
A82W/T268N/F393H/I401P	0.09	150.11

The known primary scavengers in *E. coli* – KatG, KatE, and AhpC – have molecular weights of 80 [120], 84 [121], and 22 kDa [122] in monomeric form, respectively. Measurements of H₂O₂ production required NaN₃, a catalase inhibitor, to obtain a positive signal as described in Section 3.2.7, suggesting that catalase is present in at least trace amounts. However, none of the scavengers' molecular weights matched that of the main impurity present in the A82W/T268N/F393H, T268N/F393H/I401P, and A82W/T268N/F393H/I401P protein preparations. While the impurity has a molecular weight corresponding approximately to that of the reductase domain (65 kDa), it is unlikely that the impurity is the reductase domain because it would imply cleavage of the polypeptide at or near the linker, and thus would also result in a band for the oxidase domain (55 kDa), which is absent from the gels. The main impurity must be native to *E. coli*, but our results did not determine its identity.

3.3.3 Steady state kinetics, spin state, and analysis of reaction products

After using site-directed mutagenesis to generate both variants previously studied [105–107] as well as combinations thereof, we analyzed their spin-state contents using spectrophotometric characterization (Figure 3.5). WT and the T268N/F393H and A82W/T268N/F393H variants resided completely in the low-spin state, as evidenced by their strong Soret peaks at 417 nm. The A82W, I401P, and A82W/I401P variants, on the other hand, had approximately 60% high-spin state content, as shown by their mixed Soret peaks at 390 and 417 nm.

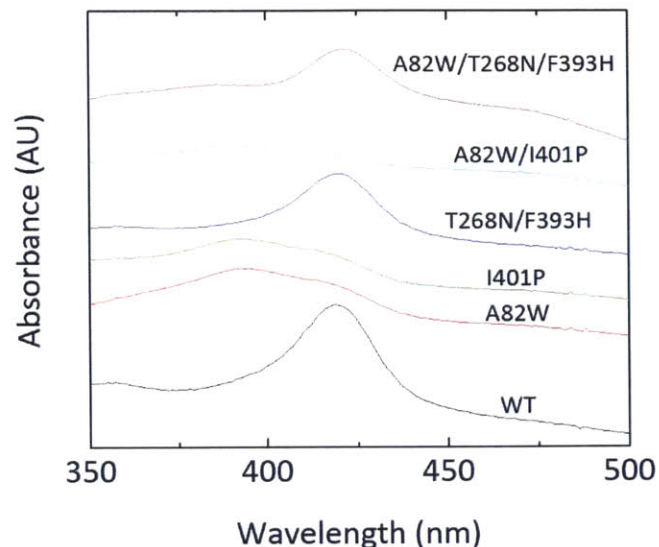


Figure 3.5. Absorption spectra of oxidized variants of P450 BM3. All spectra save for that of the WT protein were offset along the y-axis to aid interpretation. Concentrations of each enzyme as determined by reduced CO-bound difference spectra were 1.6 μM (WT), 0.8 μM (A82W), 0.7 μM (I401P), 0.9 μM (T268N/F393H), 0.6 μM (A82W/I401P), and 0.7 μM (A82W/T268N/F393H). T268N/F393H/I401P and A82W/T268N/F393H/I401P were not included because their purities did not exceed 50% (Figure B.8).

We then kinetically characterized them by measuring their Michaelis-Menten parameters for leakage. Figure 3.6 shows the $k_{\text{cat, leakage}}$ values that resulted for variants with combinations of A82W, T268N/F393H, and I401P mutations. All variants studied here exhibited $k_{\text{cat, leakage}}$ values significantly higher than that of the WT enzyme. Interestingly, variants with two mutations – A82W/I401P and T268N/F393H – did not exhibit $k_{\text{cat, leakage}}$ values higher than that of single-mutation variants, i.e. A82W and I401P. Moreover, A82W/I401P had a K_m 5-fold greater than that of the next highest (A82W) and more than an order of magnitude greater than those of all other variants measured in this work (Table 3.5). The combined effects of the high-spin state content and more oxidizing reduction potential of the I401P variant (-303 mV versus -445 mV for the WT protein [106]) seem to be manifested in the $k_{\text{cat, leakage}}$ of A82W/I401P, but the addition of A82W, which individually also induces a shift to the high-spin state through a different structural change [107], appears to be redundant.

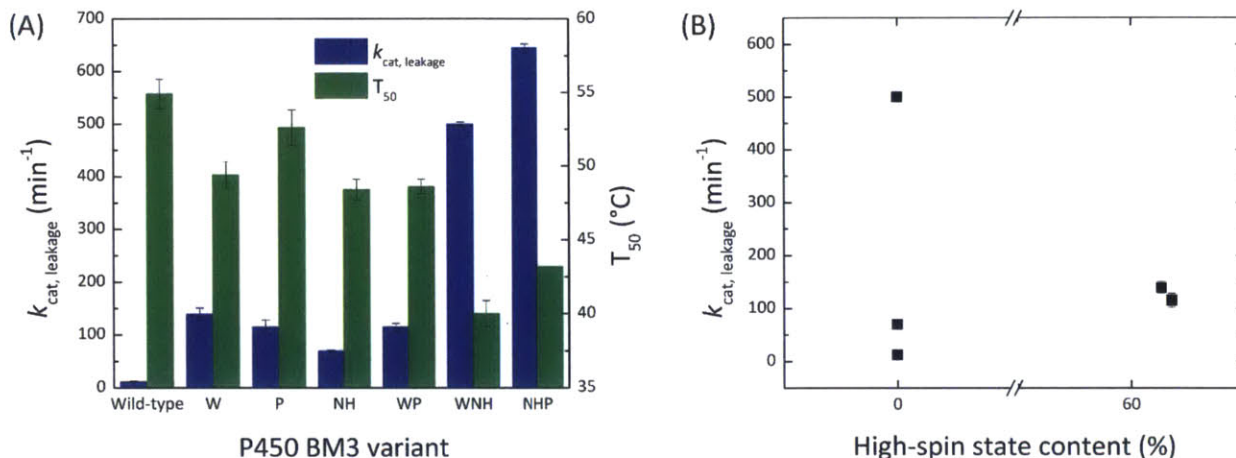


Figure 3.6. (A) Plot showing $k_{cat,leakage}$ and T_{50} of P450 BM3 variants studied here. W = A82W, N = T268N, H = F393H, P = I401P. T_{50} of A82W/T268N/F393H/I401P not measured due to prohibitively poor expression (Table 3.4). (B) Plot of high-spin state content versus $k_{cat,leakage}$. High-spin state contents calculated using absorbance spectra in Figure 3.5. Three of the variants – WT, T268N/F393H, and A82W/T268N/F393H – had high-spin state contents of 0% and three others – A82W, I401P, and A82W/I401P – had high-spin state contents of approximately 60%. When bound to and saturated with palmitate substrate, the WT protein has high-spin state content of 100% and activity of 4860 ± 1020 min⁻¹ [117]. While high-spin state content is well correlated with high activity for hydroxylation, there is no apparent correlation between high-spin state content and leakage. Data points for I401P and A82W/I401P largely overlapped. Error bars generally not visible due to magnitudes less than the size of the data point symbols.

Table 3.5. Measured $K_{m,leakage}$ and proportion of product comprised by H₂O₂.

Variant	$K_{m,leakage}$ (μM)	% H ₂ O ₂
WT	1.3 ± 0.4	-
A82W	4.0 ± 0.9	24 ± 1.7
I401P	1.7 ± 0.3	62 ± 5.7
T268N/F393H	$< 1^a$	89 ± 11
A82W/I401P	20.1 ± 4.4	59 ± 15
A82W/T268N/F393H	$< 1^a$	53 ± 7.4
T268N/F393H/I401P	$< 1^a$	$> 0^b$

^a NADPH absorbance not detectable at concentrations less than 1 μM

^b positive signal indicated presence of H₂O₂ but was not quantifiable due to inability to generate a standard curve

When three of the four mutations were combined – A82W/T268N/F393H and T268N/F393H/I401P – $k_{cat,leakage}$ increased dramatically to several fold higher than the $k_{cat,leakage}$ of any of the one- or two-mutation variants. The $K_{m,leakage}$ of these three-mutation variants also remained below 1 μM. When combined in numbers greater than two, the mutations in this chapter dramatically increase leakage. The combination of all mutations, A82W/T268N/F393H/I401P, which we do not show in Figure 3.6a, resulted in a variant that was the most active with respect to leakage as shown in Figure 3.6a. While the variant was

extremely difficult to express and purify (Table 3.4), enough active enzyme was obtained to measure the leak rate using 100 μM NADPH: $1198 \pm 43 \text{ min}^{-1}$. Given the $K_{m, \text{leakage}}$ of all other variants, it is likely that A82W/T268N/F393H/I401P was assayed at a saturating level of NADPH, and thus the leak rate can be approximated as the $k_{\text{cat, leakage}}$.

The WT protein undergoes a transition from completely low spin to predominantly high spin when it binds native fatty acid substrate, which displaces the water ligand bound as the sixth axial ligand to the heme iron [119]. This displacement was found in the crystal structure of the I401P variant [123], consistent with its mixed spin state. This feature may also be present in the A82W variant, as suggested by its similar spin state content. These findings are consistent with previously reported mixed spin states [106,107]. Yet the other variants in this study, such as T268N/F393H and A82W/T268N/F393H, also had relatively high leakages and exist primarily in the low-spin state (Figure 3.6b). Thus, there is no clear correlation between spin state content and leakage activity for the variants in this chapter, marking a clear biophysical distinction between leakage and coupled hydroxylation in terms of relevant protein properties. In short, these results suggest that substrate binding and the consequent shift to high spin do not seem to be strictly necessary as a redox switch for catalytic oxidation of NADPH, contrasting what has been previously suggested [119].

Other biophysical changes that occur when the WT protein binds substrate for hydroxylation are changes in the reduction potential, which becomes more oxidizing, and overall conformation. In previous reports, the substrate-free I401P and T268N/F393H variants exhibited reduction potentials that were 142 and 145 mV more oxidizing than the WT protein in each study's experimental conditions, respectively [105,106]. Furthermore, the I401P variant was found to adopt a conformation resembling that of substrate-bound WT [123]. Whether these trends hold for the variants in this chapter was difficult to address due to low expression (Table 3.4). Spectroelectrochemical titrations to measure reduction potential and crystallographic studies were thus experimentally inaccessible.

Each variant other than WT produced different amounts of H_2O_2 as indicated by measurements of H_2O_2 in Table 3.5. No variant produced only H_2O_2 ; thus, each variant also produced either O_2^- , water, or both, in addition to H_2O_2 . Notably, the T268N/F393H variant exhibited the highest percentage, which may be due to its particular conformation. In the structure of the T268N variant, the amine on N268 points into the active site and is able to donate a hydrogen bond to the ferrous dioxygen species, but cannot accept a hydrogen bond from the hydroperoxy ferric species [105]. This makes the hydroperoxy ferric species less stable, increasing the chance that H_2O_2 will be released as a product, which is consistent with the percentage obtained for T268N/F393H.

3.3.4 Thermostability

To measure the thermostability of each variant, T_{50} was determined. T_{50} is an activity-based measure of thermostability, defined as the temperature at which a 10 min incubation causes a 50 percent decrease in the active concentration of the enzyme. The thermostabilities of the one and two-mutation variants were slightly less than that of the WT enzyme and comparable to each other; beyond two mutations, the thermostability decreased much further (Figure 3.6a).

The variants in this study exhibit a tradeoff between leakage and stability (Figure 3.7); the one and two-mutation variants show an increase in $k_{\text{cat, leakage}}$ and decrease in T_{50} relative to the WT enzyme, the three-mutation variants do so relative to the one and two-mutation variants, and the four-mutation

variant likely does so as well relative to the three-mutation variants. A decrease in stability also means decreased robustness for evolvability, as shown in previous work [124]; thus, the leakage-enhancing mutations studied in this work decrease the ability of P450 BM3 to be engineered towards other purposes, and give rise to the possibility of a fundamental tradeoff between leakage and stability, and consequently, evolvability.

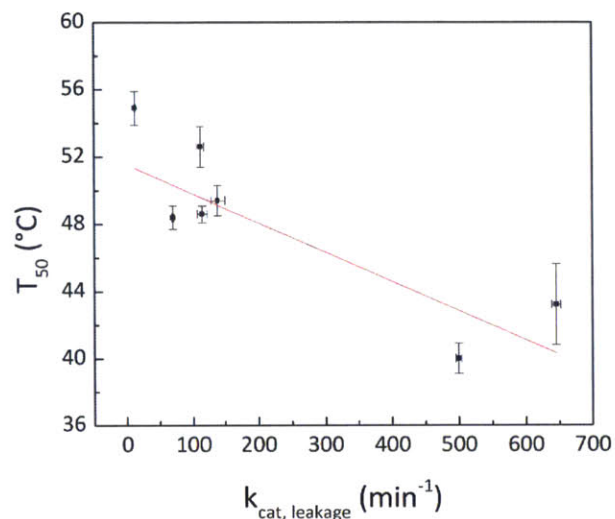


Figure 3.7. Linear correlation between k_{cat} and T_{50} of all variants in this chapter aside from A82W/T268N/F393H/I401P. R^2 was 0.72.

Interestingly, the leakage-enhancing mutations in this chapter are far more destabilizing than mutations specifically engineered to change substrate specificity. Mutations introduced to induce native-like catalytic properties with regards to propane, for instance, numbered up to 22 before a similar decrease in T_{50} was observed [125]. This suggests that mutations that promote catalysis in the absence of substrate have a far greater destabilizing effect on protein fold than mutations that increase reactivity upon a non-native substrate.

3.3.5 Mammalian expression and activity

We report here work performed outside the scope of this dissertation but the results of which still hold relevance to our evaluation of P450 BM3 and related variants as an H_2O_2 generator. The WT gene was codon optimized and encoded in the pTRE3G-IRES vector for expression in mammalian cells. The mutations in this chapter were then introduced by site-directed mutagenesis. Vectors encoding each variant were transfected into HyPer-HeLa cells, which stably contained a pHyPer-cyto vector that encoded the HyPer sensor. The variants had expression levels comparable to that of WT (Figure 3.8).

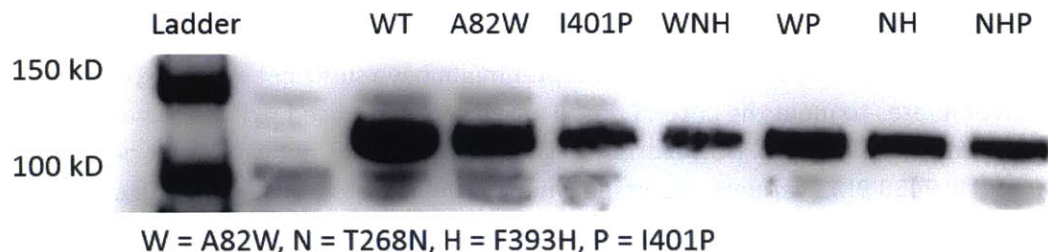


Figure 3.8. Western blot of P450 BM3 variants encoded in a pTRE3G-IRES vector and expressed in HyPer-HeLa cells. The unlabeled lane was sourced from cells transfected with an empty vector. NH = T268N/F393H, WNH = A82W/T268N/F393H, WP = A82W/I401P, NHP = T268N/F393H/I401P. Data kindly provided by Beijing Huang.

However, when cells were lysed, only WT was detectable by a CO binding assay, indicating that the variants suffered severe decreases in their expression of active enzyme relative to their general expression levels and suggesting disruptions in their protein folds. WT was detected at an active expression level of 6.7×10^6 molecules/cell. Coupled with its H_2O_2 production rate (shown later in Chapter 4), it likely does not meet the criteria of an ideal H_2O_2 generator (Figure 3.9); whether or not the variants do will require measurement of the active protein, which was inaccessible by a CO binding assay.

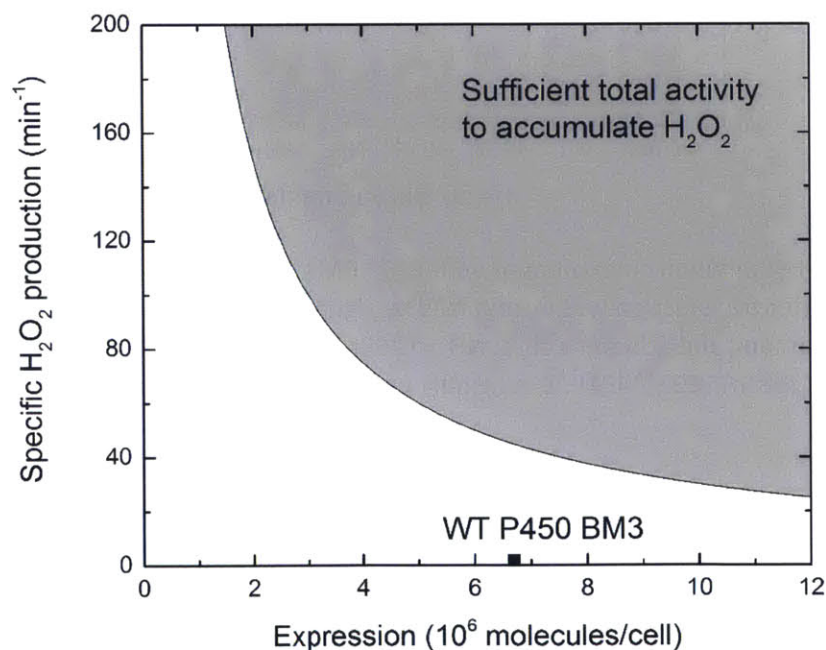


Figure 3.9. Design criterion specifying the total amount of H_2O_2 production required for a generator with WT P450 BM3 placed according to its active expression in HyPer-HeLa cells and H_2O_2 production rate. It was assumed that the criteria for HeLa and HyPer-HeLa cells was the same. Data kindly provided by Beijing Huang.

Since it was still possible that the variants in this chapter might have sufficient active expression levels and H₂O₂ production rates to meet the criteria posed in Figure 1.2, we used HyPer's signal to measure these production rates (Figure 3.10). However, the signal was not significantly different between the empty vector and all P450 BM3 variants expressed when plasmids were transfected into cells and the signal was measured at the time of transfection and 24 hours later. It is possible that the production rates are indeed significantly different, but below the detection limit of the sensor; however, this cannot be confirmed with the tools and methodologies currently available for measurement of active P450 BM3 and H₂O₂ production.

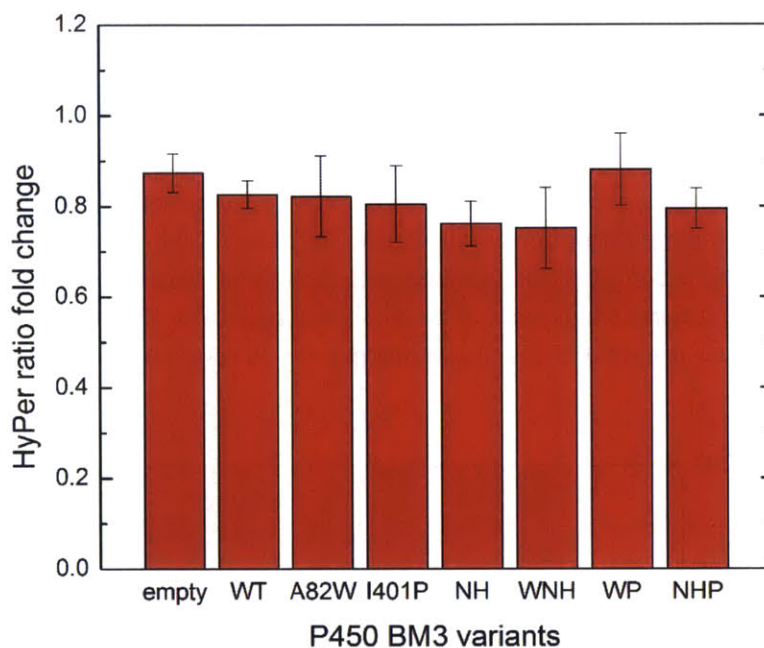


Figure 3.10. Signal of HyPer when co-expressed with P450 BM3 variants in HyPer-HeLa cells. Signal measured 24 hours after transfection was normalized by signal at the time of transfection; signals were measured using microscopy and adherent cells. NH = T268N/F393H, WNH = A82W/T268N/F393H, WP = A82W/I401P, NHP = T268N/F393H/I401P. Data kindly provided by Beijing Huang.

We note here that we did not include the A82W/T268N/F393H/I401P variant because of its extremely poor bacterial expression (Table 3.4) and likely very low thermostability. Given that none of the other variants had expression levels that could be detected by a CO binding assay or activities that significantly perturbed the signal of the HyPer sensor, the A82W/T268N/F393H/I401P is unlikely to perform any better in terms of meeting the criteria for an ideal H₂O₂ generator.

3.4 Discussion and conclusions

The combination of mutations previously found to enhance leakage in P450 BM3 resulted in increased leakage, and consequently, H₂O₂ production. Moreover, these variants revealed novel findings on the relationship between leakage and other protein properties, such as spin state. However, these

mutations were also associated with sharp decreases in bacterial expression and thermostability. These decreases may be linked to the lack of active expression observed in mammalian cells, which hinder the ability of P450 BM3 and related variants to be ideal H₂O₂ generators.

Yet it is possible that the current methodologies for measuring P450 and H₂O₂ production, i.e. CO binding and HyPer, are not sensitive enough to detect expression and production levels that are significant enough to induce biological events associated with H₂O₂. We must also consider that we have not fully explored P450 BM3's sequence space, as it is comprised of 1049 amino acids; there may exist variants with both sufficient H₂O₂ production and active mammalian expression to satisfy the criterion posed in Figure 1.2 and fulfill the requirements of an ideal H₂O₂ generator. We continued investigating P450 BM3 as a possible H₂O₂ generator by targeting it for engineering in a novel screen for enzymatic H₂O₂ production, as described in the next chapter.

Chapter 4

Use of a genetically encoded H₂O₂ sensor for whole cell screening for enzyme activity

Abstract

In this chapter, we report the use of HyPer, a genetically encoded, fluorescent sensor that reacts with hydrogen peroxide (H_2O_2), in a novel screen to engineer enzymes for enhanced production of H_2O_2 . We co-expressed HyPer with cytochrome P450 BM3 variants and, using HyPer's ratiometric signal, found variants that produce greater amounts of H_2O_2 than the wild-type enzyme through the leakage reaction. The screen avoids lysis procedures and the addition of reagents to assay intracellular contents. Less laborious screening procedures will be useful in engineering more powerful H_2O_2 generators as tools in quantitative redox biology, and increasing the utility of enzymes that produce H_2O_2 as a by-product alongside a valuable compound. This screen provides the methodology necessary to find and optimize candidate enzymes as ideal H_2O_2 generators, fulfilling the first objective of this dissertation.

Portions of this chapter have been published in:

Lim, J. B. and Sikes, H. D. Use of a genetically encoded hydrogen peroxide sensor for whole cell screening of enzyme activity. *Protein Engineering, Design & Selection*, 28, 79-83, 2015. doi: 10.1093/protein/gzv003

4.1 Introduction

In seeking an ideal H₂O₂ generator due to H₂O₂'s prominent role in redox biology, we note that H₂O₂ also holds interest as a by-product of other reactions of biotechnological interest that produce valuable compounds. Enzymes that catalyze such reactions include not only DAAO, but also L-amino acid oxidase [126,127], uricase [128,129], tyrosinase [130], alcohol oxidase [131], and glycolate oxidase [132,133]. All of these catalyze a redox reaction that reduces O₂ to H₂O₂. H₂O₂'s importance in biotechnology thus gives further merit to developing a protein engineering screen for enhanced H₂O₂ production, in addition to its importance in this thesis.

Historically, enzymatic H₂O₂ production has been screened in multi-well plates in which enzyme libraries are expressed in parallel cultures, lysed, clarified, and transferred to another set of wells containing an additional enzyme and substrate to detect H₂O₂ by reducing it to water while oxidizing the substrate into a colorimetric or fluorescent product. A common enzyme and substrate combination is HRP and ABTS [134]. This frequently used screen involves a laborious lysis procedure and addition of extra reagents to measure the cumulative amount of H₂O₂ produced.

To our knowledge, H₂O₂ production had never been screened using genetically encoded, fluorescent biosensors designed to detect and measure H₂O₂ before our work. H₂O₂ sensors of this class have features that would be advantageous for efficient screening of enzyme libraries for enhanced production of H₂O₂. The genetic encoding of the sensor allows H₂O₂ detection without the need for a time-consuming lysis procedure or addition of reagents. Moreover, the fluorescent signal of these sensors is reversible due to cellular disulfide reductase activity that returns the sensor's oxidized form to the reduced form. While a non-reversible sensor that exhibits a cumulative signal would only indicate that H₂O₂ has been produced at some point during the assay, a reversible sensor would reveal whether the enzyme has remained active up to the point of measurement, giving insight into the enzyme's lifetime *in vivo*. The use of a genetically encoded sensor in a screen could thus provide a more time-efficient, cost-effective, and informative method for finding more powerful generators of H₂O₂.

In this chapter, we asked whether a genetically encoded H₂O₂ biosensor can be used in a screen to engineer a more active H₂O₂ generator. For this proof-of-concept, we chose HyPer as the sensor and cytochrome P450 BM3 as the parent enzyme for directed evolution of an H₂O₂ generator. Because of the precedents set in the previous chapters and our interest in engineering H₂O₂ generators, we were familiar with how to use HyPer in *E. coli* and desired to further explore P450 BM3's sequence space. We thus chose P450 BM3 as the engineering target to develop a HyPer-based screen for H₂O₂ production with the goal of finding variants with higher rates of H₂O₂ production on par with those of the variants in the previous chapter. This would demonstrate the utility of the screen for identifying and optimizing H₂O₂-producing enzymes.

We thus sought to co-express the enzyme and sensor in *E. coli* to create a novel whole cell screen (Figure 4.1). To establish the screen's efficacy, we first determined a co-expression scheme that enables functional and controlled expression of the sensor and the enzyme. We then asked whether WT and I401P, one of the variants that we found to exhibit higher H₂O₂ production, could be used as baseline and positive controls, respectively, in an *in vivo* screen and confirmed their utility in these roles. In doing so, we probed whether the enzyme's expression level and activity, coupled together, are high enough to overcome *E. coli*'s antioxidant defenses (i.e. Ahp and catalase [98]) and whether supplies of NADPH and O₂ in the cell are sufficient to sustain activity at a level detectable by HyPer. We tuned other parameters

such as timing of measurement to optimize fold difference between the controls. We then established the screen's efficacy by using it to find P450 BM3 variants whose co-expression induced higher HyPer signals, and used an alternative measurement technique to confirm enhanced H_2O_2 production [135].

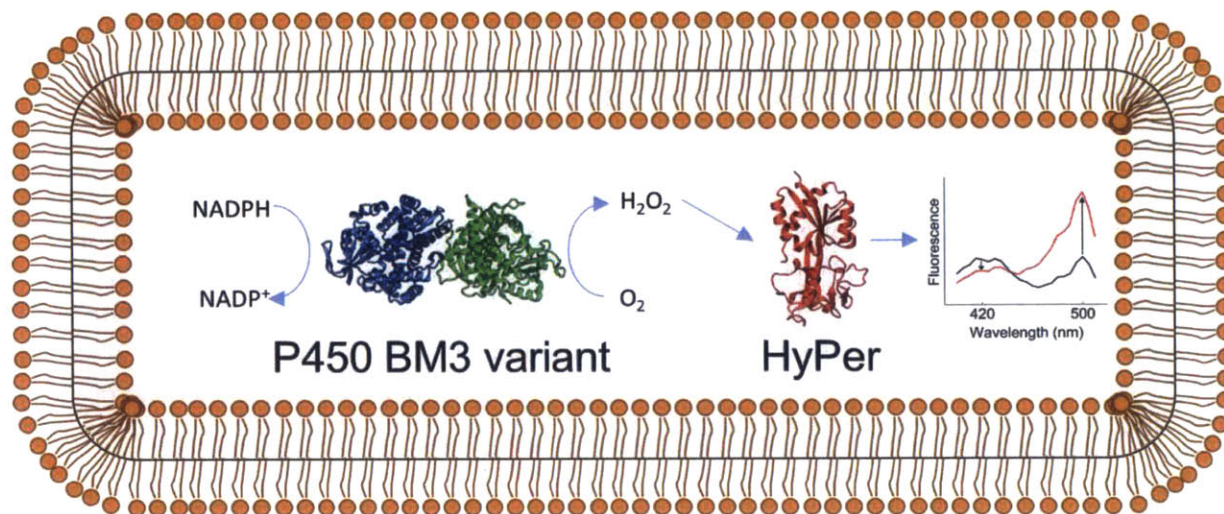


Figure 4.1. Schematic of HyPer-based screen for enhanced enzymatic production of H_2O_2 . P450 BM3 variants from a library generated by error-prone PCR were co-expressed with HyPer. The enzyme used cellular supplies of NADPH and O_2 to produce H_2O_2 , which oxidized HyPer, resulting in an increase in its excitation spectrum at 500 nm and a decrease at 420 nm when emission was measured at 545 nm. Oxidized spectrum shown in red and reduced spectrum shown in black.

4.2 Materials and methods

4.2.1 Construction of control plasmids and a random mutation library

4.2.1.1 Construction and transformation of plasmids to test schemes for co-expression

A 6X His-tag was added to the 3' end of the P450 BM3 gene encoded in the pCWori vector, which was a kind gift of Professor Frances Arnold, Caltech, Pasadena, CA. Simultaneously, the gene was cloned into the pRSFDuet-1 vector (Novagen). The primers 5'-AGGAGATATACCATGGCAATTAAGAAATGCCTCAGCC-3' and 5'-GCGGCCTGCAGGTTAATGATGATGATGATGGTG-3' were used to amplify the P450 BM3 gene and the I401P variant; these primers and all those hereafter in this chapter were ordered from Integrated DNA Technologies. The reaction mixture for 50 μ l PCR contained 1X Phusion HF buffer, 0.8 mM dNTP mixture, 0.2 μ M of each primer, 250 ng of P450 BM3/pCWori, and 2 U of Phusion High-Fidelity DNA polymerase (New England Biolabs). After denaturation for 6 min at 95 $^{\circ}$ C, the PCR was run for 30 cycles of 95 $^{\circ}$ C for 30 seconds, 54.4 $^{\circ}$ C for 30 seconds, and 72 $^{\circ}$ C for 3.5 min, with a final extension step at 72 $^{\circ}$ C for 10 min. The PCR products were run on a 1% agarose gel at 100 V for 45 min and purified using a Gel Extraction Kit (Epoch Life Sciences).

These products were then used in a 50 μ l splice-overlap extension (SOE) PCR that also contained 1X Phusion HF buffer, 0.8 mM dNTP mixture, 0.2 μ M of the oligonucleotide 5'-GCGGCCTGCAGGTTAATGATGATGATGATGGTGCCAGCCACACGTCTTTTGCATCG-3', 0.2 μ M of the

aforementioned primers, and 2 U of Phusion High-Fidelity DNA polymerase. The same aforementioned PCR cycle was run, and the PCR products were run on a 1% agarose gel at 100 V for 45 min and purified using a Gel Extraction Kit. 50 µl restriction digest reactions were performed on the purified SOE PCR products and a pRSFDuet-1 vector. Both reactions contained 1X CutSmart Buffer, 20 U of NcoI-HF, and 20 U of SbfI-HF; restriction enzymes, accompanying buffers, and those used hereafter in this chapter were sourced from New England Biolabs. After incubation at 37 °C for 1 hour, reaction products were loaded onto a 1% agarose gel and run at 100 V for 50 min. The digested vector and SOE PCR products were purified using a Gel Extraction Kit. Ligation of the purified restriction digest products was performed in a reaction with T4 DNA Ligase (New England Biolabs) at 16 °C for 16 hours and purified using a Clean & Concentrate Kit (Zymo Research). The purified ligated product was introduced into electrocompetent cells of *E. coli* DH5α by electroporation.

An overnight culture (5 ml) was started from one of the colonies of the transformed cells in LB medium (Becton Dickinson) supplemented with 50 µg/ml kanamycin (VWR) and incubated at 37 °C and 250 rpm. The plasmid was then extracted and purified from the culture using a GenCatch Plasmid DNA Mini-Prep Kit (Epoch Life Sciences), and presence of the transferred P450 BM3 gene was verified by sequencing.

After cloning WT and I401P into the first cloning site of pRSFDuet-1, an analogous procedure was performed to clone HyPer into the second cloning site. Oligonucleotides 5'-GAAGGAGATATACATATGAGAGGATCGC-3' and 5'-GCGGTTAACTCGAGTCTGGTAAAGAAACCG-3' and the HyPer/pQE30 plasmid were used in a PCR reaction to amplify the HyPer gene in a cycle identical to that performed to amplify the P450 BM3 gene encoded in pCWori, except the annealing temperature was 51 °C and the extension time at 72 °C was 1.5 min. After purification of the product using a 1% agarose gel and a Gel Extraction Kit, restriction digest reactions were performed on the purified product and the pRSFDuet-1 vector encoding WT or I401P in the first cloning site, with conditions analogous to those described above and using the NdeI and XhoI restriction enzymes. The digested products were purified using a 1% agarose gel and Gel Extraction Kit and ligated in a procedure described above. The ligated products were transformed into DH5α and overnight cultures and sequencing verified the presence of the HyPer gene in the second cloning site.

Thus, the following plasmids were now available: pRSFDuet-1 with only WT or I401P in the first cloning site, pRSFDuet-1 with WT or I401P in the first cloning site and HyPer in the second cloning site, and pQE30 encoding HyPer. The pRSFDuet-1 vector encoding both proteins was transformed into BL21 (DE3) Tuner cells. The pRSFDuet-1 vector encoding only the P450 BM3 enzyme or the I401P variant and the pQE30 vector encoding HyPer were co-transformed into BL21 (DE3) Tuner cells (Novagen). Resulting colonies were used for later assays described in section 4.2.2.

4.2.1.2 Construction and transformation of library of P450 BM3 variants

Using P450 BM3/pRSFDuet-1 as the template plasmid, the primers 5'-AGGAGATATACCATGGCAATTAAGAAATGCCTCAGCC-3' and 5'-GCGCCGTTCTTCAGCTGTTCC-3' were used to amplify the part of the gene encoding the oxidase domain of P450 BM3 from the plasmid pRSFDuet-1 containing the gene of P450 BM3 from *Bacillus megaterium*. The reaction mixture for 50 µl error-prone PCR contained 1X Mutazyme II reaction buffer, 0.8 mM dNTP mixture, 125 ng of each primer, 4.7 µg of P450 BM3/pRSFDuet-1, and 2.5 U of Mutazyme II DNA polymerase (Novagen). After denaturation for 2 min at 95 °C, the PCR was run for 30 cycles of 95 °C for 30 seconds, 58.2 °C for 30

seconds, and 72 °C for 2 min, with a final extension step at 72 °C for 10 min. The error-prone PCR products were run on a 1% agarose gel at 100 V for 45 min and purified using a Gel Extraction Kit.

50 µl restriction digest reactions were performed on the purified error-prone PCR products and P450 BM3/pRSFDuet-1. The former contained 2 µg of the error-prone PCR products and the latter contained 5 µg of the vector. Both reactions contained 1X CutSmart Buffer, 20 U of NcoI-HF, and 20 U of SacI-HF. After incubation at 37 °C for 1 hour, reaction products were loaded onto a 1% agarose gel and run at 100 V for 50 min. The digested vector with the original P450 BM3 removed, along with the digested error-prone PCR products, were purified using a Gel Extraction Kit. Ligation of the purified restriction digest products was performed in a reaction with T4 DNA Ligase at 16 °C for 16 hours and purified using a Clean & Concentrate Kit. The purified ligated product was introduced into electrocompetent cells of *E. coli* BL21 (DE3) Tuner by electroporation; these electrocompetent cells had already been previously transformed with the HyPer/pQE30 plasmid.

4.2.2 Testing effects of scheme on co-expression

To measure expression levels of HyPer when co-expressed with an enzyme with both encoded in the same vector or in two separate vectors, a colony of *E. coli* BL21 (DE3) Tuner cells harboring a pRSFDuet-1 vector encoding both P450 BM3 (or I401P) and HyPer and a colony of *E. coli* BL21 (DE3) Tuner cells containing a pRSFDuet-1 vector encoding only P450 BM3 (or I401P) and a pQE30 vector encoding HyPer were each used to inoculate 5 ml of LB medium with either only 50 µg/ml kanamycin (if cells contained only a pRSFDuet-1 vector) or 50 µg/ml ampicillin (VWR) and 25 µg/ml kanamycin (if cells contained both a pRSFDuet-1 vector and a pQE30 vector) in a 14 ml culture tube and incubated at 37 °C with orbital shaking of 250 rpm overnight. The culture was used to inoculate 50 ml of TB medium containing the same corresponding antibiotics at the same concentrations in a non-baffled 250 ml Erlenmeyer flask and incubated at 37 °C with orbital shaking of 250 rpm until mid-log phase ($OD_{600} \sim 0.6$). IPTG was added to a final concentration of 0.05 mM to induce co-expression and the culture was incubated at 20 °C with orbital shaking of 250 rpm for 22 hours. Cells were washed twice and resuspended in 0.1 M KPi at pH 8 as previously described [91] and diluted to cell concentrations of 480×10^6 per 200 µl in a black 96-well solid plate, assuming an OD_{600} of 1 correlates with 10^9 cells/ml. Fluorescence emission intensity of each well was measured with 9 nm bandwidth and excitation at 5 nm intervals from 400 to 510 nm, with emission at 545 nm, using a Tecan Infinite M200 plate reader.

4.2.3 Testing effects of timing, measurement frequency, pH, and buffer composition on signal

To determine the time of measurement optimal for fold difference between the WT and I401P controls, a colony of *E. coli* BL21 (DE3) Tuner cells harboring HyPer/pQE30 and WT P450 BM3/pRSFDuet-1 and another harboring HyPer/pQE30 and I401P P450 BM3/pRSFDuet-1 were each cultured in a flask, washed, and resuspended as described above in 1X PBS at pH 7.4. Cells were diluted to a concentration of 60×10^6 per 200 µl in three replicate wells in a black 96-well solid plate. Fluorescence emission intensity of each well was measured upon excitation at 500 nm with 9 nm bandwidth (F500) and 420 nm with 9 nm bandwidth (F420) with emission monitored at 545 nm (20 nm bandwidth) at 3 min intervals for 2 hours and 9 min using a Tecan Infinite M200 plate reader. Results indicated that the fold change maximized at approximately 2 hours; hence, all measurements hereafter were performed after 2 hours.

A side-by-side test was also performed to determine the effects on signal when cells are measured at high frequency every 3 min for 2 hours versus measured only once after 2 hours. In a sterile round-

bottom 96-deep well microplate with a lid, 8 replicate wells each of WT and I401P co-expressed with HyPer were cultured by inoculation of 500 μ l of LB medium supplemented with 50 μ g/ml ampicillin and 25 μ g/ml kanamycin. The plate was incubated at 37 °C with orbital shaking of 250 rpm overnight. 90 μ l from each well in the 96-deep well microplate was then used to inoculate a single well in another sterile round-bottom 96-deep well microplate with a lid containing 1000 μ l of TB medium supplemented with 50 μ g/ml ampicillin and 25 μ g/ml kanamycin and incubated at 37 °C with orbital shaking of 250 rpm for 3 hours. 0.5 μ l of IPTG was then added to each well to a final concentration of 0.05 mM and the cultures were incubated at 20 °C with orbital shaking of 250 rpm for 22 hours. The microplate was centrifuged at 4000 g and 4 °C for 5 min, the supernatant was removed, and each pellet in a well was resuspended in 250 μ l of 1X PBS at pH 7.4. This washing step was repeated twice to remove traces of interfering fluorescent components of the growth medium. 100 μ l of each well was mixed with 100 μ l of 1X PBS at pH 7.4 in a black 96-well solid plate.

To test the effects of buffers with different pH levels and compositions on the signal, a colony of *E. coli* BL21 (DE3) Tuner cells harboring HyPer/pQE30 and WT P450 BM3/pRSFDuet-1 and another harboring HyPer/pQE30 and I401P P450 BM3/pRSFDuet-1 were each cultured in a flask, washed, and resuspended as described above in either 1X PBS at pH 7.4, 1X PBS at pH 8, or 0.1 M KPi at pH 8. Cells were diluted to a concentration of 480×10^6 per 200 μ l in three replicate wells in a black 96-well solid plate. Fluorescence was measured as described above.

4.2.4 Screening for variants with elevated H₂O₂ production

Colonies resulting from the final transformation in Section 4.2.1.2 were each picked and inoculated in individual wells of a sterile round-bottom 96-deep well microplate as described in Section 4.2.3. For controls, 8 colonies containing HyPer/pQE30 and WT P450 BM3/pRSFDuet-1 and 8 colonies containing HyPer/pQE30 and I401P P450 BM3/pRSFDuet-1 were each used to inoculate wells. The plate was incubated at 37 °C with orbital shaking of 250 rpm overnight. 150 μ l from each well was mixed with 50 μ l of 50% v/v glycerol in a sterile Falcon flat-bottom 96-well plate (Corning) with a lid to create a glycerol cell stock and stored at -80 °C. 90 μ l from each well in the 96-deep well microplate was then used to inoculate a single well in another sterile round-bottom 96-deep well microplate (VWR), incubated, induced for protein co-expression using IPTG, and washed and resuspended in assay buffer as described in Section 4.2.3. 100 μ l of each well was mixed with 100 μ l of 1X PBS at pH 7.4 in a black 96-well solid plate (Corning). Fluorescence was measured at 3 min intervals for 2 hours as described in Section 4.2.3.

Hits were selected based on their final ratiometric signal (F500/F420) relative to the average of those of the WT controls. For each hit, the glycerol cell stock plate was used to inoculate 8 replicate wells of a sterile round-bottom 96-deep well microplate with a lid. Each plate contained 8 replicate wells of WT P450 BM3 and 8 replicate wells of the I401P variant. The procedure described above was repeated except no glycerol cell stock plate was made. Final hits were confirmed by averaging the final ratiometric signals of replicate wells and performing Student's t-test to compare with the averaged final signal of the WT controls.

To isolate the P450 BM3/pRSFDuet-1 plasmid from the HyPer/pQE30 plasmid in selected hits, overnight cultures (5 ml) were started from the glycerol cell stock plate in LB medium supplemented with 50 μ g/ml ampicillin and 25 μ g/ml kanamycin and incubated at 37 °C and 250 rpm. The plasmids were extracted and purified using a GenCatch Plasmid DNA Mini-Prep Kit. 50 μ l restriction digest reactions were performed on 900-1400 ng of the purified plasmids. Each reaction contained 1X CutSmart Buffer,

20 U of BamHI-HF, and 20 U of SbfI-HF. After incubation at 37 °C for 1 hour, reaction products were loaded onto a 1% agarose gel and run at 100 V for 1 hour. The linearized P450 BM3/pRSFDuet-1 plasmid (~7 kb) was separated from the linearized HyPer/pQE30 plasmid (~5 kb) and purified using a Gel Extraction Kit. Ligation of the purified restriction digest products was performed in a reaction with T4 DNA Ligase at 16 °C for 16 hours and purified using a Clean & Concentrate Kit. The purified ligated product was introduced into electrocompetent cells of *E. coli* DH5 α by electroporation; we note that these electrocompetent cells did not contain the HyPer/pQE30 plasmid. Each variant was cultured, and the plasmid was extracted via a DNA miniprep and verified by sequencing.

4.2.5 Confirmation of elevated H₂O₂ production by HRP/ABTS assay

Variants were separately cultured and purified as previously described in Section 3.2.3. Their rates of H₂O₂ production were determined by measuring the amount of P450 via a CO binding assay, each variant's leak rate via absorbance of NADPH, and proportion of H₂O₂ present in the product via an HRP/ABTS assay; these were previously described in Sections 3.2.4, 3.2.5, and 3.2.7, respectively. H₂O₂ production rates were calculated by multiplying the proportion by the leak rate, and Student's t-test was performed to compare leak rates and production rates.

4.2.6 Exploring the efficacy of the screen in fluorescence-activated cell sorting

The final transformation described in Section 4.2.1.2 was not plated but instead used to inoculate 5 ml of LB medium containing 50 μ g/ml ampicillin and 25 μ g/ml kanamycin and incubated at 37 °C and 250 rpm overnight. For controls, colonies containing either the WT enzyme or the I401P variant co-expressed with HyPer were also used to inoculate 5 ml of LB medium containing 50 μ g/ml ampicillin and 25 μ g/ml kanamycin and incubated at 37 °C and 250 rpm overnight. The overnight cultures were then each used to inoculate 50 ml of TB medium with the same antibiotics at the same concentrations in a non-baffled 250 ml Erlenmeyer flask and incubated and induced for protein co-expression as described in Section 3.2.3. Cells were washed and resuspended in 1X PBS at pH 7.4 as previously described [91] and diluted to a cell concentration of 90×10^6 cells/ml, assuming an OD₆₀₀ of 1 correlates with 10^9 cells/ml.

Cells were sorted using a FACSAria 1 flow cytometer (Becton-Dickinson) with 1X PBS at pH 7.4 as sheath fluid. To detect events, thresholds were set to forward and side scattering. The average sort rate was ~12000 events/second. A 70 μ m nozzle was used to excite the solid-state 488 and 405 nm lasers with emission passing the 515 ± 20 (FITC) and 525 ± 50 (AmCyan) band-pass filters, respectively, and measured. Cells were gated on HyPer's signal (emission induced by excitation at 488 nm divided by emission induced by excitation at 405 nm) and sorted into either a sterile Falcon 12 x 75 mm polypropylene tube (VWR) containing 1 ml of LB medium or a sterile Falcon flat-bottom 96-well plate containing 200 μ l of LB medium in each well using an automated cell deposition unit; in both cases, the medium contained 50 μ g/ml ampicillin and 25 μ g/ml kanamycin. Cells sorted into a tube were taken from the final transformation described in Section 4.2.1.2. Cells that were sorted into a 96-well plate were sourced from a combination of cells containing either WT or I401P, with the population comprised in a 2:3 ratio (WT:I401P); a single cell was sorted into each of the wells in the first two rows, five cells were sorted into each of the wells in the next two rows, 10 cells were sorted into each of the wells in the next two rows, and 100 cells were sorted into each of the wells in the last two rows.

For iterative screening, cells sorted into tubes were used to inoculate 5 ml total of LB medium with the same antibiotics at the same concentrations. The culture was transferred to a 14 ml culture tube (17 x 100 mm) and incubated at 37 °C and 250 rpm overnight, at which point it was used to inoculate 50 ml of TB medium with the same antibiotics at the same concentrations and incubated and induced for protein co-expression, with cells washed and resuspended in 1X PBS at pH 7.4 and sorted using a FACSAria 1 flow cytometer as described above.

Cells sorted into a 96-well plate were transferred to a sterile round-bottom 96-deep well microplate. 800 µl of LB medium with the same antibiotics at the same concentrations was added to each well. The plate was then incubated at 37 °C and 250 rpm overnight, and observable bacterial growth was evaluated in each well to determine the recovery rate of the sort.

4.3 Results

4.3.1 Design of scheme for co-expression

HyPer competes with antioxidant enzymes for reaction with H₂O₂ and does so at a kinetic disadvantage [92,96]. It follows that when H₂O₂ is the limiting reagent, the expression level of HyPer is expected to affect the kinetic competition between the sensor and the antioxidant enzymes and thus, the resulting signal. Therefore, it is preferable to ensure low variability in the expression level of HyPer when it is co-expressed with different P450 BM3 variants so that the signal of interest is not obscured by factors other than enzymatic H₂O₂ production.

To this end, we first evaluated two schemes for co-expression by determining the effects of placing the gene for HyPer in the second cloning site of pRSFDuet-1 with P450 BM3 (either WT or I401P) in the first versus placing the genes in two separate vectors, P450 BM3 (either WT or I401P) in pRSFDuet-1 and HyPer in pQE30 (Figure 4.2). While both the enzyme and HyPer are expressed when encoded in the same vector, HyPer's expression level appeared to dramatically increase by more than two-fold when co-expressed with I401P versus WT. In contrast, HyPer's expression levels were nearly identical when co-expressed with I401P and WT with HyPer encoded in the pQE30 vector. Because HyPer's expression level was better controlled when co-expressed from a separate plasmid with a different origin of replication, we implemented the screen with the two proteins expressed from two separate plasmids rather than from a single plasmid. We also devised a new electrocompetent screening strain by transforming only HyPer/pQE30 into BL21 (DE3) Tuner cells. For future transformations with the pRSFDuet-1 vector, this new strain eliminated the need for co-transformation with HyPer/pQE30 and the consequent decreased transformation efficiency known to occur with co-transformation of multiple plasmids.

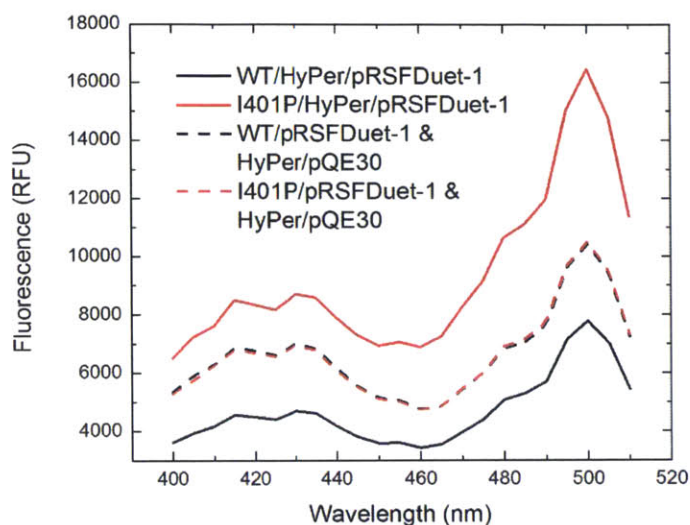


Figure 4.2. Fluorescence spectra of HyPer co-expressed with WT (black) or the I401P variant (red), encoded in either the second cloning site of pRSFDuet-1 (solid) or pQE30 (dashed). In all cases, WT or I401P was encoded in the first cloning site of pRSFDuet-1. Measurements were performed using single samples of 480×10^6 cells in 0.1 M KPi at pH 8 and $t = 0$.

4.3.2 Validation of baseline and positive controls and effects of timing, measurement frequency, pH, and buffer composition on signal

After choosing a scheme for co-expression, we sought to determine if WT and I401P could serve as baseline and positive controls, respectively. We measured HyPer's signal for the two samples at the end of protein expression. WT and I401P showed signals of 0.93 ± 0.02 and 1.12 ± 0.02 , respectively, confirming the utility of these clones as controls.

We measured the temporal behavior of the signal after resuspension and dilution of the cells and found that the signal (F500/F420) for I401P monotonically increased and plateaued, while the signal for WT decreased and flattened, with the fold difference maximizing at ~ 2 hours as WT and I401P showed final signals of 0.792 ± 0.002 and 1.812 ± 0.004 , respectively (Figure 4.3). We thus measured the signal after 2 hours in all following screening experiments.

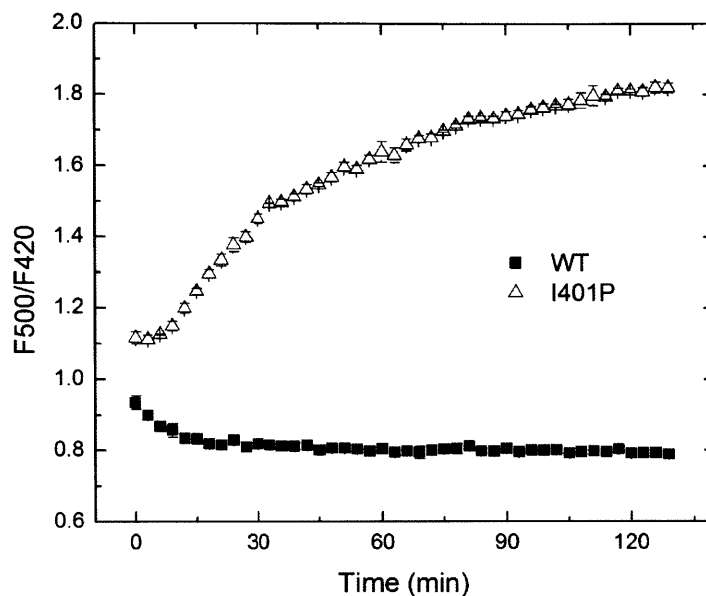


Figure 4.3. Temporal behavior of HyPer’s signal (F500/F420) measured from intact *E. coli* cells co-expressing the sensor and either WT P450 BM3 or the I401P variant. At the end of protein expression, cell suspensions were prepared in 1X PBS at pH 7.4. Because of I401P’s known higher leak rate and H₂O₂ production rate [106], it was expected to induce a signal greater than that induced by WT. While this was the case even at t = 0, the fold difference between the signals increased and plateaued at t = 2 hours, making it a more optimal time of measurement since a higher fold change enhances the probability of finding hits with enhanced H₂O₂ production during library screening. Measurements were performed in triplicate and error bars represent a single standard deviation.

After validating the controls and determining the optimal time for measurement, we performed a side-by-side test of the controls comparing signal fold change when fluorescence measurements were performed at 3 min intervals for 2 hours as was shown in Figure 4.3 versus one fluorescence measurement after a 2 hour incubation period. In the former case, WT and I401P had signals of 0.96 ± 0.05 and 1.81 ± 0.05 , respectively; in the latter case, WT and I401P had signals of 0.85 ± 0.02 and 1.12 ± 0.08 , respectively. Since cells analyzed using these two alternative procedures were taken from the same source, the samples measured at 3 min intervals can be directly compared with the samples that were measured only once. The comparison shows that the former method maximizes the fold change between the baseline and positive controls.

To investigate whether the choice of buffer impacts the magnitude of the observed fold change between the baseline and positive controls, we tested the effects of buffer pH and composition by resuspending *E. coli* co-expressing HyPer and either WT P450 BM3 or the I401P variant in three different buffers: 1X PBS at pH 7.4, 1X PBS at pH 8, and 0.1 M KPi at pH 8. Previous work has established that the external buffer can induce changes in *E. coli*’s cytosolic pH [136] and it is also known that HyPer’s signal is quite sensitive to pH changes in this range [59]. Although the F500/F420 values differed in each buffer as expected, the fold change between signals induced by WT and I401P remained consistently high and

did not change significantly across the buffers tested (Figure 4.4). We thus decided to use our initial choice of buffer, 1X PBS at pH 7.4, to implement the screen.

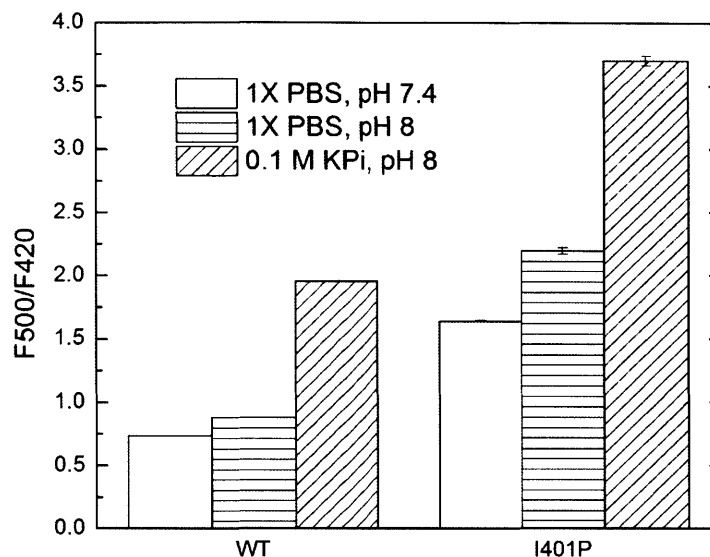


Figure 4.4. HyPer’s signal when co-expressed with WT or the I401P variant after resuspension in three different buffers: 1X PBS at pH 7.4, 1X PBS at pH 8, and 0.1 M KPi at pH 8. Signal shown two hours after resuspension and dilution. Measurements were performed in triplicate and error bars represent a single standard deviation.

4.3.3 Application of the screen to find variants with enhanced H₂O₂ production

We proceeded to engineer WT via directed evolution by performing error-prone PCR to introduce random mutations into the oxidase domain of the enzyme encoded in pRSFDuet-1 using primers described in Section 4.2.1.2. After transformation of the library into the screening strain, DNA sequence analysis of 10 randomly picked variants showed an average mutation frequency of 2.1 base pairs per P450 gene, indicating one amino acid per enzyme was changed on average. We co-expressed variants with HyPer in 96-well microplates in a procedure described in Section 4.2.4, with eight wells dedicated each to WT and I401P to provide a measure of the variability expected from clones bearing the same constructs.

One round of evolution was sufficient to increase the enzyme’s H₂O₂ production. We screened 400 clones and found 10 variants with higher signals than that induced by the WT control, as measured by fold change (Figure 4.5) and confirmed by Student’s t-test ($p < 10^{-9}$). To confirm these initial hits, we used the glycerol cell stock of each to inoculate eight wells in a separate microplate and cultured and assayed these hits again (Figure 4.5). In this re-screening with multiple replicates for each hit, 9 of the 10 original hits had statistically higher final signals than that of the WT control ($p < 10^{-6}$).

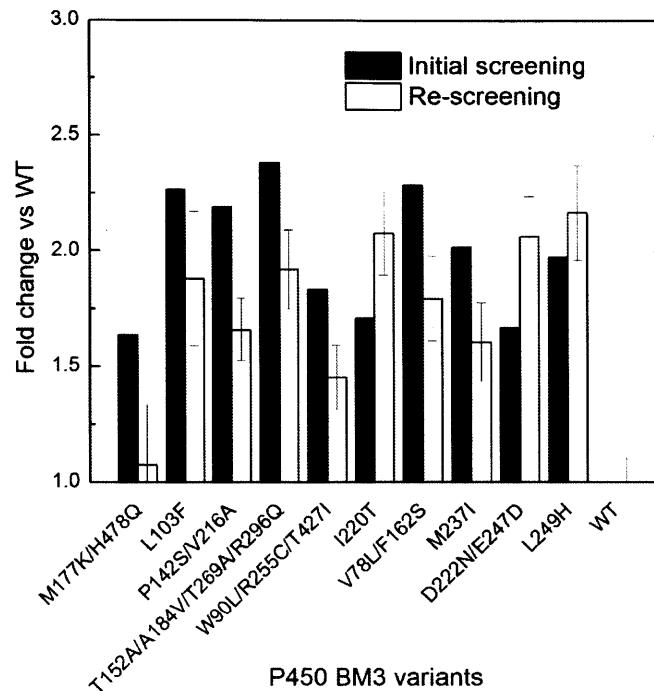


Figure 4.5. Upon co-expression with a library of P450 BM3 variants, HyPer’s fluorescent signal from intact *E. coli* cells revealed several putative H₂O₂ generators in an initial screen (n = 1) and in re-screening (n = 8). Fold change indicates HyPer’s signal (F500/F420) for each variant normalized by the signal (F500/F420) for WT. M177K/H478Q was the sole false positive in the re-screening; all other clones induced higher signals than WT ($p < 10^{-9}$). Error bars shown for this re-screening represent a single standard deviation.

To confirm whether the nine hits had elevated levels of H₂O₂ production, we extracted and transformed their plasmids into BL21 (DE3) Tuner cells. Each variant was expressed, purified, and assayed for leakage activity and H₂O₂ production. Figure 4.6 shows that all nine had leak rates higher than that of WT to varying extents, from 2- to 30-fold greater ($p < 0.05$). The proportion of product comprised by H₂O₂ was measured using an HRP/ABTS assay. When the proportion was multiplied by leak rate to determine the H₂O₂ production rate, three of the hits – P142S/V216A, W90L/R255C/T427I, and D222N/E247D – had higher production rates than WT with $p < 0.05$, and two others – T152A/A184V/T269A/R296Q and L249H – had higher rates with $p < 0.1$, demonstrating the screen’s efficacy in finding novel variants with higher H₂O₂ production than the parent enzyme. Overall, 5 of the original 10 hits had higher H₂O₂ production, indicating a percentage of confirmed hits of 50%.

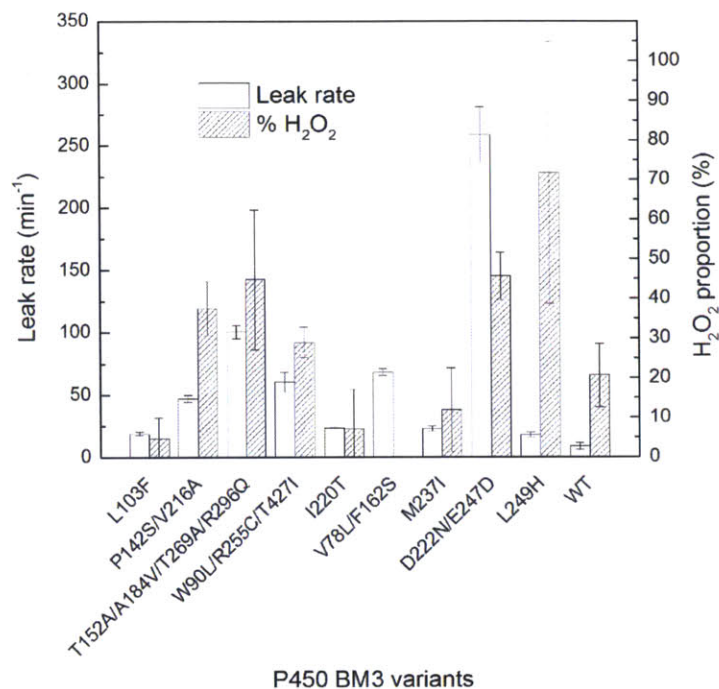


Figure 4.6. *In vitro* evaluation of putative H₂O₂ generators identified using the HyPer-based screen of intact cells. Measurements were performed using purified enzymes and well-established analytical methods. Leak rates were determined by monitoring absorbance at 340 nm as a function of time to measure NADPH oxidation by each variant. The percentage of leakage product comprised by H₂O₂ for each variant was measured using an HRP/ABTS assay. V78L/F162S did not exhibit any positive signal in the HRP/ABTS assay. All nine variants exhibited higher leakage than WT ($p < 0.05$), while five variants – P142S/V216A, W90L/R255C/T427I, D222N/E247D, T152A/A184V/T269A/R296Q, and L249H – exhibited higher H₂O₂ production rates than WT when leak rate was multiplied by the H₂O₂ percentage ($p < 0.1$), giving a final percentage of confirmed hits of 50%. Measurements were performed in triplicate and error bars represent a single standard deviation.

4.3.4 Efficacy of the screen in fluorescence-activated cell sorting

Because the screen is based upon a fluorescent signal, we explored the efficacy of the screen when performed on individual cells using FACS. We analyzed homogenous populations of cells containing the WT enzyme and the I401P variant, as well as a heterogeneous population of cells containing variants generated by error-prone PCR of the WT enzyme (Figure 4.7a).

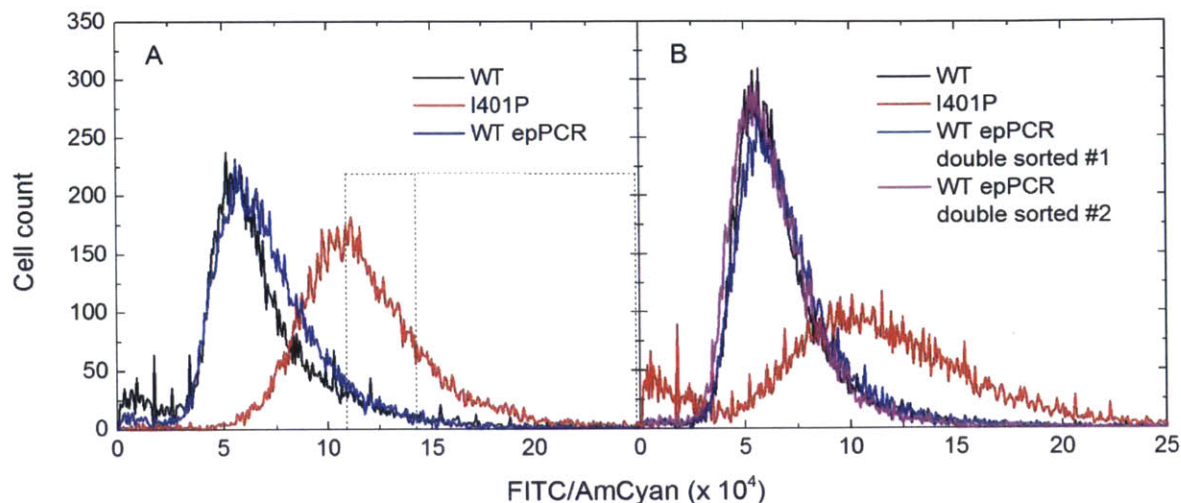


Figure 4.7. Fluorescence histograms depicting HyPer's signal co-expressed with WT, I401P, or variants derived from WT via error-prone PCR after the first sort (a) and the second sort (b). WT epPCR double sorted #1 denotes random variants from the first sort (WT epPCR in (a)) with gates set at the mean and one standard deviation above the mean. WT epPCR double sorted #2 denotes random variants from the first sort (WT epPCR in (a)) with gates set at one and two standard deviations above the mean. Gates are indicated by dashed lines.

Cells containing the I401P variant had an average signal approximately two-fold higher than that of cells containing the WT enzyme. Interestingly, the I401P population showed a greater cell count relative to that of the WT population at a range of ratios less than the maximum signal measured. For this reason, gates used for sorting of the variants generated by error-prone PCR were set at the mean ratio and the ratio one standard deviation above the mean of the I401P population, as this region was judged to be the range within which the ratio of the cell count of the I401P population to that of the WT population was optimal. Gates set at one and two standard deviations above the mean ratio were also used to sort the population to test if cells with very high signals were required to enrich for cells with variants with high H_2O_2 production.

Cells within these two sets of gates were sorted into separate tubes and regrown for an iterative sorting, the results of which are shown in Figure 4.7b. The regrown population of cells was nearly indistinguishable from the WT population, suggesting that cells with lower amounts of H_2O_2 production outcompeted the cells with higher amounts that were responsible for the high signal in the previous sort shown in Figure 4.7a.

We also note that the signal for all populations increased over time throughout the sort. After cells were sorted, the same populations were analyzed immediately (Figure 4.8a), 15 min (Figure 4.8b), and 30 min (Figure 4.8c) afterward. The increase in mean signal for all populations suggests that the cells undergo oxidative stress throughout the assay, and shows that the time at which analysis and sorting are performed must be well controlled between trials to prevent any confounding effect on the signal.

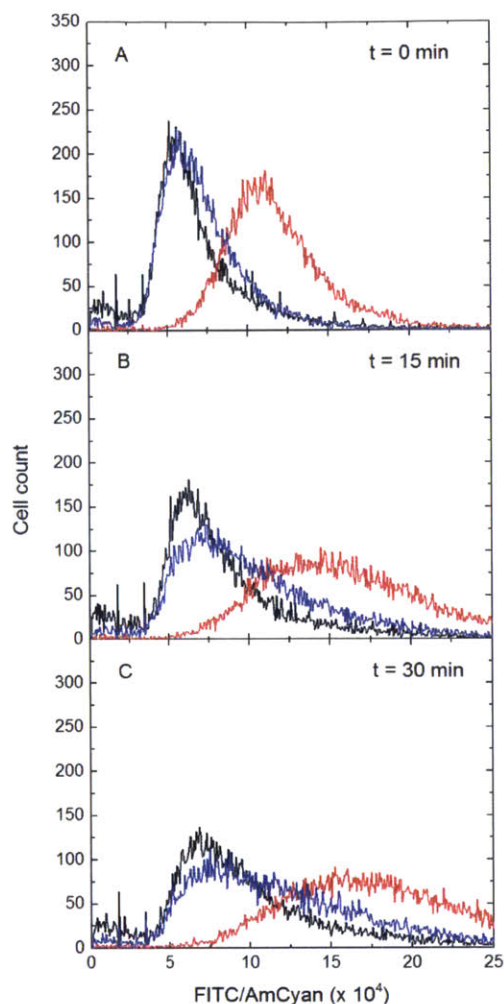


Figure 4.8. Fluorescence histograms depicting HyPer's signal co-expressed with WT, I401P, or variants derived from WT via error-prone PCR at t = 0 (a), t = 15 min (b), and t = 30 min (c) after sorting.

We also tested the viability of combinations of cells containing both the WT and I401P populations in a 2:3 ratio and sorted this population into a 96-well plate, with one cell, five cells, 10 cells, and 100 cells each sorted into 24 wells. This resulted in bacterial growth only in wells into which 10 or more cells were deposited; all other wells with depositions of one or five cells did not show any bacterial growth. All wells with 100 deposited cells showed growth, while only 10 of 24 wells with 10 deposited cells showed growth. Sequencing revealed that the only surviving cells in these wells contained the WT enzyme, meaning that cells containing the I401P variant were not viable or were outcompeted. Although cells containing the I401P variant clearly showed a higher signal, their rate of recovery seems to be compromised to the extent that only cells containing the WT enzyme, even when outnumbered, survive a sort and outcompete other cells. This suggests an innate disadvantage in any attempt to use cells to engineer enzymes that produce higher amounts of H₂O₂ and related species, possibly due to their cytotoxicity. Because of the limited fold increase in HyPer's signal when co-expressed with a variant such as I401P, and because cells with higher amounts of H₂O₂ production appear to be less viable and

outcompeted, we ultimately deemed the screen performed in 96-well plates to be more efficient in this study.

4.3.5 Exploration of additional variants for H₂O₂ generation

After verifying the efficacy of the screen, we screened an additional 640 clones from the library and found 18 more hits with signals significantly higher than that of the WT control. We chose the variants with the 11 highest signals, including those previously screened in the first 400 clones, and expressed them side-by-side along with WT in a 96-well microplate, with eight wells dedicated to each variant. After expression, we lysed the cells with lysozyme and performed a CO binding assay to measure the amount of active P450 in the lysate (Figure 4.9). Simultaneously, we also measured the leak rate of the lysate by adding NADPH and following absorbance at 340 nm over time (Figure 4.10). Although measurement in lysate is obscured by the effects of the lysis procedure and other intracellular contents, we chose this method for an efficient side-by-side comparison of variants, to avoid having to purify them separately for *in vitro* assays.

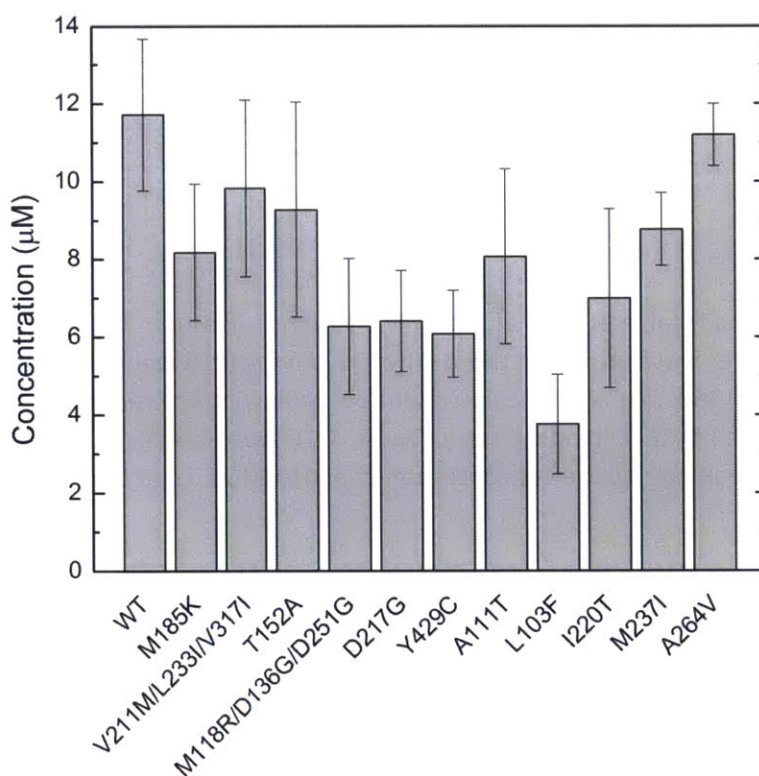


Figure 4.9. Expression levels of P450 BM3 variants measured in lysate and expressed in a 96-well microplate. Cultures were grown on three different days, with 8 wells dedicated to each variant each day (n = 24). Error bars represent a single standard deviation.

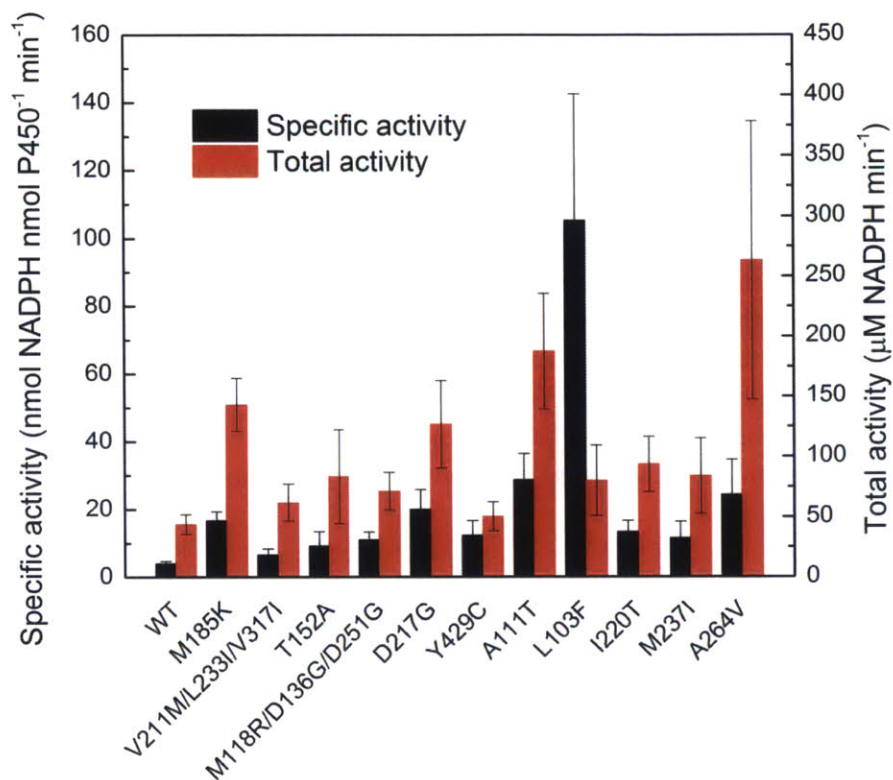


Figure 4.10. Specific and total leak rates of P450 BM3 variants measured in lysate and expressed in a 96-well microplate. Cultures were grown on three different days, with 8 wells dedicated to each variant each day (n = 24). Total leak rate was calculated without taking into consideration the concentration of active P450 as measured by a CO binding assay (Figure 4.9); specific leak rate was calculated by normalizing the total leak rate by the concentration of active P450. Error bars represent a single standard deviation.

Although the data contains wide variability likely due to the measurements having been performed in lysate, they still offer insights into the variants as they compare with each other in terms of bacterial expression and leakage. All variants experienced decreased expression relative to WT, though several – namely, M185K, V211M/L233I/V317I, T152A, A111T, I220T, and A264V – had expressions that could not be statistically distinguished from that of WT ($p > 0.05$). We also found that several variants – M185K, D217G, A111T, I220T, and A264V – had both statistically higher total and specific leak rates ($p < 0.05$).

Since the variants discussed in Chapter 3 experienced severely decreased expression in both *E. coli* and mammalian cells, we hypothesized that variants with higher expression in *E. coli* would also be expressed at higher levels in mammalian cells. If verified, this would open another avenue for engineering enzymes to be ideal H₂O₂ generators; an enzyme could be engineered by its H₂O₂ production rate as well as its mammalian expression, which could be linked to its bacterial expression, thermostability, and other factors. We took the set of variants that had expression statistically comparable with that of WT and total and specific leakage statistically higher than that of WT – M185K,

A111T, I220T, and A264V – and introduced each by site-directed mutagenesis into the WT gene codon optimized for mammalian expression and encoded in the pTRE3G-IRES vector.

Indeed, we found that each variant expressed to levels detectable by a CO binding assay, something not achieved by the variants in Chapter 3. M185K, A111T, I220T, and A264V had expression levels of 3.3, 6.5, 5.5, and 3 x 10⁶ molecules/cell, respectively; for comparison, WT expression amounted to 9.1 x 10⁶ molecules/cell. It is important to consider, however, that the plasmids were transfected into HEK293 cells rather than HeLa cells; while HEK293 cells are still mammalian cells, expression of a foreign gene may vary between this cell line and HeLa cells, in which the variants in Chapter 3 were previously tested. Additionally, the antioxidant capacities of these two cell lines may also be different, which would entail different H₂O₂ production rates required of an ideal generator. To account for this and estimate whether the activities of the M185K, A111T, I220T, and A264V variants may meet the criteria for HeLa cells, we normalized their expression levels by the ratio of WT's expression in HeLa cells to its expression in HEK293 cells (Figure 4.11).

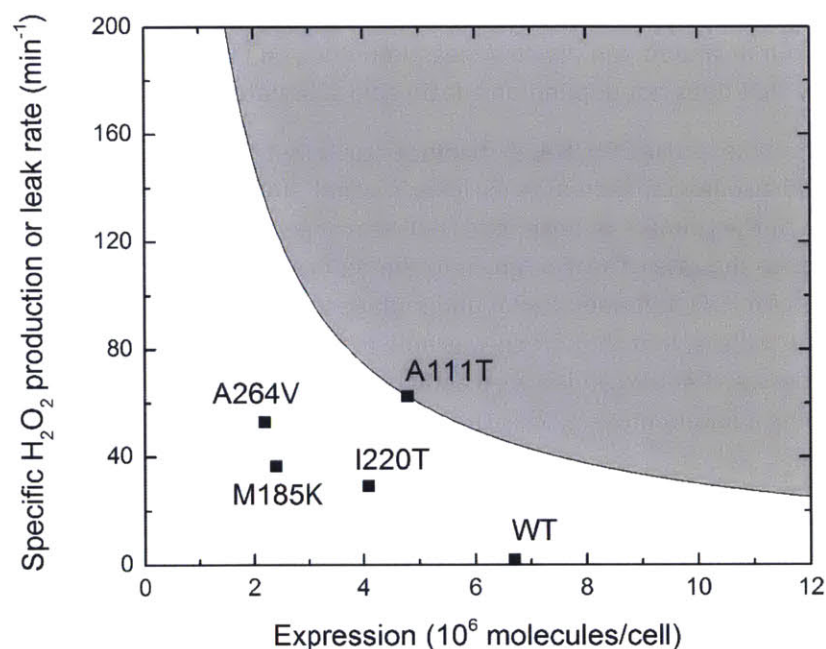


Figure 4.11. Design criterion specifying the total amount of H₂O₂ production required for a generator. WT was placed according to its active expression in HyPer-HeLa cells and H₂O₂ production rate. The other variants were placed according to expression levels in HEK293 cells that were normalized by the ratio of WT's expression in HeLa cells to its expression in HEK293 cells. H₂O₂ production rates for these variants were based on specific leak rates measured in lysate. It was assumed that leakage produced only H₂O₂ for these variants and that the criteria for HeLa and HyPer-HeLa cells was the same.

We assumed that each of the variants in Figure 4.11 produced only H₂O₂ when performing leakage and that expression in HeLa cells would scale down from expression in HEK293 cells in the same ratio observed for WT. It is very well probable and perhaps even likely that neither of these assumptions are true. However, that the variants were detectable by a CO binding assay confirms the hypothesis of some

correlation between bacterial and mammalian expression. This opens bacterial expression as one potential metric to use for engineering more impactful H₂O₂ generators in future work.

4.4 Discussion

The confirmed hit rate of 50% suggests differences between the *in vivo* and *in vitro* measurements. The former is a function of enzyme concentration and activity in the cytoplasm while the latter is specific activity, i.e. normalized by enzyme concentration, measured using purified enzymes in a KPi buffer. Within the cytoplasm, in addition to leakage activity, a variant could bind P450 BM3's native substrate, a long chain fatty acid, and produce H₂O₂ via uncoupled hydroxylation. The competition between the former and the latter will depend on the concentration of free fatty acids and k_{on}/k_{off} binding rates between enzyme and substrate. While numerous studies have reported the yields of free fatty acids from different strains [137], the steady state cytoplasmic concentration of free fatty acids has, to our knowledge, not been reported; indeed, it has been hypothesized that most fatty acids produced by *E. coli* are sequestered within the inner membrane rather than the cytoplasm [138]. We thus do not know for certain whether uncoupled hydroxylation or leakage in the absence of substrate dominates in the production of H₂O₂ in our *in vivo* screen. *In vitro* measurements, on the other hand, are guaranteed to reflect leakage activity that does not depend on a fatty acid substrate since none was supplied.

We also note that differences in NADPH/NADP⁺ balance resulting from consumption of NADPH that does not produce H₂O₂ could also lead to increases in HyPer's signal. NADPH is known, for instance, to reduce the KatE catalase, one of the primary endogenous H₂O₂ scavengers in *E. coli* [98,139]; depletion of NADPH could thus reduce the rate of KatE's return to the reduced state, which in turn could influence the kinetic competition for H₂O₂ between HyPer and endogenous scavengers in HyPer's favor, thus raising the signal. Nevertheless, that the screen was able to find confirmed hits shows that these potential differences between *in vivo* and *in vitro* activity do not significantly impede the screen's effectiveness in scanning a library more quickly than past screens to find enzymes with elevated H₂O₂ production.

We also note that our initial HRP/ABTS measurements using only enzyme and NADPH in experimental reactions and H₂O₂ in the standard curve did not yield any positive signal. We thus used NaN₃, a catalase inhibitor, in the experimental reactions and were able to detect positive signals thereafter, suggesting that there may have been trace amounts of antioxidants such as catalase in the protein preparation able to consume H₂O₂ and decrease the amounts measured in the *in vitro* assay. Hence, the H₂O₂ proportions in Figure 4.6 represent lower limits to the true *in vitro* proportions, and the percentage of confirmed hits may increase if *in vitro* activity free of any influence from antioxidants is measured.

Increased levels of enzyme expression, an *in vivo* parameter, would result in increased H₂O₂ production, which would raise the signal. To increase the screen's stringency and better distinguish more impactful hits, one possible strategy is to systematically decrease all clones' expression levels by tuning the IPTG concentration used in induction. This may identify only those variants that exhibit a sufficiently high enough H₂O₂ production rate at lower expression levels to increase HyPer's signal.

Interestingly, none of the hits had any mutations at shared amino acid positions. While the roles of certain residues have been elucidated in past studies [105,107,140–142], none of the amino acid positions in the hits in this study have ever been investigated. The screen in this study may thus serve as

a robust platform for systematically exploring leakage in the P450 BM3 reaction cycle and finding mutations that contribute to leakage and uncoupling.

Indeed, we used the screen to investigate 640 more variants in addition to those evaluated and which yielded a confirmed hit rate of 50%. We found 18 more hits, and while we did not culture and purify each of them separately to confirm enhanced H₂O₂ production, we did express those with the 11 highest signals along with WT in a 96-well microplate to perform a side-by-side test of their bacterial expression and leakage. Four hits with expression comparable with that of WT and total and specific leakage higher than that of WT, as measured in lysate, were detectable by a CO binding assay when expressed in mammalian cells, confirming the hypothesis of a linkage between bacterial and mammalian expression and opening the possibility of using bacterial expression as another method to engineer an ideal H₂O₂ generator.

4.5 Conclusions

In conclusion, we have established a new use for genetically encoded H₂O₂ sensors that improves upon traditional methods of screening enzyme libraries for enhanced H₂O₂ production. We fine-tuned the screen's design regarding co-expression and measurement timing and established its efficacy using controls. We also demonstrated the screen's robustness with respect to assay buffer pH and composition; fold difference between controls remained high as these variables changed, highlighting the screen's versatility. The screen allowed facile identification of novel P450 BM3 variants with elevated H₂O₂ production and leakage. Furthermore, not only should the screen prove advantageous in comparison with other methods for screening for H₂O₂ production because of its lack of need for any time-consuming lysis procedure or additional expensive reagents, the screen may serve as a platform for systematically exploring sequence-structure-function relationships in oxygen-activating enzymes such as P450 BM3. We thus anticipate the screen finding great use in addition to enabling identification and optimization of H₂O₂-producing enzymes in biotechnology and quantitative redox biology. Finally, we used the screen to find variants that demonstrated a linkage between bacterial and mammalian expression, suggesting it may be possible to engineer H₂O₂-producing enzymes as ideal generators not just through the H₂O₂ production rate, but also through bacterial expression levels.

Chapter 5

Development of a transport model for H₂O₂ in mammalian cells

Abstract

While kinetic models have provided useful insights into the reactions involved in H_2O_2 generation and scavenging, they leave open important questions regarding spatial variations in the concentration profile of intracellular H_2O_2 . A transport model would fill this missing gap of knowledge and yield testable predictions that would initiate feedback between experiment and theory. In steps towards this model, we first used a kinetic model to provide order-of-magnitude estimates of the length and time scales for H_2O_2 diffusion through the cytosol, which were on the order of one micron and one millisecond, respectively, supporting the notion of H_2O_2 localization. We also found that in the context of intracellular H_2O_2 scavenging in the cytosol, oxidation of peroxiredoxin by H_2O_2 is the dominant reaction and the overall concentration of reduced peroxiredoxin is not significantly affected by physiological increases in intracellular H_2O_2 concentration and subsequent scavenging by peroxiredoxin. We used this information to reduce the model from 22 parameters and reactions and 21 species to a single analytical equation with only one dependent variable, i.e. H_2O_2 , and reproduced results from the complete model. Finally, we integrated this single equation into a transport model and applied the finite Fourier Transform technique to derive a mathematical expression for the concentration profile of intracellular H_2O_2 in the context of bolus addition. Predictions from the transport model can be tested by experiment and used to refine model parameters, which in turn should inform the design of next-generation H_2O_2 generators and sensors and fulfills the last main objective of this dissertation.

Portions of this chapter are included in:

Lim, J. B., Huang, B. K., Deen, W. M., and Sikes, H. D. Analysis of the lifetime and spatial localization of hydrogen peroxide generated in the cytosol using a reduced kinetic model. Submitted.

Lim, J. B., Huang, B. K., Deen, W. M., and Sikes, H. D. A reaction-diffusion model of cellular hydrogen peroxide. In preparation.

5.1 Introduction

As previously noted, the kinetic redox model developed by Adimora et al. [8] was valuable in determining the H_2O_2 production rate required to overcome the cell's antioxidant capacity as shown in Figure 1.2, but does not take into consideration spatial distributions of H_2O_2 and related generators and scavengers. The model thus leaves open questions regarding H_2O_2 localization, including how far H_2O_2 produced in a particular location would be expected to diffuse before reacting with a signaling target. Furthermore, any generators or sensors designed based on the criteria derived from the kinetic model may not be suited for physiological perturbations or measurements of H_2O_2 in subcellular locales; although a generator, for instance, that meets the design criteria in Figure 1.2 would be able to accumulate H_2O_2 in the cytosol, it would also conflate unwanted global effects with those that come from localized increases in H_2O_2 concentration. This gives rise to the need for a transport model of H_2O_2 , one that includes both kinetics and diffusion of H_2O_2 and other related molecular species.

A transport model of H_2O_2 that addresses the aforementioned questions left unanswered by a kinetic model would predict the relevant length and time scales for H_2O_2 diffusion when generated at a particular location and in a certain quantity. A transport model would also predict concentration profiles of H_2O_2 within the cell, which would show how much H_2O_2 is expected to reach other proteins at specific distances from the site of H_2O_2 generation. This would also determine whether the location and amount of H_2O_2 generation are such that a significant amount of H_2O_2 would be expected to diffuse through the membrane and potentially act as an intercellular messenger [33]. Model predictions could also be tested against past experimental observations, such as the different outcomes observed when cells are treated with bolus addition of H_2O_2 versus continuous low-level exposure [25,65,143], and thus potentially provide a mechanistic explanation for these differences.

It is important to note here the most plausible model to date on the mechanism by which H_2O_2 can exhibit localized effects, which is based on Prx acting as a transmitter of H_2O_2 signaling by forming a redox relay with another signaling target [14,15]. Quantification of the localization of H_2O_2 upon intracellular generation and its role in signaling requires knowledge of not only the diffusion distance and lifetime of H_2O_2 , but those of oxidized Prx and possibly other scavengers such as GPx as well.

We sought to address the open questions of how far and for how long H_2O_2 and oxidized Prx diffuse when generated within the cell before being scavenged by antioxidants (H_2O_2) or reduced (oxidized Prx). To do so, we used the kinetic redox model previously used to generate the design criteria in Figure 1.2 [32] to implement simulations and determine the overall kinetic rate constant for H_2O_2 scavenging. We also used this result and a previous measurement for the kinetic rate constant of reduction of oxidized Prx to generate order-of-magnitude estimates for the length and time scales of H_2O_2 and oxidized Prx diffusion in the cytosol. These theoretical estimates can be compared with previous experimental results [33] and validated in future efforts by an experimental system with next-generation sensors of H_2O_2 .

We also showed that the network of reactions that eliminate H_2O_2 from the cytosol can be reduced to a two-parameter analytical equation with only H_2O_2 concentration as the dependent variable. This reduction highlights which reactions are most important in the context of intracellular generation and scavenging of H_2O_2 , and enabled us to develop a transport model that provides more precise predictions of the spatiotemporal variations in H_2O_2 concentration. We modeled the cell as an idealized sphere and implemented an FFT solution to generate concentration profiles of intracellular H_2O_2 and determine the time at which the profile reaches steady state. Finally, we implemented the model in COMSOL software,

to determine how well a computational solution compares with the exact solution and evaluate the viability of using COMSOL to extend the model.

5.2 Computational methods and modeling

5.2.1 Overview of kinetic model

We based our computational model on that developed by Adimora et al., using a set of ordinary differential equations that describe mass action and Michaelis-Menten kinetics [8]. We removed any rate expressions involving diffusion of any molecular species through a membrane to a different compartment, such as diffusion from the cytosol to the extracellular media or into peroxisomes. We also removed catalase as a component since it is known to be located exclusively in peroxisomes [9,10] and we sought to simulate H₂O₂ clearance in the compartment of the cytosol only. Model parameters and initial species concentrations are shown in Tables 5.1 and 5.2, respectively. We note that rather than assume the different oxidized forms of Prx-(SH)₂, GPX_{red}, Pr-SH, Pr-(SH)₂, and Grx-SH to be 0.5% of the concentration of reduced protein [144] as Adimora et al. did [8], we used a molar balance and known rate constants and reactions to determine what the basal concentrations of oxidized protein are expected to be at steady state. We also assumed a basal concentration of H₂O₂ that we demonstrate later in the results to be valid due to reduction of the model to a single equation. Further details are provided in Appendix C.

Table 5.1. Model parameters for the kinetic redox model.

Reaction	Parameters
H ₂ O ₂ intracellular generation	$k_1 = 1.1 \times 10^7 \text{ M/s}$ [144]
k_2 ([H ₂ O ₂] ([GPX _{red}]))	$k_2 = 2.1 \times 10^7 \text{ M}^{-1} \text{ s}^{-1}$ [145,146]
k_3 ([GSH] ([GPX _{ox}]))	$k_3 = 4 \times 10^4 \text{ M}^{-1} \text{ s}^{-1}$ [145]
k_4 ([GSH] ([GPX-SSG]))	$k_4 = 1 \times 10^7 \text{ M}^{-1} \text{ s}^{-1}$ [145]
k_{20} ([NADP ⁺] – [NADP ⁺] _i)/([k ₅ + [NADP ⁺]])	$k_5 = 5.7 \times 10^{-5} \text{ M}$ [147]
k_6 ([H ₂ O ₂] ([Prx-(SH) ₂]))	$k_6 = 1.3 \times 10^7 \text{ M}^{-1} \text{ s}^{-1}$ [32]
k_7 ([H ₂ O ₂] ([Prx-SOH]))	$k_7 = 1.2 \times 10^4 \text{ M}^{-1} \text{ s}^{-1}$ [32]
k_8 ([Prx-SO ₂ H])	$k_8 = 3 \times 10^{-3} \text{ s}^{-1}$ [148]
k_9 ([Prx-SOH])	$k_9 = 2 \text{ s}^{-1}$ [32]
k_{10} ([Prx-SS] ([Trx _{red}]))	$k_{10} = 2.1 \times 10^6 \text{ M}^{-1} \text{ s}^{-1}$ [8,149]
k_{11} ([GSH])	$k_{11} = 7.4 \times 10^{-5} \text{ s}^{-1}$ [150]
k_{12} ([Pr-(SH)] ([H ₂ O ₂]))	$k_{12} = 1 \times 10^2 \text{ M}^{-1} \text{ s}^{-1}$ [32]
k_{13} ([GSH] ([Pr-SOH] – [Pr-SOH] _i))	$k_{13} = 1.2 \times 10^5 \text{ M}^{-1} \text{ s}^{-1}$ [151,152]
k_{14} ([Grx-SH] ([Pr-SSG] – [Pr-SSG] _i))	$k_{14} = 9.1 \times 10^4 \text{ M}^{-1} \text{ s}^{-1}$ [153]
k_{15} ([Grx-SSG] – [Grx-SSG] _i) ([GSH])	$k_{15} = 3.7 \times 10^4 \text{ M}^{-1} \text{ s}^{-1}$ [154]
k_{16} ([Pr-(SH) ₂] ([H ₂ O ₂]))	$k_{16} = 1 \times 10^2 \text{ M}^{-1} \text{ s}^{-1}$ [32]
k_{17} ([Trx _{red}] ([Pr-SS] – [Pr-SS] _i))	$k_{17} = 1 \times 10^2 \text{ M}^{-1} \text{ s}^{-1}$ [32]
k_{18} ([GSSG] – [GSSG] _i) ([NADPH])	$k_{18} = 3.2 \times 10^6 \text{ M}^{-1} \text{ s}^{-1}$ [155]
k_{19} ([Trx _{ox}] – [Trx _{ox}] _i) ([NADPH])	$k_{19} = 2 \times 10^7 \text{ M}^{-1} \text{ s}^{-1}$ [156]
k_{20} ([NADP ⁺] – [NADP ⁺] _i)/([k ₅ + [NADP ⁺]])	$k_{20} = 3.75 \times 10^{-4} \text{ M/s}$ [147]
GSH synthesis	$k_{21} = 4.1 \times 10^{-7} \text{ M/s}$ [157]
Trx synthesis	$k_{22} = 7 \times 10^{-10} \text{ M/s}$ [158]

Table 5.2. Species initial concentrations for the kinetic redox model specific to HeLa cells. Molar balances and known rate constants were used to derive calculated values (Appendix C).

Species	Initial condition (M)
[H ₂ O ₂]	0.01 to 100 x 10 ⁻⁶ (assigned for pulse generation of H ₂ O ₂) 8 x 10 ⁻¹¹ (calculated in the absence of pulse generation of cytoplasmic H ₂ O ₂ for the purposes of calculating basal concentrations of oxidized proteins below)
[GPx _{red}]	0.55 x 10 ⁻⁶ [32]
[GPx _{ox}]	6.64 x 10 ⁻¹¹ (calculated)
[GPx-SSG]	2.66 x 10 ⁻¹³ (calculated)
[GSH]	3.68 x 10 ⁻⁴ [8]
[GSSG]	1.78 x 10 ⁻⁶ [8]
[Prx-(SH) ₂]	1 x 10 ⁻⁴ [32]
[Prx-(SOH)]	5.49 x 10 ⁻⁸ (calculated)
[Prx-(SOOH)]	1.86 x 10 ⁻¹¹ (calculated)
[Prx-SS]	5.57 x 10 ⁻¹¹ (calculated)
[Trx _{red}]	4.27 x 10 ⁻⁷ [8]
[Trx _{ox}]	7.54 x 10 ⁻⁸ [8]
[Pr-SH]	1 x 10 ⁻⁹ [32]
[Pr-SOH]	1.92 x 10 ⁻¹⁹ (calculated)
[Pr-SSG]	1.33 x 10 ⁻¹⁶ (calculated)
[Grx-SH]	7 x 10 ⁻⁷ [32]
[Grx-SSG]	6.21 x 10 ⁻¹⁹ (calculated)
[Pr-(SH) ₂]	1.09 x 10 ⁻³ [8]
[Pr-(SS)]	2.16 x 10 ⁻⁷ [144]
[NADPH]	3 x 10 ⁻⁵ [159]
[NADP ⁺]	3 x 10 ⁻⁷ [160]

In the simplified model comprised of a single analytical equation with two parameters, we simply removed all reactions except for H₂O₂ intracellular generation and k_6 ([H₂O₂] ([Prx-(SH)₂]), and also set the concentration of Prx-(SH)₂ to be constant over time. We implemented both the complete and simplified models using the ode15s function in Matlab (MathWorks), the code and further details for which can be found in Appendix C.

5.2.2 Sensitivity analysis

The finite difference approximation method was used to calculate the sensitivity of [H₂O₂] to each model parameter. Sensitivity was determined using the following equation [161]:

$$s_i(t) = \frac{\partial C(t)}{\partial k_i} = \frac{C(k_i + \Delta k_i, t) - C(k_i, t)}{\Delta k_i}$$

where s_i is the sensitivity corresponding to the model parameter k_i and C is [H₂O₂]. All parameters were perturbed by 10% to reflect typical experimental errors, and sensitivities were evaluated at $t = 0.001$

seconds. Since parameters differed by orders of magnitude to various degrees, we used a previous normalization method [161]:

$$\bar{s}_i(t) = \frac{\partial C(t)/C(t)}{\partial k_i/k_i}$$

All sensitivities in this chapter were reported as \bar{s}_i .

5.2.3 Transport model formulation

5.2.3.1 Calculation of permeability constant

Diffusion of H_2O_2 through the plasma membrane was previously described in the following equation [162]:

$$\frac{d[H_2O_2]_{media}}{dt} = ([H_2O_2]_{cytosol} - [H_2O_2]_{media}) \times 10^{-3} \left(\frac{L}{cm^3} \right) \times P \left(\frac{cm}{s} \right) \times A (cm^2) \times \frac{cells}{l}$$

where $[H_2O_2]_{media}$ is the concentration of H_2O_2 in the extracellular media, $[H_2O_2]_{cytosol}$ is the concentration of H_2O_2 in the cytosol, P is the permeability constant of H_2O_2 through the membrane, A is the surface area of the cell, t is time, and $\frac{cells}{l}$ is the cell density of the experimental system. As the average radius of a HeLa cell was previously measured to be $10 \mu m$ [163], we modeled the cell as an idealized sphere and estimated the surface area, A , to be $1.3 \times 10^{-5} cm^2$. It was also previously estimated that in a bolus addition of H_2O_2 to cell culture, the gradient between $[H_2O_2]_{media}$ and $[H_2O_2]_{cytosol}$ is 650-fold [32]. We thus assumed that $[H_2O_2]_{cytosol}$ was negligible relative to $[H_2O_2]_{media}$ and derived the following equation to be fitted to experimental data to obtain the permeability constant:

$$[H_2O_2]_{media} = \exp \left[-10^{-3} \left(\frac{l}{cm^3} \right) \times P \left(\frac{cm}{s} \right) \times A (cm^2) \times \frac{cells}{l} \times t \right]$$

5.2.3.2 Justification of assumptions

As previously mentioned, we modeled the cell as an idealized sphere of radius a ($= 10 \mu m$) [163] with cytosolic concentration $C(r, t)$ for H_2O_2 at radial position r and time t . We define two dimensionless groups shown below: the Biot number, which is the rate of membrane permeation relative to cytosolic diffusion, and the Sherwood number, which is the rate of external mass transfer relative to cytosolic diffusion. We assumed the cell to be surrounded by a stagnant fluid and calculated the ratio of the Biot number to the Sherwood number accordingly to determine whether external mass transfer resistance is negligible relative to that of the membrane.

$$Bi = \frac{Pa}{D}$$

$$Sh = \frac{k_c a}{D}$$

$$\frac{Bi}{Sh} = \frac{P}{k_c}$$

Here, k_c is the external mass transfer coefficient, D is the diffusion coefficient for H_2O_2 [164], and P is the permeability of the membrane to H_2O_2 . For a sphere in a stagnant fluid, the Sherwood number must

be no less than 2 [165], allowing us to calculate the upper limit for the ratio to be 0.012. This, in turn, allows us to neglect external mass transfer since this upper limit is significantly less than unity. In determining this ratio, we calculated the Biot number to be 0.024, which is also significantly less than unity, allowing us to assume that mass transfer at the membrane is limited by diffusion through the membrane and consequently use a Neumann boundary condition in our model development.

5.2.3.3 Governing equations

In assuming the cell to be an idealized sphere with negligible external mass transfer, we devised the conservation equation for H_2O_2 in the cytosol to be

$$\frac{D}{r^2} \frac{\partial}{\partial r} \left(r^2 \frac{\partial C}{\partial r} \right) + R = \frac{\partial C}{\partial t}$$

As detailed later in Section 5.3.3, we found that the reaction for H_2O_2 can be reduced to a single equation with a parameter for zeroth-order generation of H_2O_2 and a parameter for first-order scavenging by peroxiredoxin (Prx), which can be written as

$$\frac{dC}{dt} = k_1 - k_s C$$

$$k_s = k_{Prx,Ox} [Prx_{red}]$$

where k_1 is the parameter for zeroth-order generation, $k_{Prx,Ox}$ is the first-order parameter for the reaction between reduced Prx and H_2O_2 , and $[Prx_{red}]$ is the intracellular concentration of reduced Prx, which we found to not be depleted by H_2O_2 scavenging in physiologically relevant ranges of H_2O_2 concentrations. Reducing the reaction to a single equation allowed us to pose the conservation equation as

$$\frac{D}{r^2} \frac{\partial}{\partial r} \left(r^2 \frac{\partial C}{\partial r} \right) + k_1 - k_s C = \frac{\partial C}{\partial t}$$

At the cell center, symmetry requires that

$$\frac{\partial C}{\partial r} (0, t) = 0$$

At the membrane, i.e. $r = a$, we can apply a Neumann boundary condition due to a sufficiently low Biot number:

$$D \frac{\partial C}{\partial r} (a, t) = PC_{ext}$$

where C_{ext} is the concentration of the bolus H_2O_2 added to cell culture.

If we set the reaction term to zero to assume steady state, we can derive the initial condition for H_2O_2 before perturbation by bolus addition:

$$C(r, 0) = \frac{k_1}{k_s}$$

5.2.3.4 Parameter values and additional dimensionless groups

Model development was based on the parameter values in Table 5.3, which lists the required reaction rate constants, diffusion coefficient, membrane permeability constant, and size of a typical HeLa cell.

Table 5.3. Model parameters for the transport model.

Parameter	Value	References
k_1	$1.1 \times 10^{-7} \text{ M/s}$	[8,144]
$k_{Prx,Ox}$	$1.3 \times 10^7 \text{ M}^{-1} \text{ s}^{-1}$	[32]
D	$1.83 \times 10^{-9} \text{ m}^2/\text{s}$	[164]
P	$4.4 \times 10^{-4} \text{ cm/s}$	[32]
a	$10 \text{ }\mu\text{m}$	[163]
$[Prx_{red}]$	$1 \times 10^{-4} \text{ M}$	[32]

We note that Adimora et al. calculated k_1 [8] based upon O_2 consumption rates and proportions of H_2O_2 production for the entire body rather than any particular cell type and which could be in error by two-fold [144]; nevertheless, we deemed this value to be an adequate order-of-magnitude estimate for intracellular H_2O_2 production.

For further convenience, we define another dimensionless group, the Damköhler number, which is the rate of H_2O_2 generation or scavenging relative to cytosolic diffusion:

$$Da_0 = \frac{k_1 a^2}{DBiC_{ext}}$$

$$Da_1 = \frac{k_s a^2}{D}$$

These correspond to zeroth-order generation and first-order scavenging of intracellular H_2O_2 , respectively. We note that we included the Biot number in the denominator of Da_0 to scale the group in anticipation of a several hundred fold difference between intracellular and extracellular H_2O_2 in model results [32].

To facilitate derivation of the solution to the conservation equation, we also used the following dimensionless variables:

$$\eta = \frac{r}{a}$$

$$\theta = \frac{C}{BiC_{ext}}$$

$$\tau = \frac{Dt}{a^2}$$

We included the Biot number in the denominator of θ for the same reasons that we did so for Da_0 . The dimensionless variables resulted in the following forms of the conservation equation and boundary conditions:

$$\frac{1}{\eta^2} \frac{\partial}{\partial \eta} \left(\eta^2 \frac{\partial \theta}{\partial \eta} \right) + Da_0 - Da_1 \theta = \frac{\partial \theta}{\partial \tau}$$

$$\begin{aligned}\frac{\partial \theta}{\partial \eta}(0, \tau) &= 0 \\ \theta(\eta, 0) &= \frac{k_1}{k_s Bi C_{ext}} = \frac{Da_0}{Da_1} \\ \frac{\partial \theta}{\partial \eta}(1, \tau) &= 1\end{aligned}$$

Using this set of parameters and equations, we derived the analytical solution to the transport model using the FFT method. We show the transient solution and accompanying details and Matlab code in Appendix C, and note that we found 30 eigenvalues to be sufficient for convergence of the transient solution (Figure C.1). We present the steady solution here in both the dimensionless and dimensional forms:

$$\begin{aligned}\theta(\eta) &= \left(\frac{1}{\sqrt{Da_1} \cosh(\sqrt{Da_1}) - \sinh(\sqrt{Da_1})} \right) \frac{\sinh(\sqrt{Da_1} \eta)}{\eta} + \frac{Da_0}{Da_1} \\ C(r) &= \frac{Pa^2 C_{ext}}{D} \left(\frac{1}{a \sqrt{k_s/D} \cosh(a \sqrt{k_s/D}) - \sinh(a \sqrt{k_s/D})} \right) \frac{\sinh(\sqrt{k_s/D} r)}{r} + \frac{k_1}{k_s}\end{aligned}$$

Finally, we derived the volumetric average concentration by integrating the concentration over the dimensions of the sphere and show the dimensional form here:

$$\bar{C} = \frac{1}{V} \int_0^{2\pi} \int_0^\pi \int_0^a C(r) r^2 \sin \theta dr d\theta d\phi = \frac{3PC_{ext}}{ak_s} + \frac{k_1}{k_s}$$

5.2.4 COMSOL simulations

We implemented the model in COMSOL software (Stockholm, Sweden) with the same geometry, boundary conditions, and parameter values. We used an extremely fine mesh and simulated the model up to 3 ms with a 1 μ s interval; we also simulated the model at steady state. We obtained concentration profiles by extracting the concentration along the line between the center of the sphere and $x = a, y = 0, z = 0$.

5.3 Results

5.3.1 Order-of-magnitude estimates for length and time scales for diffusion of H₂O₂ generated in the cytosol

Adimora et al. demonstrated that limited membrane permeability is highly significant in the cell's defense against exogenous H₂O₂ [8]. However, we were interested in determining the kinetic rate constant for H₂O₂ scavenging in response to endogenous, rather than exogenous, generation of H₂O₂. Thus, we were interested solely in H₂O₂ scavenging inside the cell, without any contributions from other processes such as H₂O₂ diffusion through the plasma membrane or into subcellular compartments such as peroxisomes; in other words, we sought to simulate the dynamics of the system as if all of the molecular species involved in the kinetic redox model were mixed in a single compartment that suddenly experienced pulsed, intracellular generation of H₂O₂. We hence removed any rate expressions

involving the transfer of any cytosolic species to another compartment and simulated the response when H_2O_2 at $t = 0$ was increased to a concentration ranging from 0.01 to 1 μM ; we chose this range because we estimated the basal concentration of H_2O_2 to exist in the picomolar range as described in Appendix C and previous work suggests that cytotoxicity may occur at low nanomolar increases to the basal concentration of H_2O_2 [32].

We confirmed pseudo-first order kinetics for H_2O_2 scavenging [32] and calculated a kinetic rate constant, k_{eff} , that ranged from 1.30×10^3 to $1.31 \times 10^3 \text{ s}^{-1}$. We used this rate constant and the known diffusion coefficient for H_2O_2 in water at 37 °C [164] to calculate order-of-magnitude estimates for the length and time scales for H_2O_2 diffusion based on the following equations, which are well-known in engineering literature [165]:

$$L = \sqrt{\frac{D}{k_{eff}}}$$

$$t = \frac{1}{k_{eff}}$$

Here, L is the length scale, D is the diffusion coefficient, and t is the time scale. The length and time scales for H_2O_2 diffusion were calculated to be 1.18 μm and 0.76 ms, respectively, giving credence to the notion of H_2O_2 localization and limited diffusion due to the strength of the cellular antioxidant network. To quantify the relative magnitudes of homogeneous H_2O_2 depletion and diffusion, we calculated the Damköhler number, which is expressed here as

$$Da = \frac{k_{eff}R^2}{D}$$

where R is the radius of the cell and, for HeLa, is 10 μm [163]. The Damköhler number was calculated to be ~ 71 , which is significantly greater than unity and indicates that the depletion of H_2O_2 by antioxidant scavenging is greater than the extent to which H_2O_2 diffuses through the cell, implying H_2O_2 localization.

5.3.2 Comparison of reaction rates and sensitivity analysis

After using the full kinetic model as presented in Figure 1.1 to determine k_{eff} and calculate order-of-magnitude estimates for the length and time scales of H_2O_2 diffusion, we sought to determine which reactions in the network are most important. We calculated the rates of the reactions in the model, taking into account the reaction rate constants as well as the concentrations of the antioxidant enzymes involved in each reaction (Figure 5.1 and Figures C.2-C.9).

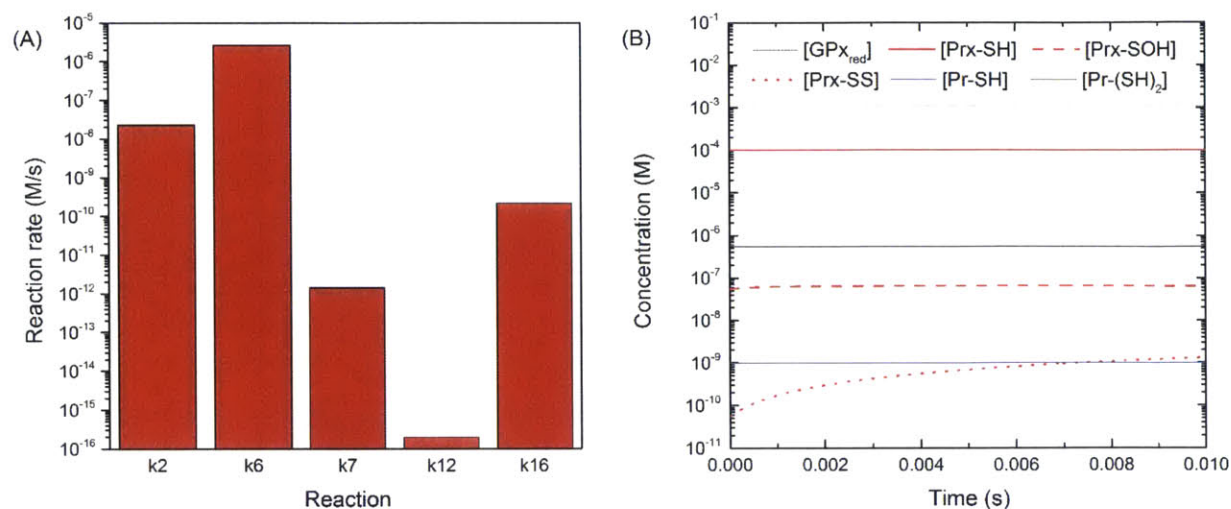


Figure 5.1. (A) Rates of reactions directly involved in H_2O_2 scavenging with initial $[\text{H}_2\text{O}_2]$ of $0.01 \mu\text{M}$. Each reaction is designated by its accompanying rate constant as shown in Table 5.1; k_2 , for instance, indicates the reaction $k_2 ([\text{H}_2\text{O}_2]) ([\text{GPx}_{\text{red}}])$. (B) Concentrations of antioxidant enzymes directly involved in H_2O_2 scavenging over time with initial $[\text{H}_2\text{O}_2]$ of $0.01 \mu\text{M}$.

Figure 5.1 shows that the reaction directly involved in H_2O_2 scavenging with the highest rate by at least two orders of magnitude is that between $\text{Prx}-(\text{SH})_2$ and H_2O_2 , with the rate constant k_6 . Furthermore, the concentration of $\text{Prx}-(\text{SH})_2$ does not significantly decrease; while it is clear it is involved in H_2O_2 scavenging as evidenced by the rise in concentration of oxidized Prx (Prx-SS), the amount of initial H_2O_2 does not seem to significantly impact the concentration of $\text{Prx}-(\text{SH})_2$ over time except at higher H_2O_2 concentrations (Figures C.8 and C.9). A sensitivity analysis based on the finite difference approximation showed that perturbation of k_6 , the rate parameter for the reaction between $\text{Prx}-(\text{SH})_2$ and H_2O_2 (Figure 5.2 and Figures C.10-C.17), within its experimental error resulted in changes in the concentration of H_2O_2 by as much as 14%, while perturbation of each of the other parameters never resulted in a change greater than 0.3%. This shows the dominating influence of k_6 over the other parameters, confirming the importance of the reaction between $\text{Prx}-(\text{SH})_2$ and H_2O_2 .

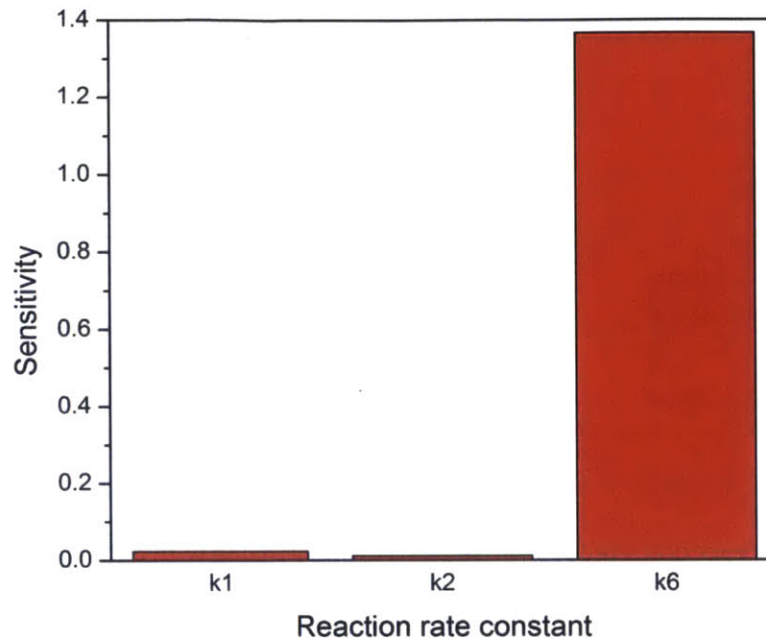


Figure 5.2. Sensitivity of $[H_2O_2]$ to reaction rate constants with initial $[H_2O_2]$ of $0.01 \mu M$. Other reaction rate constants were not shown because the sensitivities of $[H_2O_2]$ to those parameters were at least one order of magnitude less than the lowest sensitivity shown in the plot, and thus would not have been visible.

Given that Prxs dominate in H_2O_2 scavenging as well as the recent finding that oxidized Prx acts as a mediator for H_2O_2 signaling [14], we applied the same equations used to estimate length and time scales for H_2O_2 diffusion to oxidized Prx, using a previous measurement for the kinetic rate constant for reduction of Prx-SS [8,149] and a previously measured diffusion coefficient for oxidized AhpC [166], scaled to a temperature of $37^\circ C$ using the Stokes-Einstein equation [167,168]. AhpC is in the same family of peroxidases as Prx and is of similar size, and thus is expected to exhibit a diffusion coefficient similar to that of Prx-SS, which has not yet been experimentally measured. Based on these parameters, order-of-magnitude estimates for the length and time scales for reduction of Prx-SS by Trx were $9.6 \mu m$ and $1.1 s$, respectively, suggesting signaling to span nearly half of the cell; we note that these estimates are extremely dependent on the estimate for the rate constant for reduction. While Prx-SOH was calculated to have an initial concentration higher than that of Prx-SS, the latter visibly rose in concentration after the H_2O_2 pulse while the former did not; in any case, the oxidation state responsible for signaling redox relay reactions remains an open question. Direct quantitative measurement of the relay reaction between both oxidation states and a signaling target such as STAT3 would be required to confirm which Prx species is involved and also estimate the localization of signaling with more certainty [169].

5.3.3 Reduction of kinetic model

Because of the overwhelming importance of Prx in H_2O_2 scavenging, we calculated the rate constant of the reaction between Prx-SH and H_2O_2 , taking into account both k_6 and the concentration of Prx-(SH)₂,

and found it to be $1.3 \times 10^3 \text{ s}^{-1}$ [32], quite close to k_{eff} . Since the concentration of Prx-(SH)₂ was also found to be nearly constant throughout the simulation except at higher, nonphysiological initial [H₂O₂] as previously mentioned, we reduced the kinetic model to a two-parameter model with only the concentration of H₂O₂ as the dependent variable and a constant level of Prx-(SH)₂, described here:

$$\frac{d[H_2O_2]}{dt} = k_1 - k_s[H_2O_2]$$

$$[H_2O_2] = \frac{k_1}{k_s} + \left([H_2O_2]_0 - \frac{k_1}{k_s} \right) e^{-k_s t}$$

$$k_s = k_6[Prx - (SH)_2]$$

where k_1 is the zeroth-order rate constant for H₂O₂ generation within the cell and k_s is the product of the kinetic rate constant for the reaction between Prx-(SH)₂ and H₂O₂ (k_6) and the intracellular concentration of Prx-(SH)₂. The results from the simplified, analytical equation completely capture the results of the complete kinetic redox model across the physiologically relevant concentration range of initial H₂O₂ that we tested (Figure 5.3). Although the analytical equation does break down in mimicking the results of the original model at higher initial H₂O₂ concentrations due to significant depletion of Prx-(SH)₂ (Figure C.18), these concentrations are not within a reasonable physiological range [32]. Our results show that the rate of H₂O₂ scavenging within the cell is fast enough that the concentration of Prx-(SH)₂ available to scavenge H₂O₂ can be approximated as constant within physiologically relevant ranges of initial H₂O₂.

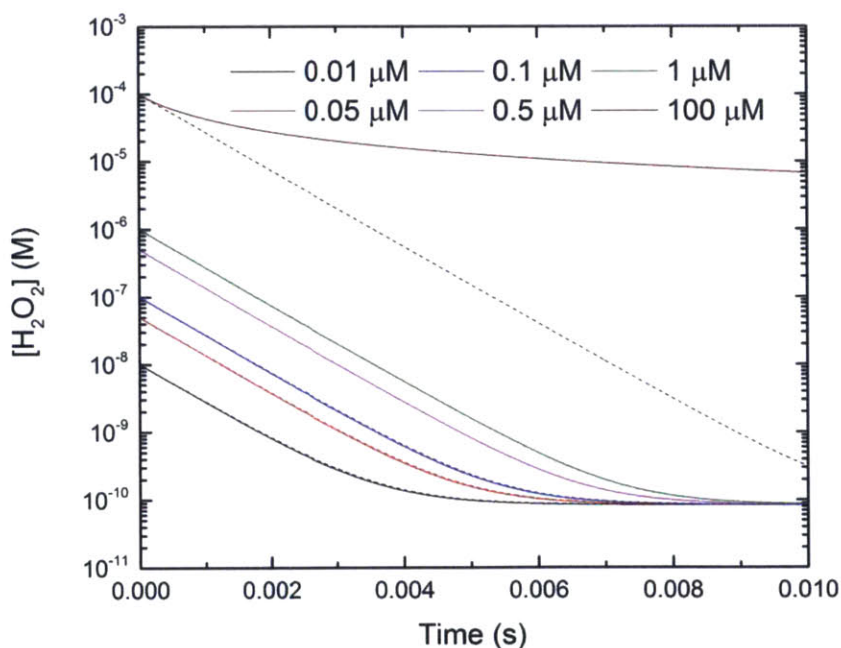


Figure 5.3. Simulated kinetic curves for clearance of a pulse addition of H₂O₂ to baseline levels in a single compartment. Solid curves represent the original complete model sans transfer of H₂O₂ to other compartments, such as extracellular media or peroxisomes. Dashed curves represent a simplified model in which only H₂O₂ generation and scavenging by Prxs, without any oxidation of the enzyme, are simulated as an analytical equation. Solid and dashed curves overlap except for 100 μM.

We note that given the validation of this approximation as shown by Figure 5.3, we can estimate the basal concentration of H₂O₂ by assuming steady state and setting the single differential equation for H₂O₂ equal to zero:

$$\frac{d[H_2O_2]}{dt} = k_1 - k_s[H_2O_2] = 0$$

$$[H_2O_2] = \frac{k_1}{k_s}$$

This results in an estimate of ~80 pM. We note that before implementing simulations, we initially hypothesized that the basal concentration is largely controlled by only its generation and reduction by Prx-(SH)₂, and thus estimated the basal concentration of H₂O₂ to be ~80 pM from the outset as calculated by the above equation. We used this concentration in estimations for the initial concentrations of oxidized proteins, such as Prx-SOH and Prx-SS, as detailed in Appendix C, and used these values in the simulations shown in this study. Figure 5.3 validates our initial assumption and thus shows that our initial estimation for the basal concentration of H₂O₂, and consequently for the initial concentrations of oxidized proteins, is valid in this context, given the current parameter set used. We acknowledge that not all model parameters, such as the concentrations of Trx and GSH, are specific to HeLa [8]; in the absence of such data, we used these parameters as the best available proxy estimates.

We also note here that while k_1 in our model is orders of magnitude less than the $k_s[H_2O_2]$ term, even at the lowest H₂O₂ concentration simulated, the estimated basal concentration of H₂O₂ is sensitive and directly proportional to k_1 . It is thus also worth noting that the parameter was calculated by Adimora et al. [8] based on data corresponding to O₂ consumption rates and proportions of H₂O₂ production for the entire human body and which could be in error by two-fold [144]. While the value used here may provide an adequate order-of-magnitude estimate for intracellular H₂O₂ production and give reason to believe that the basal level of H₂O₂ exists in the picomolar range, the rate may vary between cell types and with changing physiological conditions [144,170,171]. This consequently has implications for the basal levels of both intracellular H₂O₂ and oxidized proteins as derived in Appendix C, giving merit to measurement of the basal generation rate specific to the cell line being studied in future work. Endogenous H₂O₂ production could also be increased experimentally through the use of a genetically encoded enzyme such as DAAO [30,56,57,60] or small molecule generators [31,65].

5.3.4 Time scale for consumption of bolus addition of H₂O₂ and expected gradient

In our development of the transport model for cellular H₂O₂, we first plotted previous experimental data measuring the consumption of a bolus addition of H₂O₂ by suspended HeLa cell culture [32] in Figure 5.4. We also plotted the anticipated average intracellular concentration throughout the entire cell at each time point using the equation developed in Section 5.2.3.4. The gradient between extracellular and intracellular H₂O₂ is approximately 980-fold throughout the entire assay; this has modest agreement with the experimental estimate of 650-fold, which was determined by measuring the kinetic rate constants of individual scavengers after cell lysis rather than *in vivo*, which may have affected the measurements [32].

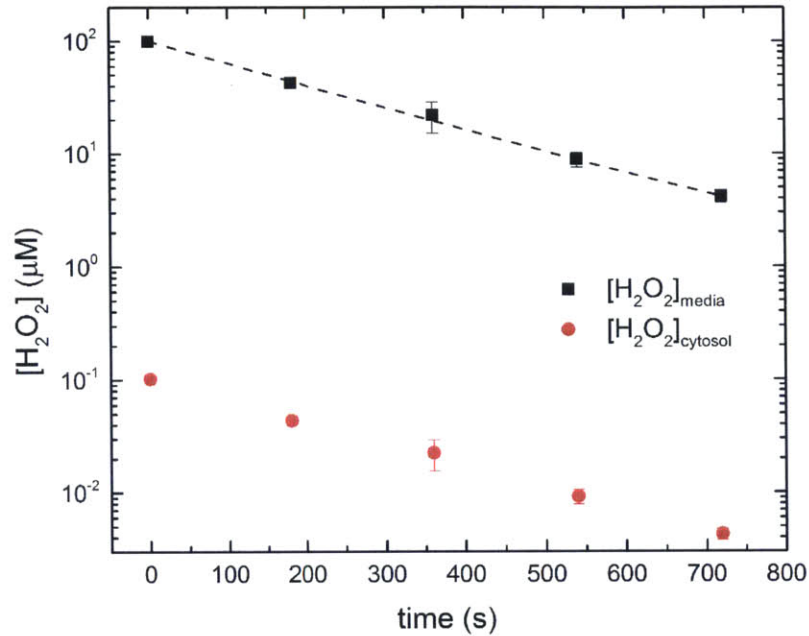


Figure 5.4. Extracellular and intracellular H_2O_2 over time upon bolus addition of $100 \mu M$ to HeLa cells with density of 0.8×10^9 cells/l. An exponential curve was fit to the concentration of external H_2O_2 . Concentration of intracellular H_2O_2 was averaged over the entire volume of the sphere. Error bars represent standard deviation of three independent trials.

A priori, we assumed the intracellular concentration would be significantly less than the extracellular concentration based on previous evidence [32] and consequently would be negligible relative to the extracellular concentration in the equation described in Section 5.2.3.1. We thus fit an exponential curve to the data as shown in Figure 5.4 and used the second equation in Section 5.2.3.1, as well as the assay parameters of 0.8×10^9 cells/l [32] and an idealized spherical surface area of $1.3 \times 10^{-5} \text{ cm}^2$, to determine the cell permeability to be $4.4 \times 10^{-4} \text{ cm/s}$. While we used this parameter in calculation of the average intracellular concentration, these calculations show that the extracellular and intracellular concentrations indeed differ by several orders of magnitude, justifying our a priori assumption that the intracellular concentration is negligible relative to the extracellular concentration and our consequent calculations for obtaining the permeability constant.

We note that the average intracellular concentrations could be verified by a sensor expressed in the cytosol. For instance, Mishina et al. recently developed a methodology using the genetically encoded H_2O_2 sensor HyPer-2 [93] fused to the cytoskeleton in live-cell stimulated emission depletion (STED) microscopy to monitor the production of H_2O_2 within living cells with high spatial and temporal resolution [172]. By their estimates, they were able to detect nanomolar concentrations within the cell [172], suggesting their methodology to be suitable for confirming the intracellular estimates shown in Figure 5.4.

5.3.5 Time and length scales for intracellular H_2O_2 diffusion after step change in external concentration and justification of intracellular pseudo-steady state

After solving the conservation equation, we generated intracellular concentration profiles of H_2O_2 after a step change increase in the external concentration to $25 \mu\text{M}$ (Figure 5.5), assuming the same experimental conditions used to measure the permeability constant.

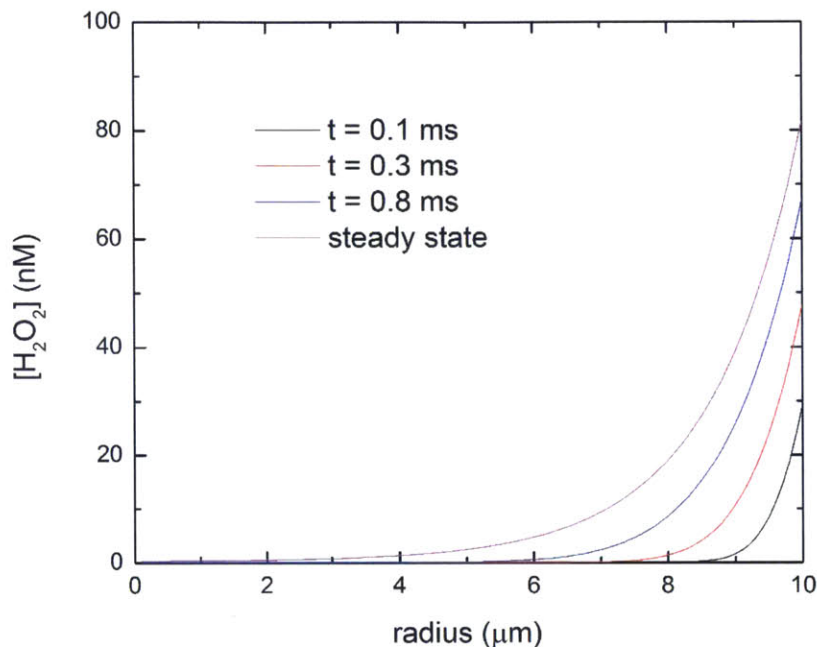


Figure 5.5. Development of intracellular concentration profile of H_2O_2 after bolus addition of $25 \mu\text{M}$ to HeLa cells with density of 0.8×10^9 cells/l.

We note that the profile reaches steady state on a time scale too rapid to be experimentally accessible and thus verifiable; however, while they may be predicated upon a hypothetical instantaneous step change in the external concentration, the idealized response in Figure 5.5 still provides value in showing the time and length scales of H_2O_2 diffusion after permeation through the membrane. The concentration profile reaches steady state within a time scale on the order of 1-2 ms, and H_2O_2 penetrates approximately 4-5 μm into the cell before being almost completely scavenged. This is consistent with previous order-of-magnitude estimates for the time and length scales of H_2O_2 based on dimensional analysis, which were 1 ms and 1 μm , respectively.

We also draw attention to the steep decline of H_2O_2 after diffusing through the membrane and the lack of any appreciable amount of H_2O_2 at the center of the cell. The prediction of localization of H_2O_2 close to the membrane due to scavenging contradicts the assumption of a well-mixed cytosol, providing a possible explanation for the differences in phenotype observed between bolus addition and steady state intracellular generation throughout the entire cytosol [65]. The presence of H_2O_2 close to the membrane and lack of H_2O_2 at the center of the cell could be verified by localized sensors [71,173,174]. The predictions could also be tested by the previously mentioned methodology by Mishina et al. [172].

While the intracellular concentration profile requires only ms to reach steady state, the extracellular concentration takes approximately 12 min to be consumed by suspended cell culture (Figure 5.4). The

discrepancy between these two time scales allows us to approximate the intracellular concentration profile at any point to be at the pseudo-steady state indicated in Figure 5.5, as the pseudo-steady state is valid in the case of two time scales orders of magnitude apart [165]. Furthermore, it suggests that any experimental measurement will, for practical purposes, measure this pseudo-steady state profile.

5.3.6 Pseudo-steady state concentration profiles over time

In our last set of predictions, we plotted the pseudo-steady state at different times in the assay for consumption of bolus H_2O_2 (Figure 5.6).

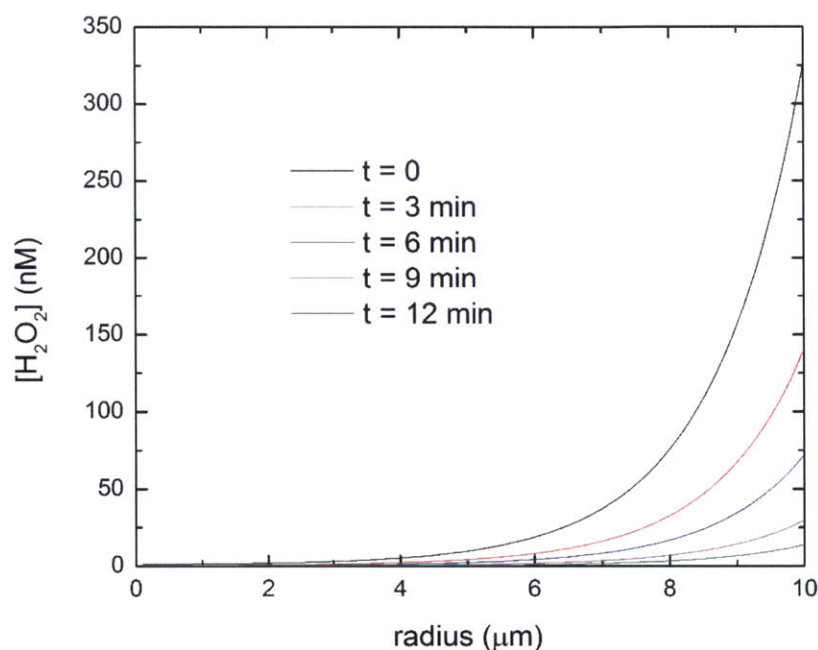


Figure 5.6. Development of pseudo-steady state intracellular concentration profile after bolus addition of $100 \mu\text{M}$ to HeLa cells with density of 0.8×10^9 cells/l.

The profile essentially retains its characteristic shape, with the concentration at the membrane gradually decaying over time in accordance with the decay of the extracellular species. The effective penetration distance also decreases as the overall H_2O_2 concentration drops over time, with H_2O_2 only effectively diffusing about a micron through the cell and at very low nanomolar levels before being completely scavenged at the 12 min time point. Again, these profiles could be verified by the previously mentioned experimental system developed by Mishina et al. [172].

5.3.7 Comparison of computational and analytical solutions

After making testable predictions using the analytical transport model for H_2O_2 derived using the FFT method, we implemented the same model in COMSOL to determine if a computational solution based on finite element analysis could be a viable alternative (Figure 5.7).

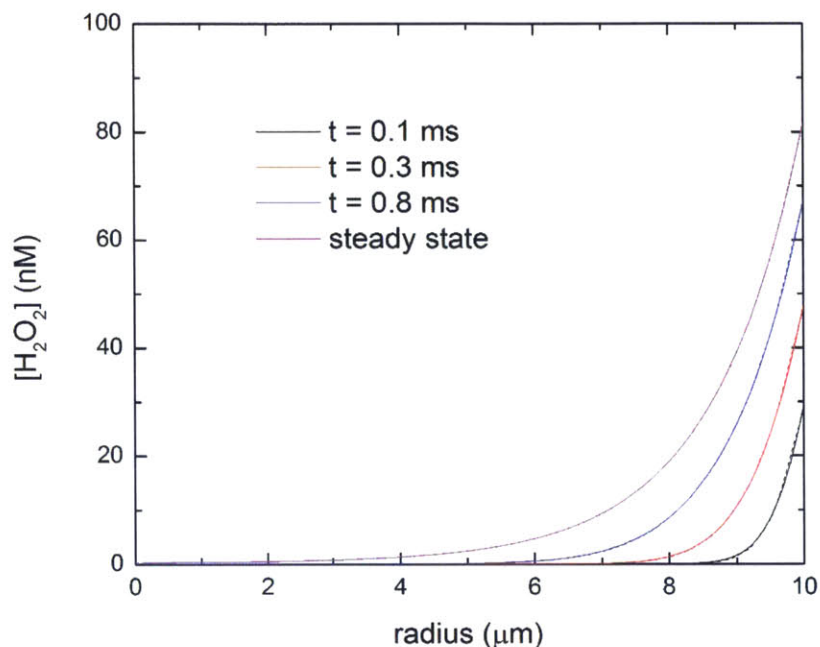


Figure 5.7. Development of intracellular concentration profile of H_2O_2 after bolus addition of $25 \mu\text{M}$ to HeLa cells with density of 0.8×10^9 cells/l, with analytical (solid) and computational solutions (dashed). Computational solutions were generated by COMSOL software and overlap with analytical solutions at all time points considered and steady state. An “extremely fine” mesh was used for the computational solution.

We observed no visible difference between the analytical and computational solutions: at the time points shown in Figure 5.7 and at spatial intervals of $0.1 \mu\text{m}$ from the center of the cell to radius a , the difference never exceeded 1.1 nM and the sum of squared differences never exceeded 2.6 nM^2 . We do note that reducing the spatial resolution by adjusting the mesh from “extremely fine” to “extra fine” decreased the accuracy of the solutions (Figure C.19), showing that the highest possible resolution of any computational solution may be necessary. Nevertheless, based on the above metrics, we deemed the computational solution to be a viable method for generating concentration profiles in this context. Thus, any extensions to the model in future work that prove intractable using analytical methods may be implemented using computational software such as COMSOL.

5.4 Discussion

We extracted a simple analytical expression for H_2O_2 generation and scavenging from a kinetic redox model with 22 parameters and 21 species. This approximation is predicated on the finding that Prx is by far the predominant H_2O_2 scavenger in the cytosol. We integrated the expression into the classic transport equation for a solute in a cell idealized as a sphere and applied various mathematical techniques to derive the expected concentration profile of H_2O_2 upon bolus addition. We also found that the COMSOL software package provides predictions that closely match the exact solution, giving it credibility as an alternative solution method. This model could be extended to provide predictions of H_2O_2 concentration profiles when produced in a local fashion inside the cell.

However, currently the literature lacks reports of signal responses that have been correlated with absolute local H_2O_2 concentrations, making it difficult to compare model results with experimental data. Furthermore, colocalizing generators and sensors in the same subcellular location would only confirm the amount of H_2O_2 being produced in that location, and only if the signal has been calibrated and correlated with absolute concentrations. Validation of a transport model will require H_2O_2 sensors [175] and generators that can be localized to different parts of the cell. Current state-of-the-art H_2O_2 sensors such as HyPer [59] have indeed been localized to different cellular compartments [174,176–179], and although enzymes previously used for H_2O_2 generation, such as DAAO, do not meet all the criteria of an ideal H_2O_2 generator, they are also capable of being targeted to certain organelles within the cell [56]. A fusion of HyPer and DAAO also demonstrated improved dynamic range in response to enzymatic H_2O_2 production and could serve as a dual-purpose sensor and generator [60].

To verify length and time scales of diffusion of H_2O_2 when generated at a particular location, sensors must be present both at the site of H_2O_2 generation and at a location sufficiently far away. If the second location is farther than the predicted length scale, then a high, positive signal at that location would contradict the model prediction; conversely, if the second location is not as far as the predicted length scale, then lack of a signal would also contradict the model prediction. The reverse of these potential outcomes would confirm the model prediction. An experimental system to enable verification of these predictions could be constructed by using peptide tags to localize a generator and sensor at a particular organelle and another sensor at another organelle; DAAO and HyPer could be localized to the plasma membrane [33], for instance, while another genetically encoded sensor, roGFP2-Orp1 [79], could be localized in the nucleus [56] or centrosome [180]. If a bolus addition is used, it may be sufficient to localize only one sensor at a distance significantly greater than a few microns from the membrane, and test whether the predicted penetration of H_2O_2 into the cell is consistent with the observation of a positive signal or lack thereof.

A system designed to verify or refute model predictions for length and time scales of H_2O_2 diffusion could also be used to measure concentrations that can be compared with predicted concentration profiles. This would require quantitative calibration of the sensors and knowledge of how far apart the different sensors are expected to be; if the latter is unknown, it could be attained by saturating the cell with H_2O_2 through bolus addition, for instance, and using fluorescence microscopy to measure the distance between activated sensors. It has been claimed that cytosolic expression of a sensor may only provide an overall intracellular measurement, rather than a spatial concentration profile, due to potential diffusion of the sensor throughout the cell [33]; if this is the case, then a sensor could be attached to the cytoskeleton of the cell [181], thus immobilizing the sensor and eliminating the potential problem of sensor diffusion. Indeed, as mentioned before, Mishina et al. recently developed such a measurement system using a fusion of HyPer-2 [93] to the cytoskeleton and STED microscopy to visualize H_2O_2 dynamics and claimed measurement sensitivity in the nanomolar range, which should make it suitable to verify the predictions we generated [172].

5.5 Conclusions

Although there does not yet exist quantitative experimental data for the model to match with predictions, the transport model of H_2O_2 described in this chapter still holds value. The predicted concentration profiles generated by the model can be tested against past experimental observations as well as future experimental efforts that are accessible with the set of tools currently available;

agreement between model and experiment would validate the model, while disagreement would suggest deficiencies in the model, or possibly a flawed experimental system. The predictions of a validated transport model also inform the design of next-generation sensors and generators of H_2O_2 , as they provide a test for the kinetic parameters that have been used to elucidate the design criteria shown in Figure 1.2. While models generally gain credibility by experimental verification, the transport model of H_2O_2 still provides predictions with great utility in the field and initiates the feedback between experiment and theory that will help refine the experimental tools as well as the model upon which these tools are based.

Chapter 6

Conclusions and future directions

Abstract

This thesis was designed to provide a foundation comprised of novel methodologies and criteria refinement towards an ideal H₂O₂ generator, for use in quantitative redox biology studies. This chapter summarizes each of the aims of the thesis and the resulting findings, and concludes with future directions for developing next-generation H₂O₂ generators.

6.1 Conclusions

While H_2O_2 is of great interest in redox biology due to its role in numerous physiological processes and the qualitative correlation between H_2O_2 levels and various phenotypes, it remains unknown at what levels these processes and phenotypes occur. To make physiologically meaningful perturbations to the intracellular H_2O_2 level free of other conflating effects, a promising tool is what we define as an ideal enzymatic generator. Such a generator would be soluble, localizable, and genetically encoded, and would exhibit a tunable H_2O_2 production rate capable of overcoming the cell's antioxidant capacity with minimal or no byproducts and using only ample, endogenous substrates.

The objective of this thesis was to provide a foundation and framework for engineering next-generation H_2O_2 generators that meet the criteria of an ideal generator. We devised a novel enzyme engineering methodology to explore and optimize candidate enzymes, and derived a transport model for H_2O_2 to refine the criteria. We summarize the main findings and conclusions in the rest of this section.

6.1.1 Use of an H_2O_2 sensor *in vivo*

The most current state-of-the-art sensor for measuring intracellular H_2O_2 is HyPer, a genetically encoded protein with a ratiometric signal [59]. Yet often the signal is reported only with the concentration of the bolus of H_2O_2 added to culture, without considering other potential variables, such as number of cells, cell type, and timing of measurement. Furthermore, the signal has never been fully characterized in bacteria, which we saw as a potential platform for a novel protein engineering screen for enhancing H_2O_2 production.

In Chapter 2, we expressed HyPer in the *E. coli* strains BL21 (DE3) and DH5 α and characterized the signal, developing dose-response curves and finding that the cell density, bacterial strain, and timing of measurement all do indeed impact the signal significantly. We also observed that the signal lags behind the amount of H_2O_2 actually present in solution; thus, while the sensor has often been advertised as real-time [59], it is more appropriate to characterize it as reversible, at least in the context of H_2O_2 measurement inside bacteria.

Finally, we fitted the dose-response curve to a Hill equation, providing a framework with statistically meaningful parameters that, when the above assay variables are also controlled, should enable side-by-side comparisons of the signal across studies. Our work reported in this chapter provided a protocol for using the sensor in *E. coli* [91], allowing us to extend its use to a novel protein engineering methodology, as described in the following section.

6.1.2 Screening for enzymatic H_2O_2 production

Since previously used oxidases for H_2O_2 production have high activities capable of inducing relevant signaling events and phenotypes but fail to meet other criteria of an ideal generator, we turned to another candidate enzyme, cytochrome P450 BM3. Its main shortcoming was its low H_2O_2 production rate which, coupled with its mammalian expression, did not allow it to overcome the cell's antioxidant capacity. In Chapter 3, we explored variants that past studies indicated might be capable of higher production rates [105–107] and found that not only did they produce H_2O_2 at higher rates, but that combining their mutations increases the leak rate and consequently the H_2O_2 production rate. However, this set of variants experienced severe decreases in bacterial expression and thermostability and were not detectable by a CO binding assay when expressed in mammalian cells. While this did not preclude

P450 BM3 entirely from consideration as an ideal H₂O₂ generator, we did not consider this set of variants viable for this application.

We were also interested in developing a novel screening methodology for H₂O₂ production [135], one that took advantage of the properties of a genetically encoded sensor and improved upon previous methodologies that require time-consuming lysis procedures and extra reagents [134]. In Chapter 4, we hence targeted P450 BM3 and co-expressed it with HyPer in *E. coli*. We first determined a co-expression scheme that minimized variability in expression of the sensor. We then confirmed that WT and the I401P variant could be used as baseline and positive controls, respectively, and refined the fold difference between the controls with respect to timing of measurement and suspension buffer (both pH and composition). We applied a directed evolution approach and generated a library of P450 BM3 variants by random mutagenesis, targeting the oxidase domain. After screening 400 clones, we found 10 hits and confirmed that five of them did indeed exhibit enhanced H₂O₂ production rates based on an alternative measurement technique, thus providing proof-of-concept for the screen.

We further explored the sequence space of P450 BM3 by screening 640 more variants and detecting 18 additional hits. We chose the hits with the 11 highest signals and expressed them along with WT in a 96-well microplate to perform a side-by-side comparison of their expression levels and leak rates as measured in bacterial lysate. We chose the four hits with expression comparable with that of WT and enhanced leakage, and found that unlike the variants explored in Chapter 3, they were detectable by a CO binding assay. This confirmed at least a qualitative correlation between bacterial and mammalian expression and suggested that P450 BM3 may yet still be engineered in future studies to become an ideal H₂O₂ generator, screening by either bacterial expression or enhanced specific H₂O₂ production.

6.1.3 Development of a transport model for H₂O₂

The criterion for H₂O₂ production by an enzymatic generator as presented in Figure 1.2 was based on a valuable kinetic model [8,32]. However, it only accounted for H₂O₂ production through the entire cytosol, rather than in subcellular locales as is often the case in physiologically relevant events [16–20]. The extent to which H₂O₂ signaling is localized is also not yet well understood, at least quantitatively.

In Chapter 5, we used a kinetic model to gain order-of-magnitude estimates of the length and time scales of H₂O₂ localization when generated inside the cell, which were on the order of 1 micron and 1 ms, respectively. We then simplified the model in that context, pruning it into a single equation, and integrated this equation into the governing transport equation for solutes, assuming the cell to be an idealized sphere. After applying mathematical techniques such as FFT, we derived the intracellular concentration profile of H₂O₂ to be expected after bolus treatment. This provides experimentally testable predictions and initiates feedback between experiment and theory, allowing us to directly test the model parameters and refine the criteria for an ideal H₂O₂ generator.

6.2 Future directions

This thesis provides a foundation for developing next-generation H₂O₂ generators. It is our hope that future work will build upon this foundation and apply our findings, namely our novel methodologies and transport model. We describe in this section possible directions for these efforts.

6.2.1 Exploration of P450 BM3 as an H₂O₂ generator

We explored P450 BM3 as an H₂O₂ generator by first studying variants that were found to exhibit enhanced leakage in past studies [105–107]. When variants with these mutations and combinations thereof did not express to significant amounts in mammalian cells, we applied our novel screen to find other variants [135]. Four of these – M185K, A111T, I220T, and A264V – showed promise by not only exhibiting higher leakage in bacterial lysate but also expressing in mammalian cells to detectable amounts higher than what was observed for the variants explored in Chapter 3.

In future work, these variants should be isolated, cultured, and purified separately to confirm *in vitro* that they do indeed have higher leak and H₂O₂ production rates. P450 BM3 could also be engineered further, using WT or one of the above variants as a starting point. Although our screen considers only total H₂O₂ production and thus does not take into separate consideration the expression level of the enzyme or its specific activity, this may prove useful since both properties are vital to the criterion posed in Figure 1.2. It may also be advantageous to screen for bacterial expression separately.

While this thesis focuses on H₂O₂, we also note again that P450 BM3 is capable of producing O₂⁻. Thus, if a viable sensor for O₂⁻ measurement becomes available, it may be of interest to use this sensor in another novel screen for O₂⁻ production and target P450 BM3 similarly. This would extend the current methodologies available for perturbing H₂O₂ and O₂⁻ levels and enable this to occur in a specific fashion, allowing us to parse the effects of these species separately and more fully understand their underlying biology.

6.2.2 Verification and extension of a transport model for H₂O₂

We developed a transport model for H₂O₂ that provides testable predictions of the intracellular concentration profile. These predictions could indeed be tested in future experiments. We predicted, for instance, that H₂O₂ should not penetrate any further than a few microns upon bolus addition to cell culture. This could be tested by localizing a sensor near the center of the cell, perhaps at the centrosome [180]. To immobilize the sensor, one could attach the sensor to the cytoskeleton [181], thus directly measuring the concentration profile rather than only testing the length and time scales. The reader is referred to Section 5.4 for further details on possible experiments to verify the model.

The model could also be extended beyond bolus treatment and H₂O₂. Since the COMSOL software package has proven to match the exact solutions quite well, the model implementation could be extended to make predictions when H₂O₂ generation is localized at a single point inside the cell. We have also sporadically mentioned O₂⁻ throughout this thesis, and propose that if cell permeability, diffusion coefficient, and the reaction network for O₂⁻ become well understood, this knowledge could be applied to develop a similar model for O₂⁻. In this thesis, we provide the mathematical steps and computational framework that we hope assists with development of such a model.

6.2.3 Next-generation generators and sensors of H₂O₂

It is worth emphasizing that the objective of this thesis has been to establish a framework for developing next-generation H₂O₂ generators. Future work should, of course, entail this, but we also expect our work to assist with development of next-generation sensors as well. A generator that uncovers the physiologically relevant levels of H₂O₂ production, for instance, should inform the dynamic range and detection limit required of a corresponding sensor.

The development of next-generation generators and sensors should also initiate meaningful feedback to the methodologies and modeling efforts presented in this thesis. A sensor with improved dynamic range, for instance, could be applied in a fashion similar to our novel protein engineering screen but also enable the use of FACS, which would dramatically increase the screen's throughput. Additionally, the model should provide predictions of where and how much H_2O_2 and other related species are expected to be upon their perturbation, setting the relevant parameter space for next-generation generators and sensors.

References

- [1] K.E. Iles, H.J. Forman, Macrophage signaling and respiratory burst, *Immunol. Res.* 26 (2002) 95–105. doi:10.1385/IR:26:1-3:095.
- [2] F.C. Fang, Antimicrobial reactive oxygen and nitrogen species: concepts and controversies, *Nat. Rev. Microbiol.* 2 (2004) 820–32. doi:10.1038/nrmicro1004.
- [3] C. Nathan, A. Cunningham-Bussel, Beyond oxidative stress: an immunologist’s guide to reactive oxygen species, *Nat. Rev. Immunol.* 13 (2013) 349–61. doi:10.1038/nri3423.
- [4] R.H. Burdon, Superoxide and hydrogen peroxide in relation to mammalian cell proliferation, *Free Radic. Biol. Med.* 18 (1995) 775–794. doi:10.1016/0891-5849(94)00198-S.
- [5] M.L. Circu, T.Y. Aw, Reactive oxygen species, cellular redox systems, and apoptosis, *Free Radic. Biol. Med.* 48 (2010) 749–62. doi:10.1016/j.freeradbiomed.2009.12.022.
- [6] J.R. Stone, S. Yang, Hydrogen peroxide: a signaling messenger, *Antioxid. Redox Signal.* 8 (2006) 243–70. doi:10.1089/ars.2006.8.243.
- [7] E. Veal, A. Day, Hydrogen peroxide as a signaling molecule, *Antioxid. Redox Signal.* 15 (2011) 147–51. doi:10.1089/ars.2011.3968.
- [8] N.J. Adimora, D.P. Jones, M.L. Kemp, A model of redox kinetics implicates the thiol proteome in cellular hydrogen peroxide responses, *Antioxid. Redox Signal.* 13 (2010) 731–43. doi:10.1089/ars.2009.2968.
- [9] S.G. Rhee, S.W. Kang, W. Jeong, T.-S. Chang, K.-S. Yang, H.A. Woo, Intracellular messenger function of hydrogen peroxide and its regulation by peroxiredoxins, *Curr. Opin. Cell Biol.* 17 (2005) 183–9. doi:10.1016/j.ceb.2005.02.004.
- [10] H.A. Woo, S.H. Yim, D.H. Shin, D. Kang, D.-Y. Yu, S.G. Rhee, Inactivation of peroxiredoxin I by phosphorylation allows localized H₂O₂ accumulation for cell signaling, *Cell.* 140 (2010) 517–28. doi:10.1016/j.cell.2010.01.009.
- [11] A. Laurent, C. Nicco, C. Chereau, C. Goulvestre, J. Alexandre, A. Alves, et al., Controlling Tumor Growth by Modulating Endogenous Production of Reactive Oxygen Species, *Cancer Res.* 65 (2005) 948–956.
- [12] Z.A. Wood, L.B. Poole, P.A. Karplus, Peroxiredoxin evolution and the regulation of hydrogen peroxide signaling, *Science* (80-.). 300 (2003) 650–3. doi:10.1126/science.1080405.
- [13] S.G. Rhee, H.A. Woo, I.S. Kil, S.H. Bae, Peroxiredoxin functions as a peroxidase and a regulator and sensor of local peroxides, *J. Biol. Chem.* 287 (2012) 4403–10. doi:10.1074/jbc.R111.283432.

- [14] M.C. Sobotta, W. Liou, S. Stöcker, D. Talwar, M. Oehler, T. Ruppert, et al., Peroxiredoxin-2 and STAT3 form a redox relay for H₂O₂ signaling, *Nat. Chem. Biol.* 11 (2015) 64–70. doi:10.1038/nchembio.1695.
- [15] C.C. Winterbourn, M.B. Hampton, Redox biology: Signaling via a peroxiredoxin sensor, *Nat. Chem. Biol.* 11 (2015) 5–6. doi:10.1038/nchembio.1722.
- [16] M. Ushio-Fukai, Localizing NADPH oxidase-derived ROS, *Sci. Signal.* 2006 (2006) re8. doi:10.1126/stke.3492006re8.
- [17] M. Ushio-Fukai, Compartmentalization of redox signaling through NADPH oxidase-derived ROS., *Antioxid. Redox Signal.* 11 (2009) 1289–99. doi:10.1089/ARS.2008.2333.
- [18] T.L. Leto, S. Morand, D. Hurt, T. Ueyama, Targeting and regulation of reactive oxygen species generation by Nox family NADPH oxidases, *Antioxid. Redox Signal.* 11 (2009) 2607–19. doi:10.1089/ARS.2009.2637.
- [19] F.D. Oakley, D. Abbott, Q. Li, J.F. Engelhardt, Signaling components of redox active endosomes: the redoxosomes, *Antioxid. Redox Signal.* 11 (2009) 1313–33. doi:10.1089/ARS.2008.2363.
- [20] J.F. Woolley, J. Stanicka, T.G. Cotter, Recent advances in reactive oxygen species measurement in biological systems, *Trends Biochem. Sci.* 38 (2013) 556–65. doi:10.1016/j.tibs.2013.08.009.
- [21] B.C. Dickinson, C.J. Chang, Chemistry and biology of reactive oxygen species in signaling or stress responses, *Nat. Chem. Biol.* 7 (2011) 504–11. doi:10.1038/nchembio.607.
- [22] C.E. Paulsen, K.S. Carroll, Cysteine-mediated redox signaling: chemistry, biology, and tools for discovery, *Chem. Rev.* 113 (2013) 4633–79. doi:10.1021/cr300163e.
- [23] E. Panieri, V. Gogvadze, E. Norberg, R. Venkatesh, S. Orrenius, B. Zhivotovsky, Reactive oxygen species generated in different compartments induce cell death, survival, or senescence, *Free Radic. Biol. Med.* 57 (2013) 176–87. doi:10.1016/j.freeradbiomed.2012.12.024.
- [24] B.A. Maron, T. Michel, Subcellular Localization of Oxidants and Redox Modulation of Endothelial Nitric Oxide Synthase, *Circ. J.* 76 (2012) 2497–2512. doi:10.1253/circj.CJ-12-1207.
- [25] M.C. Sobotta, A.G. Barata, U. Schmidt, S. Mueller, G. Millonig, T.P. Dick, Exposing cells to H₂O₂: a quantitative comparison between continuous low-dose and one-time high-dose treatments, *Free Radic. Biol. Med.* 60 (2013) 325–35. doi:10.1016/j.freeradbiomed.2013.02.017.
- [26] H.J. Forman, Use and abuse of exogenous H₂O₂ in studies of signal transduction, *Free Radic. Biol. Med.* 42 (2007) 926–32. doi:10.1016/j.freeradbiomed.2007.01.011.
- [27] V.J. Thannickal, B.L. Fanburg, Reactive oxygen species in cell signaling, *Am. J. Physiol. Lung Cell. Mol. Physiol.* 279 (2000) L1005–1028.

- [28] K.K. Griendling, D. Sorescu, M. Ushio-Fukai, NAD(P)H Oxidase: Role in Cardiovascular Biology and Disease, *Circ. Res.* 86 (2000) 494–501. doi:10.1161/01.RES.86.5.494.
- [29] D.R. Gough, T.G. Cotter, Hydrogen peroxide: a Jekyll and Hyde signalling molecule, *Cell Death Dis.* 2 (2011) e213. doi:10.1038/cddis.2011.96.
- [30] R.E. Haskew-Layton, J.B. Payappilly, N.A. Smirnova, T.C. Ma, K.K. Chan, T.H. Murphy, et al., Controlled enzymatic production of astrocytic hydrogen peroxide protects neurons from oxidative stress via an Nrf2-independent pathway, *Proc. Natl. Acad. Sci. U. S. A.* 107 (2010) 17385–90. doi:10.1073/pnas.1003996107.
- [31] E.W. Miller, N. Taulet, C.S. Onak, E.J. New, J.K. Lanselle, G.S. Smelick, et al., Light-Activated Regulation of Cofilin Dynamics Using a Photocaged Hydrogen Peroxide Generator, *J. Am. Chem. Soc.* 132 (2010) 17071–17073. doi:10.1021/ja107783j.
- [32] B.K. Huang, H.D. Sikes, Quantifying intracellular hydrogen peroxide perturbations in terms of concentration, *Redox Biol.* 2 (2014) 955–962. doi:10.1016/j.redox.2014.08.001.
- [33] N.M. Mishina, P.A. Tyurin-Kuzmin, K.N. Markvicheva, A. V Vorotnikov, V.A. Tkachuk, V. Laketa, et al., Does cellular hydrogen peroxide diffuse or act locally?, *Antioxid. Redox Signal.* 14 (2011) 1–7. doi:10.1089/ars.2010.3539.
- [34] N. Mody, Oxidative stress modulates osteoblastic differentiation of vascular and bone cells, *Free Radic. Biol. Med.* 31 (2001) 509–519. doi:10.1016/S0891-5849(01)00610-4.
- [35] D. Siwik, P. Pagano, W. Colucci, Oxidative stress regulates collagen synthesis and matrix metalloproteinase activity in cardiac fibroblasts, *Am. J. Physiol. Cell Physiol.* 280 (2001) C53–C60.
- [36] B. Wung, J. Cheng, H. Hsieh, Y. Shyy, D. Wang, Cyclic strain-induced monocyte chemotactic protein-1 gene expression in endothelial cells involves reactive oxygen species activation of activator protein 1, *Circ. Res.* 81 (1997) 1–7.
- [37] S. Shull, N. Heintz, M. Periasamy, M. Manohar, Y. Janssen, J. Marsh, et al., Differential regulation of antioxidant enzymes in response to oxidants, *J. Biol. Chem.* 266 (1991) 24398–24403.
- [38] H. Zhao, S. Kalivendi, H. Zhang, J. Joseph, K. Nithipatikom, J. Vásquez-Vivar, et al., Superoxide reacts with hydroethidine but forms a fluorescent product that is distinctly different from ethidium: potential implications in intracellular fluorescence detection of superoxide, *Free Radic. Biol. Med.* 34 (2003) 1359–1368. doi:10.1016/S0891-5849(03)00142-4.
- [39] X. -c. Bai, D. Lu, A. -l. Liu, Z. -m. Zhang, X. -m. Li, Z. -p. Zou, et al., Reactive Oxygen Species Stimulates Receptor Activator of NF- B Ligand Expression in Osteoblast, *J. Biol. Chem.* 280 (2005) 17497–17506. doi:10.1074/jbc.M409332200.
- [40] B. Troxell, J.-J. Zhang, T.J. Bourret, M.Y. Zeng, J. Blum, F. Gherardini, et al., Pyruvate protects pathogenic spirochetes from H₂O₂ killing, *PLoS One.* 9 (2014) e84625. doi:10.1371/journal.pone.0084625.

- [41] A. Huber, P. Thongphasuk, G. Erben, W.-D. Lehmann, S. Tuma, W. Stremmel, et al., Significantly greater antioxidant anticancer activities of 2,3-dehydrosilybin than silybin, *Biochim. Biophys. Acta.* 1780 (2008) 837–47. doi:10.1016/j.bbagen.2007.12.012.
- [42] R.A. Harrison, C. Sumners, Redox regulation of macrophage migration inhibitory factor expression in rat neurons, *Biochem. Biophys. Res. Commun.* 390 (2009) 171–5. doi:10.1016/j.bbrc.2009.09.112.
- [43] D.F. Cortes, W. Sha, V. Hower, G. Blekherman, R. Laubenbacher, S. Akman, et al., Differential gene expression in normal and transformed human mammary epithelial cells in response to oxidative stress., *Free Radic. Biol. Med.* 50 (2011) 1565–74. doi:10.1016/j.freeradbiomed.2011.03.002.
- [44] M. Gonzalez-Ramos, S. de Frutos, M. Griera, A. Luengo, G. Olmos, D. Rodriguez-Puyol, et al., Integrin-linked kinase mediates the hydrogen peroxide-dependent transforming growth factor- β 1 up-regulation., *Free Radic. Biol. Med.* 61 (2013) 416–27. doi:10.1016/j.freeradbiomed.2013.04.029.
- [45] R. Aitken, D. Buckinham, D. Harkiss, Use of a xanthine-oxidase free-radical generating-system to investigate the cytotoxic effects of reactive oxygen species on human spermatozoa, *J. Reprod. Fertil.* 97 (1993) 441–450.
- [46] D.A. Wink, I. Hanbauer, M.C. Krishna, W. DeGraff, J. Gamson, J.B. Mitchell, Nitric oxide protects against cellular damage and cytotoxicity from reactive oxygen species, *Proc. Natl. Acad. Sci. U. S. A.* 90 (1993) 9813–7.
- [47] J. Griveau, E. Dumont, P. Renard, J. Callegari, D. Lelannou, Reactive oxygen species, lipid-peroxidation and enzymatic defense systems in human spermatozoa, *J. Reprod. Fertil.* 103 (1995) 17–26.
- [48] R. Harrison, Structure and function of xanthine oxidoreductase: where are we now?, *Free Radic. Biol. Med.* 33 (2002) 774–797. doi:10.1016/S0891-5849(02)00956-5.
- [49] E.E. Kelley, N.K.H. Khoo, N.J. Hundley, U.Z. Malik, B.A. Freeman, M.M. Tarpey, Hydrogen peroxide is the major oxidant product of xanthine oxidase, *Free Radic. Biol. Med.* 48 (2010) 493–8. doi:10.1016/j.freeradbiomed.2009.11.012.
- [50] A.B. Fisher, Redox signaling across cell membranes, *Antioxid. Redox Signal.* 11 (2009) 1349–56. doi:10.1089/ARS.2008.2378.
- [51] V. Massey, Iron-Sulfur Flavoprotein Hydroxylases, in: W. Lovenberg (Ed.), *Iron-Sulfur Proteins*, 1st ed., Academic Press Inc., London, 1973: pp. 301–85.
- [52] S. Mueller, G. Millonig, G.N. Waite, The GOX/CAT system: a novel enzymatic method to independently control hydrogen peroxide and hypoxia in cell culture, *Adv. Med. Sci.* 54 (2009) 121–35. doi:10.2478/v10039-009-0042-3.

- [53] L.D. Stegman, H. Zheng, E.R. Neal, O. Ben-Yoseph, L. Pollegioni, M.S. Pilone, et al., Induction of cytotoxic oxidative stress by D-alanine in brain tumor cells expressing *Rhodotorula gracilis* D-amino acid oxidase: a cancer gene therapy strategy, *Hum. Gene Ther.* 9 (1998) 185–93. doi:10.1089/hum.1998.9.2-185.
- [54] K. Ryuichi, Y. Yoshihiro, d-Amino-Acid oxidase and its physiological function, *Int. J. Biochem.* 24 (1992) 519–524. doi:10.1016/0020-711X(92)90322-R.
- [55] J. Li, Y. Shen, A. Liu, X. Wang, C. Zhao, Transfection of the DAAO gene and subsequent induction of cytotoxic oxidative stress by D-alanine in 9L cells, *Oncol. Rep.* 20 (2008) 341–346. doi:10.3892/or_00000012.
- [56] P.J. Halvey, J.M. Hansen, J.M. Johnson, Y.-M. Go, A. Samali, D.P. Jones, Selective oxidative stress in cell nuclei by nuclear-targeted D-amino acid oxidase, *Antioxid. Redox Signal.* 9 (2007) 807–16. doi:10.1089/ars.2007.1526.
- [57] I. Alim, R.E. Haskew-Layton, H. Aleyasin, H. Guo, R.R. Ratan, Spatial, temporal, and quantitative manipulation of intracellular hydrogen peroxide in cultured cells, *Methods Enzymol.* 547 (2014) 251–73. doi:10.1016/B978-0-12-801415-8.00014-X.
- [58] H. Guo, H. Aleyasin, S.S. Howard, B.C. Dickinson, V.S. Lin, R.E. Haskew-Layton, et al., Two-photon fluorescence imaging of intracellular hydrogen peroxide with chemoselective fluorescent probes, *J. Biomed. Opt.* 18 (2013) 106002. doi:10.1117/1.JBO.18.10.106002.
- [59] V. V. Belousov, A.F. Fradkov, K.A. Lukyanov, D.B. Staroverov, K.S. Shakhbazov, A. V. Terskikh, et al., Genetically encoded fluorescent indicator for intracellular hydrogen peroxide, *Nat. Methods.* 3 (2006) 281–6. doi:10.1038/nmeth866.
- [60] M.E. Matlashov, V. V. Belousov, E. Grigori, How Much H₂O₂ Is Produced by Recombinant D-Amino Acid Oxidase in Mammalian Cells?, *Antioxid. Redox Signal.* 20 (2014) 1039–44. doi:10.1089/ars.2013.5618.
- [61] M.E. Mangino, J.R. Brunner, Isolation and Partial Characterization of Xanthine Oxidase Associated with the Milk Fat Globule Membrane of Cows' Milk, *J. Dairy Sci.* 60 (1977) 841–850. doi:10.3168/jds.S0022-0302(77)83952-0.
- [62] T. Sawa, J. Wu, T. Akaike, H. Maeda, Tumor-targeting Chemotherapy by a Xanthine Oxidase-Polymer Conjugate That Generates Oxygen-free Radicals in Tumor Tissue, *Cancer Res.* 60 (2000) 666–671.
- [63] S.A.M. van Stroe-Biezen, A.P.M. Janssen, L.J.J. Janssen, A kinetic study of soluble glucose oxidase using a rotating-disc electrode, *Bioelectrochemistry Bioenerg.* 33 (1994) 55–60. doi:10.1016/0302-4598(94)87032-2.
- [64] L. Pollegioni, B. Langkau, W. Tischer, S. Ghisla, M. Pilone, Kinetic mechanism of D-amino acid oxidases from *Rhodotorula gracilis* and *Trigonopsis variabilis*, *J. Biol. Chem.* 268 (1993) 13850–13857.

- [65] T.-C. Cheong, E.P. Shin, E.-K. Kwon, J.-H. Choi, K.-K. Wang, P. Sharma, et al., Functional Manipulation of Dendritic Cells by Photoswitchable Generation of Intracellular Reactive Oxygen Species, *ACS Chem. Biol.* (2014). doi:10.1021/cb5009124.
- [66] C.C. Winterbourn, The challenges of using fluorescent probes to detect and quantify specific reactive oxygen species in living cells, *Biochim. Biophys. Acta.* 1840 (2014) 730–8. doi:10.1016/j.bbagen.2013.05.004.
- [67] E.W. Miller, A.E. Albers, A. Pralle, E.Y. Isacoff, C.J. Chang, Boronate-based fluorescent probes for imaging cellular hydrogen peroxide, *J. Am. Chem. Soc.* 127 (2005) 16652–9. doi:10.1021/ja054474f.
- [68] E.W. Miller, O. Tulyathan, O. Tulyanthan, E.Y. Isacoff, C.J. Chang, Molecular imaging of hydrogen peroxide produced for cell signaling, *Nat. Chem. Biol.* 3 (2007) 263–7. doi:10.1038/nchembio871.
- [69] A.R. Lippert, G.C. Van de Bittner, C.J. Chang, Boronate oxidation as a bioorthogonal reaction approach for studying the chemistry of hydrogen peroxide in living systems, *Acc. Chem. Res.* 44 (2011) 793–804. doi:10.1021/ar200126t.
- [70] B.C. Dickinson, C. Huynh, C.J. Chang, A palette of fluorescent probes with varying emission colors for imaging hydrogen peroxide signaling in living cells, *J. Am. Chem. Soc.* 132 (2010) 5906–15. doi:10.1021/ja1014103.
- [71] B.C. Dickinson, Y. Tang, Z. Chang, C.J. Chang, A nuclear-localized fluorescent hydrogen peroxide probe for monitoring sirtuin-mediated oxidative stress responses in vivo, *Chem. Biol.* 18 (2011) 943–8. doi:10.1016/j.chembiol.2011.07.005.
- [72] B.C. Dickinson, D. Srikun, C.J. Chang, Mitochondrial-targeted fluorescent probes for reactive oxygen species, *Curr. Opin. Chem. Biol.* 14 (2010) 50–6. doi:10.1016/j.cbpa.2009.10.014.
- [73] J. Zielonka, M. Zielonka, A. Sikora, J. Adamus, J. Joseph, M. Hardy, et al., Global profiling of reactive oxygen and nitrogen species in biological systems: high-throughput real-time analyses, *J. Biol. Chem.* 287 (2012) 2984–95. doi:10.1074/jbc.M111.309062.
- [74] J. Zielonka, A. Sikora, J. Joseph, B. Kalyanaraman, Peroxynitrite is the major species formed from different flux ratios of co-generated nitric oxide and superoxide: direct reaction with boronate-based fluorescent probe, *J. Biol. Chem.* 285 (2010) 14210–6. doi:10.1074/jbc.M110.110080.
- [75] A. Sikora, J. Zielonka, M. Lopez, J. Joseph, B. Kalyanaraman, Direct oxidation of boronates by peroxynitrite: mechanism and implications in fluorescence imaging of peroxynitrite, *Free Radic. Biol. Med.* 47 (2009) 1401–7. doi:10.1016/j.freeradbiomed.2009.08.006.
- [76] K.A. Lukyanov, V. V. Belousov, Genetically encoded fluorescent redox sensors, *Biochim. Biophys. Acta.* 1840 (2014) 745–56. doi:10.1016/j.bbagen.2013.05.030.
- [77] S. Pouvreau, Genetically encoded reactive oxygen species (ROS) and redox indicators, *Biotechnol. J.* 9 (2014) 282–93. doi:10.1002/biot.201300199.

- [78] S. García-Santamarina, S. Boronat, E. Hidalgo, Reversible cysteine oxidation in hydrogen peroxide sensing and signal transduction, *Biochemistry*. 53 (2014) 2560–80. doi:10.1021/bi401700f.
- [79] M. Gutscher, M.C. Sobotta, G.H. Wabnitz, S. Ballikaya, A.J. Meyer, Y. Samstag, et al., Proximity-based protein thiol oxidation by H₂O₂-scavenging peroxidases, *J. Biol. Chem.* 284 (2009) 31532–40. doi:10.1074/jbc.M109.059246.
- [80] A. Hernández-Barrera, C. Quinto, E.A. Johnson, H.-M. Wu, A.Y. Cheung, L. Cárdenas, Using hyper as a molecular probe to visualize hydrogen peroxide in living plant cells: a method with virtually unlimited potential in plant biology, *Methods Enzymol.* 527 (2013) 275–90. doi:10.1016/B978-0-12-405882-8.00015-5.
- [81] P. Niethammer, C. Grabher, A.T. Look, T.J. Mitchison, A tissue-scale gradient of hydrogen peroxide mediates rapid wound detection in zebrafish, *Nature*. 459 (2009) 996–9. doi:10.1038/nature08119.
- [82] J.L. Sartoretto, H. Kalwa, M.D. Pluth, S.J. Lippard, T. Michel, Hydrogen peroxide differentially modulates cardiac myocyte nitric oxide synthesis, *Proc. Natl. Acad. Sci. U. S. A.* 108 (2011) 15792–7. doi:10.1073/pnas.1111331108.
- [83] R. Ameziane-El-Hassani, M. Boufraqueh, O. Lagente-Chevallier, U. Weyemi, M. Talbot, D. Métivier, et al., Role of H₂O₂ in RET/PTC1 chromosomal rearrangement produced by ionizing radiation in human thyroid cells, *Cancer Res.* 70 (2010) 4123–32. doi:10.1158/0008-5472.CAN-09-4336.
- [84] A. Espinosa, A. García, S. Härtel, C. Hidalgo, E. Jaimovich, NADPH oxidase and hydrogen peroxide mediate insulin-induced calcium increase in skeletal muscle cells, *J. Biol. Chem.* 284 (2009) 2568–75. doi:10.1074/jbc.M804249200.
- [85] B.Y. Jin, J.L. Sartoretto, V.N. Gladyshev, T. Michel, Endothelial nitric oxide synthase negatively regulates hydrogen peroxide-stimulated AMP-activated protein kinase in endothelial cells, *Proc. Natl. Acad. Sci. U. S. A.* 106 (2009) 17343–8. doi:10.1073/pnas.0907409106.
- [86] M.P. Brynildsen, J.A. Winkler, C.S. Spina, I.C. Macdonald, J.J. Collins, Potentiating antibacterial activity by predictably enhancing endogenous microbial ROS production, *Nat. Biotechnol.* 31 (2013) 160–5. doi:10.1038/nbt.2458.
- [87] S.C. Albrecht, A.G. Barata, J. Grosshans, A.A. Teleman, T.P. Dick, In vivo mapping of hydrogen peroxide and oxidized glutathione reveals chemical and regional specificity of redox homeostasis, *Cell Metab.* 14 (2011) 819–29. doi:10.1016/j.cmet.2011.10.010.
- [88] M. Bode, S. Longen, B. Morgan, V. Peleh, T.P. Dick, K. Bihlmaier, et al., Inaccurately assembled cytochrome c oxidase can lead to oxidative stress-induced growth arrest, *Antioxid. Redox Signal.* 18 (2013) 1597–612. doi:10.1089/ars.2012.4685.

- [89] A.G. Barata, T.P. Dick, In vivo imaging of H₂O₂ production in *Drosophila*, in: E. Cadenas, L. Packer (Eds.), *Hydrog. Peroxide Cell Signaling, Part A*, Elsevier Academic Press Inc., San Diego, 2013: pp. 61–82. doi:10.1016/B978-0-12-405883-5.00004-1.
- [90] N. Castelein, M. Muschol, I. Dhondt, H. Cai, W.H. De Vos, N.A. Dencher, et al., Mitochondrial efficiency is increased in axenically cultured *Caenorhabditis elegans*, *Exp. Gerontol.* 56 (2014) 26–36. doi:10.1016/j.exger.2014.02.009.
- [91] J.B. Lim, K.A. Barker, B.K. Huang, H.D. Sikes, In-depth characterization of the fluorescent signal of HyPer, a probe for hydrogen peroxide, in bacteria exposed to external oxidative stress, *J. Microbiol. Methods.* 106 (2014) 33–39. doi:10.1016/j.mimet.2014.07.038.
- [92] L.C. Seaver, J.A. Imlay, Alkyl hydroperoxide reductase is the primary scavenger of endogenous hydrogen peroxide in *Escherichia coli*, *J. Bacteriol.* 183 (2001) 7173–81. doi:10.1128/JB.183.24.7173-7181.2001.
- [93] K.N. Markvicheva, D.S. Bilan, N.M. Mishina, A.Y. Gorokhovatsky, L.M. Vinokurov, S. Lukyanov, et al., A genetically encoded sensor for H₂O₂ with expanded dynamic range, *Bioorg. Med. Chem.* 19 (2011) 1079–84. doi:10.1016/j.bmc.2010.07.014.
- [94] D.S. Bilan, L. Pase, L. Joosen, A.Y. Gorokhovatsky, Y.G. Ermakova, T.W.J. Gadella, et al., HyPer-3: A Genetically Encoded H₂O₂ Probe with Improved Performance for Ratiometric and Fluorescence Lifetime Imaging, *ACS Chem. Biol.* 8 (2013) 535–542. doi:10.1021/cb300625g.
- [95] J. Kiefer, N. Ebel, E. Schlücker, A. Leipertz, Characterization of *Escherichia coli* suspensions using UV/Vis/NIR absorption spectroscopy, *Anal. Methods.* 2 (2010) 123–128. doi:10.1039/b9ay00185a.
- [96] C. Lee, S.M. Lee, P. Mukhopadhyay, S.J. Kim, S.C. Lee, W.-S. Ahn, et al., Redox regulation of OxyR requires specific disulfide bond formation involving a rapid kinetic reaction path, *Nat. Struct. Mol. Biol.* 11 (2004) 1179–85. doi:10.1038/nsmb856.
- [97] F. Capaldo-Kimball, S.D. Barbour, Involvement of Recombination Genes in Growth and Viability of *Escherichia coli* K-12, *J. Bacteriol.* 106 (1971) 204–212.
- [98] J.A. Imlay, The molecular mechanisms and physiological consequences of oxidative stress: lessons from a model bacterium, *Nat. Rev. Microbiol.* 11 (2013) 443–54. doi:10.1038/nrmicro3032.
- [99] H.E. Schellhorn, H.M. Hassan, Transcriptional regulation of *katE* in *Escherichia coli* K-12, *J. Bacteriol.* 170 (1988) 4286–4292.
- [100] M.F. Christman, G. Storz, B.N. Ames, OxyR, a positive regulator of hydrogen peroxide-inducible genes in *Escherichia coli* and *Salmonella typhimurium*, is homologous to a family of bacterial regulatory proteins, *Proc. Natl. Acad. Sci.* 86 (1989) 3484–3488. doi:10.1073/pnas.86.10.3484.
- [101] M.A. Noble, C.S. Miles, S.K. Chapman, D.A. Lysek, A.C. MacKay, G.A. Reid, et al., Roles of key active-site residues in flavocytochrome P450 BM3, *Biochem. J.* 339 (1999) 371–9.

- [102] C. Brewer, J. Peterson, Single turnover kinetics of the reaction between oxycytochrome P-450cam and reduced putidaredoxin, *J. Biol. Chem.* 263 (1988) 791–798.
- [103] P.K. Powell, I. Wolf, R. Jin, J.M. Lasker, Metabolism of Arachidonic Acid to 20-Hydroxy-5,8,11,14-eicosatetraenoic Acid by P450 Enzymes in Human Liver: Involvement of CYP4F2 and CYP4A11, *J. Pharmacol. Exp. Ther.* 285 (1998) 1327–1336.
- [104] I.B. Tsyrllov, I.S. Goldfarb, H. V Gelboin, Enzyme-kinetic and immunochemical characteristics of mouse cDNA-expressed, microsomal, and purified CYP1A1 and CYP1A2, *Arch. Biochem. Biophys.* 307 (1993) 259–66. doi:10.1006/abbi.1993.1588.
- [105] J.P. Clark, C.S. Miles, C.G. Mowat, M.D. Walkinshaw, G.A. Reid, S.N. Daff, et al., The role of Thr268 and Phe393 in cytochrome P450 BM3, *J. Inorg. Biochem.* 100 (2006) 1075–90. doi:10.1016/j.jinorgbio.2005.11.020.
- [106] C.J.C. Whitehouse, S.G. Bell, W. Yang, J.A. Yorke, C.F. Blanford, A.J.F. Strong, et al., A highly active single-mutation variant of P450BM3 (CYP102A1), *Chembiochem.* 10 (2009) 1654–6. doi:10.1002/cbic.200900279.
- [107] W.-C. Huang, A.C.G. Westlake, J.-D. Maréchal, M.G. Joyce, P.C.E. Moody, G.C.K. Roberts, Filling a hole in cytochrome P450 BM3 improves substrate binding and catalytic efficiency, *J. Mol. Biol.* 373 (2007) 633–51. doi:10.1016/j.jmb.2007.08.015.
- [108] P. Meinhold, M.W. Peters, A. Hartwick, A.R. Hernandez, F.H. Arnold, Engineering Cytochrome P450 BM3 for Terminal Alkane Hydroxylation, *Adv. Synth. Catal.* 348 (2006) 763–772. doi:10.1002/adsc.200505465.
- [109] R. Fasan, M.M. Chen, N.C. Crook, F.H. Arnold, Engineered Alkane-Hydroxylating Cytochrome P450BM3 Exhibiting Nativelike Catalytic Properties, *Angew. Chemie.* 119 (2007) 8566–8570. doi:10.1002/ange.200702616.
- [110] A. Seifert, S. Vomund, K. Grohmann, S. Kriening, V.B. Urlacher, S. Laschat, et al., Rational design of a minimal and highly enriched CYP102A1 mutant library with improved regio-, stereo- and chemoselectivity, *Chembiochem.* 10 (2009) 853–61. doi:10.1002/cbic.200800799.
- [111] P.S. Coelho, E.M. Brustad, A. Kannan, F.H. Arnold, Olefin cyclopropanation via carbene transfer catalyzed by engineered cytochrome P450 enzymes., *Science.* 339 (2013) 307–10. doi:10.1126/science.1231434.
- [112] M.G. Shapiro, G.G. Westmeyer, P.A. Romero, J.O. Szablowski, B. Küster, A. Shah, et al., Directed evolution of a magnetic resonance imaging contrast agent for noninvasive imaging of dopamine, *Nat. Biotechnol.* 28 (2010) 264–70. doi:10.1038/nbt.1609.
- [113] C.J.C. Whitehouse, S.G. Bell, L.-L. Wong, P450(BM3) (CYP102A1): connecting the dots, *Chem. Soc. Rev.* 41 (2012) 1218–60. doi:10.1039/c1cs15192d.

- [114] C. Jung, Leakage in Cytochrome P450 Reactions in relation to Protein Structural Properties, in: A. Sigel, H. Sigel, R.K.O. Sigel (Eds.), *Ubiquitous Roles Cytochrome P450 Proteins*, John Wiley & Sons Ltd, Chichester, England, 2007: pp. 187–234.
- [115] M.W. Peters, P. Meinhold, A. Glieder, F.H. Arnold, Regio- and enantioselective alkane hydroxylation with engineered cytochromes P450 BM-3, *J. Am. Chem. Soc.* 125 (2003) 13442–50. doi:10.1021/ja0303790.
- [116] M.B. Murataliev, M. Klein, A. Fulco, R. Feyereisen, Functional interactions in cytochrome P450BM3: flavin semiquinone intermediates, role of NADP(H), and mechanism of electron transfer by the flavoprotein domain, *Biochemistry.* 36 (1997) 8401–12. doi:10.1021/bi970026b.
- [117] C.F. Oliver, S. Modi, W.U. Primrose, L.-Y. Lian, G.C.K. Robert, Engineering the substrate specificity of *Bacillus megaterium* cytochrome P-450 BM3: hydroxylation of alkyl trimethylammonium compounds, *Biochem. J.* 327 (1997) 537–544.
- [118] M. Eigen, G.G. Hammes, Elementary Steps in Enzyme Reactions (as Studied by Relaxation Spectrometry), in: F.F. Nord (Ed.), *Adv. Enzymol. Relat. Areas Mol. Biol.*, John Wiley & Sons, Inc., Hoboken, NJ, USA, 1963: pp. 1–38. doi:10.1002/9780470122709.ch1.
- [119] A. Munro, D. Leys, K. McLean, K. Marshall, T. Ost, S. Daff, et al., P450 BM3: the very model of a modern flavocytochrome, *Trends Biochem. Sci.* 27 (2002) 250–257. doi:10.1016/S0968-0004(02)02086-8.
- [120] P.C. Loewen, B.L. Triggs, C.S. George, B.E. Hrabarchuk, Genetic mapping of *katG*, a locus that affects synthesis of the bifunctional catalase-peroxidase hydroperoxidase I in *Escherichia coli*, *J. Bacteriol.* 162 (1985) 661–7.
- [121] P.C. Loewen, J. Switala, Purification and characterization of catalase HPII from *Escherichia coli* K12, *Biochem. Cell Biol.* 64 (1986) 638–46.
- [122] F.S. Jacobson, R.W. Morgan, M.F. Christman, B.N. Ames, An alkyl hydroperoxide reductase from *Salmonella typhimurium* involved in the defense of DNA against oxidative damage. Purification and properties., *J. Biol. Chem.* 264 (1989) 1488–96.
- [123] C.J.C. Whitehouse, W. Yang, J.A. Yorke, B.C. Rowlatt, A.J.F. Strong, C.F. Blanford, et al., Structural basis for the properties of two single-site proline mutants of CYP102A1 (P450BM3), *Chembiochem.* 11 (2010) 2549–56. doi:10.1002/cbic.201000421.
- [124] J.D. Bloom, S.T. Labthavikul, C.R. Otey, F.H. Arnold, Protein stability promotes evolvability, *Proc. Natl. Acad. Sci. U. S. A.* 103 (2006) 5869–74. doi:10.1073/pnas.0510098103.
- [125] R. Fasan, Y.T. Meharena, C.D. Snow, T.L. Poulos, F.H. Arnold, Evolutionary history of a specialized p450 propane monooxygenase, *J. Mol. Biol.* 383 (2008) 1069–80. doi:10.1016/j.jmb.2008.06.060.

- [126] L. Pollegioni, P. Motta, G. Molla, L-amino acid oxidase as biocatalyst: a dream too far?, *Appl. Microbiol. Biotechnol.* 97 (2013) 9323–41. doi:10.1007/s00253-013-5230-1.
- [127] G.S. Hossain, J. Li, H. Shin, G. Du, L. Liu, J. Chen, L-Amino acid oxidases from microbial sources: types, properties, functions, and applications, *Appl. Microbiol. Biotechnol.* 98 (2014) 1507–15. doi:10.1007/s00253-013-5444-2.
- [128] Y. Zhao, X. Yang, W. Lu, H. Liao, F. Liao, Uricase based methods for determination of uric acid in serum, *Microchim. Acta.* 164 (2008) 1–6. doi:10.1007/s00604-008-0044-z.
- [129] L. Harrold, New developments in gout, *Curr. Opin. Rheumatol.* 25 (2013) 304–9. doi:10.1097/BOR.0b013e32835fd5e5.
- [130] M. Fairhead, L. Thöny-Meyer, Bacterial tyrosinases: old enzymes with new relevance to biotechnology, *N. Biotechnol.* 29 (2012) 183–91. doi:10.1016/j.nbt.2011.05.007.
- [131] P. Goswami, S.S.R. Chinnadayyala, M. Chakraborty, A.K. Kumar, A. Kakoti, An overview on alcohol oxidases and their potential applications, *Appl. Microbiol. Biotechnol.* 97 (2013) 4259–75. doi:10.1007/s00253-013-4842-9.
- [132] C. Gao, C. Ma, P. Xu, Biotechnological routes based on lactic acid production from biomass, *Biotechnol. Adv.* 29 (2011) 930–9. doi:10.1016/j.biotechadv.2011.07.022.
- [133] N.J. Turner, Enantioselective oxidation of C-O and C-N bonds using oxidases, *Chem. Rev.* 111 (2011) 4073–87. doi:10.1021/cr200111v.
- [134] L. Sun, M. Yagasaki, Screen for oxidases by detection of hydrogen peroxide with horseradish peroxidase, in: F.H. Arnold, G. Georgiou (Eds.), *Methods Mol. Biol.*, Humana Press, Clifton, NJ, 2003: pp. 177–82. doi:10.1385/1-59259-396-8:177.
- [135] J.B. Lim, H.D. Sikes, Use of a genetically encoded hydrogen peroxide sensor for whole cell screening of enzyme activity, *Protein Eng. Des. Sel.* 28 (2015) 79–83. doi:10.1093/protein/gzv003.
- [136] J.C. Wilks, J.L. Slonczewski, pH of the cytoplasm and periplasm of *Escherichia coli*: rapid measurement by green fluorescent protein fluorimetry, *J. Bacteriol.* 189 (2007) 5601–7. doi:10.1128/JB.00615-07.
- [137] H.J. Janßen, A. Steinbüchel, Fatty acid synthesis in *Escherichia coli* and its applications towards the production of fatty acid based biofuels, *Biotechnol. Biofuels.* 7 (2014) 7. doi:10.1186/1754-6834-7-7.
- [138] X. Lu, H. Vora, C. Khosla, Overproduction of free fatty acids in *E. coli*: implications for biodiesel production, *Metab. Eng.* 10 (2008) 333–9. doi:10.1016/j.ymben.2008.08.006.
- [139] A. Díaz, P.C. Loewen, I. Fita, X. Carpena, Thirty years of heme catalases structural biology, *Arch. Biochem. Biophys.* 525 (2012) 102–10. doi:10.1016/j.abb.2011.12.011.

- [140] T.W.B. Ost, C.S. Miles, A.W. Munro, J. Murdoch, G.A. Reid, S.K. Chapman, Phenylalanine 393 Exerts Thermodynamic Control over the Heme of Flavocytochrome P450 BM3, *Biochemistry*. 40 (2001) 13421–13429. doi:10.1021/bi010716m.
- [141] O. Roitel, N.S. Scrutton, A.W. Munro, Electron transfer in flavocytochrome P450 BM3: kinetics of flavin reduction and oxidation, the role of cysteine 999, and relationships with mammalian cytochrome P450 reductase, *Biochemistry*. 42 (2003) 10809–21. doi:10.1021/bi034562h.
- [142] M.G. Joyce, H.M. Girvan, A.W. Munro, D. Leys, A single mutation in cytochrome P450 BM3 induces the conformational rearrangement seen upon substrate binding in the wild-type enzyme, *J. Biol. Chem.* 279 (2004) 23287–93. doi:10.1074/jbc.M401717200.
- [143] G. Millonig, I. Ganzleben, T. Peccerella, G. Casanovas, L. Brodziak-Jarosz, K. Breitkopf-Heinlein, et al., Sustained Submicromolar H₂O₂ Levels Induce Hecpudin via Signal Transducer and Activator of Transcription 3 (STAT3), *J. Biol. Chem.* 287 (2012) 37472–37482. doi:10.1074/jbc.M112.358911.
- [144] D.P. Jones, Radical-free biology of oxidative stress, *Am. J. Physiol. Cell Physiol.* 295 (2008) C849–68. doi:10.1152/ajpcell.00283.2008.
- [145] C.F. Ng, F.Q. Schafer, G.R. Buettner, V.G.J. Rodgers, The rate of cellular hydrogen peroxide removal shows dependency on GSH: mathematical insight into in vivo H₂O₂ and GPx concentrations, *Free Radic. Res.* 41 (2007) 1201–11. doi:10.1080/10715760701625075.
- [146] J.W. Forstrom, F.H. Stults, A.L. Tappel, Rat liver cytosolic glutathione peroxidase: Reactivity with linoleic acid hydroperoxide and cumene hydroperoxide, *Arch. Biochem. Biophys.* 193 (1979) 51–55. doi:10.1016/0003-9861(79)90007-9.
- [147] G.C. Yeh, S.J. Occhipinti, K.H. Cowan, B.A. Chabner, C.E. Myers, Adriamycin Resistance in Human Tumor Cells Associated with Marked Alterations in the Regulation of the Hexose Monophosphate Shunt and Its Response to Oxidant Stress, *Cancer Res.* 47 (1987) 5994–5999.
- [148] T.-S. Chang, W. Jeong, H.A. Woo, S.M. Lee, S. Park, S.G. Rhee, Characterization of mammalian sulfiredoxin and its reactivation of hyperoxidized peroxiredoxin through reduction of cysteine sulfinic acid in the active site to cysteine, *J. Biol. Chem.* 279 (2004) 50994–1001. doi:10.1074/jbc.M409482200.
- [149] F.M. Low, M.B. Hampton, A. V Peskin, C.C. Winterbourn, Peroxiredoxin 2 functions as a noncatalytic scavenger of low-level hydrogen peroxide in the erythrocyte, *Blood*. 109 (2007) 2611–7. doi:10.1182/blood-2006-09-048728.
- [150] K. Sasaki, S. Bannai, N. Makino, Kinetics of hydrogen peroxide elimination by human umbilical vein endothelial cells in culture, *Biochim. Biophys. Acta.* 1380 (1998) 275–288. doi:10.1016/S0304-4165(97)00152-9.
- [151] M.M. Gallogly, J.J. Mieyal, Mechanisms of reversible protein glutathionylation in redox signaling and oxidative stress, *Curr. Opin. Pharmacol.* 7 (2007) 381–91. doi:10.1016/j.coph.2007.06.003.

- [152] H.-W. Lo, G.R. Antoun, F. Ali-Osman, The human glutathione S-transferase P1 protein is phosphorylated and its metabolic function enhanced by the Ser/Thr protein kinases, cAMP-dependent protein kinase and protein kinase C, in glioblastoma cells, *Cancer Res.* 64 (2004) 9131–8. doi:10.1158/0008-5472.CAN-04-0283.
- [153] M.J. Peltoniemi, A.-R. Karala, J.K. Jurvansuu, V.L. Kinnula, L.W. Ruddock, Insights into deglutathionylation reactions: Different intermediates in the glutaredoxin and protein disulfide isomerase catalyzed reactions are defined by the gamma-linkage present in glutathione, *J. Biol. Chem.* 281 (2006) 33107–14. doi:10.1074/jbc.M605602200.
- [154] U. Srinivasan, P.A. Mieyal, J.J. Mieyal, pH profiles indicative of rate-limiting nucleophilic displacement in thioltransferase catalysis, *Biochemistry.* 36 (1997) 3199–206. doi:10.1021/bi962017t.
- [155] G.B. Henderson, N.J. Murgolo, J. Kuriyan, K. Osapay, D. Kominos, A. Berry, et al., Engineering the substrate specificity of glutathione reductase toward that of trypanothione reduction, *Proc. Natl. Acad. Sci.* 88 (1991) 8769–8773. doi:10.1073/pnas.88.19.8769.
- [156] E. Arner, L. Zhong, A. Holmgren, Preparation and assay of mammalian thioredoxin and thioredoxin reductase, in: *Oxid. Antioxidants, Pt B*, Academic Press Inc., San Diego, CA, 1999: pp. 226–239.
- [157] M. Kemp, Y.-M. Go, D.P. Jones, Nonequilibrium thermodynamics of thiol/disulfide redox systems: a perspective on redox systems biology, *Free Radic. Biol. Med.* 44 (2008) 921–37. doi:10.1016/j.freeradbiomed.2007.11.008.
- [158] N. Kondo, Y. Ishii, Y.-W. Kwon, M. Tanito, H. Horita, Y. Nishinaka, et al., Redox-Sensing Release of Human Thioredoxin from T Lymphocytes with Negative Feedback Loops, *J. Immunol.* 172 (2003) 442–448. doi:10.4049/jimmunol.172.1.442.
- [159] G.G. Martinovich, S.N. Cherenkevich, H. Sauer, Intracellular redox state: towards quantitative description, *Eur. Biophys. J.* 34 (2005) 937–42. doi:10.1007/s00249-005-0470-3.
- [160] F.Q. Schafer, G.R. Buettner, Redox environment of the cell as viewed through the redox state of the glutathione disulfide/glutathione couple, *Free Radic. Biol. Med.* 30 (2001) 1191–1212. doi:10.1016/S0891-5849(01)00480-4.
- [161] H. Yue, M. Brown, J. Knowles, H. Wang, D.S. Broomhead, D.B. Kell, Insights into the behaviour of systems biology models from dynamic sensitivity and identifiability analysis: a case study of an NF-kappaB signalling pathway., *Mol. Biosyst.* 2 (2006) 640–9. doi:10.1039/b609442b.
- [162] L.C. Seaver, J.A. Imlay, Hydrogen peroxide fluxes and compartmentalization inside growing *Escherichia coli*, *J. Bacteriol.* 183 (2001) 7182–9. doi:10.1128/JB.183.24.7182-7189.2001.
- [163] L. Zhao, C.D. Kroenke, J. Song, D. Piwnica-Worms, J.J.H. Ackerman, J.J. Neil, Intracellular water-specific MR of microbead-adherent cells: the HeLa cell intracellular water exchange lifetime, *NMR Biomed.* 21 (2008) 159–64. doi:10.1002/nbm.1173.

- [164] S.A.M. van Stroe-Biezen, F.M. Everaerts, L.J.J. Janssen, R.A. Tacke, Diffusion coefficients of oxygen, hydrogen peroxide and glucose in a hydrogel, *Anal. Chim. Acta.* 273 (1993) 553–560. doi:10.1016/0003-2670(93)80202-V.
- [165] W.M. Deen, *Analysis of Transport Phenomena*, 2nd ed., Oxford University Press, New York, 2012.
- [166] Z.A. Wood, L.B. Poole, R.R. Hantgan, P.A. Karplus, Dimers to Doughnuts: Redox-Sensitive Oligomerization of 2-Cysteine Peroxiredoxins, *Biochemistry.* 41 (2002) 5493–5504. doi:10.1021/bi012173m.
- [167] A. Einstein, Über die von der molekularkinetischen Theorie der Wärme geforderte Bewegung von in ruhenden Flüssigkeiten suspendierten Teilchen, *Ann. Phys.* 322 (1905) 549–560. doi:10.1002/andp.19053220806.
- [168] M. von Smoluchowski, Zur kinetischen Theorie der Brownschen Molekularbewegung und der Suspensionen, *Ann. Phys.* 326 (1906) 756–780. doi:10.1002/andp.190632261405.
- [169] J.R. Winther, C. Thorpe, Quantification of thiols and disulfides, *Biochim. Biophys. Acta.* 1840 (2014) 838–46. doi:10.1016/j.bbagen.2013.03.031.
- [170] T.P. Szatrowski, C.F. Nathan, Production of Large Amounts of Hydrogen Peroxide by Human Tumor Cells, *Cancer Res.* 51 (1991) 794–798.
- [171] B. Chance, H. Sies, A. Boveris, Hydroperoxide metabolism in mammalian organs, *Physiol Rev.* 59 (1979) 527–605.
- [172] N.M. Mishina, A.S. Mishin, Y. Belyaev, E.A. Bogdanova, S. Lukyanov, C. Schultz, et al., Live-Cell STED Microscopy with Genetically Encoded Biosensor, *Nano Lett.* (2015). doi:10.1021/nl504710z.
- [173] D. Srikun, A.E. Albers, C.I. Nam, A.T. Iavarone, C.J. Chang, Organelle-targetable fluorescent probes for imaging hydrogen peroxide in living cells via SNAP-Tag protein labeling, *J. Am. Chem. Soc.* 132 (2010) 4455–65. doi:10.1021/ja100117u.
- [174] M. Malinouski, Y. Zhou, V. V. Belousov, D.L. Hatfield, V.N. Gladyshev, Hydrogen peroxide probes directed to different cellular compartments, *PLoS One.* 6 (2011) e14564. doi:10.1371/journal.pone.0014564.
- [175] H.S. Marinho, C. Real, L. Cyrne, H. Soares, F. Antunes, Hydrogen peroxide sensing, signaling and regulation of transcription factors., *Redox Biol.* 2 (2014) 535–62. doi:10.1016/j.redox.2014.02.006.
- [176] I. Mehmeti, S. Lortz, S. Lenzen, The H₂O₂-sensitive HyPer protein targeted to the endoplasmic reticulum as a mirror of the oxidizing thiol-disulfide milieu., *Free Radic. Biol. Med.* 53 (2012) 1451–8. doi:10.1016/j.freeradbiomed.2012.08.010.
- [177] W. Gehrman, M. Elsner, A specific fluorescence probe for hydrogen peroxide detection in peroxisomes, *Free Radic. Res.* 45 (2011) 501–6. doi:10.3109/10715762.2011.560148.

- [178] J. Weller, K.M. Kizina, K. Can, G. Bao, M. Müller, Response properties of the genetically-encoded optical H₂O₂ sensor Hyper, *Free Radic. Biol. Med.* 76 (2014) 227–241. doi:10.1016/j.freeradbiomed.2014.07.045.
- [179] B. Enyedi, M. Zana, Á. Donkó, M. Geiszt, Spatial and temporal analysis of NADPH oxidase-generated hydrogen peroxide signals by novel fluorescent reporter proteins., *Antioxid. Redox Signal.* 19 (2013) 523–34. doi:10.1089/ars.2012.4594.
- [180] A.K. Gillingham, S. Munro, The PACT domain, a conserved centrosomal targeting motif in the coiled-coil proteins AKAP450 and pericentrin, *EMBO Rep.* 1 (2000) 524–9. doi:10.1093/embo-reports/kvd105.
- [181] A.F. Straight, Mitosis in Living Budding Yeast: Anaphase A But No Metaphase Plate, *Science* (80-.). 277 (1997) 574–578. doi:10.1126/science.277.5325.574.

Appendix A

The following contains additional data corresponding to Chapter 2.

Table A.1. P-values of Student's t-tests comparing time constants of H₂O₂ uptake by *E. coli*.

Compared strains	BL21(DE3) vs DH5α	BL21(DE3) vs DH5α, no HyPer	DH5α vs DH5α, no HyPer
p-value, trial #1	1.6 x 10 ⁻⁵	1.8 x 10 ⁻¹¹	2.2 x 10 ⁻⁷
p-value, trial #2	3.4 x 10 ⁻⁹	1.2 x 10 ⁻¹²	5.4 x 10 ⁻⁴

Table A.2. P-values of Welch's t-tests comparing dose-response curves of F500/F420 and fold change versus [H₂O₂] for BL21 (DE3). P-values less than 0.05 are highlighted in yellow.

[H ₂ O ₂] (μM)	60 x 10 ⁶ vs 240 x 10 ⁶ cells		60 x 10 ⁶ vs 480 x 10 ⁶ cells		240 x 10 ⁶ vs 480 x 10 ⁶ cells	
	F500/F420	Fold change	F500/F420	Fold change	F500/F420	Fold change
20	0.007	0.0003	0.004	0.00003	0.001	0.0003
10	0.007	0.002	0.010	0.0002	0.034	0.024
5	0.022	0.007	0.025	0.001	0.089	0.026
3	0.006	0.013	0.014	0.008	0.089	0.039
2.5	0.042	0.004	0.142	0.004	0.012	0.026
2	0.107	0.010	0.684	0.008	0.010	0.030
1.5	0.537	0.018	0.116	0.005	0.011	0.221
1	0.071	0.034	0.005	0.008	0.012	0.043
0	0.024	-	0.002	-	0.010	-

Table A.3. P-values of Welch's t-tests comparing dose-response curves of F500/F420 and fold change versus amount of H₂O₂ normalized by number of cells for BL21 (DE3). P-values less than 0.05 are highlighted in yellow.

nmol H ₂ O ₂ /60 x 10 ⁶ cells	60 x 10 ⁶ vs 240 x 10 ⁶ cells		60 x 10 ⁶ vs 480 x 10 ⁶ cells		240 x 10 ⁶ vs 480 x 10 ⁶ cells	
	F500/F420	Fold change	F500/F420	Fold change	F500/F420	Fold change
1	0.059	0.155	-	-	-	-
0.5	0.005	0.050	0.013	0.277	0.96	0.070
0.25	-	-	-	-	0.0002	0.762
0.125	-	-	-	-	0.001	0.099
0.075	-	-	-	-	0.006	0.027
0.05	-	-	-	-	0.001	0.242
0	0.024	-	0.002	-	0.010	-

Table A.4. P-values of Welch's t-tests comparing dose-response curves of F500/F420 and fold change versus [H₂O₂] for DH5 α . P-values less than 0.05 are highlighted in yellow.

[H ₂ O ₂] (μ M)	60 x 10 ⁶ vs 240 x 10 ⁶ cells		60 x 10 ⁶ vs 480 x 10 ⁶ cells		240 x 10 ⁶ vs 480 x 10 ⁶ cells	
	F500/F420	Fold change	F500/F420	Fold change	F500/F420	Fold change
20	0.020	0.023	0.003	0.002	0.023	0.013
10	0.025	0.021	0.011	0.015	0.715	0.038
5	0.014	0.004	0.013	0.001	0.595	0.045
3	0.040	0.017	0.067	0.012	0.430	0.021
2.5	0.039	0.010	0.151	0.008	0.373	0.035
2	0.065	0.008	0.364	0.006	0.315	0.038
1.5	0.176	0.009	0.843	0.006	0.298	0.038
1	0.963	0.005	0.251	0.001	0.271	0.173
0	0.039	-	0.093	-	0.210	-

Table A.5. P-values of Welch's t-tests comparing dose-response curves of F500/F420 and fold change versus amount of H₂O₂ normalized by number of cells for DH5 α . P-values less than 0.05 are highlighted in yellow.

nmol H ₂ O ₂ /60 x 10 ⁶ cells	60 x 10 ⁶ vs 240 x 10 ⁶ cells		60 x 10 ⁶ vs 480 x 10 ⁶ cells		240 x 10 ⁶ vs 480 x 10 ⁶ cells	
	F500/F420	Fold change	F500/F420	Fold change	F500/F420	Fold change
1	0.870	0.077	-	-	-	-
0.5	0.240	0.277	0.013	0.087	0.956	0.210
0.25	-	-	-	-	0.0002	0.696
0.125	-	-	-	-	0.0008	0.526
0.075	-	-	-	-	0.006	0.193
0.05	-	-	-	-	0.001	0.065
0	0.039	-	0.002	-	0.010	-

Table A.6. P-values of Student's t-tests comparing parameters of Hill equation fitted to dose-response curves of BL21 (DE3) and DH5 α . P-values less than 0.05 are highlighted in yellow. Equation was fit to dose-response curves measured using 60 x 10⁶ cells and using the raw ratio as the signal.

Parameter	P-value
Dynamic range ($[F500/F420_{max}]/[F500/F420_{basal}]$)	0.0044
$K_{1/2}$ (nmol H ₂ O ₂ /60 x 10 ⁶ cells)	0.042
Hill coefficient n	0.31

Appendix B

The following contains additional details on the methodologies and data corresponding to Chapter 3.

Code in Matlab was used to determine the effects of increased leakage on hydroxylation of palmitate. The differential equations used are shown below and were solved using ode15s. The parameters are shown in Table B.1. The parameters used for leakage, $k_{cat, leakage}$ and $K_{m, leakage}$, were taken from what we found for the WT enzyme in Chapter 3. The parameters used for hydroxylation were taken from [116,117]. k_{on} values ranging from 10^5 to $10^8 \text{ M}^{-1} \text{ s}^{-1}$ were tested and used together with K_d to calculate k_{off} . The equations are shown below.

$$\frac{d[NADPH]}{dt} = -\frac{k_{cat,leakage}[P450][NADPH]}{K_{m,leakage} + [NADPH]} - \frac{k_{cat,R-H}[P450 - RH][NADPH]}{K_{m,R-H} + [NADPH]}$$

$$\frac{d[R - OH]}{dt} = \frac{k_{cat,R-H}[P450 - RH][NADPH]}{K_{m,R-H} + [NADPH]}$$

$$\frac{d[R - H]}{dt} = -k_{on}[R - H][P450] + k_{off}[P450 - RH]$$

$$\frac{d[P450]}{dt} = -k_{on}[R - H][P450] + k_{off}[P450 - RH] + \frac{k_{cat,R-H}[P450 - RH][NADPH]}{K_{m,R-H} + [NADPH]}$$

$$\frac{d[P450 - RH]}{dt} = k_{on}[R - H][P450] - k_{off}[P450 - RH] - \frac{k_{cat,R-H}[P450 - RH][NADPH]}{K_{m,R-H} + [NADPH]}$$

Table B.1. Parameters used in the modeling of leakage and hydroxylation in Matlab.

Parameter	Value
$k_{cat, leakage} (\text{min}^{-1})$	11.92207
$k_{cat, R-H} (\text{min}^{-1})$	4080
$K_{m, leakage} (\mu\text{M})$	1.32105
$K_{m, R-H} (\mu\text{M})$	1.4
Initial NADPH concentration (μM)	100
Initial R-H concentration (μM)	100
Enzyme concentration (μM)	0.1

The code used in Matlab is shown below:

```
function out = P450_leakage3
```

```

ti = 0; % Start time in min
tf = 6; % Stop time in min
step = 0.001; % Time step in min
dt = step;
tspan = ti:dt:tf;
options=odeset('AbsTol',1E-10,'RelTol',1E-4,'maxstep',step);

WT_kcat_leakage = 11.92207; % min^-1
WT_Km_leakage = 1.32105; % uM
WT_kcat_RH = 81*60; % min^-1, for hydroxylation of palmitate;
http://www.biochemj.org/bj/327/0537/3270537.pdf
WT_Km_RH = 1.4; % uM, with respect to NADPH, for hydroxylation of
palmitate; http://pubs.acs.org/doi/pdfplus/10.1021/bi970026b
WT_Kd_RH = 5; % uM, with respect to palmitate;
http://www.biochemj.org/bj/327/0537/3270537.pdf
WT_kon_RH = 1e5*60*1e-6; % uM^-1 min^-1, typical estimate for kon
for a small molecule
WT_koff_RH = WT_Kd_RH*WT_kon_RH; % min^-1, calculated from Kd =
koff/kon

NADPH = 100; % uM
Enzyme = 0.1; % uM
ROH = 0; % uM
RH = 100; % uM
Enzyme_RH = 0; % uM

% Creation of array of parameters
k = zeros(9, 1);
k(1) = WT_kcat_leakage;
k(2) = WT_kcat_leakage*10;
k(3) = WT_kcat_leakage*100;
k(4) = WT_kcat_leakage*1000;
k(5) = WT_Km_leakage;
k(6) = WT_kcat_RH;
k(7) = WT_Km_RH;
k(8) = WT_kon_RH;
k(9) = WT_koff_RH;

% Creation of array of initial conditions
x0 = zeros(20, 1);
x0(1) = NADPH;
x0(2) = ROH;
x0(3) = RH;
x0(4) = Enzyme;
x0(5) = Enzyme_RH;
x0(6) = NADPH;
x0(7) = ROH;
x0(8) = RH;
x0(9) = Enzyme;
x0(10) = Enzyme_RH;
x0(11) = NADPH;
x0(12) = ROH;

```

```

x0(13) = RH;
x0(14) = Enzyme;
x0(15) = Enzyme_RH;
x0(16) = NADPH;
x0(17) = ROH;
x0(18) = RH;
x0(19) = Enzyme;
x0(20) = Enzyme_RH;

% Solving of differential equations using ode15s
tic
[t x]=ode15s(@crank,tspan,x0,options,k);
toc
out = [t, x];

% Recording of final results
filename = 'P450_leakage.xlsx';
xlswrite(filename,x,1,'B3');
xlswrite(filename,t,1,'A3');

% Reset initial values to try kon = 1e6 M^-1 s^-1
x0(1) = NADPH;
x0(2) = ROH;
x0(3) = RH;
x0(4) = Enzyme;
x0(5) = Enzyme_RH;
x0(6) = NADPH;
x0(7) = ROH;
x0(8) = RH;
x0(9) = Enzyme;
x0(10) = Enzyme_RH;
x0(11) = NADPH;
x0(12) = ROH;
x0(13) = RH;
x0(14) = Enzyme;
x0(15) = Enzyme_RH;
x0(16) = NADPH;
x0(17) = ROH;
x0(18) = RH;
x0(19) = Enzyme;
x0(20) = Enzyme_RH;

% Trying kon = 1e6 M^-1 s^-1 and recalculating koff
k(8) = WT_kon_RH*10;
k(9) = WT_koff_RH*10;

% Solving of differential equations using ode15s
tic
[t x]=ode15s(@crank,tspan,x0,options,k);
toc
out = [t, x];

```

```

% Recording of final results
filename = 'P450_leakage.xlsx';
xlswrite(filename,x,2,'B3');
xlswrite(filename,t,2,'A3');

% Reset initial values to try kon = 1e7 M^-1 s^-1
x0(1) = NADPH;
x0(2) = ROH;
x0(3) = RH;
x0(4) = Enzyme;
x0(5) = Enzyme_RH;
x0(6) = NADPH;
x0(7) = ROH;
x0(8) = RH;
x0(9) = Enzyme;
x0(10) = Enzyme_RH;
x0(11) = NADPH;
x0(12) = ROH;
x0(13) = RH;
x0(14) = Enzyme;
x0(15) = Enzyme_RH;
x0(16) = NADPH;
x0(17) = ROH;
x0(18) = RH;
x0(19) = Enzyme;
x0(20) = Enzyme_RH;

% Trying kon = 1e7 M^-1 s^-1 and recalculating koff
k(8) = WT_kon_RH*100;
k(9) = WT_koff_RH*100;

% Solving of differential equations using ode15s
tic
[t x]=ode15s(@crank,tspan,x0,options,k);
toc
out = [t, x];

% Recording of final results
filename = 'P450_leakage.xlsx';
xlswrite(filename,x,3,'B3');
xlswrite(filename,t,3,'A3');

% Reset initial values to try kon = 1e8 M^-1 s^-1
x0(1) = NADPH;
x0(2) = ROH;
x0(3) = RH;
x0(4) = Enzyme;
x0(5) = Enzyme_RH;
x0(6) = NADPH;
x0(7) = ROH;
x0(8) = RH;
x0(9) = Enzyme;

```

```

x0(10) = Enzyme_RH;
x0(11) = NADPH;
x0(12) = ROH;
x0(13) = RH;
x0(14) = Enzyme;
x0(15) = Enzyme_RH;
x0(16) = NADPH;
x0(17) = ROH;
x0(18) = RH;
x0(19) = Enzyme;
x0(20) = Enzyme_RH;

% Trying kon = 1e8 M^-1 s^-1 and recalculating koff
k(8) = WT_kon_RH*1000;
k(9) = WT_koff_RH*1000;

% Solving of differential equations using odel5s
tic
[t x]=odel5s(@crank,tspan,x0,options,k);
toc
out = [t, x];

% Recording of final results
filename = 'P450_leakage.xlsx';
xlswrite(filename,x,4,'B3');
xlswrite(filename,t,4,'A3');

% Differential equations modeling leakage and hydroxylation
function dxdt = crank(t, x, k);
    dxdt = x;

    dxdt(1) = -k(1)*x(4)*x(1)/(k(5)+x(1))-
k(6)*x(5)*x(1)/(k(7)+x(1));
    dxdt(2) = k(6)*x(5)*x(1)/(k(7)+x(1));
    dxdt(3) = -k(8)*x(4)*x(3)+k(9)*x(5);
    dxdt(4) = -
k(8)*x(4)*x(3)+k(9)*x(5)+k(6)*x(5)*x(1)/(k(7)+x(1));
    dxdt(5) = k(8)*x(4)*x(3)-k(9)*x(5)-k(6)*x(5)*x(1)/(k(7)+x(1));

    dxdt(6) = -k(2)*x(9)*x(6)/(k(5)+x(6))-
k(6)*x(10)*x(6)/(k(7)+x(6));
    dxdt(7) = k(6)*x(10)*x(6)/(k(7)+x(6));
    dxdt(8) = -k(8)*x(9)*x(8)+k(9)*x(10);
    dxdt(9) = -
k(8)*x(9)*x(8)+k(9)*x(10)+k(6)*x(10)*x(6)/(k(7)+x(6));
    dxdt(10) = k(8)*x(9)*x(8)-k(9)*x(10)-
k(6)*x(10)*x(6)/(k(7)+x(6));

    dxdt(11) = -k(3)*x(14)*x(11)/(k(5)+x(11))-
k(6)*x(15)*x(11)/(k(7)+x(11));
    dxdt(12) = k(6)*x(15)*x(11)/(k(7)+x(11));
    dxdt(13) = -k(8)*x(14)*x(13)+k(9)*x(15);

```

```

dxdt(14) = -
k(8)*x(14)*x(13)+k(9)*x(15)+k(6)*x(15)*x(11)/(k(7)+x(11));
dxdt(15) = k(8)*x(14)*x(13)-k(9)*x(15)-
k(6)*x(15)*x(11)/(k(7)+x(11));

dxdt(16) = -k(4)*x(19)*x(16)/(k(5)+x(16))-
k(6)*x(20)*x(16)/(k(7)+x(16));
dxdt(17) = k(6)*x(20)*x(16)/(k(7)+x(16));
dxdt(18) = -k(8)*x(19)*x(18)+k(9)*x(20);
dxdt(19) = -
k(8)*x(19)*x(18)+k(9)*x(20)+k(6)*x(20)*x(16)/(k(7)+x(16));
dxdt(20) = k(8)*x(19)*x(18)-k(9)*x(20)-
k(6)*x(20)*x(16)/(k(7)+x(16));
end
end

```

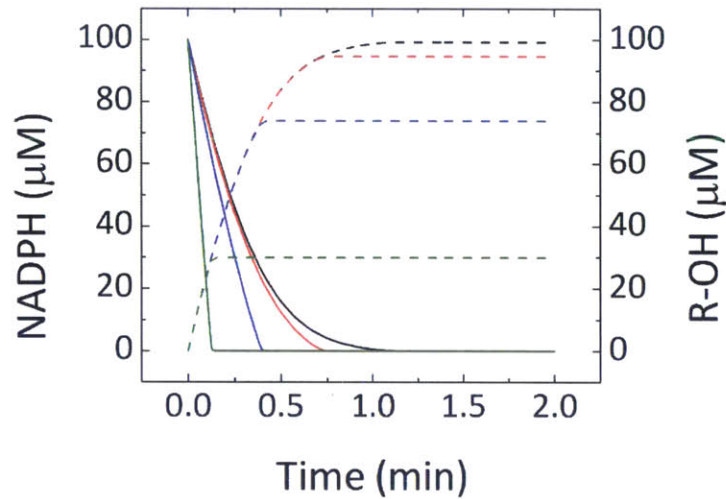


Figure B.1. Time-course plots of NADPH and hydroxylated product R-OH with different $k_{cat, leakage}$ values, assuming k_{on} for R-H and P450 BM3 to be $10^6 \text{ M}^{-1} \text{ s}^{-1}$ and using K_d , $K_{m, R-H}$, and $k_{cat, R-H}$ values for palmitate [117]. Black, red, blue, and green represent $k_{cat, leakage}$ for WT (as measured in Chapter 3) multiplied by 10^0 , 10^1 , 10^2 , and 10^3 , respectively. Solid lines represent concentration of NADPH. Dashed lines represent concentration of R-OH. $k_{cat, R-H}$ and $K_{m, R-H}$ with respect to NADPH in hydroxylation of palmitate were used for the hydroxylation reaction in competition with leakage [116].

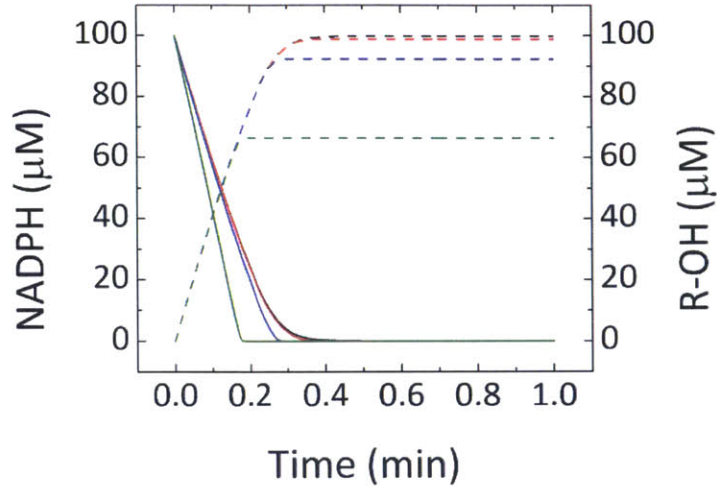


Figure B.2. Time-course plots of NADPH and hydroxylated product R–OH with different $k_{cat,leakage}$ values, assuming k_{on} for R–H and P450 BM3 to be $10^7 \text{ M}^{-1} \text{ s}^{-1}$ and using K_d , $K_{m,R-H}$, and $k_{cat,R-H}$ values for palmitate [117]. Black, red, blue, and green represent $k_{cat,leakage}$ for WT (as measured in Chapter 3) multiplied by 10^0 , 10^1 , 10^2 , and 10^3 , respectively. Solid lines represent concentration of NADPH. Dashed lines represent concentration of R–OH. $k_{cat,R-H}$ and $K_{m,R-H}$ with respect to NADPH in hydroxylation of palmitate were used for the hydroxylation reaction in competition with leakage [116].

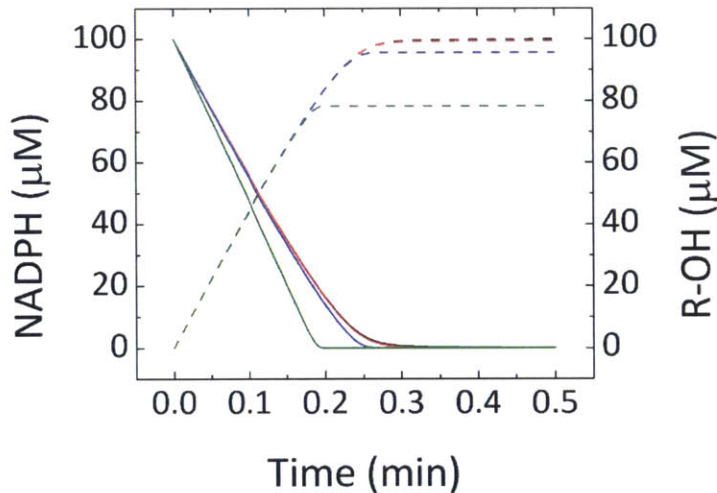


Figure B.3. Time-course plots of NADPH and hydroxylated product R–OH with different $k_{cat,leakage}$ values, assuming k_{on} for R–H and P450 BM3 to be $10^7 \text{ M}^{-1} \text{ s}^{-1}$ and using K_d , $K_{m,R-H}$, and $k_{cat,R-H}$ values for palmitate [117]. Black, red, blue, and green represent $k_{cat,leakage}$ for WT (as measured in Chapter 3) multiplied by 10^0 , 10^1 , 10^2 , and 10^3 , respectively. Solid lines represent concentration of NADPH. Dashed lines represent concentration of R–OH. $k_{cat,R-H}$ and $K_{m,R-H}$ with respect to NADPH in hydroxylation of palmitate were used for the hydroxylation reaction in competition with leakage [116].

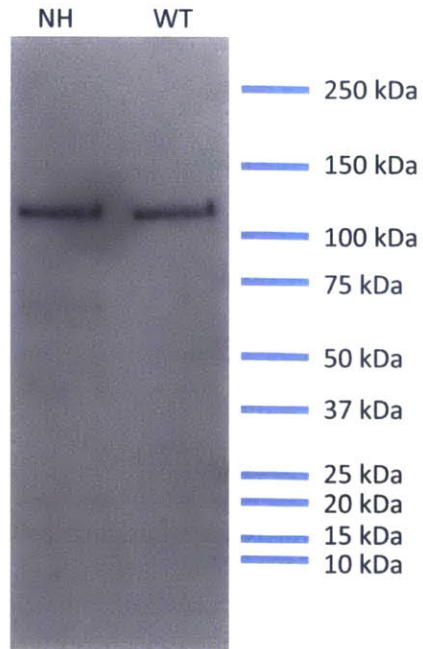


Figure B.4. SDS-PAGE gel of the WT protein and the T268N/F393H (NH) variant.

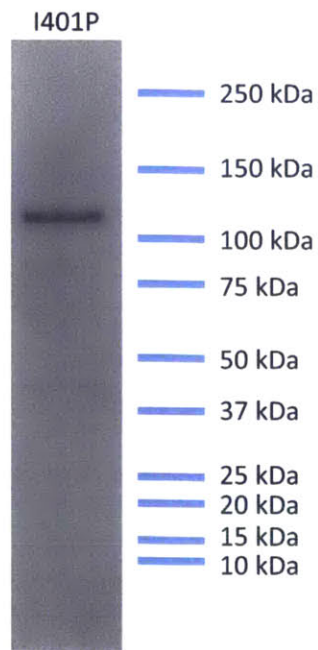


Figure B.5. SDS-PAGE gel of the I401P variant.

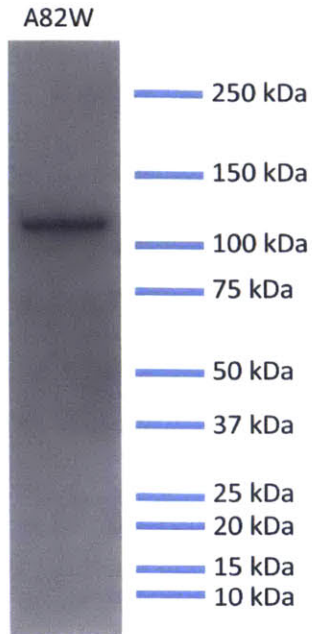


Figure B.6. SDS-PAGE gel of the A82W variant.

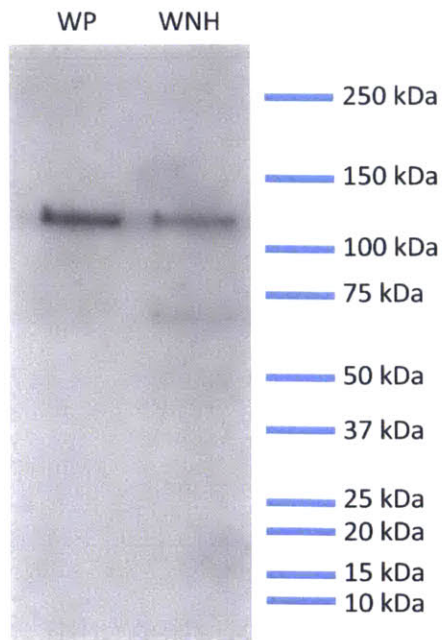


Figure B.7. SDS-PAGE gel of the A82W/I401P (WP) and A82W/T268N/F393H (WNH) variants.

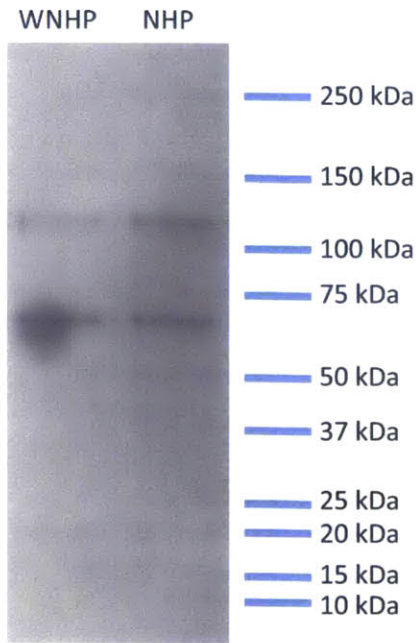


Figure B.8. SDS-PAGE gel of the T268N/F393H/I401P (WHP) and A82W/T268N/F393H/I401P (WNHP) variants.

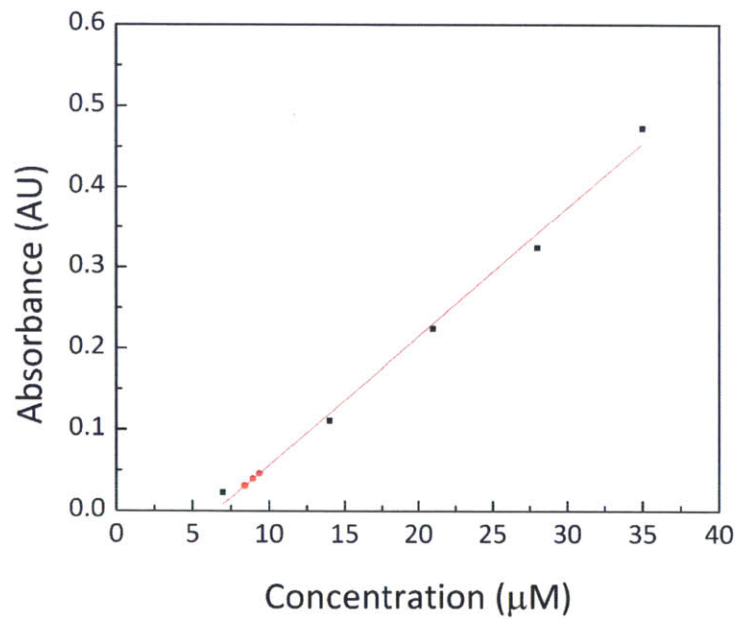


Figure B.9. Standard curve and experimental trials of HRP assay with ABTS as colorimetric substrate for A82W P450 BM3. Standard curve shown in black squares with red line fitted linearly to the points and experimental trials shown in red circles.

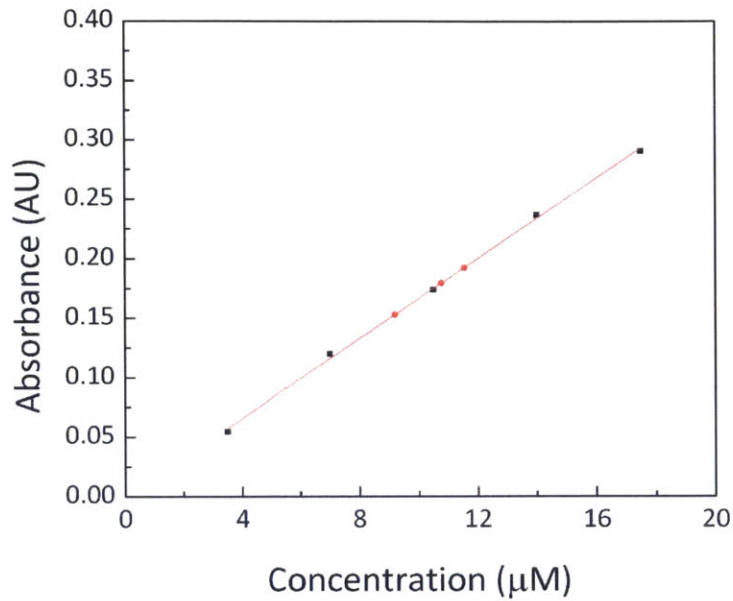


Figure B.10. Standard curve and experimental trials of HRP assay with ABTS as colorimetric substrate for T268N/F393H P450 BM3. Standard curve shown in black squares with red line fitted linearly to the points and experimental trials shown in red circles.

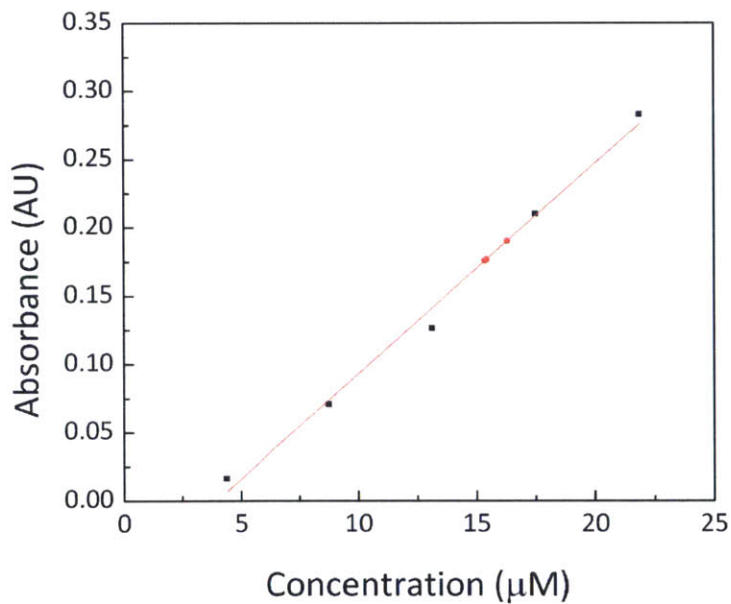


Figure B.11. Standard curve and experimental trials of HRP assay with ABTS as colorimetric substrate for I401P P450 BM3. Standard curve shown in black squares with red line fitted linearly to the points and experimental trials shown in red circles.

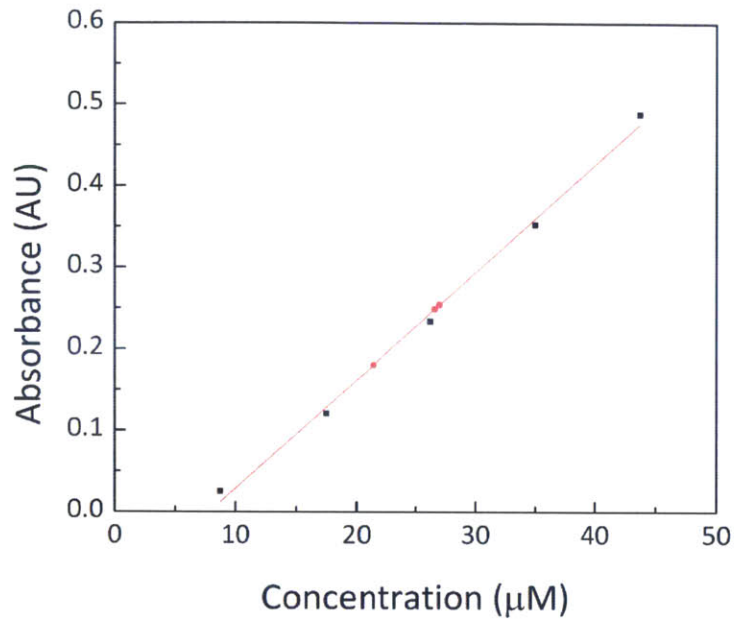


Figure B.12. Standard curve and experimental trials of HRP assay with ABTS as colorimetric substrate for A82W/T268H/F393H P450 BM3. Standard curve shown in black squares with red line fitted linearly to the points and experimental trials shown in red circles.

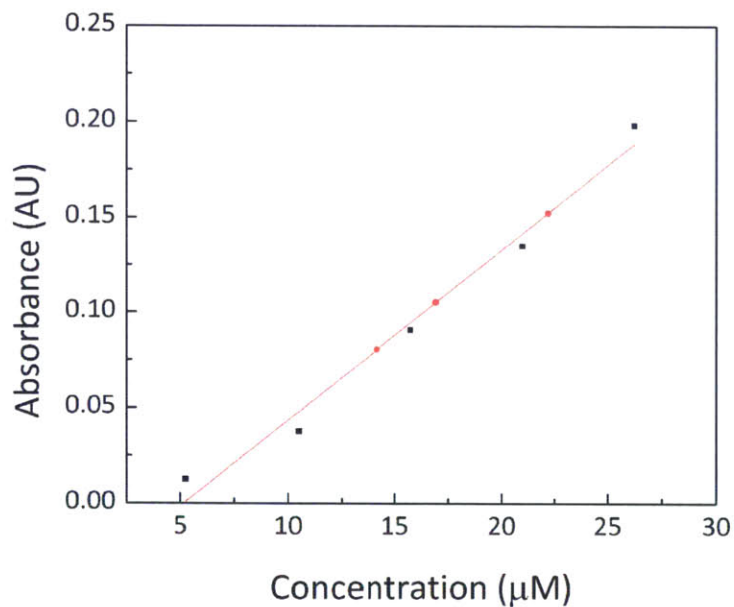


Figure B.13. Standard curve and experimental trials of HRP assay with ABTS as colorimetric substrate for A82W/I401P P450 BM3. Standard curve shown in black squares with red line fitted linearly to the points and experimental trials shown in red circles.

Appendix C

The following contains additional details on the methodologies and data corresponding to Chapter 5.

The following are the molar balance derivations used to calculate initial conditions for oxidized proteins, assuming steady state. The derivations also required an estimate for the basal H_2O_2 concentration. We hypothesized that the basal concentration is largely controlled by only its generation and reduction by $Prx-(SH)_2$, and that in the basal state, the concentrations of the oxidized forms of $Prx-(SH)_2$ are not significant enough to appreciably perturb the initial concentration of $Prx-(SH)_2$ in a molar balance. We thus used the following derivation for the estimate:

$$\frac{d[H_2O_2]}{dt} = k_1 - k_6[Prx - (SH)_2][H_2O_2] = 0$$

$$[H_2O_2] = \frac{k_1}{k_6[Prx - SH]} = 8 \times 10^{-11} M$$

While we used this estimate a priori in calculating the initial concentrations of various oxidized species, we demonstrated this to be a valid estimate, as described in both the main text and later in this section. We note that k_1 was estimated based on the H_2O_2 production rate comprising 1% of the typical, rather than maximal, O_2 consumption rate by the human body [144].

The initial conditions for the oxidation states of Prx are as follows:

$$[Prx - (SH)_2] + [Prx - SOH] + [Prx - SS] + [Prx - SOOH] = 10^{-4} M$$

$$\frac{d[Prx - (SH)_2]}{dt} = -k_6[Prx - (SH)_2][H_2O_2] + k_{10}[Prx - SS][Trx1 - SH] = 0$$

$$\frac{d[Prx - SOH]}{dt} = k_6[Prx - (SH)_2][H_2O_2] - k_7[Prx - SOH][H_2O_2] + k_8[Prx - SOOH] - k_9[Prx - SOH] = 0$$

$$\frac{d[Prx - SS]}{dt} = k_9[Prx - SOH] - k_{10}[Prx - SS][Trx1 - SH] = 0$$

$$\frac{d[Prx - SOOH]}{dt} = k_7[Prx - SOH][H_2O_2] - k_8[Prx - SOOH] = 0$$

$$[Prx - SS] = \frac{10^{-4} M}{\frac{k_{10}[Trx1 - SH]}{k_6[H_2O_2]} + \frac{k_{10}[Trx1 - SH]}{k_9} + 1 + \frac{k_7 k_{10}[Trx1 - SH]}{k_8 k_9}} = 5.57 \times 10^{-11} M$$

$$[Prx - SOH] = \frac{10^{-4} M}{\frac{k_9}{k_6[H_2O_2]} + 1 + \frac{k_9}{k_{10}[Trx1 - SH]} + \frac{k_7[H_2O_2]}{k_8}} = 5.49 \times 10^{-8} M$$

$$[Prx - SOOH] = \frac{10^{-4} M}{\frac{k_9 k_8}{k_6 k_7 [H_2O_2]^2} + \frac{k_8}{k_7 [H_2O_2]} + \frac{k_9 k_8}{k_{10} k_7 [Trx1 - SH] [H_2O_2]} + 1} = 1.86 \times 10^{-11} M$$

$$[Prx - (SH)_2] = 10^{-4} M - [Prx - SOH] - [Prx - SS] - [Prx - SOOH] \approx 10^{-4} M$$

We pay special attention to the oxidation states of Prx since it has recently been discovered that either Prx-SOH or Prx-SS is involved in redox relay reactions that mediate H₂O₂ signaling. The ratio of Prx-SOH to Prx-(SH)₂ was 5.5 × 10⁻⁴, orders of magnitude greater than the corresponding ratios for Prx-SS and Prx-SOOH, which were 5.6 × 10⁻⁷ and 1.9 × 10⁻⁷, respectively. However, pulse additions of H₂O₂ led to visible changes in Prx-SS and not Prx-SOH. While it remains to be determined which oxidation state is relevant in redox relay reactions, we note that if our calculations and the assumptions upon which they rest are validated in future work, then these values could be used to quantify the concentrations at which Prx-SOH or Prx-SS mediate signaling.

The initial conditions for the oxidation states of GPx are as follows:

$$\begin{aligned} [GPx_{red}] + [GPx_{ox}] + [GPx - SG] &= 5.5 \times 10^{-7} M \\ \frac{d[GPx_{red}]}{dt} &= -k_2[GPx_{red}][H_2O_2] + k_4[GPx - SG][GSH] = 0 \\ \frac{d[GPx_{ox}]}{dt} &= k_2[GPx_{red}][H_2O_2] - k_3[GPx_{ox}][GSH] = 0 \\ \frac{d[GPx - SG]}{dt} &= k_3[GPx_{ox}][GSH] - k_4[GPx - SG][GSH] = 0 \\ [GPx_{ox}] &= \frac{5.5 \times 10^{-7} M}{\frac{k_3[GSH]}{k_2[H_2O_2]} + 1 + \frac{k_2}{k_4}} = 6.64 \times 10^{-11} M \\ [GPx - SG] &= \frac{5.5 \times 10^{-7} M}{\frac{k_4[GSH]}{k_2[H_2O_2]} + \frac{k_4}{k_3} + 1} = 2.66 \times 10^{-13} M \\ [GPx_{red}] &= 5.5 \times 10^{-7} M - [GPx_{ox}] - [GPx - SG] \approx 5.5 \times 10^{-7} M \end{aligned}$$

The initial conditions for the oxidation states of Pr-(SH)₂ are as follows:

$$\begin{aligned} [Pr - (SH)_2] + [Pr - SS] &= 1.09 \times 10^{-3} M \\ \frac{d[Pr - (SH)_2]}{dt} &= -k_{16}[Pr - (SH)_2][H_2O_2] + k_{17}[Pr - SS][Trx1 - SH] = 0 \\ \frac{d[Pr - SS]}{dt} &= k_{16}[Pr - (SH)_2][H_2O_2] - k_{17}[Pr - SS][Trx1 - SH] = 0 \\ [Pr - SS] &= \frac{1.09 \times 10^{-3} M}{1 + \frac{k_{17}[Trx1 - SH]}{k_{16}[H_2O_2]}} = 2.16 \times 10^{-7} M \\ [Pr - (SH)_2] &= 1.09 \times 10^{-3} M - [Pr - SS] \approx 1.09 \times 10^{-3} M \end{aligned}$$

The initial conditions for the oxidation states of Pr and Grx are as follows:

$$[Pr - SH] + [Pr - SSG] + [Pr - SOH] = 10^{-9} M$$

$$\frac{d[Pr - SH]}{dt} = -k_{12}[Pr - SH][H_2O_2] + k_{14}[Pr - SSG][Grx - SH] = 0$$

$$\frac{d[Pr - SOH]}{dt} = k_{12}[Pr - SH][H_2O_2] - k_{13}[Pr - SOH][GSH] = 0$$

$$\frac{d[Pr - SSG]}{dt} = k_{13}[Pr - SOH][GSH] - k_{14}[Grx - SH][Pr - SSG] = 0$$

$$[Pr - SSG] = \frac{10^{-9} M}{\frac{k_{14}[Grx - SH]}{k_{12}[H_2O_2]} + 1 + \frac{k_{14}[Grx - SH]}{k_{13}[GSH]}} = 1.33 \times 10^{-16} M$$

$$[Pr - SOH] = \frac{10^{-9} M}{\frac{k_{13}[GSH]}{k_{12}[H_2O_2]} + 1 + \frac{k_{13}[GSH]}{k_{14}[Grx - SH]}} = 1.92 \times 10^{-19} M$$

$$[Pr - SH] = 10^{-9} M - [Pr - SSG] - [Pr - SOH] \approx 10^{-9} M$$

We note that the estimates for Pr-SH, Pr-SOH, and Pr-SSG are dependent upon Grx being mostly in the reduced state such that the concentration of Grx-SH can be approximated as $7 \times 10^{-7} M$. We confirmed that to be the case here in the following:

$$[Grx - SH] + [Grx - SSG] = 7 \times 10^{-7} M$$

$$\frac{d[Grx - SH]}{dt} = k_{15}[Grx - SSG][GSH] - k_{14}[Grx - SH][Pr - SSG] = 0$$

$$\frac{d[Grx - SSG]}{dt} = -k_{15}[Grx - SSG][GSH] + k_{14}[Grx - SH][Pr - SSG] = 0$$

$$[Grx - SSG] = \frac{7 \times 10^{-7} M}{1 + \frac{k_{15}[GSH]}{k_{14}[Pr - SSG]}} = 6.21 \times 10^{-21} M$$

$$[Grx - SH] = 7 \times 10^{-7} M - [Grx - SSG] \approx 7 \times 10^{-7} M$$

Because the concentration of Grx-SH is still approximately $7 \times 10^{-7} M$ after subtracting the concentration of the glutathionylated form, the derivations for Pr-SH, Pr-SOH, and Pr-SSG are still valid.

We note again that a majority of the estimates here depend on the basal concentration of H_2O_2 . After using that concentration and consequent initial concentrations for oxidized proteins shown above in model simulations, we found that in the context of physiologically relevant perturbations to the cytosolic concentration of H_2O_2 , we could indeed approximate the model as the single equation described in both the main text and at the start of this section. Thus, our a priori assumption still holds, lending credence to our estimate for the basal concentration of H_2O_2 and consequently for those of the oxidized species.

The following is the Matlab code used to implement the kinetic model:

```
function out = PeroxideClearanceModel_HeLa_cytosol_final(i)
    % Model for hydrogen peroxide consumption
    % i will determine which initial H2O2 concentration to use
```

```

% Solver Parameters
ti = 0; % start time
tf = 0.04; % stop time (s)
step = 0.00001; % time step (s)
dt = step;
tspan = ti:dt:tf;
options=odeset('AbsTol',1E-10,'RelTol',1E-4,'maxstep',step);

% Define model parameters
k = zeros(22,1);

% Intracellular peroxide production
k(1) = 1.1e-7; % M/s

% GPxred reacting with H2O2
k(2) = 2.1e7; % M^-1*s^-1

% GPxox reacting with GSH
k(3) = 4e4; % M^-1*s^-1

% GPx-SSG reacting with GSH
k(4) = 1e7; % M^-1*s^-1

% Km of NADP+
k(5) = 5.7e-5; % M

% Prx-SH oxidized by H2O2
k(6) = 1.3e7; % M^-1*s^-1

% Prx-SOH over-oxidized by H2O2
k(7) = 1.2e4; % M^-1*s^-1

% Reduction of overoxidized Prx by Srx enzyme
k(8) = 3e-3; % s^-1

% Self-catalyzed disulfide formation of Prx-SS from Prx-SOH
k(9) = 2; % s^-1

% Prx is reduced by thioredoxin
k(10) = 2.1e6; % M^-1*s^-1

% Auto-oxidation of GSH
k(11) = 7.4e-05; % s^-1

% Pr-SH oxidized by H2O2
k(12) = 1e2; % M^-1*s^-1

% Pr-SOH glutathionylated by GSH
k(13) = 1.2e5; % M^-1*s^-1

% Grx-SH de-glutathionylates Protein-SSG
k(14) = 9.1e4; % M^-1*s^-1

% GSH de-glutathionylates Grx-SSG

```

```

k(15) = 3.7e4; % M^-1*s^-1

% Pr-(SH)2 oxidized by H2O2
k(16) = 1e2; % M^-1*s^-1

% Pr-SS reduced by Trx
k(17) = 1e2; % M^-1*s^-1

% GSSG reduced by GR
k(18) = 3.2e6; % M^-1*s^-1

% Oxidized Thioredoxin reduced by TrxR
k(19) = 2e7; % M^-1*s^-1

% Production of NADPH by G6P-DH
k(20) = 3.75e-04; % M/s

% GSH synthesis
k(21) = 4.1e-7; % M/s

% Trx_SH synthesis
k(22) = 6.97e-10; % M/s

% Defining initial Conditions (Concentrations in M = Moles/Liter)
x0 = zeros(21,1);

% Determine which initial H2O2 concentration to use
if i == 1
    x0(1) = .01e-6;
elseif i == 2
    x0(1) = .05e-6;
elseif i == 3
    x0(1) = .1e-6;
elseif i == 4
    x0(1) = .5e-6;
elseif i == 5
    x0(1) = 1e-6;
elseif i == 6
    x0(1) = 5e-6;
elseif i == 7
    x0(1) = 10e-6;
elseif i == 8
    x0(1) = 50e-6;
else
    x0(1) = 100e-6;
end

% Specify baseline H2O2 concentration
initial_H2O2_cytosol = 1.0e-9;
x0(2) = 0.55e-6; % GPXr
x0(3) = 1e-14; % GPXo
x0(4) = 1e-14; % GPX-SG
x0(5) = 3.68e-4; % GSH
x0(6) = 1.78e-6; % GSSG
x0(7) = 1.0e-4; % Prx-SH

```

```

x0(8) = 1e-14;          % Prx-SOH
x0(9) = 1e-14;          % Prx-SOOH
x0(10) = 1e-14;        % Prx-SS
x0(11) = 4.27e-7;      % Trx1-SH
x0(12) = 7.54e-8;      % Trx1-SS
x0(13) = 1e-9;         % Pr-SH
x0(14) = x0(13)*(.5/100); % Pr-SOH
x0(15) = x0(13)*(.5/100); % Pr-SSG
x0(16) = 0.7e-6;       % Grx-SH
x0(17) = x0(16)*(.5/100); % Grx-SSG
x0(18) = 1.09e-3;      % Pr-(SH)2
x0(19) = x0(18)*(.5/100); % Pr-SS
x0(20) = 3.0e-5;       % NADPH
x0(21) = 3.0e-7;       % NADP+

% Integration
tic
[t x]=ode15s(@crank,tspan,x0,options,k);
toc
out = [t, x];
filename = 'HeLa_intracellular_cytosol_final2.xlsx';
xlswrite(filename,x,i,'B3');

% Description of derivatives
function dxdt = crank(t, x, k);
    dxdt= x; % setting up vector containing derivatives
    dxdt(1) = k(1) - k(2)*x(2)*(x(1)- initial_H2O2_cytosol) -
k(6)*x(7)*(x(1)- initial_H2O2_cytosol) - k(7)*x(8)*(x(1)-
initial_H2O2_cytosol) - k(12)*x(13)*(x(1)- initial_H2O2_cytosol) -
k(16)*x(18)*(x(1)- initial_H2O2_cytosol); % H2O2
    dxdt(2) = - k(2)*x(2)*(x(1)- initial_H2O2_cytosol) + k(4)*(x(4)-
x0(4))*x(5); % GPXred
    dxdt(3) = k(2)*x(2)*(x(1)- initial_H2O2_cytosol) - k(3)*(x(3)-
x0(3))*x(5); % GPXox
    dxdt(4) = k(3)*(x(3)-x0(3))*x(5) - k(4)*(x(4)-x0(4))*x(5); % GPX-SG
    dxdt(5) = - k(3)*(x(3)-x0(3))*x(5) - k(4)*(x(4)-x0(4))*x(5) -
2*k(11)*x(5) - k(13)*(x(14)-x0(14))*x(5) - k(15)*(x(17)-x0(17))*x(5) +
2*k(18)*(x(6)-x0(6))*x(20) + k(21); % GSH
    dxdt(6) = k(4)*(x(4)-x0(4))*x(5) + k(11)*x(5) + k(15)*(x(17)-
x0(17))*x(5) - k(18)*(x(6)-x0(6))*x(20); % GSSG
    dxdt(7) = - k(6)*x(7)*(x(1)- initial_H2O2_cytosol) + k(10)*(x(10)-
x0(10))*x(11); % Prx-SH
    dxdt(8) = k(6)*x(7)*(x(1)- initial_H2O2_cytosol) - k(7)*x(8)*(x(1)-
initial_H2O2_cytosol) + k(8)*(x(9)-x0(9)) - k(9)*x(8); % Prx-SOH
    dxdt(9) = k(7)*x(8)*(x(1)- initial_H2O2_cytosol) - k(8)*(x(9)-x0(9));
% Prx-SOOH
    dxdt(10) = k(9)*x(8) - k(10)*(x(10)-x0(10))*x(11); % Prx-SS
    dxdt(11) = - k(10)*(x(10)-x0(10))*x(11) - k(17)*(x(19)-x0(19))*x(11)
+ k(19)*(x(12)-x0(12))*x(20) + k(22); % Trx-SH
    dxdt(12) = k(10)*(x(10)-x0(10))*x(11) + k(17)*(x(19)-x0(19))*x(11) -
k(19)*(x(12)-x0(12))*x(20); % Trx-SS
    dxdt(13) = - k(12)*x(13)*(x(1)- initial_H2O2_cytosol) +
k(14)*x(16)*(x(15)-x0(15)); % Pr-SH
    dxdt(14) = k(12)*x(13)*(x(1)- initial_H2O2_cytosol) - k(13)*(x(14)-
x0(14))*x(5); % Pr-SOH

```

```

Pr-SSG      dxdt(15) = k(13)*(x(14)-x0(14))*x(5) - k(14)*x(16)*(x(15)-x0(15)); %
Grx-SH      dxdt(16) = k(15)*(x(17)-x0(17))*x(5) - k(14)*x(16)*(x(15)-x0(15)); %
Grx-SSG     dxdt(17) = k(14)*x(16)*(x(15)-x0(15)) - k(15)*(x(17)-x0(17))*x(5); %
            dxdt(18) = - k(16)*x(18)*(x(1)- initial_H2O2_cytosol) + k(17)*(x(19)-
x0(19))*x(11); % Pr-(SH)2
            dxdt(19) = k(16)*x(18)*(x(1)- initial_H2O2_cytosol) - k(17)*(x(19)-
x0(19))*x(11); % Pr-SS
            dxdt(20) = - k(18)*(x(6)-x0(6))*x(20) - k(19)*(x(12)-x0(12))*x(20) +
k(20)*(x(21)- x0(21))/(k(5) + x(21)); % NADPH
            dxdt(21) = k(18)*(x(6)-x0(6))*x(20) + k(19)*(x(12)-x0(12))*x(20) -
k(20)*(x(21)- x0(21))/(k(5) + x(21)); % NADP+
            end
end

```

We now show here our derivation of an analytical solution to the transport model for intracellular H_2O_2 . The governing equation for intracellular $[\text{H}_2\text{O}_2]$, or C , is

$$\frac{D}{r^2} \frac{\partial}{\partial r} \left(r^2 \frac{\partial C}{\partial r} \right) + R = \frac{\partial C}{\partial t}$$

$$\frac{D}{r^2} \frac{\partial}{\partial r} \left(r^2 \frac{\partial C}{\partial r} \right) + k_1 - k_s C = \frac{\partial C}{\partial t}$$

The boundary conditions are

$$\frac{\partial C}{\partial r}(0, t) = 0$$

$$D \frac{\partial C}{\partial r}(a, t) = PC_{ext}$$

$$C(r, 0) = \frac{k_1}{k_s}$$

Because Bi was previously calculated to be $\ll 1$, the boundary condition at $r = a$ is valid.

We define the following dimensionless numbers:

$$Da_0 = \frac{k_1 a^2}{DBiC_{ext}}$$

$$Da_1 = \frac{k_s a^2}{D}$$

$$Bi = \frac{Pa}{D}$$

We nondimensionalize the equations by the following:

$$\eta = \frac{r}{a}$$

$$\theta = \frac{C}{BiC_{ext}}$$

$$\tau = \frac{Dt}{a^2}$$

This results in the following governing equation and boundary conditions:

$$\frac{1}{\eta^2} \frac{\partial}{\partial \eta} \left(\eta^2 \frac{\partial \theta}{\partial \eta} \right) + Da_0 - Da_1 \theta = \frac{\partial \theta}{\partial \tau}$$

$$\frac{\partial \theta}{\partial \eta} (0, \tau) = 0$$

$$\theta(\eta, 0) = \frac{k_1}{k_s BiC_{ext}} = \frac{Da_0}{Da_1}$$

$$\frac{\partial \theta}{\partial \eta} (1, \tau) = 1$$

We pose the final solution as the following:

$$\theta(\eta, \tau) = f(\eta) + g(\tau) + \varphi(\eta, \tau)$$

We solve for $g(\tau)$ and $f(\eta)$:

$$\frac{\partial g}{\partial \tau} = \frac{1}{\eta^2} \frac{\partial}{\partial \eta} \left(\eta^2 \frac{\partial f}{\partial \eta} \right) + Da_0 - Da_1(f + g)$$

We can separate the functions and solve for each separately:

$$0 = \frac{1}{\eta^2} \frac{d}{d\eta} \left(\eta^2 \frac{df}{d\eta} \right) - Da_1 f$$

$$f = A \frac{\sinh(\sqrt{Da_1} \eta)}{\eta} + B \frac{\cosh(\sqrt{Da_1} \eta)}{\eta}$$

B must be zero to keep f finite at $\eta = 0$, resulting in

$$f = A \frac{\sinh(\sqrt{Da_1} \eta)}{\eta}$$

We use the following boundary condition:

$$\frac{df}{d\eta} (1) = 1$$

$$f = \left(\frac{1}{\sqrt{Da_1} \cosh(\sqrt{Da_1}) - \sinh(\sqrt{Da_1})} \right) \frac{\sinh(\sqrt{Da_1} \eta)}{\eta}$$

We now solve for g :

$$\frac{dg}{d\tau} = Da_0 - Da_1 g$$

$$g = \frac{Da_0}{Da_1} + A \exp(-Da_1 \tau)$$

We use the following initial condition:

$$g(0) = 0$$

$$g = \frac{Da_0}{Da_1} [1 - \exp(-Da_1 \tau)]$$

We now solve for $\varphi(\eta, \tau)$. We use FFT to do so, using homogenous boundary conditions:

$$\frac{\partial \varphi}{\partial \eta}(0, \tau) = 0$$

$$\frac{\partial \varphi}{\partial \eta}(1, \tau) = 0$$

To satisfy homogenous boundary conditions, we also note that we cannot have any internal generation (i.e. k_1 , or Da_0); we have accounted for this in the function for g . This leaves us with the following for $\varphi(\eta, \tau)$:

$$\frac{1}{\eta^2} \frac{\partial}{\partial \eta} \left(\eta^2 \frac{\partial \varphi}{\partial \eta} \right) - Da_1 \varphi = \frac{\partial \varphi}{\partial \tau}$$

Applying the FFT methodology results in

$$\varphi(\eta, \tau) = \sum_{n=1}^{\infty} \varphi_n(\tau) \Phi_n(\eta)$$

$$\varphi_n(\tau) = \int_0^1 \Phi_n(\eta) \varphi(\eta, \tau) \eta^2 d\eta$$

$$\begin{aligned} \int_0^1 \Phi_n \left[\frac{1}{\eta^2} \frac{\partial}{\partial \eta} \left(\eta^2 \frac{\partial \varphi}{\partial \eta} \right) \right] \eta^2 d\eta &= \eta^2 \left(\Phi_n \frac{\partial \varphi}{\partial \eta} - \varphi \frac{d\Phi_n}{d\eta} \right) \Big|_{\eta=0}^{\eta=1} - \lambda_n^2 \varphi_n \\ &= -\lambda_n^2 \varphi_n \end{aligned}$$

This results in

$$\frac{d\varphi_n}{d\tau} + [\lambda_n^2 + Da_1] \varphi_n = 0$$

For the initial condition, we account for f and g :

$$\theta(\eta, 0) = \frac{Da_0}{Da_1} = g(0) + f(\eta) + \varphi(\eta, 0)$$

$$\varphi(\eta, 0) = \frac{Da_0}{Da_1} - g(0) - f(\eta)$$

$$\varphi(\eta, 0) = \frac{Da_0}{Da_1} - \left(\frac{1}{\sqrt{Da_1} \cosh(\sqrt{Da_1}) - \sinh(\sqrt{Da_1})} \right) \frac{\sinh(\sqrt{Da_1}\eta)}{\eta}$$

We transform this condition into the appropriate coefficient for the basis function that will be used. For n greater than zero:

$$\varphi_n(0) = \int_0^1 \Phi_n(\eta) \varphi(\eta, 0) \eta^2 d\eta$$

$$\varphi_n(0) = -\frac{\sqrt{2}}{Da_1 + \lambda_n^2}$$

For n equal to zero:

$$\varphi_0(0) = \int_0^1 \Phi_0(\eta) \varphi(\eta, 0) \eta^2 d\eta$$

$$\varphi_0(0) = \frac{Da_0 - 3}{\sqrt{3}Da_1}$$

We use this condition to solve for φ_n . For n greater than zero:

$$\varphi_n = -\frac{\sqrt{2}}{Da_1 + \lambda_n^2} \exp[-(\lambda_n^2 + Da_1)\tau]$$

For n equal to zero:

$$\varphi_0 = \frac{Da_0 - 3}{\sqrt{3}Da_1} \exp(-Da_1\tau)$$

The overall solution becomes

$$\varphi(\eta, \tau) = \frac{Da_0 - 3}{Da_1} \exp(-Da_1\tau) - 2 \sum_{n=1}^{\infty} \frac{1}{Da_1 + \lambda_n^2} \exp[-(\lambda_n^2 + Da_1)\tau] \frac{\sin(\lambda_n\eta)}{\eta \sin(\lambda_n)}$$

Thus, combining this with f and g , we obtain:

$$\theta(\eta, \tau) = \left(\frac{1}{\sqrt{Da_1} \cosh(\sqrt{Da_1}) - \sinh(\sqrt{Da_1})} \right) \frac{\sinh(\sqrt{Da_1}\eta)}{\eta} + \frac{Da_0}{Da_1} [1 - \exp(-Da_1\tau)]$$

$$+ \frac{Da_0 - 3}{Da_1} \exp(-Da_1\tau) - 2 \sum_{n=1}^{\infty} \frac{1}{Da_1 + \lambda_n^2} \exp[-(\lambda_n^2 + Da_1)\tau] \frac{\sin(\lambda_n\eta)}{\eta \sin(\lambda_n)}$$

The parameter λ_n must satisfy the following:

$$\lambda_n = \tan \lambda_n$$

We show the steady state solution here:

$$\theta(\eta) = \left(\frac{1}{\sqrt{Da_1} \cosh(\sqrt{Da_1}) - \sinh(\sqrt{Da_1})} \right) \frac{\sinh(\sqrt{Da_1} \eta)}{\eta} + \frac{Da_0}{Da_1}$$

The solution was implemented using the following Matlab code:

```
function out = runConcentrationProfilesBolus

% Diffusivity of H2O2
D = 1.83e-9; % m^2/s

% Bolus addition of H2O2
Cext = 4.18261e-6; % M

% Mitochondrial production of H2O2
k0 = 1.1e-7; % M/s

% Parameters for peroxiredoxin
kPrxOxH2O2 = 1.3e7; % M^-1*s^-1

% Amount of peroxiredoxin for HeLa
Prx_HeLa = 1.0e-4; % M

% Radius and permeability of HeLa cells
R_HeLa = 10e-6; % m
%P_HeLa = 1e-4/100; % m/s
P_HeLa = 0.000443644/100; % m/s

% Calculation of Biot numbers and eigenvalues
Bi_HeLa = P_HeLa*R_HeLa/D;

% Number of terms for dimensionless length and time
num_eta = 100;
num_tau = 30;
eta_array = linspace(0, 1, num_eta+1);
t_array = linspace(0,0.003,num_tau+1);
tau_array = t_array*D/R_HeLa^2;

filename = 'eigenvalues_Neumann.xlsx';
eigenvalues_HeLa = xlsread(filename);
num_eig = 30;

tic

f = GetConcentrationProfilesBolusNeumannf(eta_array, tau_array, Cext, R_HeLa,
P_HeLa, k0, Prx_HeLa);
g = GetConcentrationProfilesBolusNeumanng(eta_array, tau_array, Cext, R_HeLa,
P_HeLa, k0, Prx_HeLa);
psi = GetConcentrationProfilesBolusNeumannFFT(eta_array, tau_array,
eigenvalues_HeLa, num_eig, ...
    Cext, R_HeLa, P_HeLa, k0, Prx_HeLa);
ss = GetConcentrationProfilesBolusNeumannSS(eta_array, tau_array, Cext,
R_HeLa, P_HeLa, k0, Prx_HeLa);

toc
```

```

filename = strcat('HeLa_bolus_Neumann_SS_', num2str(Cext*1e6));
filename = strcat(filename, 'uM_official.xlsx');
xlswrite(filename, ss, 1, 'B3');
xlswrite(filename, transpose(eta_array), 1, 'A3');
xlswrite(filename, tau_array, 1, 'B2');
xlswrite(filename, ss*Cext*Bi_HeLa, 2, 'B3');
xlswrite(filename, transpose(eta_array*R_HeLa), 2, 'A3');
xlswrite(filename, tau_array*R_HeLa^2/D, 2, 'B2');

filename = strcat('HeLa_bolus_Neumann_g_', num2str(Cext*1e6));
filename = strcat(filename, 'uM_official.xlsx');
xlswrite(filename, g, 1, 'B3');
xlswrite(filename, transpose(eta_array), 1, 'A3');
xlswrite(filename, tau_array, 1, 'B2');
xlswrite(filename, g*Cext*Bi_HeLa, 2, 'B3');
xlswrite(filename, transpose(eta_array*R_HeLa), 2, 'A3');
xlswrite(filename, tau_array*R_HeLa^2/D, 2, 'B2');

filename = strcat('HeLa_bolus_Neumann_psi_', num2str(Cext*1e6));
filename = strcat(filename, 'uM_n_');
filename = strcat(filename, num2str(num_eig));
filename = strcat(filename, '_official.xlsx');
xlswrite(filename, psi, 1, 'B3');
xlswrite(filename, transpose(eta_array), 1, 'A3');
xlswrite(filename, tau_array, 1, 'B2');
xlswrite(filename, psi*Cext*Bi_HeLa, 2, 'B3');
xlswrite(filename, transpose(eta_array*R_HeLa), 2, 'A3');
xlswrite(filename, tau_array*R_HeLa^2/D, 2, 'B2');

filename = strcat('HeLa_bolus_Neumann_f&g_', num2str(Cext*1e6));
filename = strcat(filename, 'uM_official.xlsx');
xlswrite(filename, f+g, 1, 'B3');
xlswrite(filename, transpose(eta_array), 1, 'A3');
xlswrite(filename, tau_array, 1, 'B2');
xlswrite(filename, (f+g)*Cext*Bi_HeLa, 2, 'B3');
xlswrite(filename, transpose(eta_array*R_HeLa), 2, 'A3');
xlswrite(filename, tau_array*R_HeLa^2/D, 2, 'B2');

filename = strcat('HeLa_bolus_Neumann_f&g&psi_', num2str(Cext*1e6));
filename = strcat(filename, 'uM_n_');
filename = strcat(filename, num2str(num_eig));
filename = strcat(filename, '_official.xlsx');
xlswrite(filename, f+g+psi, 1, 'B3');
xlswrite(filename, transpose(eta_array), 1, 'A3');
xlswrite(filename, tau_array, 1, 'B2');
xlswrite(filename, (f+g+psi)*Cext*Bi_HeLa, 2, 'B3');
xlswrite(filename, transpose(eta_array*R_HeLa), 2, 'A3');
xlswrite(filename, tau_array*R_HeLa^2/D, 2, 'B2');

end

function array_of_eigenvalues = GetEigenvaluesWrite(n)

```

```

% Diffusivity of H2O2
D = 1.83e-9; % m^2/s

% Radius and permeability of HeLa cells
R_HeLa = 10e-6; % m
P_HeLa = 1e-4/100; % m/s

Bi = P_HeLa*R_HeLa/D;

filename = 'eigenvalues_HeLa_official.xlsx';
what = xlsread(filename);
start = length(what)+1;

array_of_eigenvalues = zeros(n-start+1,3);

for i=start:n
    array_of_eigenvalues(i-start+1,1) = i*3.1415926535897;
end

syms x
for i=start:n
    if i==start
        array_of_eigenvalues(i-start+1,2) = vpasolve(tan(x)-x, x,
what(end,2)+3.1415926535897);
        array_of_eigenvalues(i-start+1,3) = vpasolve((1-Bi)*tan(x)-x, x,
what(end,3)+3.1415926535897);
    else
        array_of_eigenvalues(i-start+1,2) = vpasolve(tan(x)-x, x,
array_of_eigenvalues(i-start,2)+3.1415926535897);
        array_of_eigenvalues(i-start+1,3) = vpasolve((1-Bi)*tan(x)-x, x,
array_of_eigenvalues(i-start,3)+3.1415926535897);
    end
    i
    where = strcat('A',num2str(i));
    xlswrite(filename,array_of_eigenvalues(i-start+1,:),1,where);
end

end

function theta = GetConcentrationProfilesBolusNeumannf(eta_array, tau_array,
Cext, R, P, k0, Prx)

% Diffusivity of H2O2
D = 1.83e-9; % m^2/s

% Parameters for peroxiredoxin
kPrxOxH2O2 = 1.3e7; % M^-1*s^-1
k1 = Prx*kPrxOxH2O2; % s^-1

% Calculation of dimensionless numbers
Bi = P*R/D;
Da0 = k0*R^2/(D*Cext*Bi);
Da1 = k1*R^2/D;

```

```

% Initialize matrix for dimensionless concentration
theta = zeros(length(eta_array), length(tau_array));

% Calculate dimensionless concentration at each dimensionless length and
% time
for i=1:length(tau_array)
    for k=1:length(eta_array)
        theta(k,i) = 1/(Da1^0.5*cosh(Da1^0.5) -
sinh(Da1^0.5))*sinh(Da1^0.5*eta_array(k))/eta_array(k);
    end
end

end

function theta = GetConcentrationProfilesBolusNeumannG(eta_array, tau_array,
Cext, R, P, k0, Prx)

% Diffusivity of H2O2
D = 1.83e-9; % m^2/s

% Parameters for peroxiredoxin
kPrxOxH2O2 = 1.3e7; % M^-1*s^-1
k1 = Prx*kPrxOxH2O2; % s^-1

% Calculation of dimensionless numbers
Bi = P*R/D;
Da0 = k0*R^2/(D*Cext*Bi);
Da1 = k1*R^2/D;

% Initialize matrix for dimensionless concentration
theta = zeros(length(eta_array), length(tau_array));

% Calculate dimensionless concentration at each dimensionless length and
% time
for i=1:length(tau_array)
    for k=1:length(eta_array)
        theta(k,i) = Da0/Da1*(1-exp(-Da1*tau_array(i)));
    end
end

end

function theta = GetConcentrationProfilesBolusNeumannFFT(eta_array,
tau_array, eigenvalues, num_eig, Cext, R, P, k0, Prx)

% Diffusivity of H2O2
D = 1.83e-9; % m^2/s

% Parameters for peroxiredoxin
kPrxOxH2O2 = 1.3e7; % M^-1*s^-1
k1 = Prx*kPrxOxH2O2; % s^-1

% Calculation of dimensionless numbers
Bi = P*R/D;

```

```

Da0 = k0*R^2/(D*Cext*Bi);
Da1 = k1*R^2/D;

% Initialize matrix for dimensionless concentration
theta = zeros(length(eta_array), length(tau_array));

% Calculate dimensionless concentration at each dimensionless length and
% time
for i=1:length(tau_array)
    for k=1:length(eta_array)
        big_sum = 0;
        for j=1:num_eig
            eig = eigenvalues(j);
            term = 1/(Da1+eig^2)*exp(-(eig^2+Da1)*tau_array(i))*...
                sin(eig*eta_array(k))/eta_array(k)/sin(eig);
            big_sum = big_sum+term;
        end
        theta(k,i) = (Da0-3)/Da1*exp(-Da1*tau_array(i))-2*big_sum;
    end
end

end

function theta = GetConcentrationProfilesBolusNeumannSS(eta_array, tau_array,
Cext, R, P, k0, Prx)

% Diffusivity of H2O2
D = 1.83e-9; % m^2/s

% Parameters for peroxiredoxin
kPrxOxH2O2 = 1.3e7; % M^-1*s^-1
k1 = Prx*kPrxOxH2O2; % s^-1

% Calculation of dimensionless numbers
Bi = P*R/D;
Da0 = k0*R^2/(D*Cext*Bi);
Da1 = k1*R^2/D;

% Initialize matrix for dimensionless concentration
theta = zeros(length(eta_array), length(tau_array));

% Calculate dimensionless concentration at each dimensionless length and
% time
for i=1:length(tau_array)
    for k=1:length(eta_array)
        theta(k,i) = 1/(Da1^0.5*cosh(Da1^0.5)-
sinh(Da1^0.5))*sinh(Da1^0.5*eta_array(k))/eta_array(k)+Da0/Da1;
    end
end

end

```

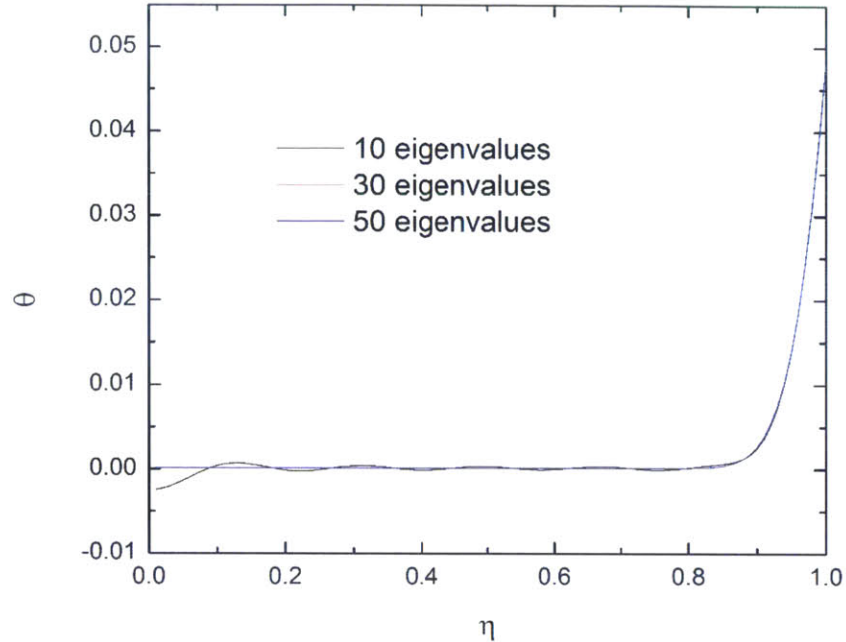


Figure C.1. Convergence of analytical solution based on FFT at 0.1 ms. The solutions using 30 eigenvalues and 50 eigenvalues overlap, showing that 30 eigenvalues is sufficient for convergence.

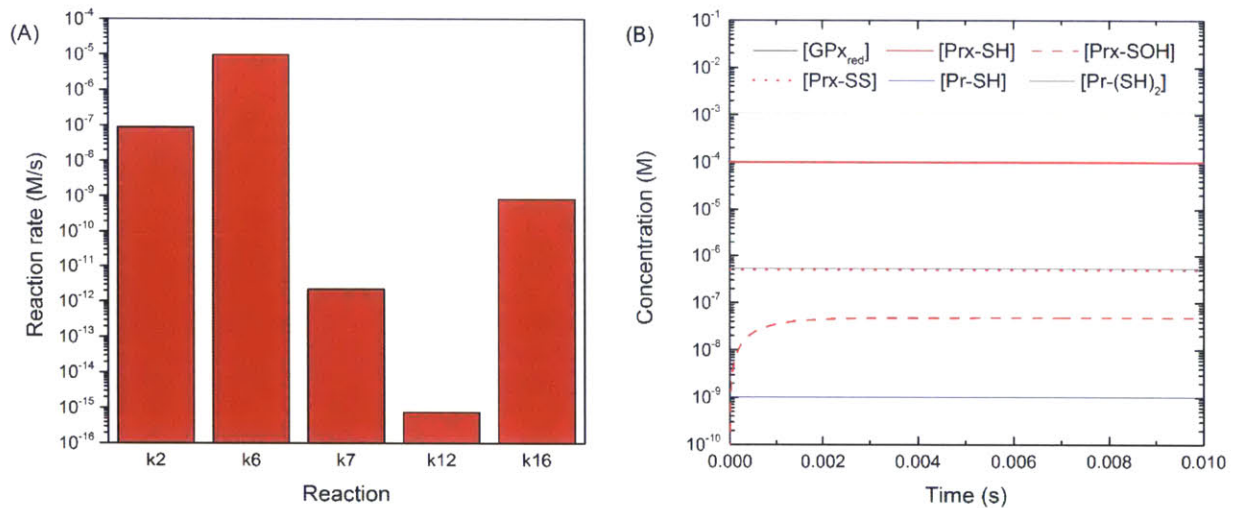


Figure C.2. (A) Rates of reactions directly involved in H_2O_2 scavenging with initial $[\text{H}_2\text{O}_2]$ of $0.05 \mu\text{M}$. Each reaction is designated by its accompanying rate constant as shown in Table 5.1; k_2 , for instance, indicates the reaction $k_2 ([\text{H}_2\text{O}_2]) ([\text{GPx}_{\text{red}}])$. (B) Concentrations of antioxidant enzymes directly involved in H_2O_2 scavenging over time with initial $[\text{H}_2\text{O}_2]$ of $0.05 \mu\text{M}$.

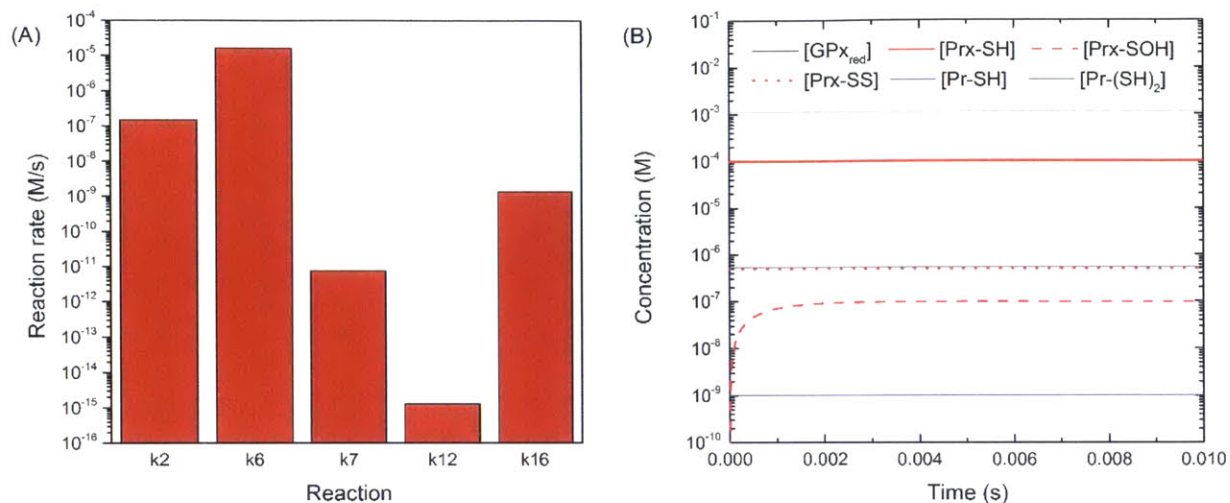


Figure C.3. (A) Rates of reactions directly involved in H_2O_2 scavenging with initial $[\text{H}_2\text{O}_2]$ of $0.1 \mu\text{M}$. Each reaction is designated by its accompanying rate constant as shown in Table 5.1; k2, for instance, indicates the reaction k_2 ($[\text{H}_2\text{O}_2]$) ($[\text{GPx}_{\text{red}}]$). (B) Concentrations of antioxidant enzymes directly involved in H_2O_2 scavenging over time with initial $[\text{H}_2\text{O}_2]$ of $0.1 \mu\text{M}$.

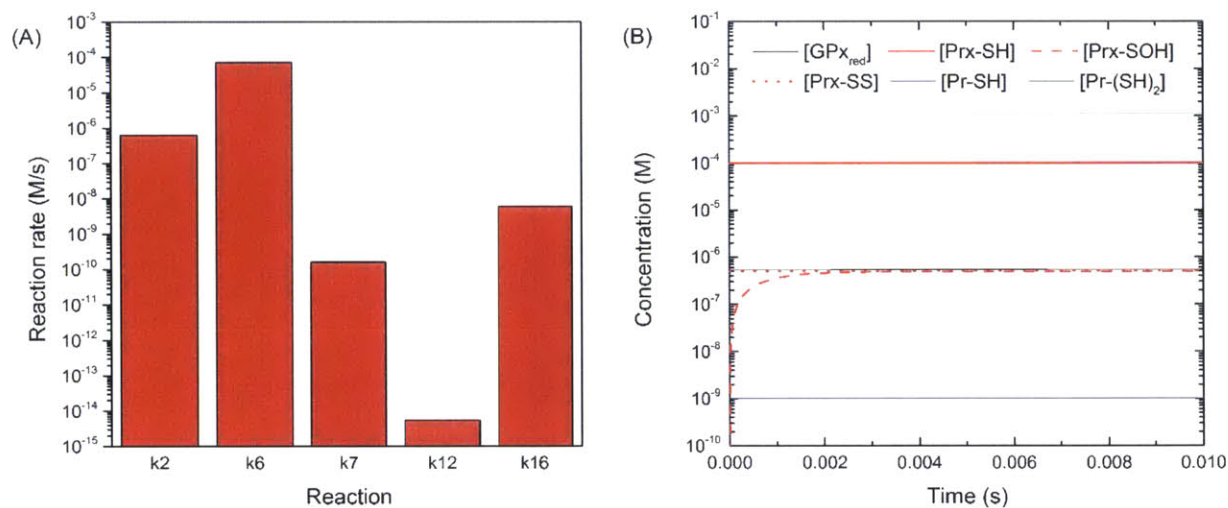


Figure C.4. (A) Rates of reactions directly involved in H_2O_2 scavenging with initial $[\text{H}_2\text{O}_2]$ of $0.5 \mu\text{M}$. Each reaction is designated by its accompanying rate constant as shown in Table 5.1; k2, for instance, indicates the reaction k_2 ($[\text{H}_2\text{O}_2]$) ($[\text{GPx}_{\text{red}}]$). (B) Concentrations of antioxidant enzymes directly involved in H_2O_2 scavenging over time with initial $[\text{H}_2\text{O}_2]$ of $0.5 \mu\text{M}$.

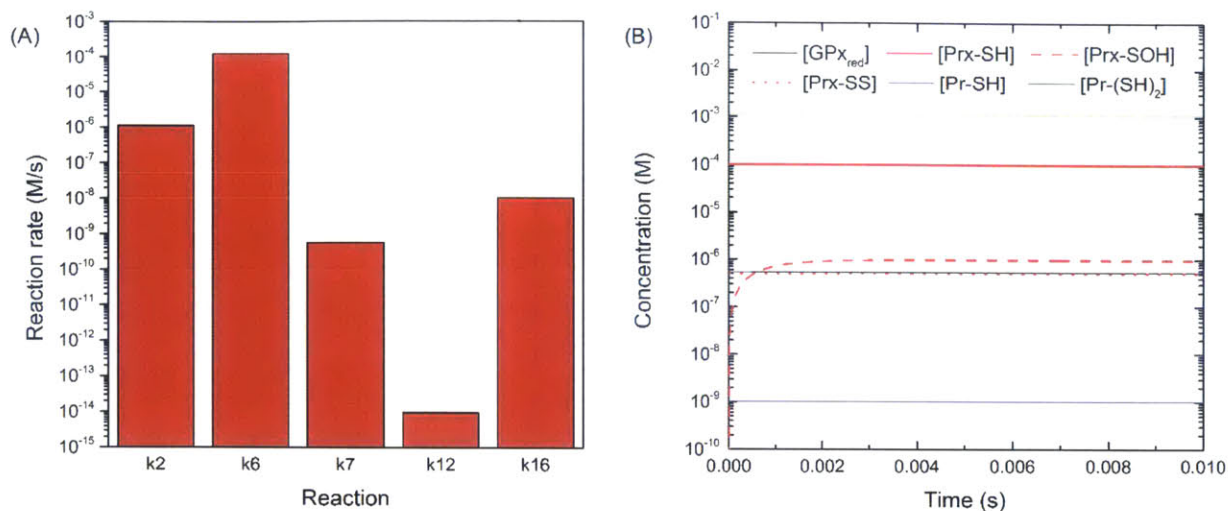


Figure C.5. (A) Rates of reactions directly involved in H_2O_2 scavenging with initial $[\text{H}_2\text{O}_2]$ of $1 \mu\text{M}$. Each reaction is designated by its accompanying rate constant as shown in Table 5.1; k2, for instance, indicates the reaction k_2 ($[\text{H}_2\text{O}_2]$) ($[\text{GPX}_{\text{red}}]$). (B) Concentrations of antioxidant enzymes directly involved in H_2O_2 scavenging over time with initial $[\text{H}_2\text{O}_2]$ of $1 \mu\text{M}$.

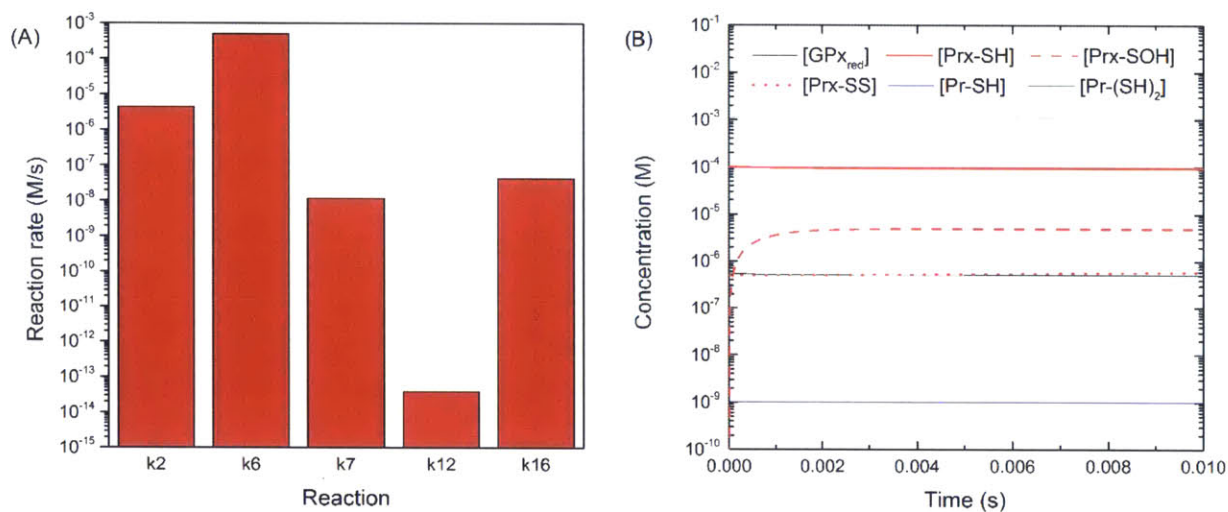


Figure C.6. (A) Rates of reactions directly involved in H_2O_2 scavenging with initial $[\text{H}_2\text{O}_2]$ of $5 \mu\text{M}$. Each reaction is designated by its accompanying rate constant as shown in Table 5.1; k2, for instance, indicates the reaction k_2 ($[\text{H}_2\text{O}_2]$) ($[\text{GPX}_{\text{red}}]$). (B) Concentrations of antioxidant enzymes directly involved in H_2O_2 scavenging over time with initial $[\text{H}_2\text{O}_2]$ of $5 \mu\text{M}$.

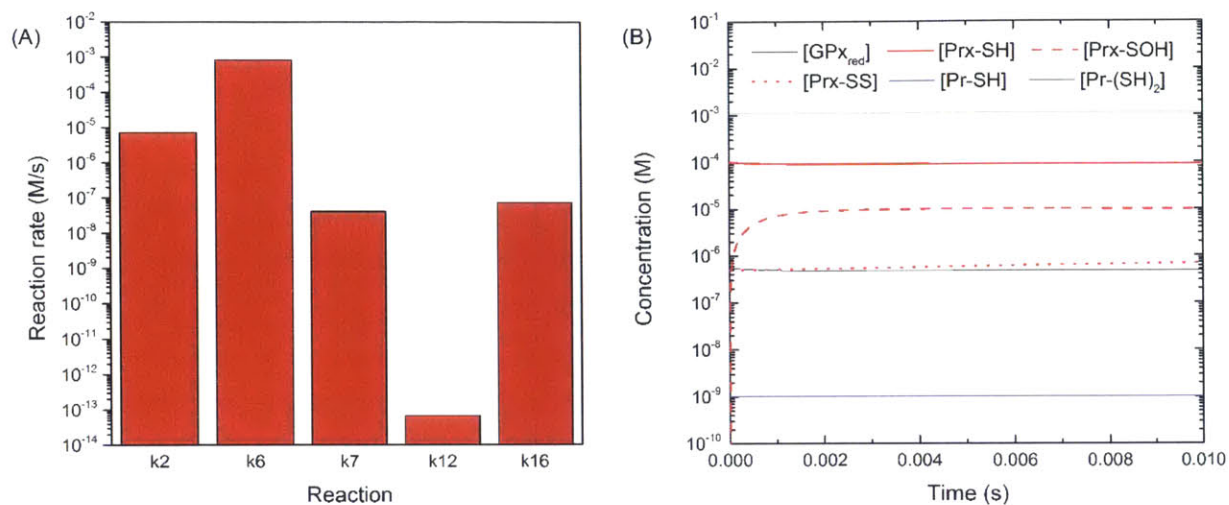


Figure C.7. (A) Rates of reactions directly involved in H_2O_2 scavenging with initial $[\text{H}_2\text{O}_2]$ of $10 \mu\text{M}$. Each reaction is designated by its accompanying rate constant as shown in Table 5.1; k2, for instance, indicates the reaction $k_2 ([\text{H}_2\text{O}_2]) ([\text{GPx}_{\text{red}}])$. (B) Concentrations of antioxidant enzymes directly involved in H_2O_2 scavenging over time with initial $[\text{H}_2\text{O}_2]$ of $10 \mu\text{M}$.

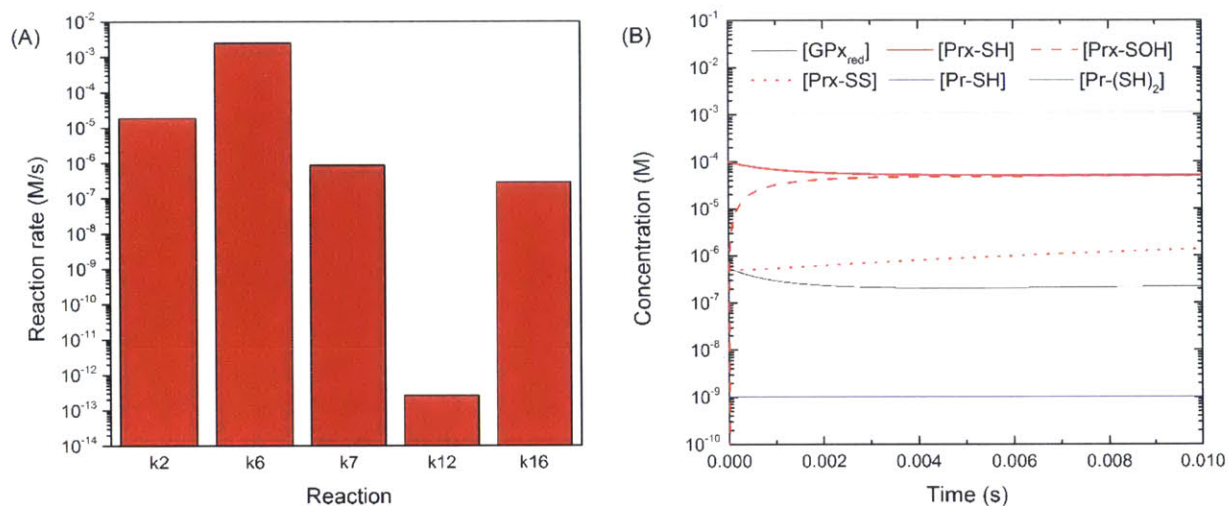


Figure C.8. (A) Rates of reactions directly involved in H_2O_2 scavenging with initial $[\text{H}_2\text{O}_2]$ of $50 \mu\text{M}$. Each reaction is designated by its accompanying rate constant as shown in Table 5.1; k2, for instance, indicates the reaction $k_2 ([\text{H}_2\text{O}_2]) ([\text{GPx}_{\text{red}}])$. (B) Concentrations of antioxidant enzymes directly involved in H_2O_2 scavenging over time with initial $[\text{H}_2\text{O}_2]$ of $50 \mu\text{M}$.

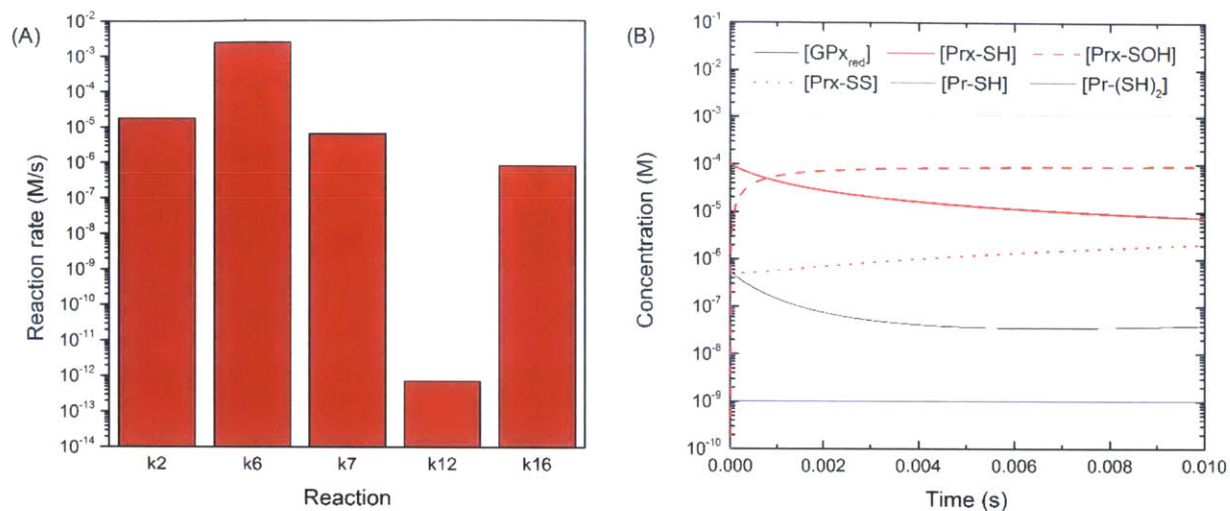


Figure C.9. (A) Rates of reactions directly involved in H_2O_2 scavenging with initial $[\text{H}_2\text{O}_2]$ of $100 \mu\text{M}$. Each reaction is designated by its accompanying rate constant as shown in Table 5.1; k2, for instance, indicates the reaction k_2 ($[\text{H}_2\text{O}_2]$) ($[\text{GPx}_{\text{red}}]$). (B) Concentrations of antioxidant enzymes directly involved in H_2O_2 scavenging over time with initial $[\text{H}_2\text{O}_2]$ of $100 \mu\text{M}$.

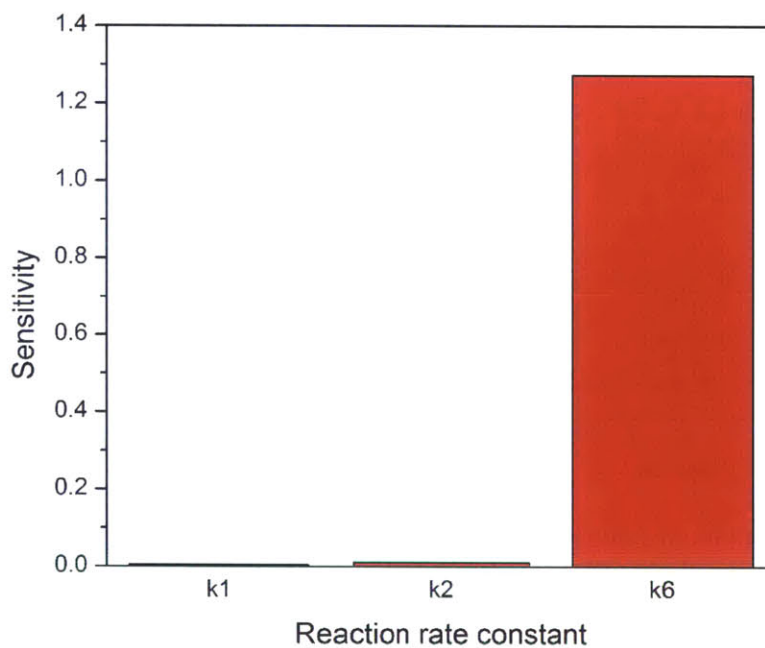


Figure C.10. Sensitivity of $[\text{H}_2\text{O}_2]$ to reaction rate constants with initial $[\text{H}_2\text{O}_2]$ of $0.05 \mu\text{M}$. Other reaction rate constants were not shown because the sensitivities of $[\text{H}_2\text{O}_2]$ to those parameters were at least one order of magnitude less than the lowest sensitivity shown in the plot, and thus would not have been visible.

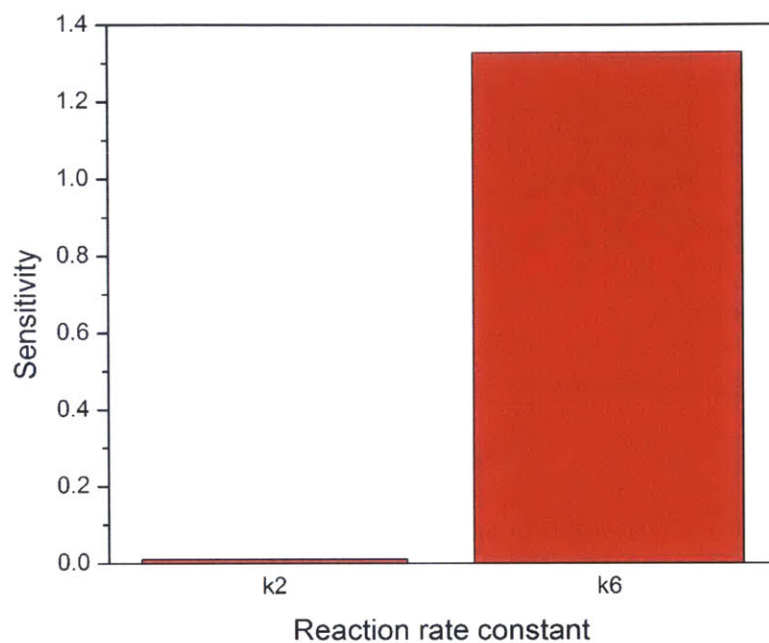


Figure C.11. Sensitivity of $[H_2O_2]$ to reaction rate constants with initial $[H_2O_2]$ of $0.1 \mu M$. Other reaction rate constants were not shown because the sensitivities of $[H_2O_2]$ to those parameters were at least one order of magnitude less than the lowest sensitivity shown in the plot, and thus would not have been visible.

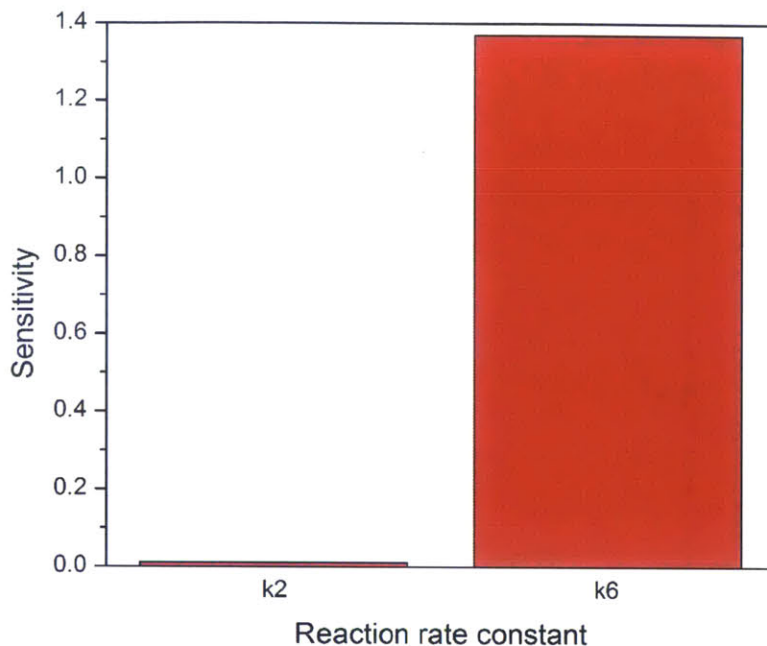


Figure C.12. Sensitivity of $[H_2O_2]$ to reaction rate constants with initial $[H_2O_2]$ of $0.5 \mu M$. Other reaction rate constants were not shown because the sensitivities of $[H_2O_2]$ to those parameters were at least one order of magnitude less than the lowest sensitivity shown in the plot, and thus would not have been visible.

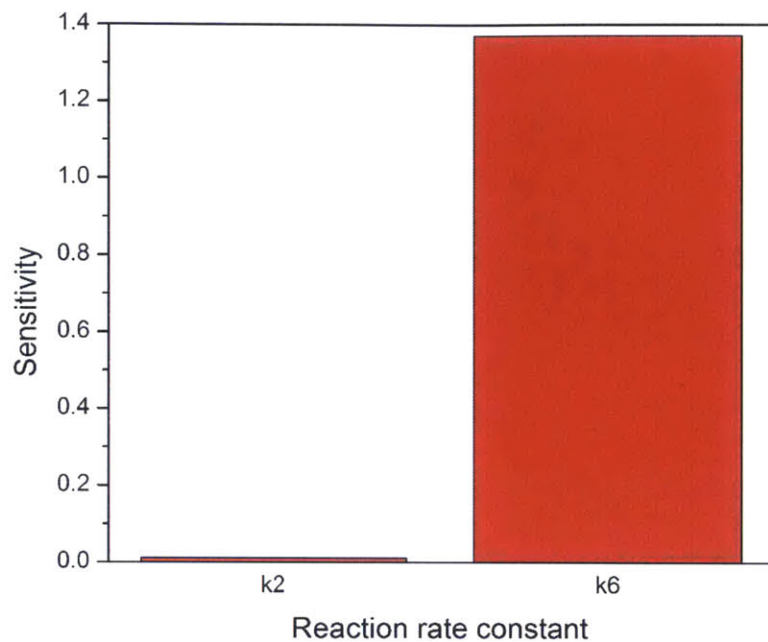


Figure C.13. Sensitivity of $[H_2O_2]$ to reaction rate constants with initial $[H_2O_2]$ of $1 \mu M$. Other reaction rate constants were not shown because the sensitivities of $[H_2O_2]$ to those parameters were at least one order of magnitude less than the lowest sensitivity shown in the plot, and thus would not have been visible.

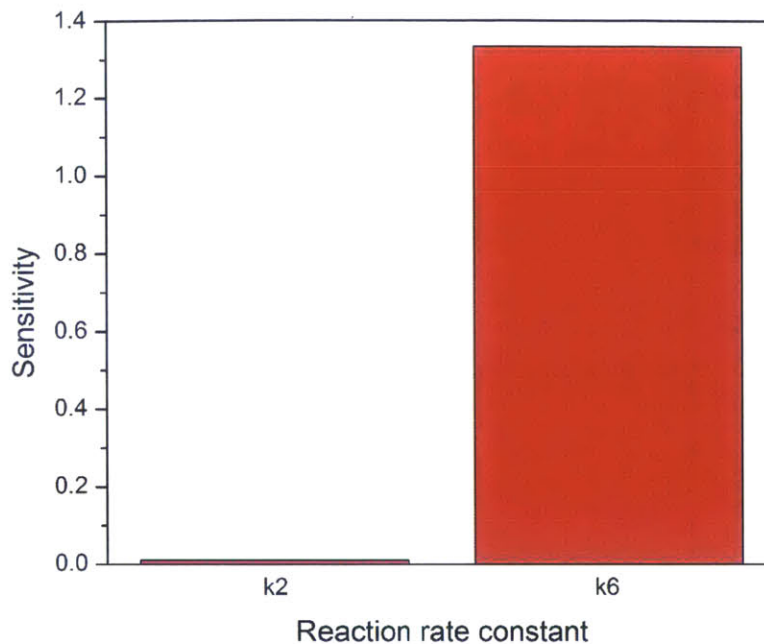


Figure C.14. Sensitivity of $[H_2O_2]$ to reaction rate constants with initial $[H_2O_2]$ of $5 \mu M$. Other reaction rate constants were not shown because the sensitivities of $[H_2O_2]$ to those parameters were at least one order of magnitude less than the lowest sensitivity shown in the plot, and thus would not have been visible.

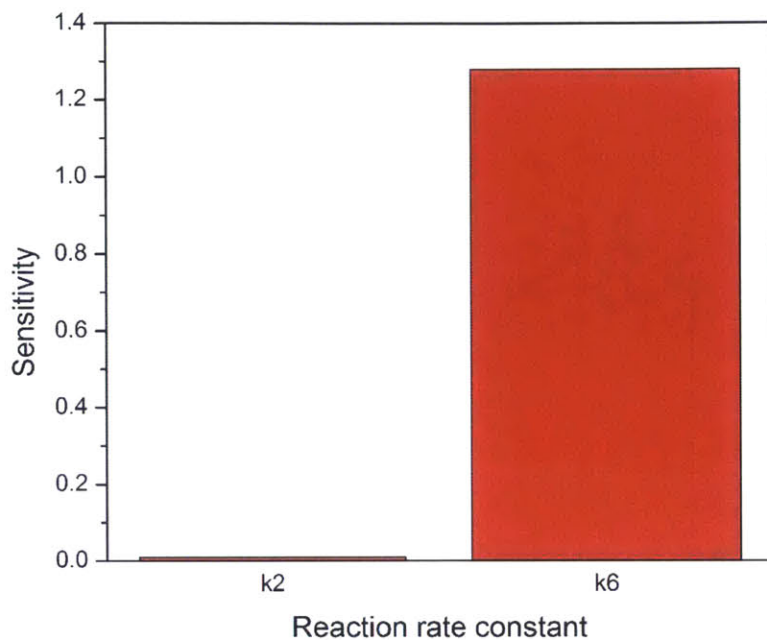


Figure C.15. Sensitivity of $[H_2O_2]$ to reaction rate constants with initial $[H_2O_2]$ of $10 \mu M$. Other reaction rate constants were not shown because the sensitivities of $[H_2O_2]$ to those parameters were at least one order of magnitude less than the lowest sensitivity shown in the plot, and thus would not have been visible.

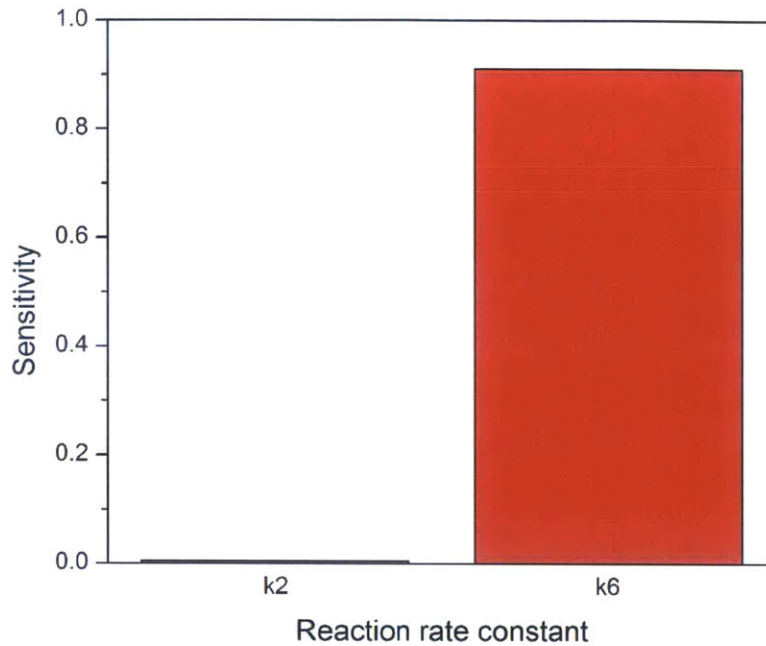


Figure C.16. Sensitivity of $[H_2O_2]$ to reaction rate constants with initial $[H_2O_2]$ of $50 \mu M$. Other reaction rate constants were not shown because the sensitivities of $[H_2O_2]$ to those parameters were at least one order of magnitude less than the lowest sensitivity shown in the plot, and thus would not have been visible.

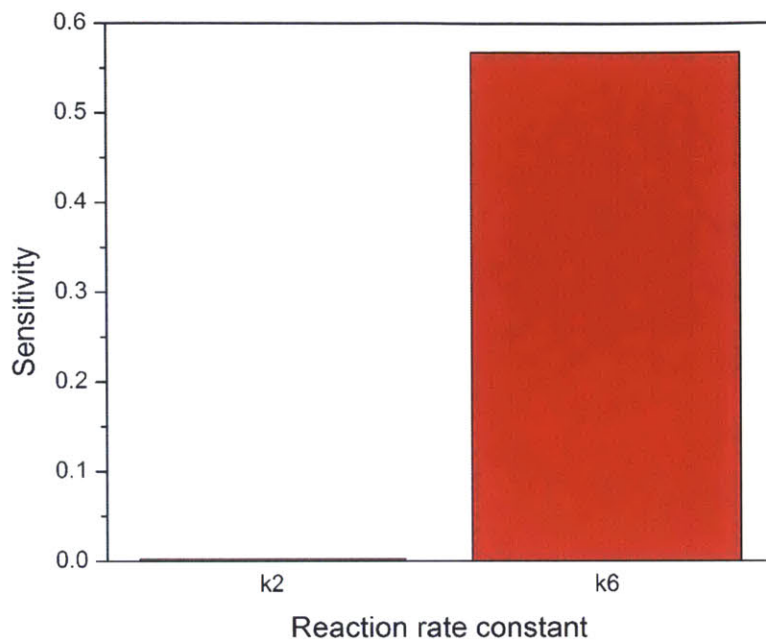


Figure C.17. Sensitivity of $[H_2O_2]$ to reaction rate constants with initial $[H_2O_2]$ of $100 \mu M$. Other reaction rate constants were not shown because the sensitivities of $[H_2O_2]$ to those parameters were at least one order of magnitude less than the lowest sensitivity shown in the plot, and thus would not have been visible.

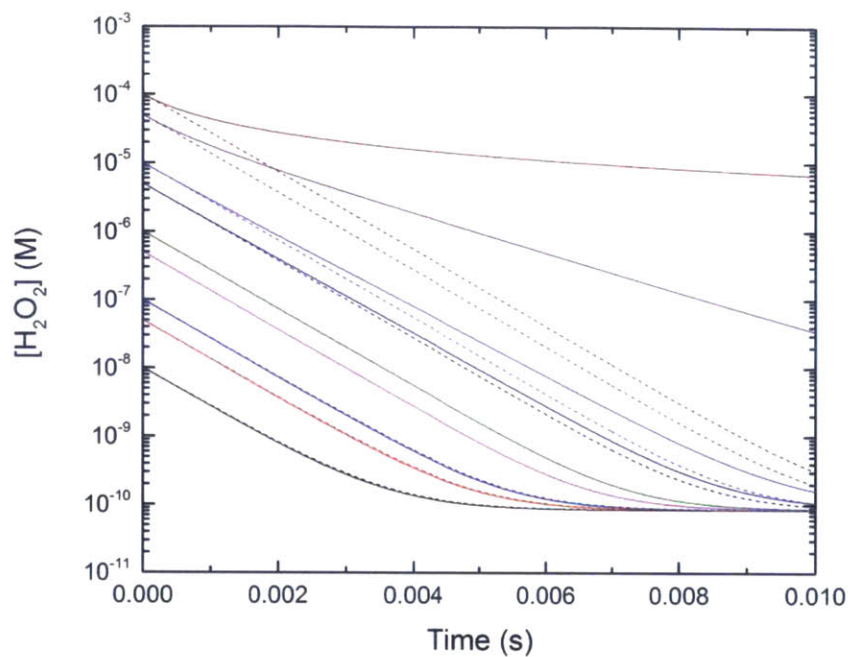


Figure C.18. Simulated kinetic curves for clearance of a pulsed addition of H_2O_2 to baseline levels in a single control volume. Solid curves represent the original complete model sans transfer of H_2O_2 to other compartments, such as extracellular media or peroxisomes. Dashed curves represent a simplified model in which only H_2O_2 generation and scavenging by Prxs, without any oxidation of the enzyme, are simulated as an analytical equation. Solid and dashed curves overlap except at initial concentrations greater than $1 \mu\text{M}$, which are not physiologically relevant, as noted in the main text.

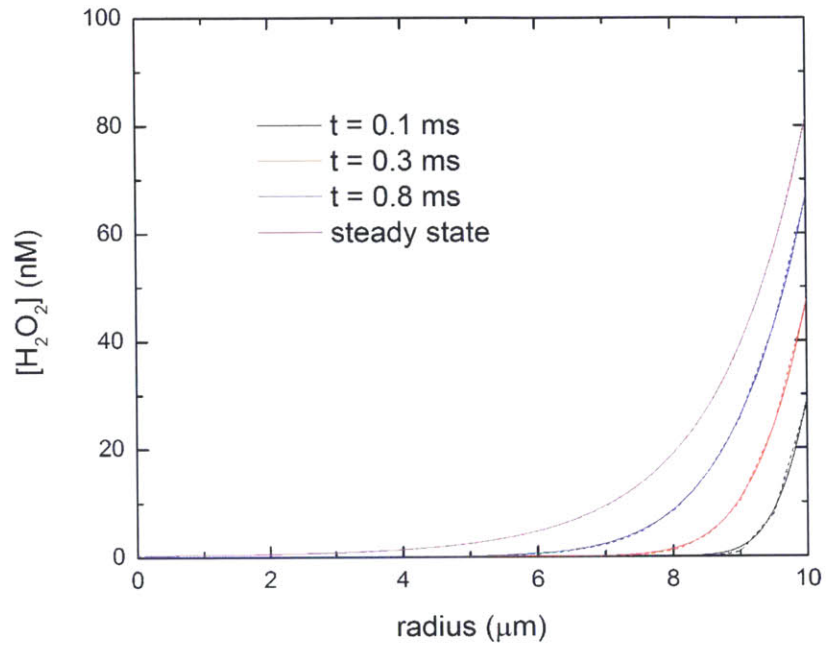


Figure C.19. Development of intracellular concentration profile of H_2O_2 after bolus addition of $25 \mu M$ with analytical (solid) and computational solutions (dashed). Computational solutions were generated by COMSOL software and overlap with analytical solutions at all time points considered and steady state. An “extra fine” mesh was used for the computational solution. Subtle but certainly visible differences were seen between the two solutions, particularly at earlier time points (e.g. at 0.1 ms).